LEGIBILITY NOTICE

A major purpose of the Technical Information Center is to provide the broadest dissemination possible of information contained in DOE's Research and Development Reports to business, industry, the academic community, and federal, state and local governments.

Although a small portion of this report is not reproducible, it is being made available to expedite the availability of information on the research discussed herein.

ANL/APS-TM--4

DE90 000163

ARGONNE NATIONAL LABORATORY
9700 South Cass Avenue
Argonne, Illinois 60439

ANL/APS-TM-4

CHEMICAL APPLICATIONS OF SYNCHROTRON RADIATION: WORKSHOP REPORT

Argonne National Laboratory
October 3-4, 1988

Workshop Co-Chairs

Mark Beno, Chemistry Division

Stuart Rice, The University of Chicago

April 1989

work sponsored by

U. S. DEPARTMENT OF ENERGY
Office of Energy Research

CONTENTS

CONTENTS (CONT'D)

ACKNOWLEDGMENTS

The Workshop on Chemical Applications of Synchrotron Radiation was jointly sponsored by the Advanced Photon Source Users Organization, the Chemistry Division and the Division of Educational Programs at Argonne National Laboratory, and The University of Chicago. The workshop organizers wish to express their thanks to the sponsors for making this meeting possible and to all the invited speakers for sharing their research and their insights.

The workshop organizers also wish to thank their colleagues at Argonne who served as session chairpersons: Lynda Soderholm, Pappannan Thiyagarajan, and Randall Winans. Also at Argonne, thanks go to Bonnie Meyer of the Advanced Photon Source Division for making sure the workshop proceeded smoothly.

CHEMICAL APPLICATIONS OF SYNCHROTRON RADIATION: WORKSHOP REPORT

ABSTRACT

The most recent in a series of topical meetings for Advanced Photon Source user subgroups, the Workshop on Chemical Applications of Synchrotron Radiation (held at Argonne National Laboratory, October 3-4, 1988) dealt with surfaces and kinetics, spectroscopy, small-angle scattering, diffraction, and topography and imaging. The primary objectives were to provide an educational resource for the chemistry community on the scientific research being conducted at existing synchrotron sources and to indicate some of the unique opportunities that will be made available with the Advanced Photon Source. The workshop organizers were also interested in gauging the interest of chemists in the field of synchrotron radiation. Interest expressed at the meeting has led to initial steps toward formation of a Chemistry Users Group at the APS.

INTRODUCTION

The Advanced Photon Source (APS), to be constructed at Argonne National Laboratory in the early 1990s, will provide high-energy x-rays with a brightness 10,000 times that currently available. This facility will provide a unique resource for cutting-edge research in many areas of science and technology, including materials science, geosciences, physics, biotechnology, medicine, biochemistry, biology, and chemistry. Synchrotron radiation has provided an invaluable probe for chemical researchers in such diverse fields as spectroscopy, surface science, molecular structure, imaging, and dynamics. Future applications to chemical problems that may become possible with a third-generation synchrotron source such as the APS include the ability to determine structures of materials using single crystals as small as one-micron and to study intermediates formed during fast chemical reactions.

The Workshop on Chemical Applications of Synchrotron Radiation was held to provide an educational resource for the chemistry community on the scientific research being conducted at current synchrotron sources and to indicate some of the extensions and unique opportunities that will be available with the enhanced capabilities of the APS. The workshop attempted to cover synchrotron studies in six different research areas: (1) Surfaces and kinetics; (2) spectroscopy, including EXAFS and XANES; (3) small-angle scattering; (4) single-crystal and powder diffraction studies; (5) topography and imaging; and (6) time-dependent phenomena. The speakers were asked to include tutorial material, as well as to summarize current, state-of-the-art applications of synchrotron radiation and to offer challenges for the future.

Although the short-time format for the workshop did not allow a complete presentation of even this limited number of topics in possible chemical applications of synchrotron radiation, those who attended the meeting were generally pleased with the sampling of topics that were included. The interest and enthusiasm expressed at the meeting has led the workshop organizers to initiate steps toward the formation of a Chemistry Users Group at the APS.

SESSION I

SURFACES AND KINETICS

The Use of X-Ray Reflectivity as a Surface Probe

Eric B. Sirota

Corporate Research Science Laboratories,
Exxon Research and Engineering Company
Route 22 East, Annandale, NJ 08801

The technique of using the reflection of x-rays from a surface to probe the electron density profile of that surface and overlayers is described with attention to data interpretation and experimental method. Examples of experiments on 3 systems are given: precursor wetting films of water, swelling of adsorbed polymers in solvent and melting of adsorbed phospholipids.

* work presented here was done in collaboration with S.K. Sinha and S. Garoff

X-ray reflectivity is a powerful probe for the investigation of surfaces and materials on surfaces. The specular reflection of x-rays from a surface gives us information regarding the average electron density profile in the direction normal to the surface.[1] Diffuse scattering in the vicinity of the specular reflection provides information regarding the lateral roughness or inhomogeneities in the electron density near the surface. [2]. This technique is complimentary to grazing incidence x-ray scattering (GIXS) [3] which probes the in-plane structure.

PERFECT INTERFACE: We first review the Fresnel theory for reflection from a perfect interface between 2 homogeneous media. If one defines **z** as the direction normal to the surface, then the average electron density is

$\rho(z)=\rho_0$ for $z<0$ (the average density of the substrate)

$\rho(z)=0$ for $z>0$ (air differs insignificantly from vacuum).

We assume that x-rays of wavelength λ are incident at grazing angle θ ($\theta=90°$ is normal incidence), on the surface of a semi-infinite slab of index of refraction n, where n is a complex number. As long as the binding energy of the electrons is less than the energy of the x-rays, (which is the case for most lower atomic number elements) one can treat the electrons as if they were free and

$n = 1 - bN\lambda^2/2\pi + i\lambda/4\pi\, l_{abs}(\lambda)$

where $b=e^2/mc^2$, N is the electron density and $l_{abs}(\lambda)$ is the absorption length.[4] In many interesting cases, the length scales probed are larger than the atomic size and one need not be concerned with the periodicity of the substrate. By Snell's law:

$\theta_{incident} = \theta_{reflected}$ and $\cos\theta = n\cos\theta_{transmitted}$.

Since $n<1$ for x-rays, ($1-n \approx 10^{-6}$) there is Total External Reflection below a critical angle $\theta_c = \cos^{-1}(n) = \lambda\,(bN/\pi)^{1/2}$ which is ~.2° for quartz. The complex reflection amplitude is given by

$$R = (\sin\theta - n\sin\theta_T) / (\sin\theta + n\sin\theta_T), \qquad (1)$$

where the reflected intensity $I_{ref}=|R|^2$. Below θ_c the reflectivity is unity and at

large angles it falls off as q^{-4}, where $q=(4\pi/\lambda)\sin(\theta)=q_z$ (we will drop the z subscript for convenience). (see Fig. 1)

GENERAL INTERFACE: We now treat the case where the surface is flat but with a graded density profile so $\rho(z)=\rho_0$ for $z=-\infty$ and $\rho(z)=0$ for $z=\infty$. There are a number of mathematical ways of looking at this problem. For the case where the density profile is due to a truly graded interface with no lateral inhomogeneities, there is no diffuse scattering and the "matrix" or "slicing" method [5] is exact. This method involves dividing the interface into many thin slabs, each with a different density, and matching the electromagnetic boundary conditions. In practice, this method can be computationally time consuming, and for a large variety of problems, other methods will suffice.

The most useful method is the Distorted Wave Born Approximation (DWBA) which gives the result [2]

$$I_{ref} = |R|^2 \left| \int_{-\infty}^{+\infty} dz \, (d\rho(z)/dz) \, (1/\rho_0) \exp(-iz(qq_T)^{1/2}) \right|^2 \qquad (2)$$

where $q_T=(4\pi/\lambda)\sin(\theta_T)$ and R is the Fresnel reflection amplitude for a perfect interface (Eqn. 1). Below the critical angle the reflectivity is 1, (neglecting the effects of absorption) and at large q, $R\sim q^{-4}$ and $q_T=q$. The main effect of absorption is to decrease the reflectivity at small angles and smear out the sharp falloff at θ_c.

For example, the reflectivity from an interface with an Error Function density profile in $\rho(z)$ with a r.m.s width σ is

$$I_{ref} = |R|^2 \exp(-qq_T \sigma^2). \qquad (3)$$

This form is useful in characterizing the roughness of a surface using a single parameter. Variation of data from this form at large q would be due to the fact that the Error Function does not exactly describe $\rho(z)$. Figure 1 shows the reflectivity from a single surface.

Another interesting case is that of a layer of density ρ_1, thickness d, and surface roughness σ_1, on a surface of roughness σ_0 and density ρ_0 (see figure 2). The DWBA can be extended for 2 interfaces giving the following expression

for the reflectivity:

$$I_{ref} = |R|^2 \, |(\rho_0-\rho_1)\exp(-q_1 q_T \sigma_0^2/2) + \rho_1 \exp(-iq_1 d)\exp(-qq_1\sigma_1^2/2)|^2 \qquad (4)$$

where q_1 is the wavevector transfer (normal to the surface) in the middle medium. This gives minima in q_1 at odd multiples of π/d. While q, q_T and q_1 are the same for large q, near the critical angle they differ, and therefore, unless d is small, one must use the correct value for the q's to get the correct position (and depth) of the first minimum.

From the above equations, one can see that while scattering from a thin layer alone may be quite weak, in the presence of a strong Fresnel reflection, the effect of the thin layer is to modulate a rather strong signal.

GRADED VS. ROUGH INTERFACE: It is important to be aware of how the scattering would differ between the cases of 1) a sharp but jagged boundary and 2) a laterally smooth interface, both of which have the same average $\rho(z)$ (see figure 3). To first order, they both give rise to the same specular scattering; However, in the case of the laterally rough surface there is nonspecular diffuse scattering as well, while the graded interface gives no diffuse scattering. This is because it is the lateral inhomogeneities which give rise to diffuse scattering. Since we know that for the case of a graded interface, the "slicing method" gives exact results, it is useful to see where it deviates in the case of lateral roughness. If one considers 2 infinitesimally thin slabs, each with the same average density, one uniform and the other with lateral density variation, one discovers that the specular reflection from each is identical, however the nonuniform slab also gives diffuse scattering at the periodicities of the in-plane density. To conserve energy, the transmitted flux must be less in the case of the nonuniform slab; However, the forward scattering, which accounts for the reduction from unity of the transmitted flux cannot be calculated using the first order Born Approximation [6]. It is this loss which results in the reduction from unity of the reflection below the critical angle in the case of a rough interface (in the absence of absorption). While in the weak scattering limit, both the graded and rough interface will give rise to the same specular

scattering, below the critical angle, this is not necessarily true, since the graded interface gives a reflectivity identically equal to unity, losses from diffuse scattering from a rough interface must reduce that number. Whether this is a measurable effect will depend on the actual roughness. We point out that if the electron density inhomogeneity is of a length $<\lambda/2$ it cannot scatter, and the photon sees the average density.

COHERENCE: An important question which arises is: Over what lateral length scale should one average the electron density to determine the r.m.s. roughness or, in general $\rho(z)$? Clearly, if the surface was microscopically smooth over a short length scale, but with 50Å steps every millimeter, one would get the reflectivity of a smooth surface which did not fall off as $\exp(-(50q)^2)$. One must then determine over what distance along the surface can x-rays reflect, and be able to interfere with each other. Since currently available x-ray sources are not phase coherent in the sense that different photons do not have a well defined phase relationship with each other, interference can only occur between a photon and itself. From the energy ($\Delta\lambda$) and angular ($\Delta q_\perp$) spread of the radiation source, and any filters such as a perfect crystal monochromator, one can determine (from the uncertainty principle) the effective "length" and "width" of the photon, and geometrically determine whether it can interfere with itself. Consider 2 parallel rays separated by Δx, incident on the surface at angle θ, and specularly reflected; such rays are probing points on the surface $r=\Delta x/\sin\theta$ apart. Since at specular reflection there is no path length difference for parallel rays, the coherence is determined by the effective width of the wavefront. For an 8keV photon with 0.005° divergence (typical for synchrotron monochromators) $\Delta q_\perp \Delta x = 2\pi$ yields $\Delta x \sim 10000$Å, thus, at $\theta=2°$, $r \sim 3\times10^5$Å, a macroscopic distance. The resolution in the direction out of the scattering plane is usually not as narrow, so the shape of the area involved in coherent scattering will in general be anisotropic.

One can apply the idea of scattering coherently and incoherently to a case of a smooth substrate ($\sigma_0=0$) with a film of average thickness d, but with local variations in thickness on many length scales. Variations in the local thickness on lateral length scales shorter than the coherence length are taken

as the roughness σ_1 in equation 4. Variations in thickness on longer length scales must be taken into account by incoherently adding I_{ref} for a range of values of d.

CONFORMAL ROUGHNESS: In the case where one has a rough substrate (ρ_0, σ_0), and a rough layer (ρ_1, σ_1), the specular reflectivity is independent of whether the roughnesses are conformal (i.e. whether the hills and valleys of the overlayer coincide with the hills and valleys of the substrate). However, if one measures the diffuse scattering along q_z at finite $q_\perp$ (in-plane), conformality of the roughness will give rise to oscillations in the diffuse scattering similar to the observed oscillation in the specular reflectivity due to the thickness of the overlayer [7]. Figure 4 shows conformal and non-conformal roughness.

EXPERIMENTS: To perform a reflectivity experiment, one requires a well defined incident beam, narrow enough in the direction of the scattering plane, that its projection will not be larger than the sample at small incident angles. It is also important that the substrate be as macroscopically flat as possible (minimum "figure error"). Slits are usually sufficient to define the reflected radiation before the detector. The specular reflection is measured by translating the surface to the center of the beam, finding the specular reflection by sitting at a fixed scattering angle and rocking the sample; and then measuring the reflectivity using a θ-2θ scan. Since the spectrometer's resolution function is not a true δ-function, a finite amount of diffuse scattering will be detected along with the specular. This scattering can be subtracted out by misseting the crystal just off the specular condition, and measuring the diffuse scattering. While in the Born Approximation and in the limiting case where $q_z\sigma<<1$, the component of roughness with in-plane wavevector k_r, gives rise to diffuse scattering k_r away from the specular. The scattering at that position is equal to the reduction in the specular reflection caused by that roughness component only in the above limit. For large $q_z\sigma$, diffuse scattering will also occur at higher harmonics of k_r (see Eqn. 2.26 of reference 2). While within the above limit, one can choose to open the detector slits and accept

more diffuse scattering (instead of subtracting it off of the specular) and thus effectively decrease the lateral length scale over which $\rho(z)$ is averaged.

One should be aware that due to the enhanced electric field at the surface caused by the standing wave formed by the incident and reflected waves, there are peaks in the diffuse scattering ("angel's wings", "anomalous reflections", "Yoneda reflections") when either the incident or the scattered ray makes an angle of θ_c with the surface. [2,8] Such peaks can be stronger than the specular reflection if the surface is very rough. It is, in fact, this enhancement of surface scattering near the critical angle, which is the basis for GIXS. A few examples of systems where reflectivity is an important probe are described below.

PRECURSOR WETTING FILM: One such experiment by Garoff, Sirota, Sinha and Stanley [7] involved measuring the reflectivity from a vertical glass substrate under dry conditions; in a high humidity water vapor atmosphere; and while the bottom was in contact with bulk water. From the dry measurement the roughness of the glass could be determined and was σ_0=7.6Å. The humid conditions gave a film of thickness d=14Å with an r.m.s. roughness σ_1=5.2Å. When in contact with bulk water a precursor film was measured to have thickness d=90Å with r.m.s. roughness σ_1=4.2Å. In this case the diffuse scattering measured near the specular peak showed that the roughness was laterally conformal at least on length scales ≥5000Å. A novel geometry was developed by Als-Nielsen and Pershan [9], to bend the incident beam downwards and thereby perform reflectivity measurements on liquid surfaces where the sample must remain horizontal. This technique was used by Braslau et al.[10] to measure the specular reflectivity and thus the roughness of a bulk water surface. They showed that the Gaussian width of the interface was 3.2Å, which is consistent with thermally generated capillary waves. In the thicknesses of the films in Garoff et al.'s [7] experiment, one would not expect substantial roughness contributions from capillary waves which get cut off at wavelengths comparable to the water depth.[11] From this data, one can see that as the water layer gets thicker the roughness imposed by the substrate decreases and is consistent with the roughness remaining conformal on length

scales greater than the thickness. By measuring the reflectivity as a function of height and history (advancing and receding) information regarding this system was obtained [7].

PHYSISORBED SURFACTANT MONOLAYER: Reflectivity has also been used to study the properties of a physisorbed monolayer of DSPC (C18-Phosphotidylcholine) on a SiO_2 surface.[12] One can use reflectivity to determine the density profile normal to the surface. Since the molecules can rearrange themselves on the surface, interesting phase transitions can take place in such systems. Of particular interest is the in-plane structure and the effect of temperature on such a monolayer. To study the in-plane structure one must perform grazing incidence x-ray scattering (GIXS) using synchrotron radiation. Using reflectivity, detailed information regarding $\rho(z)$ can be obtained. Even with a conventional x-ray source, reflectivity can yield a great deal of information regarding the average layer thickness, coverage, transition temperatures, reproducibility and kinetics.

In this case, the phospholipid was deposited on a cleaned substrate by immersing it in a dilute chloroform solution and allowing the excess solution, to run off before evaporating. In contrast to the GIXS work of Seul, Eisenberger and McConnell [13], where the monolayer sat "heads up" on a silanated substrate, these monolayers are "heads down". The measurements were carried out in a temperature controlled cell containing dry nitrogen. Upon initial heating to a temperature below 60°C the thickness of the monolayer increased irreversibly from ~24.3Å to 25.7Å. As long as the temperature did not exceed 60°C this change was irreversible. This may be due to a change in structure caused by the expulsion of trapped solvent or water. The sample thus prepared would not change thickness as the temperature was varied reversibly between 22°C and 60°C, however, the depth of the first minimum would increase systematically and reproducibly as the temperature was increased over that range. This is consistent with an increased roughness of the surface containing the hydrocarbon tails of the monolayer. At a temperature between 60°C and 65°C, the thickness of the monolayer begins to decrease. The rate of decrease increased with increasing temperature. For example, at 70°C the spacing

decreases to 22.9Å over a period of 50 hours, while at 92°C it takes 9 hours. One can interpret this result as a chain melting transition, which is know to occur in that temperature range in bulk samples [14]. In order for this transition to occur in such a monolayer, the surface area per molecule must increase and desorption must occur. Unlike chemisorbed systems where the surfactant is strongly bound to the substrate (such as silanes studied in detail using x-ray reflectivity by Tidswell et al.[15]), phospholipids can move about the surface. The kinetics, however, appear to be rather slow. Upon cooling the average spacing appears to increase again, but very slowly. After cooling from a spacing of 19.8Å, an average thickness of 25Å was observed after 3 weeks, however, the first minimum was not as deep as before desorption. This is suggestive of the possibility that the molecules are desorbed from the surface and upon cooling, one eventually gets large patches of ordered surfactants and regions of lower coverage.

Clearly such reflectivity data does not totally characterize the system, and more detailed measurement (using the synchrotron source) can yield data which can determine the normal density profile more precisely. Synchrotron GIXS is necessary to determine unambiguously the in-plane structure, but reflectivity is an extremely powerful tool. The above measurements were done using reflectivity on a rotating anode, and clearly with such slow kinetics, it would not be feasible to carry out this measurement at the synchrotron alone. By using reflectivity with an in-house x-ray source, one can precharacterize a system, and then use the synchrotron to determine the details of the density profile as well as in-plane structure.

ADSORBED POLYMERS: Another example of the use of x-ray reflectivity is to study the density profile of an adsorbed polymer. Clearly, the experimental method and interpretation would be straightforward for a polymer at a solid-gas interface. However, one of the interesting problems is what happens to the density profile of absorbed polymers in different types of solvents. X-rays experience a large amount of attenuation on passing through bulk solvent, however the flux produced by a synchrotron source can compensate for this. Neutron reflectivity on such systems has been employed

[16] by having the neutrons incident through a single crystal quartz substrate. This trick cannot be employed in the case of x-rays. With neutrons, however, the maximum incident flux is quite low (~10^6), while one can get 10^8 photons/sec from a rotating anode and >10^{12} at a synchrotron. We have found [16] that by stretching very thin mylar (such as that used in capacitors) over the substrate, one can trap a thin layer of solvent underneath. Since the mylar is not nearly as smooth or as flat as the quartz substrate, the air-mylar and mylar-solvent interfaces do not give a specular peak. They do give rise to relatively flat diffuse scattering which can be subtracted out, as described above. The specular reflectivity can then be interpreted as described above, with the addition of a correction for the attenuation of the thin mylar and solvent which decreases with increasing angle. At the synchrotron, one can increase the energy of the photons to decrease that attenuation. Preliminary rotating anode results, showed an adsorbed polystyrene layer, which was collapsed to 40Å in air, swell to 115Å in cyclohexane.

Some other applications of x-ray reflectivity include studies of liquid surfaces[17], liquid crystal surfaces[18], surfactants on liquid surfaces, organic multilayers[19], metallic and semiconductor multilayers[20], superfluid helium wetting layers on a solid substrate[21], and roughening and melting of atomic surfaces[22].

In conclusion, it is apparent that x-ray reflectivity is a powerful technique for studying many surface problems, by itself or in conjunction with other techniques. While in-house x-ray sources provide sufficient flux for many reflectivity measurements, the high brightness of the synchrotron allows measurement over many more orders of magnitude, increasing the ability to accurately determine $\rho(z)$. In addition, the brightness of the synchrotron allows the use of very small beam sizes so that samples need not be very large. The high intensity is also needed to measure diffuse scattering.

Parts of the work presented here were done in collaboration with S.K. Sinha, S. Garoff, M. Alvarez, G. Hughes and H.B. Stanley. I wish to thank K.S. Liang, G. Hughes and S.K. Sinha for help and discussions relating to the preparation of this manuscript.

REFERENCES

1) L.G. Parratt, Phys. Rev., **95**, 359 (1954).

2) S.K. Sinha, E.B. Sirota, S. Garoff and H.B. Stanley, Phys. Rev. B, **38**, 2297 (1988), and references therein.

3) P.M. Eisenberger and A.Y. Cho, J. Appl., Phys., **50**, 6927 (1979); P.H. Fuoss, K.S. Liang and P.M. Eisenberger, in Synchrotron Radiation Research: Advances in Surface Science, ed. by R.Z. Bachrach (Plenum, New York) to appear in 1989; I.K. Robinson, in Handbook on Synchrotron Radiation, vol. 3, ed. by D.E. Moncton (North-Holland, Amsterdam) 1987.

4) B.E. Warren, X-Ray Diffraction, (Addison-Wesley, Reading MA, 1969).

5) M. Born and E. Wolf, Principles of Optics, (Pergamon, New York) 1980; F. Abeles, Ann. Phys. (Paris) **3**, 504 (1948); **5**, 596 (1950); A. Herpin, Compt. Rend. **225**, 182 (1947).

6) J.D. Jackson, Classical Electrodynamics, (Wiley, New York, 1975) p453-459.

7) S. Garoff, E.B. Sirota, S.K. Sinha and H.B. Stanley (submitted to J. Chem. Phys.).

8) Y. Yoneda, Phys. Rev., **131**, 2010 (1963); O.J. Guentert, J. Appl. Phys., **30**, 1361 (1965); A.N. Nigam, Phys. Rev. A, **4**, 1189 (1965).

9) P.S. Pershan, J. Als-Nielsen, Phys. Rev. Lett. **52**, 759 (1984); J. Als-Nielsen, F. Christensen, P.S. Pershan, Phys. Rev. Lett., **48**, 1107 (1982).

10) A. Braslau, M. Deutsch, P.S. Pershan, A.H. Weiss, J. Als-Nielsen and J. Bohr, Phys. Rev. Lett., **54**, 114 (1985).

11) L.D. Landau and E.M. Lifshitz, Fluid Mechanics, (Pergamon, Oxford, 1986).

12) E.B. Sirota and S.K. Sinha (to be published).

13) M. Seul, P. M. Eisenberger and H. McConnell, Proc. Am. Acad. Sci., **80**, 5795 (1983).

14) M.J. Janiak, D.M. Small and G.G. Shipley, J. Biol. Chem., **254**, 6068 (1979).

15) I. Tidswell, B.M. Ocko, P.S. Pershan, S. Wasserman, G. Whitesides and J.D. Axe, NSLS Ann. Report 1987, 3-144 (1987).

16) E.B. Sirota, S.K. Sinha, G. Hughes and M. Alvarez (to be published).

17) A. Braslau, P.S. Pershan, G. Swislow, B.M. Ocko and J. Als-Nielsen, Phys. Rev. A, **38**, 2457 (1988); B.N. Thomas and S.A. Rice, J. Chem. Phys., **86**, 3655 (1987).

18) P.S. Pershan, A. Braslau, A.H. Weiss and J. Als-Nielsen, Phys. Rev. A, **35**, 4800 (1987); B.M. Ocko, P.S. Pershan, C.R. Safinya and L.Y. Chiang, Phys. Rev. A, **35**, 1868 (1987).

19) V. Skita, M. Filipkowski, A.F. Garito and J.K Blasie, Phys. Rev. B, **34**, 5826 (1986); M. Seul, Phys. Rev. Lett., **60**, 1150 (1988).

20) J.H. Underwood and T.W. Barbee, in Low Energy X-Ray Diagnostics, ed. D. Atwood and B. Henke, (Am. Inst. of Phys., Proc. No. 75, NY, 1981).

21) L. Lurio, P.S. Pershan, A. Rabedeau and I.F. Silvera, Bull. APS, **33**, 685 (1988).

22) B.M. Ocko and S.G.J. Mochrie; D. Gibbs, B.M. Ocko, D.M. Zehner and S.G.J. Mochrie, Phys. Rev. B, Oct 15 (1988).

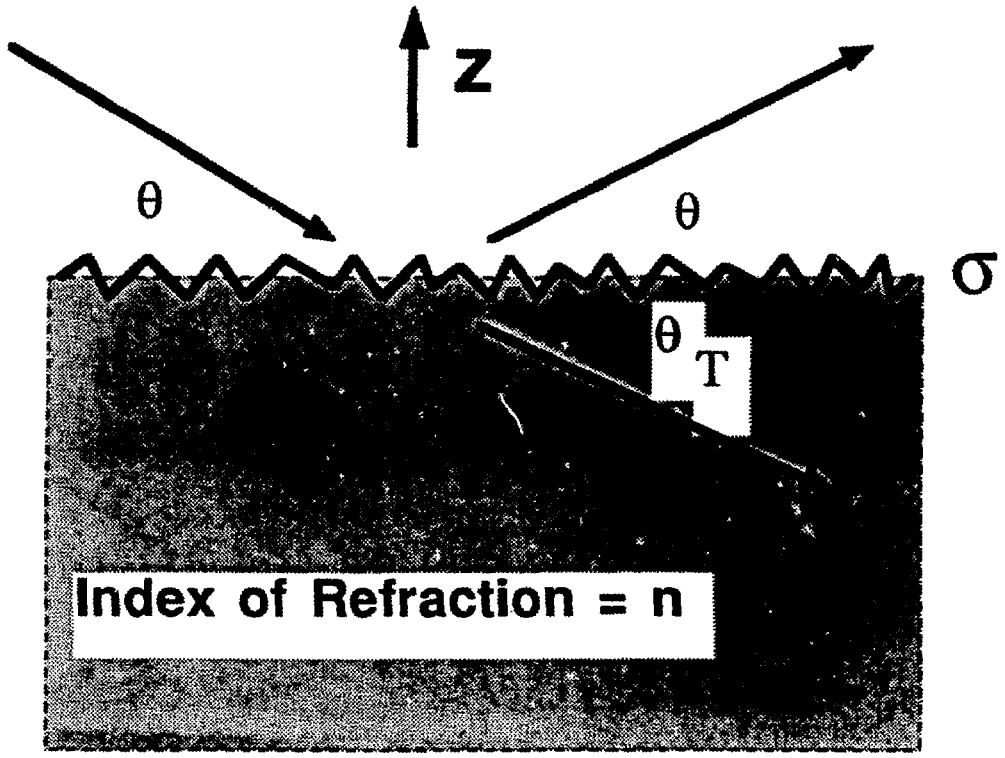

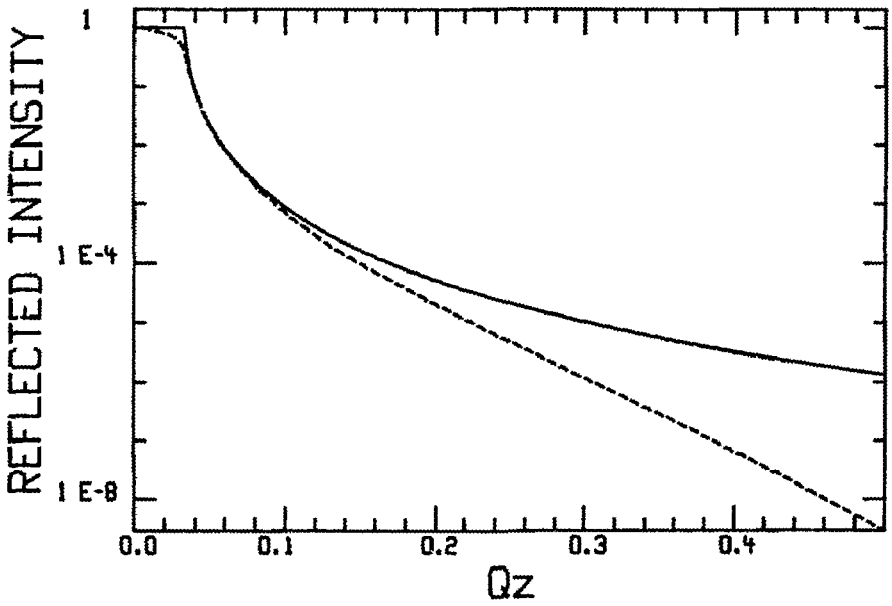

Fig. 1) Schematic showing reflection from a single interface of width σ. (solid curve) Computed reflectivity from a smooth surface with no absorption. (dashed curve) Computed reflectivity from a rough surface (σ=5Å) with absorption. Absorption decreases reflectivity near the critical angle. Roughness decreases reflectivity at large q_z.

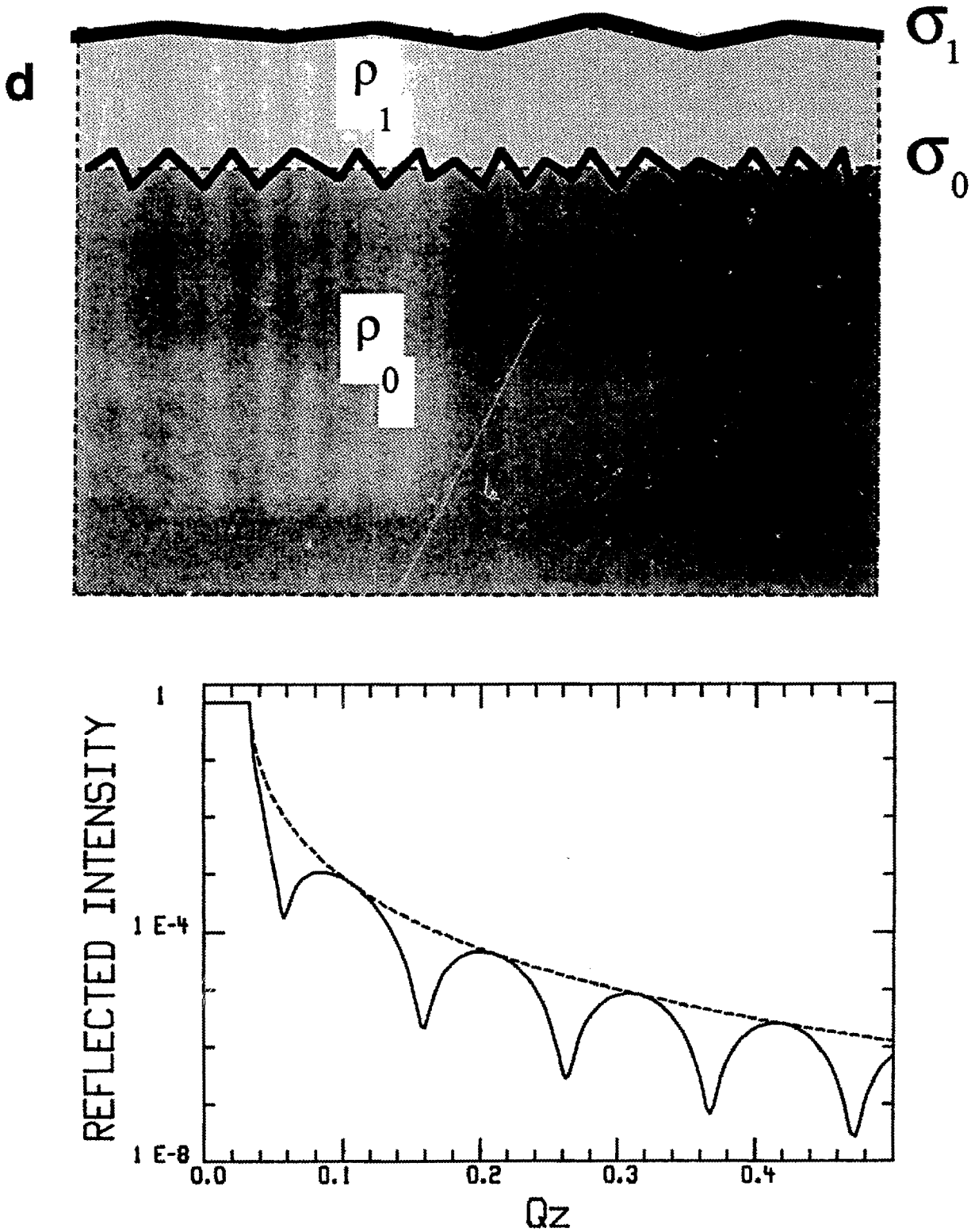

Fig. 2) Schematic of a layer of material with electron density ρ_1, thickness d and roughness σ_1 on a surface of a material with density ρ_0 and roughness σ_0. (solid) Computed reflectivity curve for ρ_1=0.35 electrons/Å^3, ρ_0=0.8, σ_0=σ_1=0 and d=50Å. (dashed) Smooth surface.

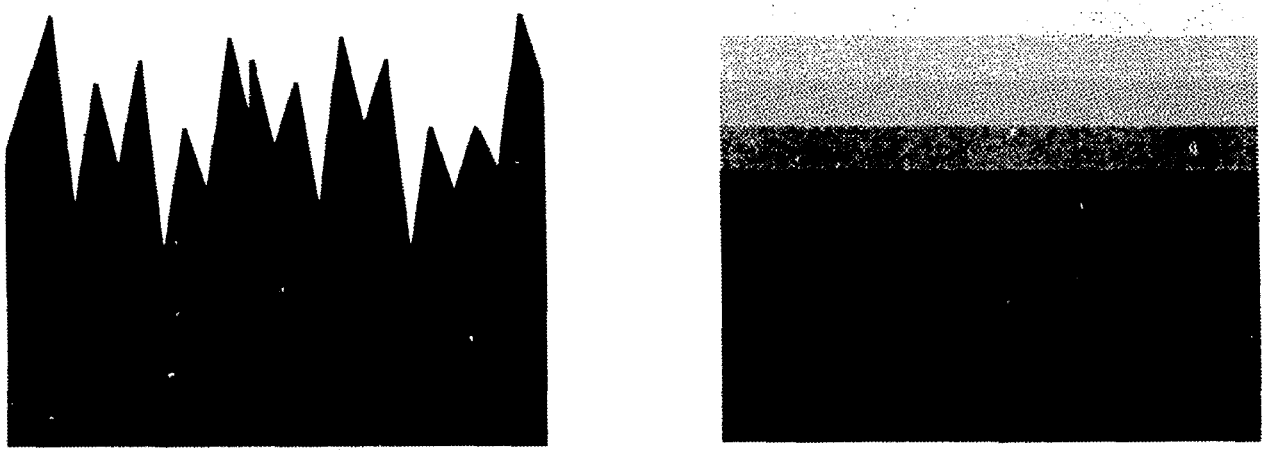

Fig. 3) Schematic showing the difference between rough and graded interfaces.

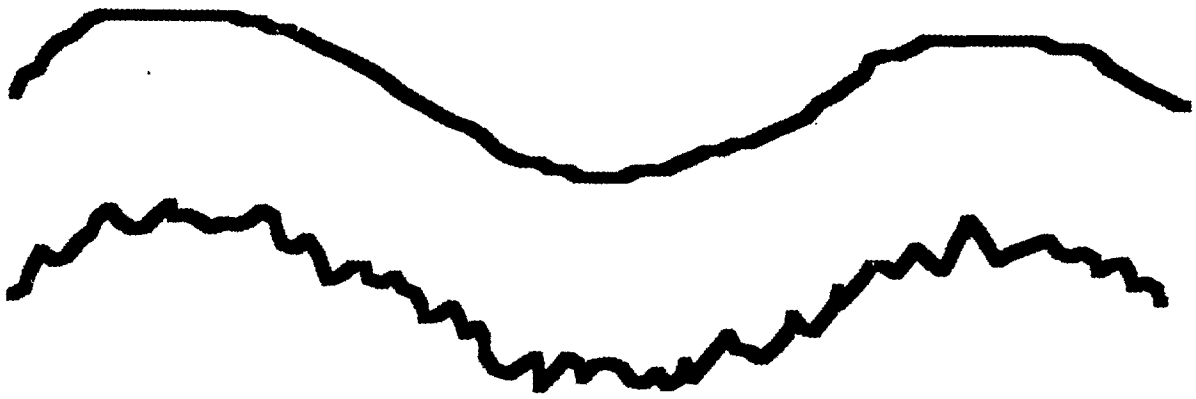

Fig. 4) Schematic showing 2 surfaces whose roughnesses are conformal on long length scales, but non-conformal on shorter length scales.

THE STRUCTURE OF LIPID MONOLAYERS ON WATER:

A Summary of Recent X-ray Diffraction Results

P. Dutta

Dept. of Physics & Astronomy, Northwestern University, Evanston, IL 60208

Most insoluble molecules that have a hydrophilic portion ('head') and a hydrophobic portion ('tail') will form monomolecular films on the surface of water. Of all monolayer systems, these are by far the most familiar, since such 'amphiphilic' molecules are ubiquitous: soap is a well-known example. Langmuir's discovery that fatty acid and salt monolayers show discontinuities [1] marked the beginning of over seventy years of monolayer phase transition studies [2]. Membrane phospholipids are also members of this class of molecules; the membrane bilayer structure is a low-energy configuration within an aqueous environment, just as the monolayer is at the surface. Recent studies [3] showing that the isotherms of highly purified materials have unambiguously flat sections (rather than the rounded transitions previously reported), have helped to reconcile membrane specific heat data (showing first-order transitions) with monolayer isotherm data. It can now reasonably be claimed that Langmuir monolayers are model membrane systems [4]. Monolayers have an obvious advantage over membranes in that they are easier to manipulate; in particular, the density can easily be varied over a wide range in a Langmuir trough. Moreover, the air-water interface is in principle more accessible to experimental probes such as X-rays than membranes in a bulk aqueous environment.

However, it was only in 1987 that the first X-ray diffraction results from Langmuir monolayers were reported [5,6]. The substrate is disordered and thus creates a

high background even when one stays below the critical angle for total external reflection; unfortunately, the critical angle is low (about $2x10^{-3}$ radians), which means that the number of incident photons is reduced. Moreover, the monolayers have turned out not to be single crystalline when ordered, but are powders in the plane, so it is not surprising that diffraction peak intensities are low (about 10-50/sec above a background of perhaps 100-200/sec.) even with synchrotron radiation. The diffraction plane must of course be horizontal, which means that achieving even moderately high resolution requires a loss of intensity when horizontally-polarized bending magnet radiation is used. It is probably unnecessary to belabor the fact that intense, highly-collimated, preferably vertically polarized radiation--as produced by, say, an undulator at the Advanced Photon Source--would be ideal for this kind of research.

Langmuir film isotherms usually show either a 'kink' (a discontinuous increase in slope as the area per molecule is decreased), a 'flat section' (often not quite flat, but separating two steeper sections), or both. Reasonably enough, 'kinks' are presumed to indicate continuous transitions, while 'flat' sections are considered to be first-order transitions. If an isotherm has one such feature, it is labelled a solid-liquid transition; if it has both, the transition at higher density is assumed to be the melting transition, while the other is thought to be a transition between two kinds of liquids. Such postulates have been made for many years in the absence structural information.

Our studies of heneicosanol ($C_{21}H_{43}OH$) [8], whose isotherm has a kink but no flat section, show that there is a single diffraction peak at about 1.5 $Å^{-1}$ whose height is independent of pressure above the kink; its height slowly drops as the pressure is lowered below the kink, and finally vanishes a few dynes below it. The peak width remains constant, however, indicating that the kink is <u>not</u> a continuous melting transition. It may mark a tilting transition that moves the diffraction peaks out of the horizontal plane in which scans are being performed; or perhaps the kink is the point at which all gauche configurations are squeezed out. Using a different system, DMPA

(dimyristoyl phosphatidic acid, a phospholipid whose isotherm has both a kink at high pressure and a flat section at lower pressure), Kjaer et al. [5,7] also find that the peak drops when the pressure is reduced below the kink, and finally vanishes well above the flat section; however, their peak also widens by a factor of 10.

Very recently we have studied heneicosanoic acid ($C_{20}H_{41}COOH$), whose isotherm shows the same qualitative features as DMPA. This material shows strong hysteresis as a function of pressure: nucleation occurs (with a time scale of several minutes at 5^{o}C) several dynes above the flat section if the pressure is being increased, but the diffraction peak persists several dynes below this discontinuity when the pressure is being decreased. This would seem to indicate a first-order melting transition (or a hysteretic tilting transition). For DMPA [5,7], as stated earlier, no diffraction peaks are reported until the pressure is several dynes higher than the pressure at the flat section. I do not know if the results were identical for both increasing and decreasing pressure, and the authors do not report seeing any time-dependent nucleation. On the other hand, fluorescence microscopy [5] confirms that the flat section in the DMPA isotherm is a first-order transition, since a coexistence of phases is seen with one phase increasing at the expense of the other phase as one moves across the flat section. Apparently the denser phase is not a solid phase (or, of course, it may be tilted!)

As the temperature is lowered at high pressure, we find [8] that the single peak in heneicosanol splits into two; in other words, the films undergo a transition from a hexagonal structure to a distorted (pseudohexagonal) structure. No evidence of this phase transition is visible in the isotherms, providing further support for the commonly expressed belief that isotherms are a poor basis from which to deduce phase diagrams. We also see a 'superheated' pseudohexagonal structure--possibly induced by the shear resulting from uniaxial compression--even above the transition temperature [9]; this structure gradually decays into the hexagonal phase, with the nucleation rate being a strong function of temperature. It is well known (although not always readily acknowl-

edged) that Langmuir films sometimes relax with time; it is now clear that at least part of this relaxation is due to microscopic mechanisms, rather than 'spurious' effects such as slow collapse.

As the above selective summary makes clear, these studies are at an exciting stage. Here is an incomplete list of possible future research directions. Of course, vertical scans along the diffraction rods are needed to determine whether the molecules are tilting uniformly or forming a disordered phase when the in-plane peaks lose intensity and vanish. Neither we nor Kjaer et al. see second-order peaks, although Wolf et al. [10] do see a second-order peak using palmitoyl-(R)-lysine, a molecule selected for its ability to cross-link in the plane. To unambiguously determine structure, it is of course essential that higher-order peaks be seen in the classical, well-characterized systems in which no chemical bonding occurs. After the behavior of classical systems is fully understood and the apparent differences between different systems reconciled, we hope to go on to more exotic systems, such as unusual molecules (e.g. valinomycin, a ring-shaped surfactant whose isotherm has never been fully explained), or mixtures of two or more film-forming compounds. In the long term, with radiation from the Advanced Photon Source, it is possible that ordered arrays (2D superlattices) of macromolecules (e.g. proteins imbedded in a phospholipid monolayer) can be studied.

REFERENCES

1. I. Langmuir, *J. Am. Chem. Soc.* **39**, 354 (1917)

2. See, e.g. G.L. Gaines, "Insoluble Monolayers at Liquid-Gas Interfaces" (Interscience, new York, 1966)

3 N.R. Pallas and B.A. Pethica, *Langmuir* **1**, 509 (1985)

4. J.F. Nagle, *Faraday Discuss. Chem. Soc.* **81**, 151 (1986)

5. K. Kjaer, J. Als-Nielsen, C.A. Helm, L.A. Laxhuber and H. Mohwald, *Phys. Rev. Lett.* **58**, 2224 (1987)

6. P. Dutta, J.B. Peng, B. Lin, J.B. Ketterson, M. Prakash, P. Georgopoulos and S. Ehrlich, B *Phys. Rev. Lett.* **58**, 2224 (1987)

7. K. Kjaer, J. Als-Nielsen, C.A. Helm, P. Tippmann-Krayer and H. Mohwald, *Thin Solid Films* **159**, 17 (1988)

8. "X-ray diffraction study of a Langmuir monolayer of $C_{21}H_{43}OH$", S.W. Barton, B.N. Thomas, S.A. Rice, B. Lin, J.B. Peng, J.B. Ketterson and P. Dutta, *J. Chem. Phys.* **89**, 2257 (1988)

9. "Kinetics of a structural phase transition in Langmuir films studied using X-ray diffraction", B. Lin, J.B. Peng, J.B. Ketterson, P. Dutta, B.N. Thomas, J. Buontempo and Stuart A. Rice, *J. Chem. Phys.*, to be published.

10. S.G. Wolf, L. Leiserowitz, M. Lahav, M. Deutsch, K. Kjaer and J. Als-Nielsen, *Nature* (London) **328**, 63 (1987)

X-RAYS AS PROBES OF ELECTROCHEMICAL INTERFACES

Héctor D. Abruña
Department of Chemistry
Cornell University
Ithaca, New York 14853-1301 USA

We have employed x-ray absorption spectroscopy, including surface EXAFS (extended x-ray absorption fine structure) and x-ray standing waves (XSW) in the in-situ study of electrochemical interfaces.

In the case of surface EXAFS, we have studied the underpotential deposition (UPD) of copper on Pt (111). Experiments were performed at half-monolayer coverage and the plane of polarization of the x-ray beam was parallel to the electrode surface so that the experiment was most sensitive to in-plane scattering of copper by other copper neighbors. From analysis of the data, we determined a Cu-Cu distance of 2.85Å which is very close to the Pt-Pt distance in the (111) direction and suggests that the copper atoms are present at three-fold hollow sites and that they form a commensurate layer with the platinum substrate. More important, however, was the finding that the average number of Cu near neighbors was six. This strongly suggests that at half-monolayer coverage the surface is better represented by one that has large clusters than by a surface that is randomly decorated with copper atoms or covered with a lattice with a large interatomic spacing. This is significant since it is a direct experimental documentation of a mechanism where monolayer formation involves nucleation and growth rather than random deposition with subsequent coalescence.

We have also performed in-situ EXAFS measurements on chemically modified electrodes. Specifically, we have studied films of $[M(v\text{-}bpy)_3]^{2+}$ (v-bpy is 4-vinyl,4'methyl-2,2'bipyridine; M = Ru, Os) and $[Os(v\text{-}bpy)_2(phen)]^{+2}$ electropolymerized onto a platinum electrode and in contact with an acetonitrile/0.1M TBAP (tetra n-butyl ammonium perchlorate) solution and under potential control. We find that for electrodes modified with five or more monolayers of $[Ru(v\text{-}bpy)_3]^{+2}$ the spectra are indistinguishable from that of the bulk material. (It should be mentioned that a monolayer of $[Ru(v\text{-}bpy)_3]^{+2}$ represents about 5.4×10^{13} molecules/cm^2 which is about 5% of a metal monolayer. This is mentioned since it is the metal centers that give rise to the characteristic fluorescence employed in the detection.) Upon fitting of the data for phase and amplitude we obtain a Ru-N distance of 2.06Å and a coordination number of six. These correlate very well with the known values of 2.056Å and six, respectively. In addition, we also find that there is little difference between the electrodeposited polymer and the monomeric parent compound in terms of the near edge spectral features, pointing to a similar geometric disposition of scatterers. Furthermore, changes in oxidation state can be monitored by the shift in the position of the edge. For example, upon oxidation of the polymer film (at +1.60 V) from Ru(II) to Ru(III), the edge position shifts to higher energy by about 1.5 eV. Thus, one can determine the oxidation state of the metal inside a polymer film on an electrode surface.

These results indicate that the structure of electroactive polymer films and the oxidation state of the metal center can be obtained at relatively low coverages and this should have important implications in trying to identify the structure of reactive intermediates in electrocatalytic reactions at chemically modified electrodes.

Since in x-ray absorption spectroscopy the magnitude of the edge jump is proportional to the number of absorbers, its potential dependence can be employed in constructing electrosorption isotherms in-situ and we have carried out such a study on

iodide adsorption on a Pt(111) electrode surface in contact with a solution containing 0.05mM NaI, 0.1 M Na_2SO_4 at a pH of 6.7. The isotherm, shown in Figure 1A exhibits

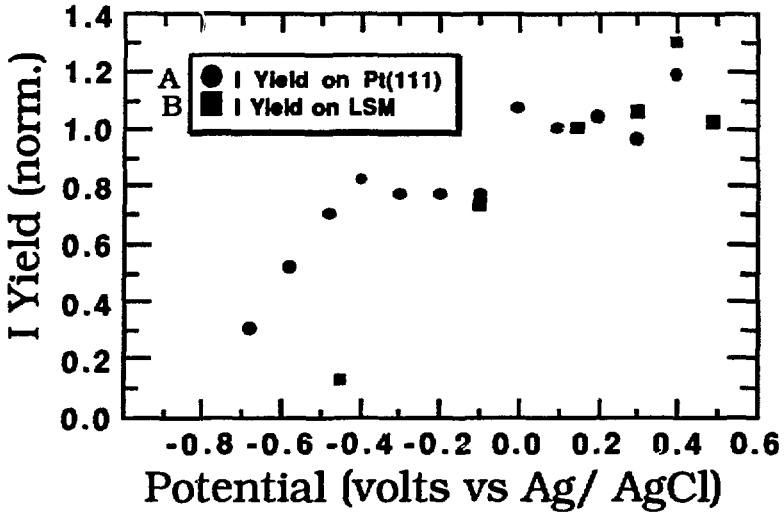

Figure 1

several noticeable features. At the most negative potentials, the iodine coverage drops rapidly with decreasing potential, attaining essentially zero coverage at -0.90 V. At potentials above +0.30 V, the iodine coverage increases rapidly with potential and at intermediate potentials there are two plateaus separated by a transition. The behavior at negative potentials is ascribed to repulsion of the iodide by the electrode whereas as the most positive potentials the increase in the signal is ascribed to faradaic charge flow (to generate tri-iodide or a related species) followed by association with the adsorbed iodine layer. The two plateaus at intermediate potentials appear to represent a change in structure and coverage from 3/9 to 4/9 of a monolayer.

In the area of x-ray standing waves, have studied the potential dependence of the adsorption of iodide onto a Pt/C LSM. In this experiment we simultaneously monitored the reflectivity across the first order Bragg reflection as well as the characteristic iodine fluorescence intensity.

Figure 2 shows curves for the normalized iodide fluorescence intensity as a function of potential as well as a reflectivity profile. The data indicate that at the most negative potentials, (e.g. -0.90 V) the iodide coverage is essentially zero as the electrode repels the negatively charged ion. As the potential is made progressively positive, the iodide fluorescence intensity increases and the peak maximum shifts to lower angles up to a potential of +0.40 V. At +0.49 V, the fluorescence intensity begins to decrease and the peak maximum again moves towards higher angles. Qualitatively, these data appear to indicate that at -0.90 V there is no iodide adsorbed and that the coverage increases as the potential is made progressively positive. The movement of the peak maximum to lower angles indicates that, on average, the interfacial iodine density is moving away from the electrode surface. This is ascribed to association of the product(s) of faradaic charge flow (such as tri-iodide or a related species) followed by association with the adsorbed iodine layer. The subsequent decrese in intensity is ascribed to discharge of this layer (possibly in the form of iodate).

The iodide fluorescence intensity was normalized and plotted vs. potential to yield the electrosorption isotherm shown in Figure 1B which is in excellent agreement the

previously discussed results obtained via x-ray absorption spectroscopy on a platinum (111) electrode (Figure 1A).

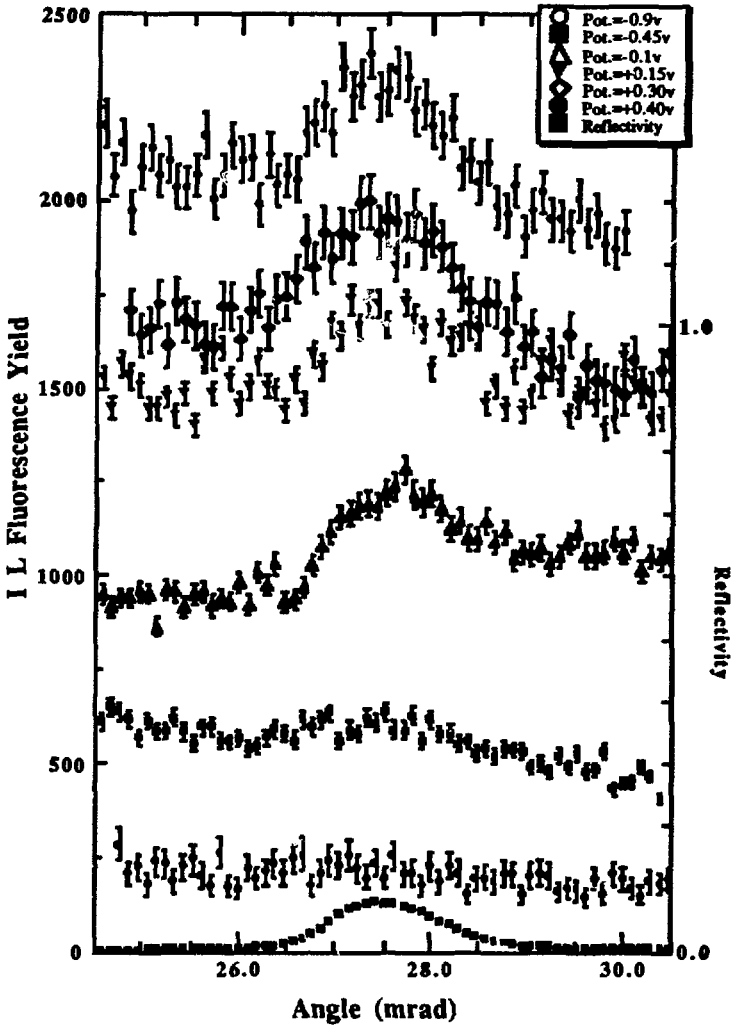

Figure 2

Acknowledgements:

This work was generously supported by the Materials Chemistry Initiative of the National Science Foundation, the Materials Science Center at Cornell University, the Office of Naval Research, the Army Research Office, the Dow Chemical Co. and Xerox Corp.

X-ray Scattering Studies of Transitions on Metal Surfaces

G. A. Held

IBM Research Division

Thomas J. Watson Research Center

Yorktown Heights, NY 10598-0218

Synchrotron x-ray scattering provides an important tool in the study of surface phase transitions. High resolution as well as weak interactions with matter make x-ray synchrotron radiation unique amongst surface scattering probes. In the case of a clean unreconstructed surface, scattering from in-plane (ie, grazing incidence), anti-Bragg points along the crystal truncation rods (these points are commonly known as bulk-forbidden or surface peaks) provides important information about the surface morphology as well as the statistical distribution of atomic steps. In the case of a clean reconstructed surface, superlattice peaks as well as surface peaks are present. These can be used to probe the structure of the reconstruction, as well as the mechanism by which the surface "deconstructs" with temperature. In a third case, when a monolayer of rare gas is adsorbed incommensurately onto a metal substrate, the corrugation potential which the metal substrate exerts on the rare gas is an order of magnitude weaker than the corrugation potential of a graphite substrate. The scattering from the incommensurate surface rods can provide information about the 2-dimensional melting of the rare gas monolayer as a function of temperature. Examples of these three cases follow.

Ag (110) is an unreconstructed surface which is found to roughen as a function of temperature[1]. Using scattering from the bulk forbidden $(1\bar{1}0)$ surface peak as a probe, one obtains direct information about thermal variations in the height-height correlation function. Specifically, it is found that the surface undergoes a roughening transition at $T_R = 450 \pm 25°$ C. Below T_R the surface peak is a superposition of Bragg (δ-function) and power law lineshapes, with the Bragg component falling to zero at T_R . Above T_R, the peak is well described by a power law lineshape, indicating that the rough phase is characterized by logarithmically divergent height fluctuations. The lineshape exponent $\eta \cong 0.6$ at T_R.

At low temperatures, the Au (110) surface is known to reconstruct. At T_c= 485°C, the 1x3 reconstructed surface undergoes a reversible deconstruction transition. Observing the temperature dependence of the superlattice and integral order bulk-forbidden (anti-Bragg) surface peaks, it is found that at T_c the 1x3 reconstructed surface becomes incommensurate with the bulk crystalline lattice[2]. During this commensurate-incommensurate transition, the surface both roughens and deconstructs.

In the third experiment, a Xe monolayer is adsorbed on Ag (111). At high temperatures (T>100K) all features of the melting transition are, within errors, found to be the same as those found for xenon on graphite. Specifically, in both cases the xenon solid melts into a "hexatic phase" with essentially identical hexatic stiffness. This strongly suggests that the existence of the hexatic phase is a feature of the two dimensional melting process rather than the adsorbate-substrate interaction[3] .

This work was done in collaboration with R. J. Birgeneau, R. Frahm, R. L. Greene, N. Greiser, P. M. Horn, J. L. Jordan-Sweet, A. Mak, and R. M. Suter.

References

1. G. A. Held, J. L. Jordan-Sweet, P. M. Horn, A. Mak, and R. J. Birgeneau, Phys. Rev. Lett. **59**, 2075 (1987).

2. G. A. Held, J. L. Jordan-Sweet, P. M. Horn, A. Mak, and R. J. Birgeneau, submitted for publication.

3. N. Greiser, G. A. Held, R. Frahm, R. L. Greene, P. M. Horn, and R. M. Suter, Phys. Rev. Lett. **59**, 1706 (1987).

SESSION II

SPECTROSCOPY

The Use of Polarization in X-ray Absorption Spectroscopy Applications to Chemical Problems

James E. Penner-Hahn
Department of Chemistry, University of Michigan
Ann Arbor, MI 48109-1055

The goal of this review is to illustrate some of the advantages to be gained from utilizing the plane-polarized nature of synchrotron radiation when measuring x-ray absorption spectra. This is a field which has grown dramatically in recent years [1-3], and I have made no attempt to present an exhaustive review of the literature. In particular, studies which emphasize surface characterization have been excluded. This is in part because such work is discussed in detail elsewhere (for example the discussion by Stohr in this volume). In addition, this bias is based on the recognition that surface scientists, perhaps because of the inherently anisotropic nature of their samples, have long recognized the value of polarized measurements. On the other hand, those making "bulk" x-ray absorption measurements (frequently of biological or chemical systems) have largely ignored the advantages of polarization dependent measurements. It is toward this latter audience that this review is directed.

In the most general sense, x-ray absorption spectroscopy (XAS) experiments are performed either to learn about the structure of a sample or to learn about the basic nature of the x-ray absorption process. In both regards, polarization dependent measurements play an important role. The requirements for such measurements are simple: A polarized x-ray source and an oriented sample. The former is a natural property of synchrotron radiation, and oriented samples can be produced by a variety of methods.

Single crystals are the most obvious source of oriented samples. It may seem on first consideration that there is no point in measuring x-ray absorption spectra for crystalline samples, since x-ray diffraction can provide more detailed structural information than is available from XAS.

One of the goals of this review is to refute this view. In addition, polarized XAS can be extremely useful in structural studies of ordered, but non-crystalline samples. Recent examples include studies of fibers, membranes, and films.

A particularly interesting method for "orienting" samples is illustrated by a recent study of gaseous CH_3Cl [4]. Polarized fluorescence spectra are observed at the Cl K edge. The "orientation" of the sample is accomplished by the fact that dipole selection rules limit the initial photoabsorption to molecules having a particular orientation relative to the electric field vector of the x-ray beam. Since x-ray fluorescence is rapid in comparison with molecular rotations, the resultant emission spectra are polarized.

For purposes of the following discussion, polarized measurements are divided according to whether they seek to determine structural properties of a completely unknown sample, to investigate in detail a particular structural feature of a structurally characterized material, or to use a structurally oriented sample to investigate a particular feature of x-ray absorption spectroscopy.

Structural Characterization of Unknown Samples.

Cramer, George, and co-workers have made extensive use of polarized XAS to structurally characterize metalloproteins. One system which they have studied is the Fe/Mo/S protein nitrogenase. Extensive solution EXAFS measurements had demonstrated that the Mo environment consisted of ca. 3 sulfurs at 2.3 Å and ca. 3 Fe atoms at 2.7 Å, with possibly one or two low-Z ligands [5]. On the basis of these measurements, a variety of structures having varying degrees of asymmetry had been proposed. Since crystalline samples of nitrogenase were available, it was possible to use polarized measurements to distinguish between the possible structural models. Although the structure of this protein has not yet been solved, the available crystallographic information was sufficient to identify the molecular 2-fold axes. Given this information, the orientation dependence of the polarized EXAFS spectra for nitrogenase single crystals could be used to determine the asymmetry of the Mo site [6]. For different orientations,

the Mo-Fe component of the Mo EXAFS varied in intensity by a factor of 2.5 while the Mo-S component varied by only ±15%. From this it was concluded that highly asymmetric models (e.g. linear Fe-Mo-Fe) and totally symmetric models (e.g. tetrahedral $MoFe_4$) were both inconsistent with the data, while intermediate models (e.g. tetrahedral $MoFe_3$ or square-pyramidal $MoFe_4$) were possible.

Similar studies have been carried out on the membrane bound protein cytochrome oxidase [7] and on the photosynthetic oxygen evolving complex [8]. In these cases, approximate one dimensional order is afforded by partial dessication of membraneous proteins on Mylar films. The membranes, and hence the membrane bound proteins, are oriented such that all of the membrane normals are parallel, however there is no preferred angular orientation within the membrane. For cytochrome oxidase, polarized EXAFS measurements have provided information on not only the distances but also the directions for the M···ligand vectors (M= both Cu and Fe). Since the heme environments are known from polarized optical and EPR spectroscopy, these EXAFS results can be used to develop a more complete three dimensional structure for the metal sites.

Oyanagi and co-workers [9,11-14] and Krone and co-workers [10] have used polarized XAS to investigate the structure of halogen doped polyacetylene. As with membranes, polyacetylene fibers have two unique directions: parallel and perpendicular to the fiber axis. The most recent XAS results suggest that the halide ions are present as X_3^- chains at low halide doping and are covalently bound to the chain at higher doping levels (> 10%). A particular advantage of polarized measurements for this work is the fact that they allow one to distinguish between Br-Br and Br-C EXAFS due to the different orientation dependence of these signals.

Other areas where polarized measurements have found application include Langmuir-Blodgett films [15] and intercalated graphite [16]. In both cases, the samples have known two-dimensional structures. With this information in hand, the XAS polarization dependence can be used both to determine sample orientation and to enhance the sensitivity to particular

structural features (distinguishing, for example, between intra-intercalate EXAFS and intercalate-graphite EXAFS).

In depth Study of Structurally Characterized Samples.

Even when complete three dimensional structures are available, useful information can be obtained from polarized XAS. One particularly productive such area has been the investigation of pair-distribution functions using polarized EXAFS. It is well known that EXAFS provides information about thermal motion (the so-called Debye-Waller factor) which is complementary to that obtained from crystallography. In particular, EXAFS can be used to determine relative inter-atomic motion while crystallography generally gives only information on the motion of individual atoms about their mean positions.

In analysis of the polarized EXAFS spectra for metallic zinc [17], Beni and Platzman [18] were able to determine the mean-square relative displacements (MSRD) of Zn atoms parallel and perpendicular to the basal plane. The experimental results agreed well with simple calculations in a Debye model. Similar information was obtained from polarized GeS EXAFS [19]. For metallic Cd, polarized measurements [20] revealed that the MSRD values were very different for the first and second shell Cd neighbors, thus providing an explanation for fact that the second shell Cd atoms are not detectable in room temperature EXAFS [21].

In the examples thus far, the principal use of polarization has been to determine the anisotropy of the MSRD. A somewhat less obvious application of polarized measurements is to improve the resolution of the EXAFS experiment. Thus for ZnF_2, polarized EXAFS measurements permitted resolution of two different shells of fluoride at 2.042 and 2.015 Å [22]. Such resolution would not have been possible in isotropic measurements.

For the blue-copper protein plastocyanin, polarized XAS was used to investigate the Cu-S(Met) interaction [23]. The plastocyanin crystal structure had shown that there was a methionine sulfur at 2.9 Å from the

Cu, however there was no evidence for a S(Met) component in the isotropic Cu EXAFS. Possible explanations included thermal disorder (large MSRD as discussed above for Cd) and/or destructive interference. In the latter model, destructive interference between Cu-S(Met) and Cu-C(imidazole) EXAFS could lead to the non-detectability of Cu-S(Met) EXAFS. Polarized measurements showed that Cu-S(Met) EXAFS was not detectable even for an orientation which maximizes the Cu-S(Met) contributions and minimizes the Cu-C(imidazole) contributions to the EXAFS, thus ruling out destructive interference. More recent measurements at cryogenic temperatures [24] have confirmed the EXAFS non-detectability of Cu-S(Met) EXAFS, thus indicating that the thermal motion of these atoms must be largely uncorrelated.

A third application of polarized measurements for structurally characterized materials arises when one wishes to determine interatomic distances with a precision better than that which is obtainable using diffraction. This most often arises in the case of metalloproteins, where the best available structures can only provide metal-ligand bond lengths with a precision of ca. ±0.05 to ±0.10 Å. Bianconi and co-workers have examined the polarized XANES of CO myoglobin in an attempt to determine the Fe-C-O angle [25]. This question is difficult to answer using crystallography, both because of resolution limitations and because of disorder in the CO. Polarized XAS measurements should, in principle, be helpful in elucidating this problem. Recent results [26] suggest that Bianconi's conclusion, that the Fe-C-O unit is bent, is probably incorrect. This does not, however, indicate any intrinsic limitation in the polarized method, but rather is a reflection of the difficulty in obtaining quantitative structural information from XANES spectra.

Polarized XAS measurements have also been used to investigate the structure of the Fe/S clusters in the 7 Fe ferredoxin from *Azotobacter vinelandii*. Crystallographic studies had indicated that this protein contained a symmetric 4Fe/4S cluster and a novel, planar 3Fe/3S cluster [27]. The latter had Fe-Fe distances of 4.2 Å, in contrast with the 2.7 Å Fe-Fe distances found in other Fe/S clusters. The large number of different Fe atoms in this protein complicate interpretation of the EXAFS, however the

cluster orientations were such that crystals could be aligned so as to either maximize or minimize the contribution of the 3Fe/3S Fe-Fe signal to the overall EXAFS. Polarized EXAFS measurements [28] showed no evidence for a 4.2 Å Fe-Fe distance (which is perhaps not surprising in view of the long distance), however, surprisingly, they showed pronounced orientational dependence for the 2.7 Å Fe-Fe EXAFS features. Since the 4Fe/4S cluster is highly symmetric the 2.7 Å Fe-Fe EXAFS from this cluster will have no orientational dependence. These results thus demonstrated that the 3Fe/3S cluster must contain a 2.7 Å Fe-Fe distance. This conclusion has recently been confirmed by a redetermination of the crystal structure [29]. Isotropic EXAFS spectra of the 7 Fe protein would have been of little value in distinguishing between the original and the current structures since, from the Fe perspective, these differ only in the number of Fe-Fe neighbors at 2.7 Å, and EXAFS is notoriously bad at determining coordination numbers.

Detailed Studies of XAS.

The examples discussed thus far have illustrated some of the ways in which one can utilize polarized measurements to enhance the structural information which is obtained from XAS. Of at least equal importance are those experiments which utilize polarized measurements of structurally characterized materials to investigate fundamental properties of x-ray absorption. In an early such study, Stern, Sayers, and Lytle [30] investigated the polarized XAS of TaS_2 at the Ta L_3 edge. This was among the first studies of L-edge EXAFS and the polarized measurements helped to establish that the EXAFS expressions used for K-edge studies could also be applied to L edge measurements.

In contrast to this EXAFS study, most of the examples in the present category involve XANES, since XANES spectra remain poorly understood. Although there is general agreement on the fundamental nature of the processes which give rise to XANES spectra, there does not, at present, exist a theory which is capable of uniquely associating an observed XANES spectrum with a molecular structure. Polarized XANES spectra of model compounds are valuable in this regard, since they can be used to test

prospective theories more rigorously than is possible using isotropic measurements. In addition, polarized measurements are an important contribution to an empirical library of XANES spectra which can aid in the interpretation of the XANES structure of unknown compounds.

The 1s→3d transition for first transition series metals appears as a weak feature ca. 5-10 eV below the main edge. Although this transition is formally forbidden in a centrosymmetric environment, it is observed to be weak, *but not absent*, for all samples having at least one unoccupied d orbital. The observed intensity could arise either from direct quadrupole coupling of the 1s and 3d orbitals or from dipole-allowed vibronic coupling. In order to distinguish between these mechanisms, a crystal containing $Cu(II)Cl_4^{2-}$ ions was oriented with the $CuCl_4$ plane parallel to the **e** and **k** vectors of the x-radiation [31]. The 1s→3d intensity showed 4-fold periodicity as the crystal was rotated about the normal to the $CuCl_4$ plane, thus providing unambiguous evidence that direct quadrupole coupling is the dominant mechanism contributing to 1s→3d intensity. Recent work [32] shows that the same phenomemon is observed for $Co(III)(NH_3)_6^{3+}$ ions, giving in this case the unusual observation of orietational anisotropy for an octahedral molecule, due to the quadrupole selection rules.

Certain low-symmetry complexes, particularly those having very short M-O bonds (e.g., vanadyl complexes) have extremely intense transitions in the 1s-3d region. Polarized measurements [33,34] have shown these transitions to be polarized in the M=O direction, leading to the suggestion that they are charge-transfer like transitions, involving excitation from the 1s orbital to a M-O π^* antibonding molecular orbital. It is the mixing of p-symmetry oxygen orbitals with the metal 3d ground state that gives rise to the strongly allowed character of these transitions.

The higher energy XANES features have also been studied using polarized measurements. Kosugi et al. have reported an extensive series of polarized XANES measurements for Cu and Ni complexes [35-37]. The observed spectral features are interpreted in terms of the local electronic

structure of the metal site, including 1s→np transitions and multielectron (shakedown) transitions. A rather different interpretation of similar spectra has been provided by Smith et al., using an Xα framework [38-39]. It is not clear at this point whether the apparent differences in these two treatments represent real differences of interpretation or merely different ways of describing the same result. Regardless of interpretation, it is clear that XANES spectra are frequently highly anisotropic. In particular, square-planar complexes are frequently found to have an intense z-polarized transition on the low energy side of the absorption edge. Scott has used this finding to interpret XANES spectra for Ni in CO dehydrogenase [40].

At higher energy still, above the principal absorption discontinuity, there are a number of absorption features which appear, empirically, to be sensitive the the three-dimensional structure of the absorbing atom. In the case of iron porphyrins, Chance has dubbed two of these features, lying 40-60 eV above the absorption edge, as the "ligand-field indicator region" (LFIR). Recent polarized XANES of 6-coordinate Fe(III) porphyrins have shown [41] that the LFIR peaks are in fact a complicated superposition of resonances arising from axial ligands and resonances from in-plane scattering. From these spectra it is clear that the relative intensitites of the LFIR transitions are related to expansion of the porphyrin core and not to displacement of the Fe from the porphyrin plane.

Future Prospects.

It has been the intent of this review to illustrate some of the areas in which polarized XAS measurements have provided unique information which could not have been obtained from conventional isotropic XAS spectra. As regards future work, there exist a number of areas in which polarized measurements could be useful. For biological systems, it is likely that there will continue to be structural questions which cannot be answered by even high resolution protein crystallography. This will become particularly true as larger crystal structures are solved, since the metal sites in such structures are often poorly defined. The combination of crystallography to determine overall three-dimensional structure and

polarized EXAFS to refine local metal-site structure is particularly powerful. A second area likely to see substantial future work is high T_c superconductors. Many of these materials are naturally anisotropic and thus well suited to polarized measurements.

Another area ripe for future advances is the orientation of materials for polarized studies. Polarized XAS of membrane bound proteins was discussed above, however the potential of this area has yet to be fully exploited. Other orientation methods which could be explored include liquid crystals and magnetically ordered materials. A particularly interesting examples of the latter is the x-ray circular dichroism which has been observed for ferromagnets in a magnetic field [42]. Also of potential interest are polarized EXAFS studies of poorly crystalline materials, i.e. crystals that are not sufficiently "perfect" to permit high-resolution crystallographic investigation, but which are nevertheless sufficiently ordered to permit polarized EXAFS studies.

The next generation of synchrotron sources will create a variety of new opportunities for polarized XAS studies. The high brightness of these sources will permit measurement of polarized XAS data for crystals which are too small to be studied using current sources. Another area which has not yet been fully exploited is the use of circularly polarized x-ray beams to study chiral materials. The next generation of x-ray sources will faciliate such measurements.

Acknowledgements.

Support for this work was provided in part by a grant from the National Institutes of Health (GM-02419).

References

1. Hahn, J.E.; Hodgson, K.O. *ACS Symp. Ser., 211*, **1983**, 431-44 .
2. Penner-Hahn, J.E.; Hodgson, K.O. in *Structural Biological Applications of X-Ray Absorption, Scattering, and Diffraction*, Bartunik, H. D.; Chance, Britton (eds.) Academic: Orlando, Fla.**1986**.

3. Penner-Hahn, J. E.; Smith, T. A.; Hedman, B.; Hodgson, K. O.; Doniach, S. *J. Phys., Colloq. C8*, **1986**, C8/1197-C8/1200.
4. Lindle, D.W.; Cowan, P.L.; LaVilla, R.E.; Jach, T.; Deslattes, R.D.; Karlin, B.; Sheehy, J.A.; Gil, T.J.; Langhoff, P.W., *Phys. Rev. Lett., 60*,**1988**, 1010-13.
5. For a recent review of this literature see Cramer, S.P., in *Advances in Inorganic and Bioinorganic Mechanisms*, Vol. II, A.G. Sykes (Ed.), Academic, London, **1983**, 259-316.
6. Flank, A.M.; Weininger, M.; Mortenson, L.E.; Cramer, S.P., *J. Am. Chem. Soc., 108*, **1986**, 1049-1055.
7. George, G.N.; Cramer, S.P.; Frey, T.G.; Prince, R.C., in *Advances in Mambrane Biochem. and Bioenergetics*, C.H. Kim (ed.), Plenum, New York, **1987**.
8. George, G.N.; Cramer, S.P.; Prince, R.C., personal communication.
9. a) Oyanagi, H.; Tokumoto, M.; Ishiguro, T.; Shirakawa, H.; Nemoto, H.; Matsushita, T.; Kuroda, H. *Springer Proc. Phys., 2*, **1984**, 397-9. b) Oyanagi, H.; Tokumoto, M.; Ishiguro, T.; Shirakawa,H.; Nemoto, H.; Matsushita, T.; Ito, M.; Kuroda,H. *J. Phys. Soc. Jpn., 53*, **1984**, 4044-53.
10. a) Krone, W.; Wortmann, G.; Frank, K. H.; Kaindl, G.; Menke, K.; Roth, S. *Springer Proc. Phys., 2*, **1984**, 394-6. b) Krone, W.; Wortmann, G.; Frank, K. H.; Kaindl, G.; Menke, K.; Roth, S. *Solid State Commun., 52*, **1984**, 253-6.
11. Fujikawa, T.; Oizumi, H.; Oyanagi, H.; Tokumoto, M.; Kuroda, H. *J. Phys. Soc. Jpn., 55*, **1986**, 4074-89 .
12. Fujikawa, T.; Oizumi, H.; Oyanagi, H.; Tokumoto, M.; Kuroda, H. *J. Phys. Soc. Jpn., 55*, **1986**, 4090-102 1986.
13. Oyanagi, H.; Tokumoto, M.; Ishiguro, T.; Shirakawa,H.; Nemoto, H.; Matsushita, T.; Kuroda, H. *J. Phys., Colloq.*, **1986**, C8/615-C8/618 .
14. Oyanagi, H.; Tokumoto, M.; Ishiguro, T.; Shirakawa, H.; Nemoto, H.; Matsushita, T.; Kuroda, H. *Synth. Met.,17*, **1987**, 491-6 .
15. For recent examples see: a) Oyanagi, H.; Sugi, M.; Kuroda, S.; Iizima, S. Ishiguro, T.; Matsushita, T. *Thin Solid Films, 133*, **1985**,181-8 b) Outka, D. A.; Stohr, J.; Rabe, J. P.; Swalen, J. D. *J. Chem. Phys., 88*, **1988**, 4076-87.
16. For recent examples see: a) Loupias, G.; Chomilier, J.; Tarbes, J.; Ascone, I.; Goulon, J.; Guerard, D.; Elalem, N. *J. Phys., Colloq.*, **1986**, C8/891-

C8/895. b) Fretigny, C.; Bonnin, D.; Cortes, R. *J. Phys., Colloq.*, **1986**, C8/869-C8/873. c) Feldman, J. L.; Elam, W. T.; Ehrlich, A. C.; Skelton, E. F.; Dominguez, D. D.; Chung, D. D. L.; Lytle, F. W. *Phys. Rev. B:*, *33*, **1986**, 7961-82

17. Brown, G. S.; Eisenberger, P.; Schmidt, P. *Solid State Commun.*, *24*, **1977**, 201-3.
18. Beni, G.; Platzman, P.M. *Phys. Rev. B.*, *14*, **1976**, 1514-1518.
19. Rabe, P.; Tolkiehn, G.; Werner, A. *J. Phys. C*, *13*, 1857-64, **1980**.
20. Hitchcock, A. P.; Tyliszczak, T. *J. Phys. C: Solid State Phys.*, *20*, **1987**, 981-92.
21. Thulke, W.; Rabe, P. *J. Phys. C., Solid State Phys.*, *16*, **1983**, L955.
22. Cox, A. D.; Beaumont, J. H. *Philos. Mag., B, 42*, **1980**, 115-26.
23. Scott, R.A.; Hahn, J.E.; Doniach, S.; Freeman, H.C.; Hodgson, K.O. *J. Am. Chem. Soc.*, *104*, **1982**, 5364-9.
24. Penner-Hahn, J.E.; Hodgson, K.O.; Freeman, H.C., submitted to *J. Am. Chem. Soc.*, **1988**.
25. Congiu-Castellano, A.; Bianconi, A.; Dell'Ariccia, M.; Giovannelli, A.; Burattini, E.; Durham, P. J. *Springer Proc. Phys.*, *2*, 164-6, **1984**.
26. Li, X.-Y.; Spiro, T.G., *J. Am. Chem. Soc.*, *110*, **1988**, 6024-6033.
27. Ghosh, D.; O'Donnell, W.F. Jr.; Robbins, A.H.; Stout, C.D., *J. Mo. Biol.*, *158*, **1982**, 73.
28. Scott, R.A.; Penner-Hahn, J.E.; Hodgson, K.O.; Beinert, H.; Stout, C.D., in *Springer Proceedings in Physics*, *2*, **1984**, 105-110.
29. Stout, G.H., et al., *Proc. Natl. Acad. Sci.*, **1988**.
30. Stern, E. A.; Sayers, D. E.; Lytle, F. W. *Phys. Rev. Lett.*, *37*, **1976**, 298-301.
31. Hahn, J.E.; Scott, R.A.; Hodgson, K.O.; Doniach, S.; Desjardins, S.R.; Solomon, E.I. *Chem. Phys. Lett.*, *88*, ,**1982**, 595
32. Wang, S.; Waldo, G.S.; Penner-Hahn, J.E., in *Proceedings of the Fifth International Conference on XAFS*, Seattle, WA, **1988**.
33. Templeton, D.H.; Templeton, L.K. *Acta Crystallogr., A36*, **1980**, 237-41.
34. Penner-Hahn, J.E.; Benfatto, M.; Hedman, B.; Takahashi, T.; Doniach, S.; Groves, J.T.; Hodgson, K.O *Inorg. Chem.*, *25*, **1986**, 2255-9.
35. a) Kosugi, N.; Yokoyama, T.; Kuroda, H. *Springer Proc. Phys.*, *2*, **1984**, 55-7. b) Kosugi, N.; Yokayama, T.; Asakura, K.; Kuroda, H., *Chem. Phys.*, *91*, **1984**, 249-56.

36. Yokoyama, T.; Kosugi, N.; Kuroda, H. *Chem. Phys., 103*, **1986**, 101-9.
37. Kosugi, N.; Yokoyama, T.; Kuroda, H. *Chem. Phys., 104*, **1986**, 449-53.
38. Smith, T.A.; Penner-Hahn, J.E.; Berding, M.A.; Doniach, S.; Hodgson, K.O. *J. Am. Chem. Soc., 107*, 5945-55, **1985**.
39. Smith, T.A. G. Ph.D. Thesis, Stanford Univ.,Stanford, CA, USA, **1985**.
40. Cramer, S.P.; Eidsness, M.K.; Pan, W.H.; Morton, T.A.; Ragsdale, S.W.; DerVartanian, D.V.; Ljundahl, L.G.; Scott, R.A., *Inorg. Chem., 26*, **1987**, 2477-2479.
41. Wang, S.; Waldo, G.S.; Fronko, R.; Penner-Hahn, J.E., in *Proceedings of the Fifth International Conference on XAFS*, Seattle, WA, **1988**.
42. Lindner, T.; Somers, J. *Phys. Rev. B, 37*, **1988**, 10039-44.

THE ROLE OF X-RAY ABSORPTION SPECTROSCOPY IN ELECTRONIC STRUCTURE STUDIES

E.Ercan Alp
Argonne National Laboratory, Argonne, Illinois 60439

The X-ray Absorption Near Edge Structure (XANES) spectroscopy has been profitably exploited in recent years to obtain electronic as well as structural information about bulk materials, surfaces, microclusters, molecules, and of highly dispersed catalysts. The x-ray absorption process involves electronic transitions between initial states which are atomic-like core levels and empty final states above the Fermi level. The final states accessible are determined by the electric dipole selection rules. However, some forbidden transitions become allowed for atoms in a lower symmetry environment. This feature essentially forms the basis of structural information that can be obtained from XANES studies. It should be noted, however, that this spectroscopy provide information about the excited state of the atoms, due to the existence of a core-hole state. This is a mixed blessing; the nature of relaxation of the core hole provides information about the interaction strength between ligands and the atom, despite the fact that it is difficult to calculate this effect exactly. Hence, the information about the ground state of the absorbing atom is indirect.

The atom specific nature of this spectroscopy requires x-ray sources that are broadly tunable in energy. The absorption energies of elements can range from few electron volts (16 eV for hydrogen 1s to 2p transition) to over 100 kilo electron volts (115,606 eV for uranium 1s to 7p transition). Naturally, there is no single light source which can provide photons covering this energy range with enough intensity to make a measurement practical. However, with the availability of synchrotron x-ray sources, this has been overcome to a great extent. Ultraviolet and soft x-ray sources as well as hard x-ray sources are now routinely available in the USA as well as abroad. On the other hand, there are limitations in our ability to monochromatize this white radiation. The methods used to monochromatize radiation vary as the energy is changed. For example, grating monochromators provide good energy resolution below 1000 eV, while silicon or germanium crystals can be used between 2.4 and 20 keV. This leaves a gap between 1 to 2.4 keV. Unfortunately, this region covers K absorption edges (1s to 2p) of Na, Mg, Al, Si, and P, which are commonly found in many systems. The efforts to use InSb, Beryl, or YB_{66} and artificially grown multilayers with suitable periodicity to monochromatize radiation from synchrotron sources proves to be overcoming this problem (1)

The near edge absorption region in x-ray absorption spectrum is typically defined between 10 to 20 eV below the atomic absorption energy, and 30 to 50 eV above, before the EXAFS oscillations start. These oscillations are due to the interference between outgoing and

backscattered electron waves, and contains structural information in terms of interatomic distances, and coordination numbers. The electronic information in XANES spectrum is pronounced in different forms. While the relative location of the absorption edge reveals the effective charge on the absorbing atom, the location and intensity of the resolvable features provide additional details about the relative width and occupancy of the final states. Furthermore, the polarized nature of the synchrotron radiation provides an additional dimension to study the anisotropy of the final electronic states in single crystals or oriented samples. Below, examples are provided to demonstrate these capabilities, as well as their limitations.

The XANES spectroscopy can be performed in transmission, or in fluorescence mode when x-rays are detected, or in total electron yield count-mode when secondary conversion electrons are detected. The transmission experiments provide best signal-to-noise ratio, and also the measurement is representative of the bulk. For dilute samples, the fluorescence mode is necessary. The lowest concentration that can be detected in flourescence mode depends on various factors like subtended detection angle, the photon flux, and the ratio of the absorption cross-section of the element of interest to that of the total cross-section of the material. As a rule of thumb, the dilution ratio can be as low as 10^{-5}. The penetration of x-rays below 3 keV requires very thin samples such that not only it is impratical to prepare them, but also signal-to-noise ratio also becomes a problem. In such cases, total electron yield count can be used to measure absorption spectrum. These measurements require ultra high vacuum environment, and also they are very surface sensitive.

The examples provided below are selected from this author's and his collaborators' data base, and hence represent only a small fraction of XANES spectroscopy studies currently being conducted at numerous places.

1. The determination of effective charge on an atom in a solid:

One of the common problems faced in solid state studies is the non-destructive determination of effective charge on an atom in a solid or at a surface. In addition to other spectroscopic techniques like Mossbauer, photoelectron, or other resonance spectroscopies, XANES spectroscopy proves to be a complementary, and at times a unique technique. We will demonstrate this point with an example regarding compounds containing copper. The copper atom in its ground state has $(Ar)3d^{10}4s^{1}$ configuration. As copper is oxidized, the energy required to excite an electron from a 1s level to empty 4p levels increases. The relative location of Cu K-edge in energy can be shown to be related to the effective charge on Cu. However, the absorption edge itself has a width of 10-25 eV. This makes it difficult to make a quantitative comparison between different compounds. Recently, a method based on analysis of energy moments of the area under x-ray absorption spectrum has been developed (2). This method allows a quantitative

estimate of the location of absorption edge. Fig.1 (a) shows the XANES spectra of a series of copper compounds, obtained in transmission mode. The zero of the energy scale corresponds to the location of the first peak in the derivative of copper metal spectrum. In Fig. 1(b), the location of absorption edges, which is denoted "characteristic energy", as determined with the procedure described in Ref. (2), is plotted versus the formal valence.

This characteristic energy represents the overall effective charge on the absorbing atom. Sometimes, it is necessary to go a step further, and identify some of the resolvable features, in an attempt to gain additional information about the degree of anisotropy, and its behavior with chemical doping , pressure or temperature. The example below demonstrates this point:

2. Polarized X-ray Absorption Studies in $La_{2-x}Sr_xCuO_4$:

The compound $La_{2-x}Sr_xCuO_4$ is an oxide superconductor with a transition temperature of 36 K for x=0.15. The undoped compound, x=0.0, is an antiferromagnetic insulator, eventhough it can be made superconducting with oxygen doping. Copper in this compound has a distorted orthorombic environment, with 4 oxygen atoms at 1.90Å distance in the basal plane of octahedral (x=0.0) or tetragonal (x=0.15) structure, and 2 oxygen at 2.43Å distance along the crystallographic c-axis. The XANES spectra at the copper K-edge for x=0.0 and x=0.15 powder samples are shown in Fig. 2 (a). Doping a trivalent atom site (La) with a divalent ion (Sr) should cause a change in the oxidation state of copper and/or oxygen. When the two powder absorption spectra are compared, it is difficult to see a visible change. However, when magnetically oriented samples are measured, there is a considerable shift in the spectra obtained where the electric vector of the x-rays are perpendicular to the crystallographic c-direction, as shown in Fig. 2(b).

At this point it is worthwhile to mention that it is possible to simulate near edge absorption spectrum using multiple scattering (MS) formalism. This method works well, provided that the scattering potential used represents the material under study. Recently, Goodman et.al. has developed a method in which MS potential has been derived from ground and transition state calculations by self consistent discrete variational X-a method with the clusters embedded in an extended lattice (3). The calculations indicated that the peak labeled 2 in Fig. 2 (b), is the result of excitation of an electron from 1s levels into final states consisting of 80 % $4p_z$ character. The same calculations indicate that peak 3 in Fig. 2 (b) is due to transitions into orbitals of 91% $4p_{x,y}$ character. The $4p_z$ orbitals are calculated to be lying some 3.4 eV below the $4p_{x,y}$ orbitals. This shift in energy is comparable to the measured value, and it is in the right direction (4)

3. Probing empty 5f and 6d levels in actinides with M-edge XANES :

Uranium compounds show a rich variety of electronic and magnetic behavior, including mixed-valency, narrow band effects, and superconductivity. In a given series of alloys,

one can see transition from a localized to itinerant behavior.Using multiple edge XANES at the L-edge or at the M edge one can selectively study the differences in the localization of final 6d and 5f states. The example below demonstrates such a case.

The M_V and M_{IV} absorption edges in uranium correspond to 3d to 5f transitions, while M_{II} and M_{III} -edges correspond to 3p to 6d, and M_I-edge corresponds to 3s to 7p transitions. As a result, by complete analyses of all absorption edges, one can probe the entire unoccupied valence electron bands. In the case of U intermetallic compounds, the main interest is in 5f electrons which are in an intermediate regime where the 5f electron-electron correlation energy is comparable to 5f bandwidth. This makes it possible to synthesize intermetallic systems with varying degrees of localization of 5f bands with proper doping. For example, in URh_3B_x ($0 < x < 0.8$) the electronic character changes from itinerant to localized as x increases as determined by electrical resistance, magnetic susceptibility, specific heat (5), and X-Ray Photoemission Spectroscopy (6). The M_5 and M_3 edge XANES spectra are shown in Fig. 3 (a) and (b). The analysis of the M_{IV} and M_V-edges indicate that there are changes in the line widths and intensities of the "white line" (i.e. the most intense line, indicating the availability of large empty states, closely located in energy space). On the other hand, M_{III}-edges broaden and split in URh_3B_x as x increases. This result is compatible with band structure calculations, which indicate that with boron doping, 6d levels of uranium broadens, and lowers in energy towards the Fermi level (9).

These examples give just a glimpse of how XANES spectroscopy can be used. For experiments currently underway, it is useful to consult annual reports of National Synchrotron Light Source (NSLS) at Brookhaven National Laboratory, Cornell High Energy Synchrotron Source (CHESS), Stanford Synchrotron Radiation Laboratory (SSRL), and Synchrotron Radiation Center in Stoughton, Wisconsin (SRC). There are several review articles covering the developments in this field. The one by Röhler (7) is especially worth mentioning.

Acknowledgements:

I would like to acknowledge my collaborators G.K. Shenoy, S.M. Mini, M. Ramanathan, G.L. Goodman, J. Guo, D.E. Ellis, L. Soderholm, A. Bommannavar and P. A. Montano who have contributed to most of the experiments mentioned above experimentally and theoretically. The experiments mentioned in this report are carried out at X18-B and X11-A beamlines at NSLS. The support of US DOE, BES Materials and Chemical Sciences under contract # W-31-109-ENG-38, and its role in the development and operation of X-11 beamline at the NSLS under contract # DE-AS05-ER107-42 is also acknowledged. The NSLS is supported by US DOE, BES Materials and Chemical Sciences under contract # DE-AC02-76CH00016 .

References

1. J. Wong, SSRL Activity Report, Stanford, CA. (1988).

2. E.E. Alp, G. Goodman, S. M. Mini, M. Ramanathan, L. Soderholm, G.K. Shenoy, (J. Phys.: Condensed Matter, submitted).

3. G. Goodman, D. E. Ellis, E. E. Alp, L. Soderholm, (J. Chem. Phys., submitted).

4. E.E. Alp, S. M. Mini, M. Ramanathan, B.W. Veal, L. Soderholm, G.L. Goodman, B. Dabrowski, G.K. Shenoy, J. Guo, D.E. Ellis, A. Bommanavvar, O.B. Hyun, Synchrotron Radiation in Materials Research, MRS Symposium Proceedings, vol 143, eds. R. Clark, J. Gland, J. H. Weaver, Boston (1989) 97.

5. B.D. Dunlap, F.J. Litterst, S.K. Malik, H.A. Kierstead, G.W. Crabtree, W. Kwok, D.J. Lam, A.W. Mitchell, "f-Band Narrowing in Uranium Intermetallics", Proc. of 5th Int. Conf.on Valence Fulctuations, Jan 5-9,1987, Bangalore, India.

6. A. J. Arko, B. Yates, B.D. Dunlap, D.D. Koelling, A.W. Mitchell, D.J. Lam, "Understanding Photoemission Spectra in Uranium Based Heavy Fermion Systems", Proc. of 5th Int. Conf.on Valence Fulctuations, Jan 5-9,1987, Bangalore, India.

7. J. Röhler, "X-ray Absorption and Emission Spectra" in Handbook on the Chemistry and Physics of Rare-Earths, eds. K. A. Gschneider, Jr., L. Eyring, S. Hüfner, vol 10, pp. 453-545 (1987).

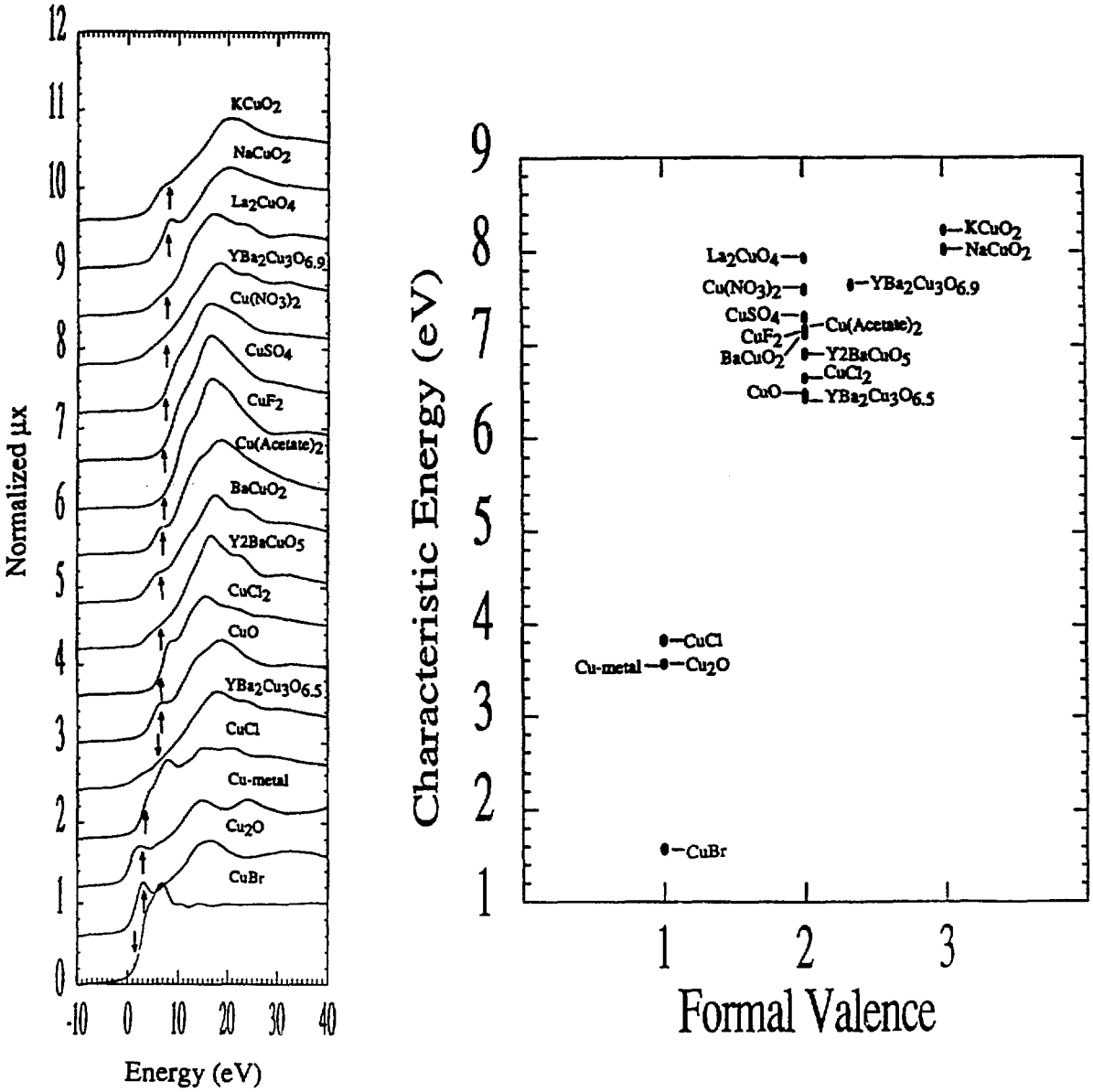

Figure 1. The normalized Cu K-edge x-ray absorption spectra of several copper compounds (a), and the "characteristic energy" of the same compounds plotted versus the formal Cu valence.

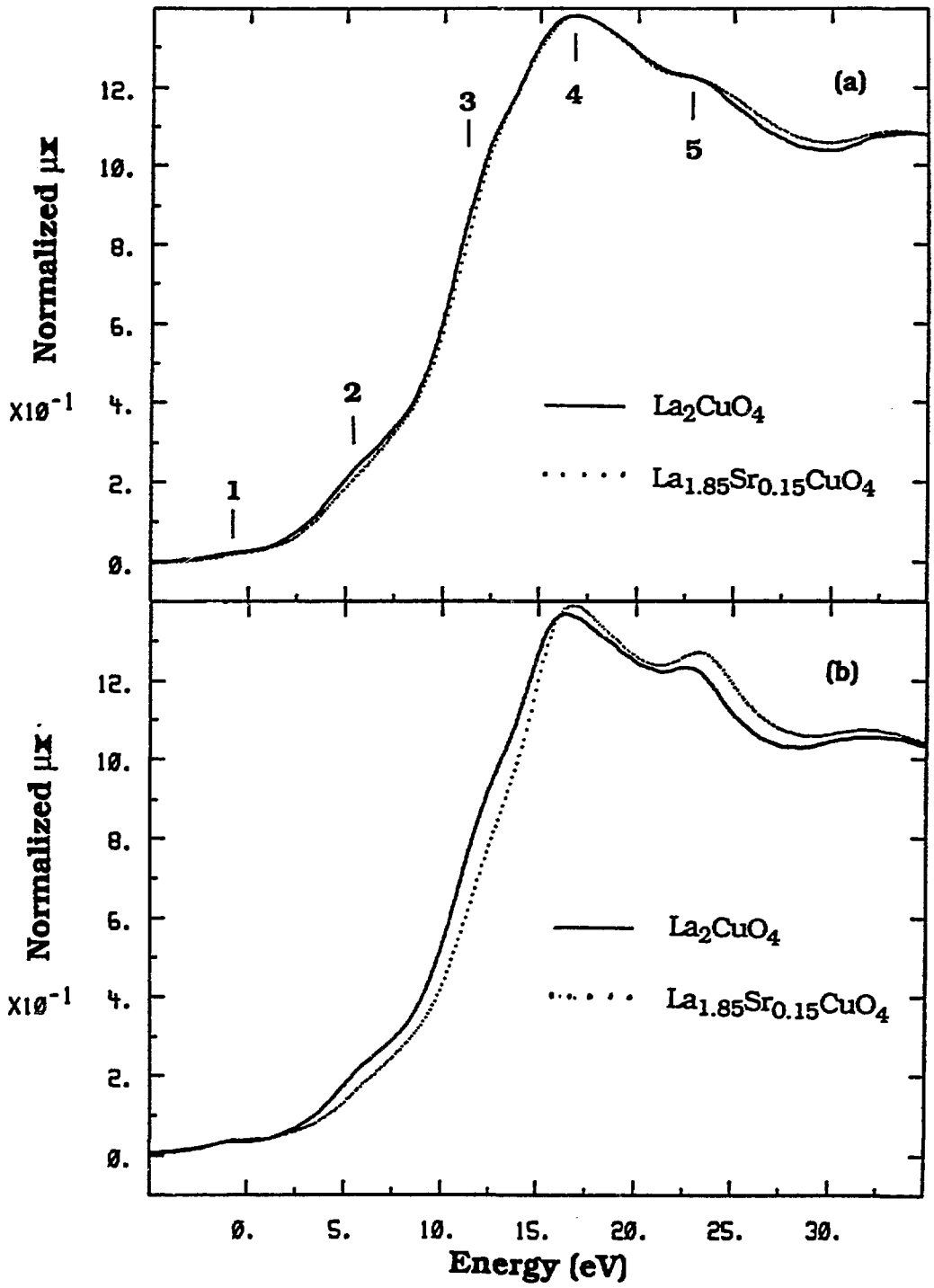

Figure 2. The normalized Cu Kedge x-ray absorption spectra of $La_{2-x}Sr_xCuO_4$ for x=0.0 and x=0.15 for powders (s), and for magnetically oriented samples in which the crystallographic c-direction is perpendicular to the polarization direction of synchrotron x-rays. The numbers indicate the resolvable features, which can be identified with the help of multiple scattering calculations (Ref 4).

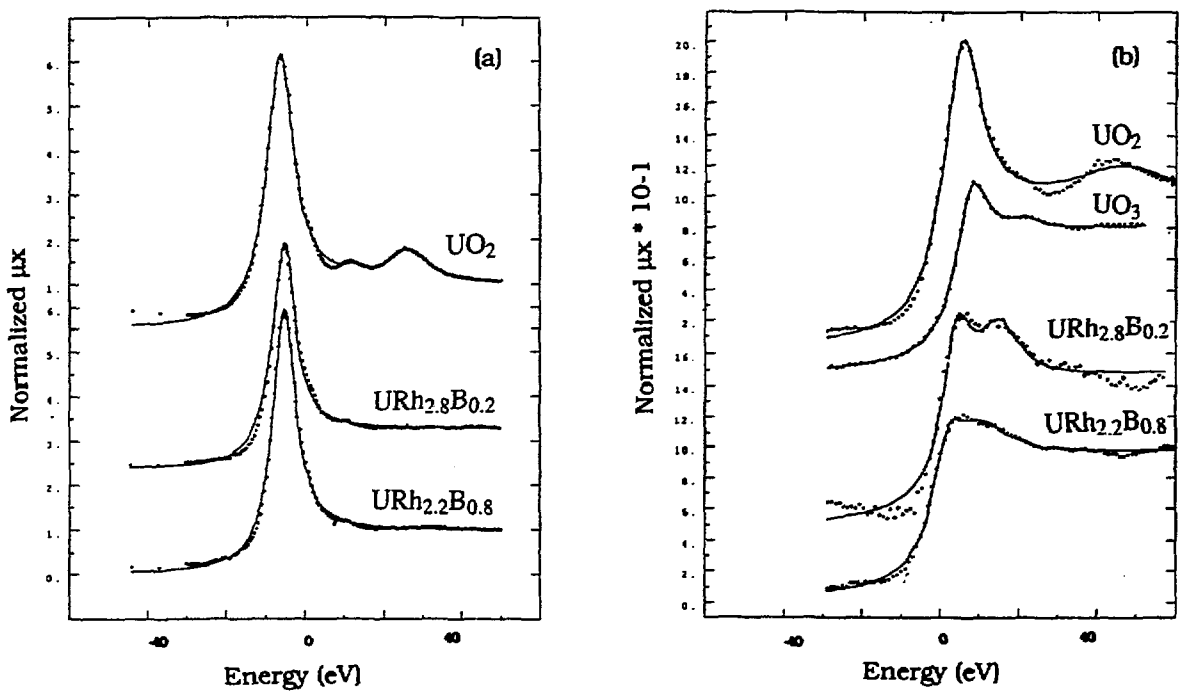

Figure 3. The uranium M_5 x-ray absorption edge, indicating the similarity of the final empty 5f states inspite of the heavy B doping in $URh_{3-x}B_x$ (a), and M3 edges showing the sensitivity of the final 6d states to alloying (b).

SESSION III

SMALL-ANGLE SCATTERING

SOME APPLICATIONS OF SMALL ANGLE SCATTERING IN CHEMISTRY

S. J. Henderson, L. Dai and J. W. White
Research School of Chemistry
Australian National University
GPO Box 4 Canberra ACT 2601
Australia

Lecture Given at Workshop on Chemical Applications of Synchrotron Radiation, October 3-4, 1988, Argonne National Laboratory, Argonne, Illinois.

INTRODUCTION

Small angle x-ray scattering is an established method for determining the microstructure of alloys, disordered solids, biological and inorganic colloids and polymer solutions.[1,2,3] The related neutron small angle scattering[3] method has risen into prominence because the use of long wavelength neutrons avoids multiple Bragg scattering effects, results in little absorption of the beam by samples of millimeter thickness and profits from the very important contrast variation that can be produced by isotopic labeling (e.g. with deuterium against hydrogen) of components[3,4] of a dispersed system. This paper presents data from both techniques to define some of the scope for small angle X-ray scattering in chemistry using synchrotron radiation.

The high intensity and beam quality from synchrotron x-ray sources allow the present supremacy of neutron small angle scattering to be challenged, and a particular virtue of x-ray scattering compared to neutrons is the very small incoherent scattering. This means that in principle, measurements of a scattering pattern can be taken to high wave vector transfers with less interference from sample dependent background, an essential aspect for the correct imposition of absolute intensity constraints on model scattering functions. The same advantage arises in measurements of the critical external reflection profile of x-rays at interfaces, a closely related technique of chemical interest. Measurements in this area are also included here. Our objectives are to highlight areas of interest as well as technique and intensity limitations for both methods. The subject areas covered include studies of: (a) designer clay catalysts in relation to their synthesis and structure, (b) the structure of block copolymer solutions and (c) the

structure of polymer-solution interfaces using present-day x-ray and neutron methods. We conclude with some technical developments to improve small angle scattering instruments at a synchrotron source.

For consistency in nomenclature it is convenient to define a number of quantities and relationships commonly used in small angle work. These definitions are given in Table 1. A more complete discussion of these quantities is given in standard texts.[1,2]

Table 1

Definitions of Quantities in Small Angle Scattering

Small Angle Region	for $\lambda = 1.5\text{Å}$	$10^{-3\circ} < 2\theta < 10^{\circ}$ $3'' < 2\theta < 10^{\circ}$
Scattering Vector	$Q = \frac{4\pi}{\lambda} \sin\theta$	$0.0001 > Q/\text{Å}^{-1} < 0.7$
Scattering Length/e^-	$b = \frac{e^2}{mc^2}$	$= 2.81 \times 10^{-13}\text{cm}$
Scattering Length Density	$\bar{\rho}/10^{-5}\text{Å}^{-2}$	$= \frac{n\rho}{MW} A.b = \frac{n\rho}{MW} \times 1.695$
Contrast between media (1,2)	$\bar{\rho}_1 - \bar{\rho}_2$	
Example: Isolated Particle	$I(Q) = P(Q) = \lvert \int dV\bar{\rho}(r) e^{-iQ.r} \rvert^2$	
Sphere	$I(Q) = (\Delta\bar{\rho})^2 V^2 \left[\frac{3 \sin QR_0 - QR_0 \cos QR_0}{(QR_0)^3} \right]$	
Guinier Region	$\lim_{Q \to 0} \ln I(Q) \text{ vs } Q^2$	$I(Q) = (\Delta\bar{\rho})^2 V^2 \cdot \exp -[QR_g^2/3]$
Porod Region	$\lim_{Q \to \infty} I(Q) \text{ vs } Q$	$I(Q) = KQ^{-4}$

THE SMALL ANGLE X-RAY SCATTERING CAMERA

X-ray small angle scattering measurements were made with a double focusing (Huxley Holmes) camera constructed in the Research School of Chemistry at the Australian National University. The characteristics of this camera, whose performance approximates to the present state of the art using rotating anode systems, are described as a datum for the improvements expected with a synchrotron source.

The camera is based upon the Enraf-Nonius (GEC) GX-13 "large wheel" rotating anode x-ray source where approximately 3 kW are delivered to a 100μ x 1 mm spot on the copper anode. This spot is viewed at 6° and so the effective source dimension is 0.1 x 0.1 mm^2. The x-rays are collimated and focused onto a one-dimensional position sensitive detector - kindly supplied by M. Andre Gabriel (European Molecular Biological Laboratory, Grenoble) which has a nominal spacial resolution of 0.14 mm. The optics and intensity have been optimized for maximum brightness and comparisons with other high performance x-ray cameras are shown in Table 2 below. Figure 1 illustrates the optics of the system.

Table 2

Comparison of X-ray Small Angle Scattering Cameras

at Rotating Anode Sources

(date from J. Appl. Cryst. 17, 337-343)

	OAK RIDGE* National Laboratory	TAKASAKIA Japan Atomic Energy	A.N.U. R.S. Chem
Real source power	3.2kW	1.2kW	1.2kW
Effective source size	1*1mm	0.1*0.1mm	0.1*0.1mm
Relative brilliance	3.2 kW/mm^2	120kW/mm^2	1201W/mm^2
Monochromator	pyrolitic graphite graphite	(bent mirror + bent quartz)	
Minimum angle to which data are recorded	2.7 mrad	0.6mrad	1.5mrad
Area of entrance slit	0.79 mm^2	1.02mm^2	0.6mm^2
Power incident on specimen	2.8* $10^6 X.s^{-1}$	0.71*$10^6 X.s^{-1}$	7*$10^6 X.s^{-1}$
Background equivalent in water thickness	? ?	0.2	
Count rate at the beam stop edge:	? ?	5$X.s^{-1}$	

*This camera now has considerably enhanced performance - G. Wignall private communication.

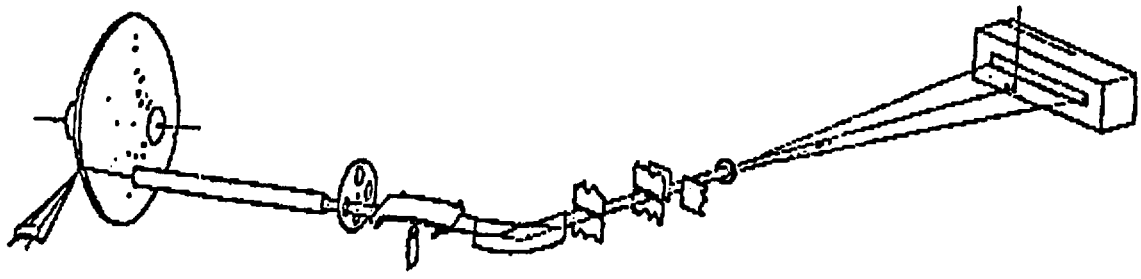

Figure 1

Schematic diagram of the small angle x-ray camera at Research School of Chemistry, Australian National University.

In setting up the camera, particular attention was paid to minimizing electronic noise and x-ray background. Figure 2 shows the scattering from a 1 mm water sample where the overall scattering is about five times the background from all sources. The scattering in this camera can thus be measured in absolute units using the scattering of water as standard.

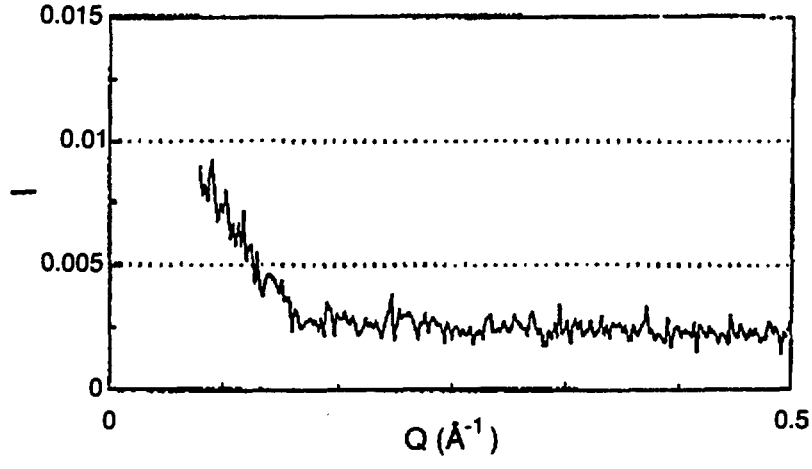

Figure 2

Low angle x-ray scattering from a 1 mm water sample.

The resolution of the instrument is illustrated in Figure 3 which compares the small angle neutron[5] and x-ray scattering patterns from dry collagen fibers. In using the camera, the vertical smearing function has been measured by translating the counter vertically across the focused x-ray beam. This smearing function, used with the procedure of Lake[6] allows "deconvolution" of the measured scattering function by iterative fitting of resolution convoluted models against the data. The first order of diffraction peak at d = 660 Å is clearly resolved as are diffraction orders out to at least the 22nd order.

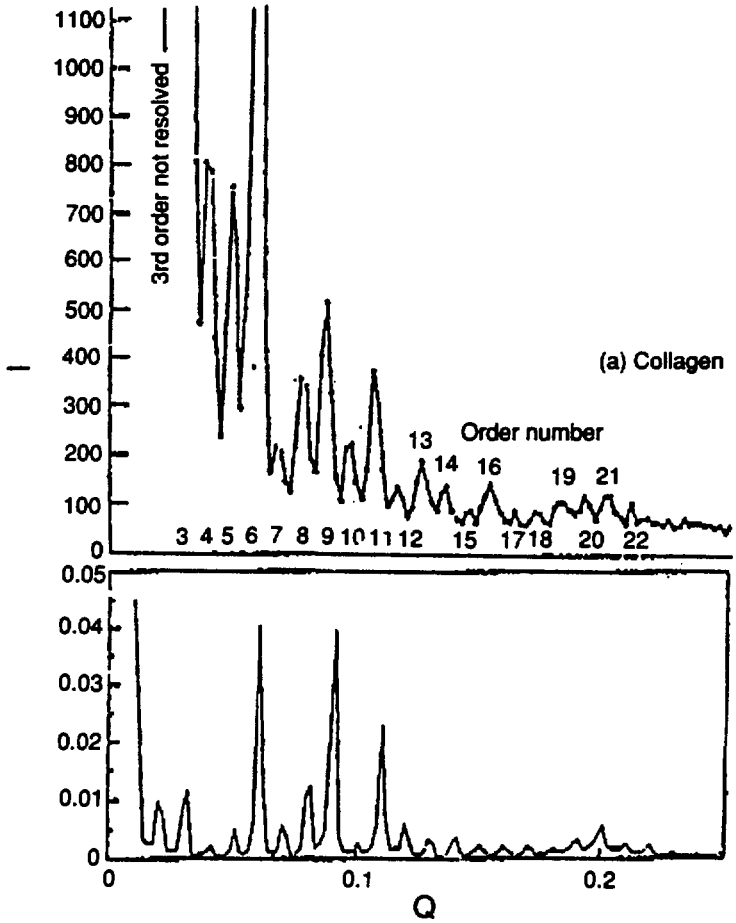

Figure 3

Comparison of calibration samples; rat tail collagen measured with the best neutron camera (D11 at ILL Grenoble, counting time 12 hours (1975) top, with the SAS camera at RSC (counting time 1 h) bottom.

The camera is currently used for studying the nucleation and crystallization of zeolite catalysts[7], the pillaring reactions[8,9,10] of clays to make specific, wide channeled adsorbants and cracking catalysts and the structure of polymer solutions.[11,12]

"DESIGNER" CLAYS

Pillared Clay Structure

Zeolites are the materials of choice for many petroleum cracking, reforming and general hetrogenious catalytic applications, because of their uniform pore sizes and relatively controlled synthetic chemistry. Clays were previously used for many of these applications and again look promising for new synthetic processes. Natural and synthetic clays are sheet like structures which may be either exfolliated to high surface area powders or intercalated to produce gallery structures. Both properties offer synthetic routes to catalysts with wider pore size distributions than zeolites and with predesigned prosthetic groups attached to "pillars" chemically inserted into the gallery structure. Wide pore size distributions open up the possibility, for example, to "crack" branched as well as straight chain petroleum fractions.[13] These new clays have been called "designer clays".

Clay minerals, pillared with polyhydroxy aluminum cations, are effective petroleum catalysts,[13] the acidity of the pillars the free lateral surface and pore size being important determinants of performance. Our work aims to control these factors through accurate control of the pillar chemistry and the interpillar distances and goes beyond a simple use of stoichiometry[14] to

determine the latter. An analogy with alkali metal intercalation into graphite for which, however, rather more is known structurally,[15,16] appears to be worth drawing.

By choosing pillaring cations with different charges and clay minerals of different exchange capacity we have been able to systematically vary the lateral distribution of the pillars and hence vary the gas adsorption properties at will. The smectites chosen were pillared by different diamsar cage compounds[17] of general formula:

a

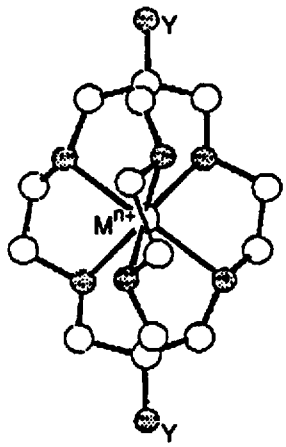

b

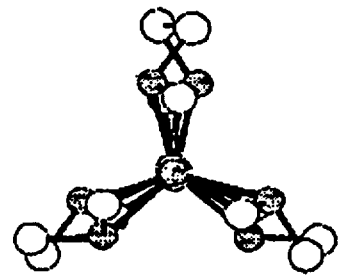

where M^{n+} is Ir^{+3}, Hg^{+2} and Y = NH_2, NH_3^+. At the x-ray intensities available to us scattering from the in plane ordering of the conci pillars was only observable when third row transition elements or mercury were the encaged ions.

For example, (Ir-diamsar)-fluorhectorite, (Hg-diamsar)-montmorillonite I and II and (Hg-diamsar)-fluorhectorite I and II were prepared under conditions of different pH and initial ion concentrations to vary the pillar/clay sheet charge ratio. The charge of the pillar ions varied from +3 for

(Ir-diamsar)$^{+3}$-flurohectorite with unprotonated amino groups to +4 for (Hg-diamsar H_2)$^{+4}$-fluorhectorite 1 and (Hg-diamsar H_2)$^{+4}$ montmorillonite 1 were all amino groups are protonated. The fluorhectorite had a (negative) charge per unit sheet surface 1.7 times that of the montmorillonite. Figure 4 shows the diffraction pattern of the iridium compound. Good layer packing of the pillared smectite sheets is shown by the, at least, six orders of c-axis diffraction resolved in reflection for all samples that have been checked. The basal spacing of these compounds increased due to penetration of cage molecules into interlayer space and was 16.4Å for (Ir-diamsar)$^{+3}$-fluorhectorites and 16.8Å for clays pillared with mercury containing ions.

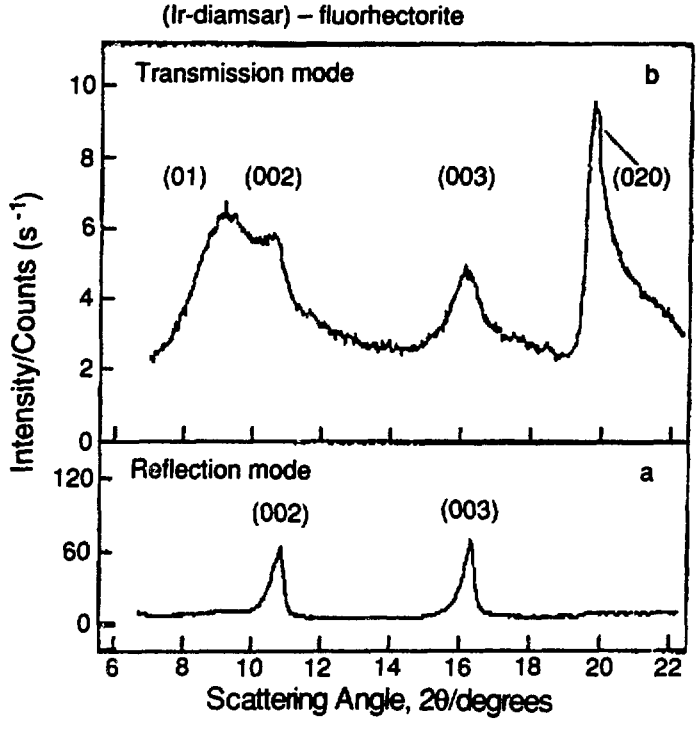

Figure 4

X-ray powder diffraction patterns of Ir-diamsar)-fluorhectorite (a) in reflection mode and (b) on transmission mode: Cu Kα radiation.

Diffraction with the scattering vector in the clay sheet plane, transmission mode, showed the (00l) peaks greatly reduced in intensity and new broad peaks, not observed in reflection. These peaks arise due to diffraction from the lateral ordering of the pillars. The peaks fit the Warren[18] lineshape expected from a two dimensional lattice and are quite broad, especially for montmorillonite-containing samples, where the concentration of pillars is at least 50% lower than in synthetic fluorhectorite for reasons of change balance. Calculations of diffraction peak shape by Warren's formula for two-dimensional layers[18] and least squares fitting to the data gives the real $2\theta_o$ corresponding to the interpillar distances "d", (see Table 3) and the two dimensional coherence lengths "L" of the diffracting particles.

Table 3

Hg-diamsar pillars

Interpillar Distances, d, and Domain Coherence Lengths

	Mole P/ Mole Clay	Pillar Charge	d/A	L/A
Mont I	0.19	+4	15.0	19.7
Mont II	0.23	+3.3	12.6	28
Fhect I	0.34	+4	10.8	62
Fhect II	0.39	+3.5	10.8	46
Fhect III	0.45	+3.0	9.5	44
		Charge/Unit Cell		Meg/100g
Montmorillonite		$0.74c^-$		95
Fluorhectorite		$1.36e^-$		170

The interpillar distances observed are not commensurate with either fluorhectorite or montmorillonite basal plane spacings. The dimensions of the fluorhectorite unit cell measured in the present work for the unpillared clay are a=5.29Å and b=9.07Å. Barrer et al.[19] reported for fluorhectorite quite similar cell parameters: a=5.16Å, b=9.08Å. For montmorillonite, the unit cell has a =5.18Å and b=9.00Å[20]. The dependence of d on pillar concentration measured by microanalysis (Figure 5) indicates the formation of a two-dimensional pillar lattice on the smectite surface with a characteristic scale which is a function of a pillar charge.

With more intense x-ray beams the inplane distribution of lower atomic weight pillars could be determined and the expected domain structure (and

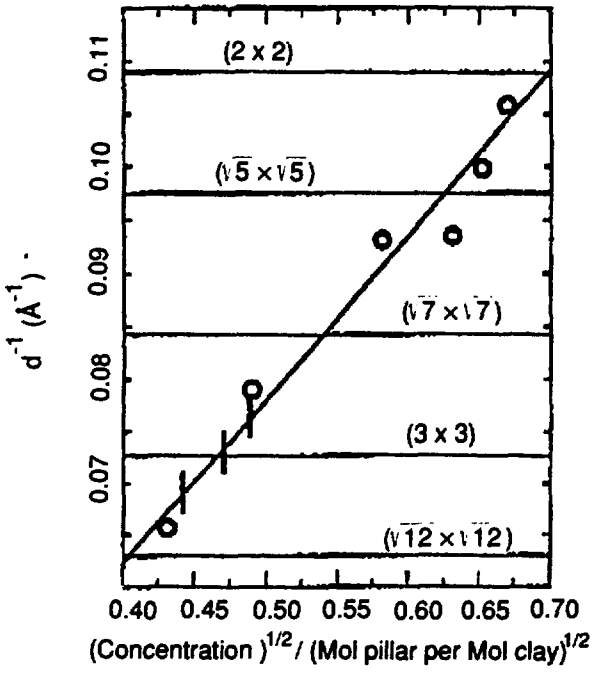

Figure 5

Dependence of 1/d on $(p)^{1/2}$, where p is pillar concentration given in Mol pillar per Mol clay and d is the experimental distance between pillars centers.

hence shape selectivity for gas adsorption) worked out. The high crystallinity observed for samples were the pillar packing is near to registry with the clay also indicates that very small single crystals might be found allowing three dimensional structures to be worked out when more intense x-ray beams became available.

Studies Of The Pillaring Process - Clay Intercalation

The process whereby regular gallery structures are established in smectites by intercalation is both intrinsically interesting and controllable for different synthetic ends. Figure 6 shows the small angle scattering from suspensions in water of the synthetic clay perfluoro hectorite. At low concentrations of the clay the small angle scattering pattern is a monotonic function of the momentum transfer, Q. This function is well fitted by the scattering function for isolated sheets whose thickness is about 8Å. The decoration of such isolated sheets by heavy metal cations and the subsequent aggregation of these sheets is currently being studied as one of the modes of aggregation leading to pillared caly formation. From the practical point of view of producing highly crystalline and regular materials control of this process is of importance.

It can also be seen from Figure 6 that at clay concentrations in water above 1% W/W, structure appears at lower momentum transfers. This structure we associate with the formation of clay tactoids. The peaks are diffraction peaks associated with interferences between regularly packed clay sheets and the inter sheet distance varies systematically with the clay concentration. Figure 7 shows the variation of clay sheet separation (deduced from the maxima

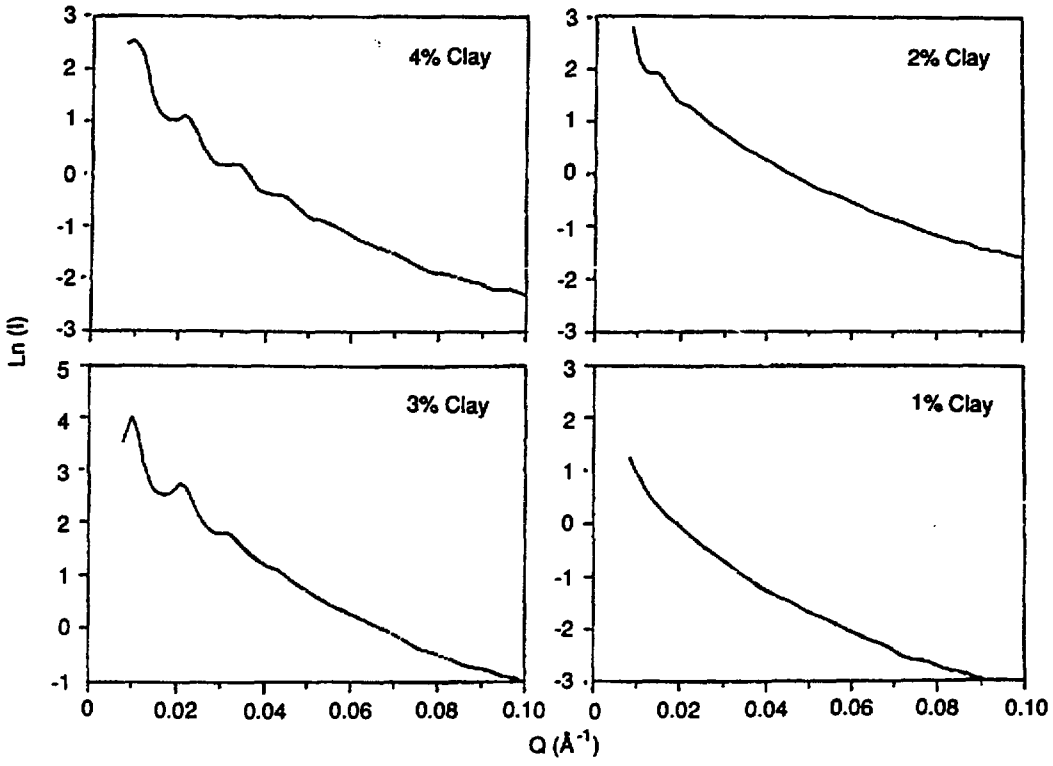

Figure 6

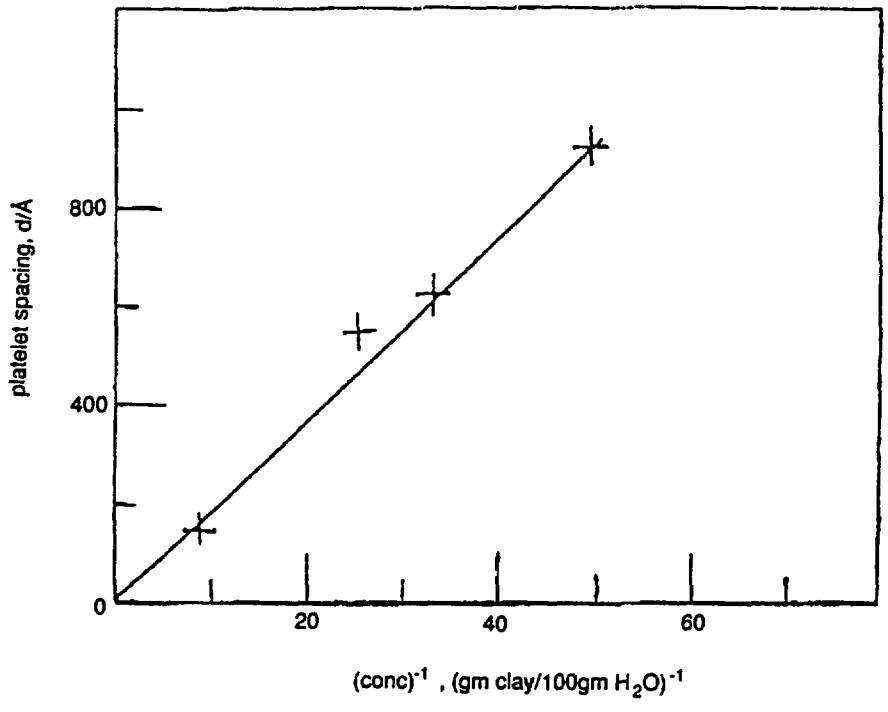

Figure 7

in the interference function) as a function of clay concentration in the solution. The slope of this curve is very close to the unit cell area of the clay particles as expected.

When pillared clays are produced from high concentration clay suspensions pillaring of clay tactoids must play a role or there must be an equilibrium between the clay tactoids and the isolated clay sheets pillared by the process described above. Again, it is possible to follow this phenomenon with the rotating anode x-ray camera but times are of the order of many hours. The higher intensities available from synchrotron sources should allow experiments to be performed with milliseconds time resolution from the onset of sol mixing.

Finally the fundamental aspects of pillar adsorption at the clay water interface may be followed using synchrotron radiation. It has been demonstrated that good diffraction patterns from krypton adsorbed on single crystal faces of graphite can be obtained with synchrotron beams.[21] An analogous experiment, allowing the domain structure as a clay sheet change, ionic charge and ionic concentration of the contact solution could be done using synchrotron intensities and single clay sheet surfaces.

Electrical Conducting Polymers

Polyacetylene, the simplest electrically conducting polymer (when doped) is a hard infusible and brittle material. Its immense variation in electrical conductivity (10^{-8}S-10^{5}S) subsequent to doping is of intrinsic interest and has recently allowed the construction of the first polymer transistor.[22] In

that experiment extremely thin films were produced from spun precursor materials. Since polyacetylene may be made soluble in organic solvents by copolymerisation[23,24] there are alternative routes to thin films. Figure 8a shows the structure of polyacetylene and polyisoprene[25] the two species in the co-polymer. The solubilization of polyacetylene by the polyisoprene tail in many ways resembles the solubilization of a fatty acid chain by the acidic head group of a soap, Figure 8b. Solutions of polyacetylene-polyisoprene PA-PIP thus have potentially useful amphiphilic properties. We have studied the concentration dependence of the aggregation in PA-PIP/toluene solutions as a function of concentration and temperature. Both the structure of the copolymer in dilute solution and in the interface between solution and air have been addressed, the first using neutron small angle scattering and the second using neutron critical external reflection at the air solvent interface[11,12] following the recent observation of a surface excess in homopolymer solutions.[26]

Polyacetylene $(CH)_x$, "PAH"

Very insoluble
Infusible
$\rho = 1.16\ gcc^{-1}$
crystalline

Polyisoprene 1:4 $(C_5H_8)_n$, "PIP"

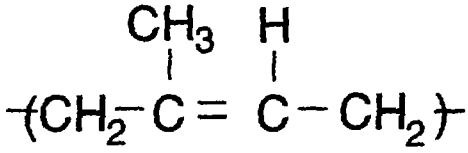

Soluble
Fusible
$\rho = 0.913\ gcc^{-1}$
rubbery

Figure 8a

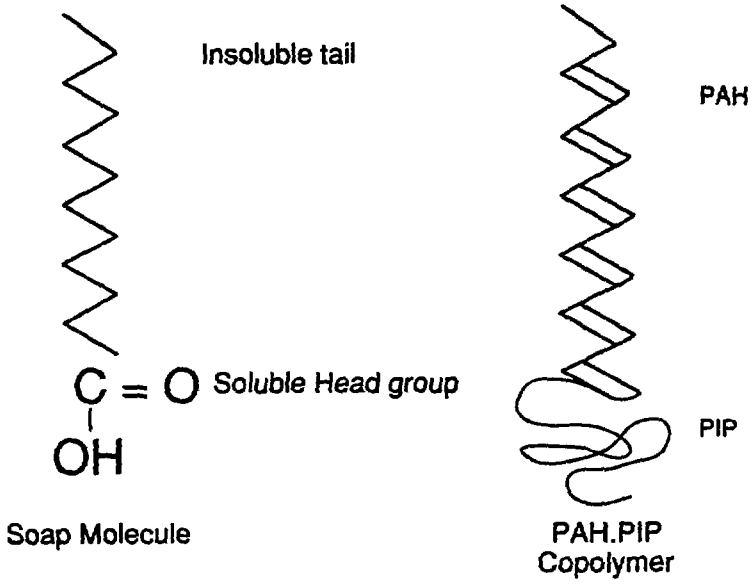

Figure 8b

By analogy with surfactant solutions we expect, at very low concentrations, that there will be isolated copolymer molecules in solution. At somewhat higher concentrations a critical micellar concentration will be reached and at this concentration and above micellar structures will exist. As the concentration is further increased - for example in the process of concentrating or evaporating the solution to make a thin film, the appearance of various mesophases is expected. Some comparisons of the relative strengths of neutron and x-ray methods in the small angle domain can be developed using results from this copolymer system as a model. Table 4 shows the scattering length densities for the two polymer components and for the solvent, toluene, for x-rays and neutrons.

For the neutron experiments the scattering length densities for both the hydrogenous (PAH) and deuterated (PAD) polyacetylene components are needed and illustrate the good contrast variation obtained by isotopic substitution. By deuterating the acetylenic component a contrast difference of $0.79 \times 10^{-5} A^{-2}$ is produced relative to the solvent producing dominant scattering from the acetylenic component. Moreover by mixing deuterated and protonated toluene the scattering length of the solvent may be matched to 0.15, equal to that of the H-polyacetylene when necessary. Scattering from polyisoprene is nearly equal to that from h8-toluene which resolves the problem of separating the scattering from the isoprene and acetylenic parts of the copolymer in these solutions. Regrettably with present neutron intensities, small angle neutron scattering is only useful for studying concentrations well above the critical micellar concentration in these systems and so one must look to the possibility of exploring the much lower contrasts in x-ray scattering using the high intensities of synchrotron radiation to gain precision.

For x-rays it is immediately obvious that the differences in scattering length density between all components are much smaller. It is possible, however, to achieve the same form of contrast variation as the neutron experiment by an appropriate addition of another slightly higher density solvent to the toluene to match the isoprenyl tail. The low scattering length density difference ($0.1 \times 10^{-5} A^{-2}$) between solvent and polyacetylene and the need for absolute scaling however, require high measurement precision. This is an interesting challenge.

The neutron small angle scattering results, at relatively high concentrations of PAD.PIP (solid and gel phases) are shown in Figure 9.[27] The different slopes for the log/log plots indicate immediately that the scattering is from particles of different dimensionality for the two phases. Such results may be obtainable at low concentrations with synchrotron x-rays and some contrast matching. The data for the 20% PAD,PIP can be quite well fitted to the scattering from fairly monodisperse, long cylinders with a cylinder radius (for the PAD component) of about 30A but the scattering from the 20% system is from objects of higher dimensionality. It is likely that microphase separation has occurred for the solid phase.

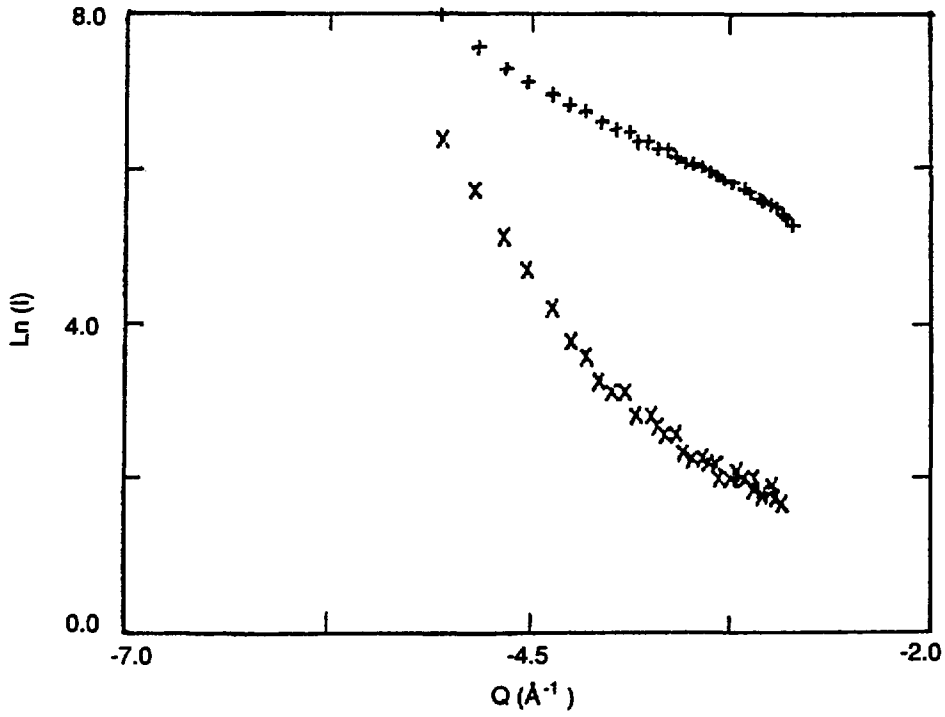

Figure 9

The limits to what can presently be done with x-rays, given the very low contrast between a polymer coil in solution and the solvent around it, are illustrated by Figure 10. This shows a log I versus Q^2 plot (Guinier plot) of the x-ray scattering from polyisoprene (MW 16,000) in cyclohexane at 25°C. The polymer concentration was 0.049 grams per milliliter corresponding to 3.1 x 10^{-3} mols per litre. At this concentration a small angle scattering pattern of the statistical reliability shown can be obtained in about 12 hours on our camera. From this we can obtain reliable values of the radius of gyration and from the concentration[12,28] dependence, the molecular weight, activity coefficient and other thermodynamic properties of the solution can be extracted reliably.

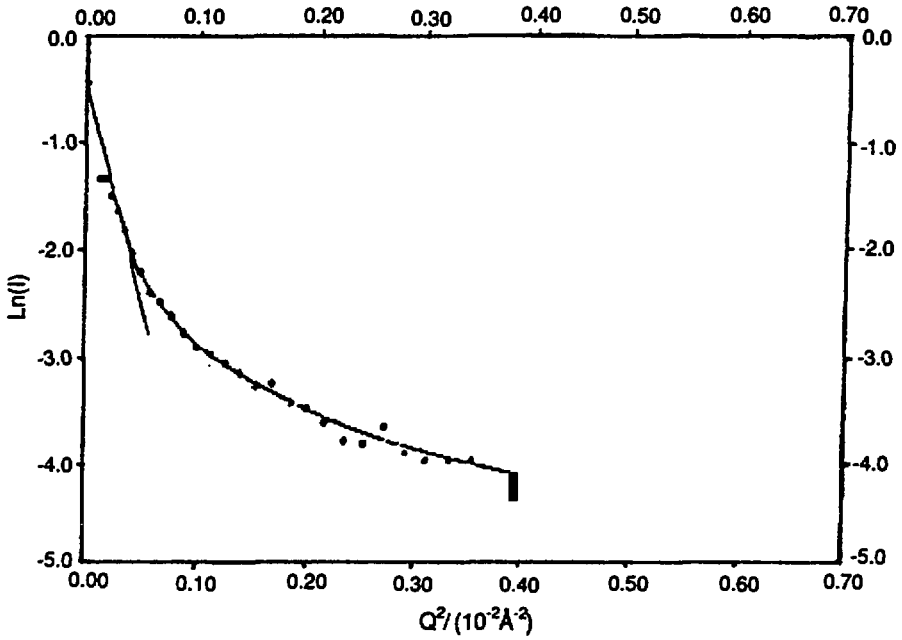

Figure 10

Guinier plot of the desmeared small angle x-ray scattering curve of PI(16000) in cyclohexane at 25°C and concentration 0.049 g/ml.

Co-polymer Solutions

A desirable inorganic effect of copolymer atom appears in the surface tension. Figure 11 shows the surface tension of 1:4 PIP,PAD [8000:530] copolymer solution in toluene at 25°C as a function of the copolymer concentration. The surface tension was determined by the drop weight method. The apparent critical micellar concentration, C.M.C., lies at about 10^{-3} mols per litre and so to make meaningful studies of the non-aggregated solutions one must make measurements below this. At present x-ray intensities measuring times for a study through the C.M.C. are very long. We have made pilot measurements for a few samples with long running times and very good temperature and beam stability.

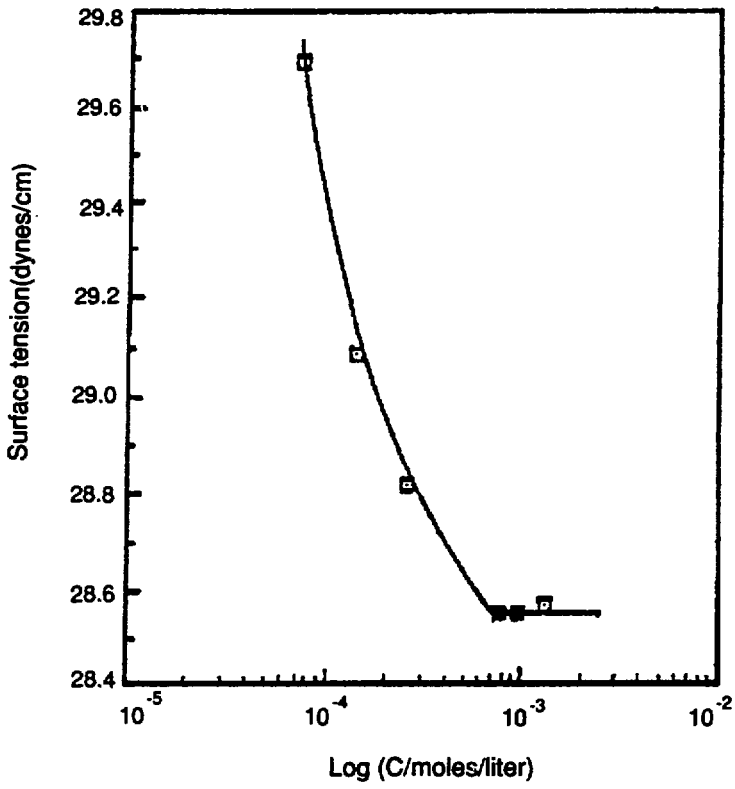

Figure 11

The surface tension vs. log concentration curves of PIP8000-b-PAH530 in toluene.

Figure 12a shows the concentration dependence of the radius of gyration for polyisoprene homopolymer solutions in cyclohexane at 25°C. For this polymer (molecular weight 8,000) there is little dependence of the radius of gyration upon concentration up to 0.1 grams per milliliter. The corresponding curve for the concentration dependence of the radius of gyration for polyisoprene (8,000) - polyacetylene in toluene at 20°C is shown in Figure 12b. There is an appreciable variation of the radius of gyration at concentrations about an order of magnitude less than those in the homopolymer solutions illustrating that interpolymer interactions and possibly aggregation are now strong. To make effective measurements on these very low concentration solutions and determine thermodynamic parameters the intensity of synchrotron radiation is needed.

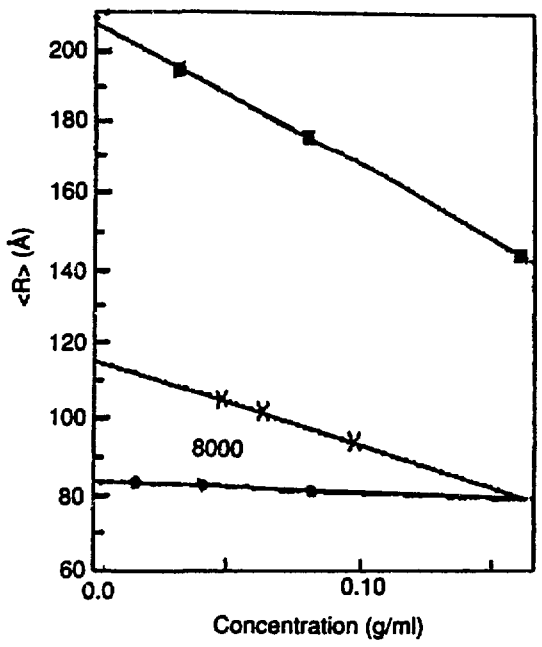

Figure 12a

Concentration dependence of the radius of gyration for PI in cyclohexane at 25°

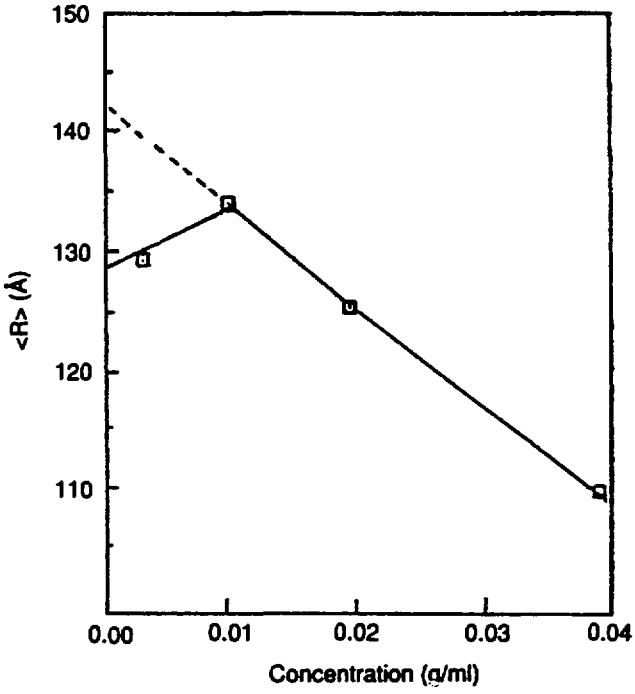

Figure 12b

Concentration dependence of the radius of gyration for PIPP8000 PAH530 in toluene at 20°C

CRITICAL EXTERNAL REFLECTION FROM POLYMER SOLUTION SURFACES

The reflectivity of neutron beams as a function of neutron momentum transfer, perpendicular to the surface is a sensitive probe of interfacial structure and may be applied to polymer solutions to determine the structure of the surface excess inferred from bulk surface tension measurements. This method is very convenient at a pulsed neutron source.[29,30] Figure 13 shows the neutron reflectometer, CRISP, on ISIS at the Rutherford Appleton Laboratory, England which we have used to study the distribution of polyacetylene-polyisoprene at the toluene-air interface. Again isotopic substitution in the acetylenic component allows the contributions of the two copolymer components to be studied.

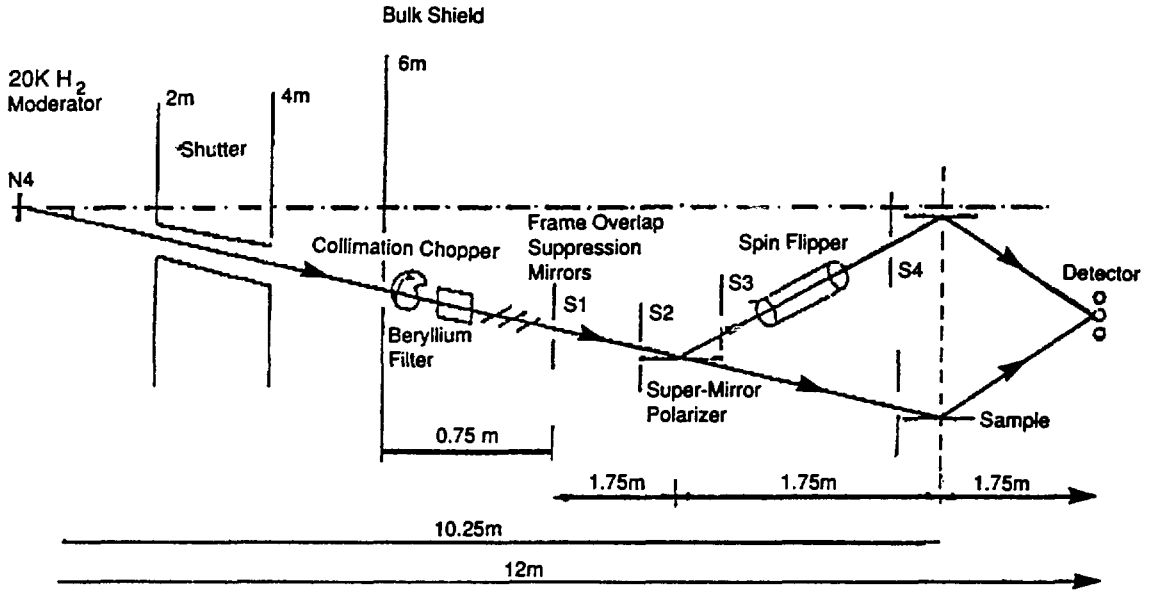

Figure 13 Neutron reflectometer, CRISP at the ISIS pulsed neutron source.

The instrumentation uses all neutron wavelengths, in the range $0.5 < \lambda/\text{Å} < 20$. The sample, in our case liquid toluenes and copolymer solutions, was contained in a vibration protected trough which could be raised or lowered so that reflection was measured using the full physical height of the neutron beam. Instead of measuring the reflectivity all the way from the

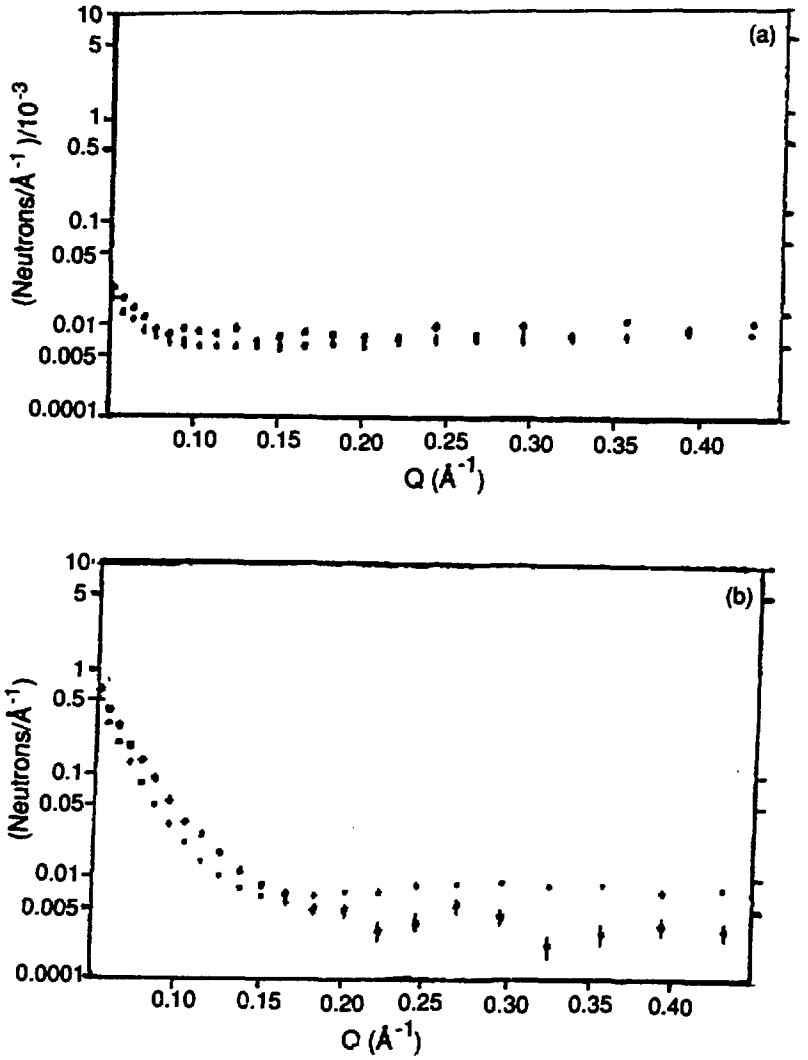

Figure 14

Critical external reflection profiles from (a) h8 toluene and (b) d8 toluene-air interface taken 6 months apart. The range of reflectivity measurable in the second set of runs (#1300 et seq) is smaller than before due to instrumental effects.

critical external reflection angle to the highest Q's ($Q = 4\pi/\lambda \cdot \sin\theta$) where θ is the angle of reflection with respect to the surface, the reflectivity of the sample at a chosen low Q (0.05 $Å^{-1}$) was scaled to its absolute value by comparison with the known reflectivity of heavy water at this Q. The

reflectivity coordinate is thus in absolute units (neutrons per Å-1). Two separate sets of experiments separated by four months were done. In that time, the sample and spectrometer characteristics had evolved. The sample may have aggregated somewhat and the amount of sample vibration (characterized by increased surface roughness) had increased.

The effects of this are seen in Figure 14 which shows part of the reflectivity profiles for h8 toluene (Figure 14a) and d8 toluene (Figure 14b) taken earlier (run numbers 1259, 1260) and later (run numbers 1303, 1300). For h8 toluene the low reflectivity (scattering length density only 0.09) and the incoherent scattering background obscure the vibration effect at high Q, but it is observable in the lower absolute intensity at Q = 0.05 Å-1. There is an obvious effect at both high and low Q for toluene d8. We return to this point in presenting the results.

Table 4

Scattering and Contrast in Polyacetylene-polyisoprene Copolymers System for Neutrons and X-rays.

NEUTRON SCATTERING LENGTH DENSITIES $10^5\bar{\rho}/A^{-2}$

	PAH/D	PIP	h8-TOLUENE	d8-TOLUENE
PAH	0.15	0.027	0.09	0.55
PAD	0.71	0.027	0.09	0.55

X-RAY SCATTERING LENGTH DENSITIES $10^5\bar{\rho}/A^{-2}$

	PAH/D	PIP	h8-TOLUENE
PAH	1.06	0.86	0.80
PAD	1.0	0.86	0.80

TABLE 5

Scattering Length Densities

Conducting Polymer Solutions

	MW	(MW)1	n*	Σ Nb/10-5A-2	Neutrons Nb/$10^{-5}A^{-2}$	x-rays
Polyisoprene (PIP)	8000	68	118	0.913	0.27	0.86
Isoprene C_5H_8	68	68	1	0.20	0.64	
Polyacetylene	2000					
deutero (PAD)	2000	14	140	1.24	0.71	1.00
proto (PAH)	2000	13	140	1.16	0.15	1.06
Toluene h8		92		0.867	0.09	0.797
Toluene d8		100		0.867	0.55	0.798
75%V/V PIP/h8					0.34	
75%V/V PIP/d8					0.225	
7%V/V PIP/d8				0.53		
7%V/V PIP/h8					0.103	

*n = number of monomers in polymers

Critical External Reflection Of Neutrons From Polyacetylene Solutions

At a particular neutron wavelength, ... the neutron refractive index (relative to vacuum) of a medium of coherent scattering length, b, is given by

$$n = 1 - \frac{\lambda^2 Nb}{2\pi} = 1 - \frac{\lambda^2}{2\pi} \cdot \bar{\rho}$$

where N is the number of nuclei cm^{-3} in the medium and $\bar{\rho}$ the coherent

scattering length density. For most materials, b, is positive and so n < 1. Critical external reflection at the air/liquid interface thus occurs. Table 5 lists the scattering length densities, $\bar{\rho}/Å^{-2}$ for the principal components of our polyacetylene-polyisoprene solutions.

The reflection profile from an infinite slab may be calculated analytically[31] as may that from a series of thin slices of different refractive indices.[32] The latter case approximates to our liquid/air interface and so we model the absolute reflectivity and the profile in Q with the minimum number of thin slices. To enhance the effects of preferential adsorption of the copolymer at the interface, we vary the contrast by deuterium substitution in the polyacetylene and the solvent.

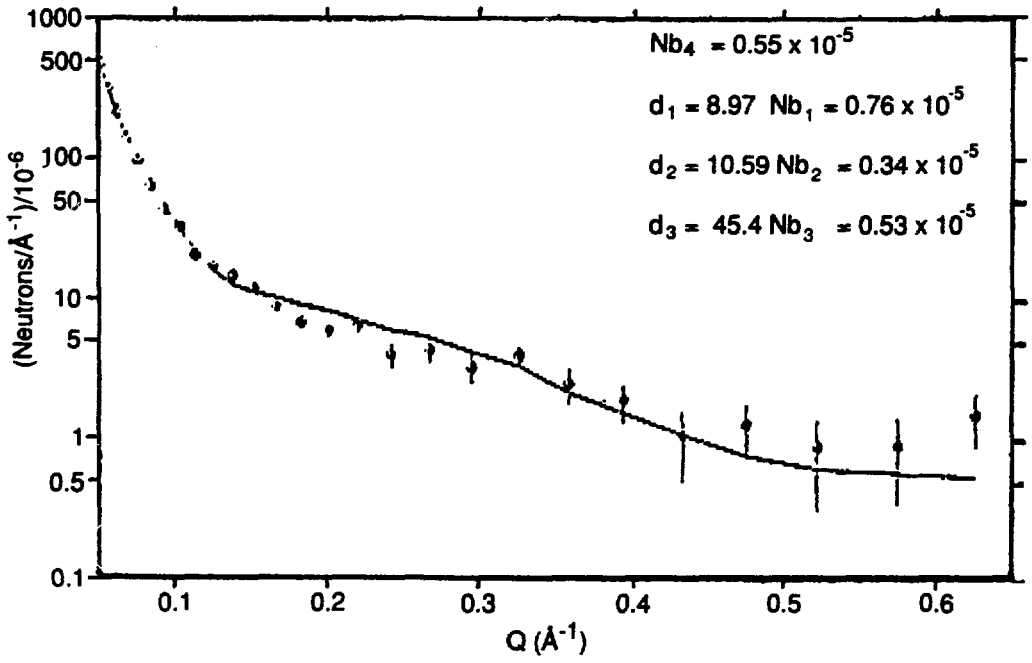

Figure 15

Critical external reflection profile for 0.05 < Q/Å-1 < 0.65 of 2.5% solution of 1:4 polyisoprene:perdeuteropolyacetylene (PIP,PAD) in deutero toluene at 25°C. The full line is a model fit-see text.

Figure 15 shows the reflection profile for a 2.5% W/W solution of PIP(8000), PAD(2000) in deutero toluene at 300 K for $0.05 < Q/\AA^{-1} < 0.65$. The striking feature of this curve-compared to the pure solvent reflection profiles (Figure 14) is the large excess reflectivity for $0.1 < Q/\AA^{-1} < 0.35$ and possibly the further change in reflectivity for $0.42 < Q/\AA^{-1} < 0.6$. The

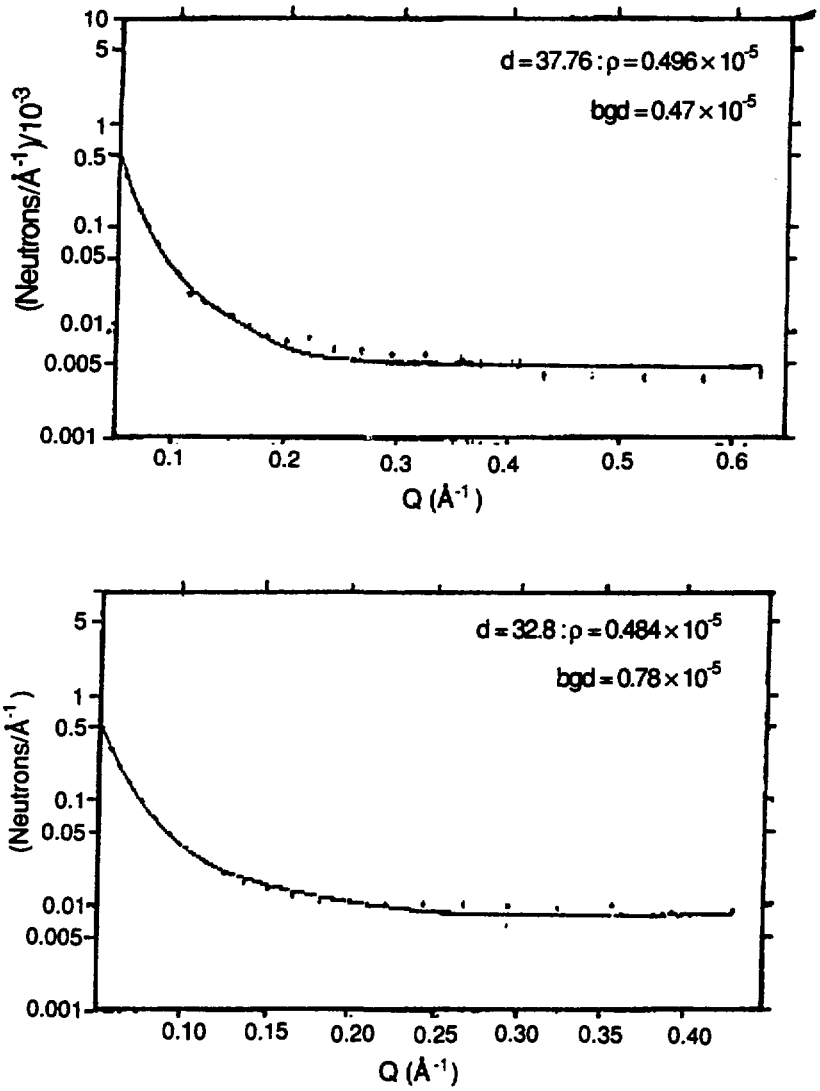

Figure 16

Fits to first and second runs of PIP,PAD in d8 toluene of a single surface layer model.

reflectivity was measurable to good precision down to one in 106 of the intensity of that just below the critical angle. At $Q = 0.05\text{Å}^{-1}$ the reflectivity of the PIP,PAD solution is only slightly less than that of the solvent.

Figure 16 shows best fits to the reflectivity profiles in the range $0<Q<0.6\text{Å}^{-1}$, of a model with a PIP layer thickness d, between air and the bulk d8 toluene. The parameters of the fits are:

	PIP Layers Thickness	PIP Layers $\rho/\text{Å}^{-2}$	Toluene-d8 $\rho/\text{Å}^{-2}$	Background
(a)	37.76	$0.496\text{x}10^{-5}$	$0.55\text{x}10^{-5}$	$0.47\text{x}10^{-5}$
(b)	32.8	$0.484\text{x}10^{-5}$	$0.55\text{x}10^{-5}$	$0.78\text{x}10^{-5}$

The higher background of the later run is as expected. Qualitatively, a layer of scattering length density ca 0.49 x 10-5Å^{-2} and about 40 Å thick at the interface represents both sets of data quite well. Referring to Table 5, this could be either due to a PIP layer (of volume fraction PIP/d toluene = 8% or to a PIP,PAD surface excess layer [$< \overline{\rho} >$ PIP,PAD = 0.51 in the solvent (volume fraction PIP,PAD/d8 toluene = 100%. By observing the reflectivity profile to higher Q for the sample series #1261-1264 the first hint of how the PAD is arranged relative to the PIP at the interface (in a fresh solution) is obtained. The full reflection profile (Figure 16) has been fitted with a three layer (+ bulk solvent) model to take into account the further decrease in reflectivity to lx10-6 levels above Q=0.4 Å-1. The best, though still by no means perfect, fit was obtained with

(1) An interfacial layer d_1 = 8.87Å; $\bar{\rho}_1$ = 0.76 x 10-5Å^{-2}PAD

(2) An interfacial layer d_2 = 10.57Å; $\bar{\rho}_2$ = 0.34 x 10-5Å^{-2}PIP

(3) Third layer under this d_3 = 45.4Å; $\bar{\rho}_3$ = 0.53 x 1-0-5Å^{-2}PIPd8

d8 toluene $\bar{\rho}$ = 0.55x10-5Å^{-2}

These results suggest that for fresh PIP, PAD/toluene solutions the PAD head group adsorbs preferentially at the toluene-air interface, it being supported by progressively more swollen PIP "tails" deeper into the solution. The neutron measurements are consistent with the schematic representation of Figure 17 for the surface excess.

The usefulness of X-ray critical external reflection to determine these surface excesses and the distribution function of the copolymer species in the surface excess still remains to be demonstrated. Some idea of its value can be gauged by reference to the scattering ' ngth densities for x-rays and neutrons (Table 4). A similar argument to that made with respect to neutron small angle scattering is appropriate as the differences in contrast are the same. Again by tuning of the solvent the polyisoprenyl component could be contrast matched to solvent, a limitation being that for polymer solutions conformation and aggregation is strongly solvent dependent.

One Component Surface Excess

Two Component Surface Excess

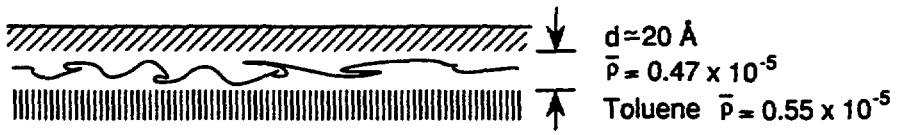

Figure 17

INSTRUMENT DESIGN AND INSTRUMENTAL IMPROVEMENTS

Some of the characteristics of the ideal x-ray small angle camera are shown in Table 6. This instrument, rather than using the converging optics of the Huxley-Holmes camera, essential when one wishes to use the divergent beams from conventional x-ray sources, would have parallel beam optics based upon either a Bonse-Hart or CCCC system.[33] It is this latter that we particularly draw attention to as it seems to offer important properties both for small angle scattering, critical external reflection and x-ray imaging devices. A preliminary designation of a multipurpose small angle camera using the CCCC system[34] has been given to the Photon Factory Conference (August 1988). The essential element is the condensing collimator channel cut, CCCC, monochromator of Wilkins and Stevenson.[33] A design for this is shown in Figure 18.

Condensing Collimator
Channel Cut
monochromator (CCCC)

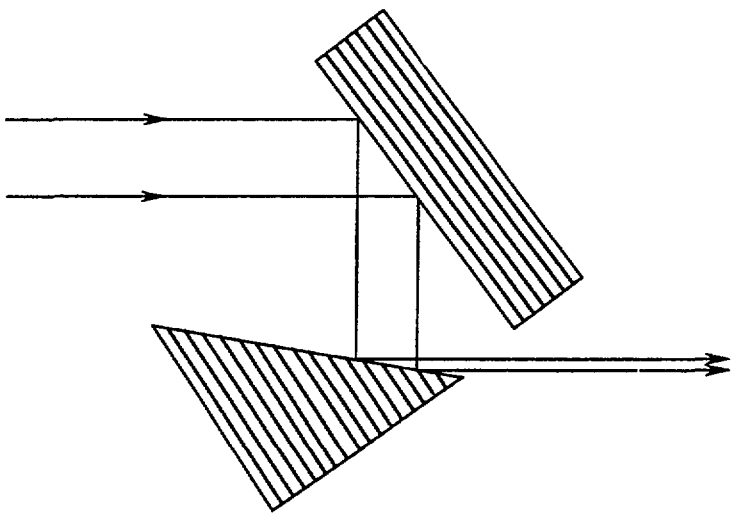

Figure 18

Condensing Collimator Channel Cut Monochromator

It can be seen that by using the same crystal planes but different channel cuts considerable reduction in the beam cross section is obtained at the same time as good wavelength selection. Most importantly, for small angle scattering this channel cut monochromator acts as a very good slit system, the wings of the beam falling off as Q^{-4}. Table 7 shows some of the flux and divergence properties of various channel cut options.

CONCLUSIONS

For a number of chemical problems using small angle scattering and critical reflection measurements to define structure in solutions and at interfaces the scope of enquiry is limited to both contrast (between different components of the system), available x-ray intensity or both. The extra intensity and collimation from synchrotron sources open up very attractive possibilities for overcoming some of the limitations of contrast, for measurements to high scattering vectors and ultimately for time resolved studies of kinetic processes in sol-gel synthetic chemistry.

Table 6

AN "IDEAL" X-RAY SMALL ANGLE CAMERA

	HUXLEY-HOLMES OPTICS	BONSE-HART CCCC OPTICS
BEAM INTENSITY	$10^{7}xs^{-1}$	
DEFINITION $\Delta\lambda/\lambda$	10^{-2}	
	10^{-4}	
SMALL BEAM	3 x 0.5 mm^2	<0.5 x 0.5 mm^2
HARMONIC SUPPRESSION		YES (MIRROR) YES
COLLIMATION, Q_{MIN}	$0.005A^{-1}$	$<0.001A^{-1}$
CONSTANT δQ		
$\delta Q/Q_{MIN}$	<0.05	
LOW BACKGROUND		
VARIABLE CAMERA LENGTH		
FAST DETECTOR		
2 D DETECTOR		
TIME GATING		
EASY CONVERSION TO REFLECTOMETER		

Table 7

Performance parameters for a 2-reflection CCC monochromator with $\alpha_1 = 0$ and various values for α_2 relative to the corresponding symmetric-cut monochromator $\alpha_2 = 0$. Values in parentheses are absolute values for the symmetric case. All values relate to $\lambda = 1.54$ oA : σ -mode of polarization and Si 111 Bragg planes:

PROPERTIES OF TWO-REFLECTION CCC MONOCHROMATORS

RELATIVE TO SYMMETRIC CASE

α_2 (deg.)		intens	diverg	condens	(α_1 = 0°) fluxl/flux
0	1 (6.05")	1 (4.51")	1 1	1 (6.05")	1
10°	2.35	3.34	5.6	0.42	2.38
12°	3.28	5.7	11.4	0.29	3.45
13°	4.40	9.25	21.47	0.21	4.88
13.6°	6.0	15.9	43.09	0.14	7.14
14.0°	9.06	36.81	122.9	.074	13.5

REFERENCES

1. Guinier and G. Fournet, Small Angle Scattering of X-rays, Wiley NY 1955.

2. O. Glatter and O. Kratky, Small Angle X-ray Scattering, Academic Press, 1982.

3. B. Jacrot, Rep. Prog. Physics 39, 911 (1976).

4. H.B. Stuhrmann, Chapter 6 in O. Glatter and O. Kratkey op. cit. ref. 2 above.

5. J.W. White, A. Miller and K. Ibel, Faraday Trans. Chem. Soc. (Lond.)II 72, 435, 1976 and A. Miller, B. Brodsky-Doyle, D.J.S. Hulmes, G.T. Jenkins, J.W. White, J. Haas, K. Ibel, P. Timmins "Neutron Scattering for the Analysis of Biological Structures", No.27 Brookhaven National Laboratory Series of Symposia in Biology 1976.

6. J.A. Lake, Acta Cryst. 23, 191 (1967).

7. L. Iton and J.W. White, Langmuir 1989.

8. T.J. Pinnavaia, V. Rainey, J.W. White, J. Mol. Catalysis, 27, 213-224 (1984).

9. F. Tsvetkov and J . White, Aggregation of Organometallic Complex Pillars in Synthetic Flu hectorite and Montmorillonite, J. Am. Chem. Soc. 110, 3183 (1988).

10. F. Tsvetkov and J.W. White, J. of Materials (ACS) Vol. 1, January 1989.

11. L. Dai, Ph.D. Thesis, Australian National University, 1989.

12. L. Dai, J.W. White, J. Kerr, R.K. Thomas, J. Penfold and M. Aldissi, Molecular Metals (Special Issue on the 3 International Symposiums on Molecular Metals, Santa Fe 1988).

13. Pinnavaia, T. Science 1983, 22, 365.

14. Barrer, R.M. Journal of Inclusion Phenomena 1986, 4, 109.

15. Solin, S.A. Adv, Chem, Phys. 1982, 49, 455.

16. Clarke, R.; Gray, J.N.; Homma, H.; Winokur, M.J. Phys. Rev. Lett, 1981, 47, 1407.

17. Comba, P.' Sargeson A.M.; Engelhardt, L.M.; Harrowfield, J.M.; White, A.H.; Horn, E.; Show, M.R.J. Am. Chem. Soc. 1984, 24, 2325 and references within.

18. Warren, B.E. Phys. Rev. 1941, 59, 693.

19. Barrer, R.M.; Jones, D.L.J. Chem. Soc. (A) 1970, 1531.

20. Wilson A.J.C. (ed.) Structure Reports 1952, 16, 363.

21. K.L. D'Amico, D.E. Moncton, E.D. Spect. R.J. Birgeneau, S.E. Nagler and P.M. Horn, Phys. Rev. Let. 53, 2250 (1984).

22. R. Friend, Cavendish Laboratory, Cambridge, Private Communication.

23. M. Aldissi, J. Chem. Soc. Chem. Commun, 1347, (1984).

24. A Novel Route for Producing Soluble Polyacetylene-Polyisoprene Block Copolymers, S.P. Armes, B. Vincent and J.W. White, J. Chem. Soc. Chem. Commun., 1525, 1986.

25. See for example, A.D. Jenkins, Polymer Science, North Holland, 1972.

26. E. Bouchard, B. Farnoux, X Sun, M. Daoud and G. Jannink, Europhys. Lett. 2(4), 315 (1986).

27. S.J. Henderson and J.W. White, J. Appl. Crystallography, 1988.

28. L. Dai and J.W. White unpublished results.

29. G.P. Felcher, R.O. Hilleke, R.K. Crawford, J. Haumann, R. Kleb, G. Ostrowski, Re. Sci. Instr. 58, 609, 1987.

30. "A Pulsed Source Neutron Reflectrometer for Surface Studies;, J. Penfold and W.G. Williams, Rutherford Appleton Laboratory Report RAL-85-045.

31. S.A. Werner and A.G. Klein, Neutron Scattering, D.L. Price and K. Skold eds. Acad. Press 1984, Ch IV.

32. O.S. Heavens "Optical Properties of Thin Solid Films", Dover Publications, NY 1965.

33. S.W. Wilkins and A.W. Stevenson, Nucl. Instrum. and Methods, A269, 321-328, 1988.

34. Z. Barnea, R. Clapp, D.C. Creagh, T.M. Sabine, A.W. Stevenson, J.W. White, S.W. Wilkins, J. Harada, H. Hashizume, Y. Kashihara, M. Sakata and T. Zemlo. Proc. Conference on Synchrotron Instrumentation. Photon Factory, Tsukuba, Japan. August 1988.

SYNCHROTRON RADIATION STUDIES ON POLYMERS

T. P. Russell
IBM Research Division
Almaden Research Center
650 Harry Road
San Jose, CA 95120-6099

Synchrotron radiation sources are being used in a wide variety of ways to investigate the behavior of polymers in the solid state and in solution (1). Real time and time resolved studies have been used to study the kinetics of irreversible and reversible phase transitions in homopolymers and block copolymers. Static small angle scattering have been used to probe the morphology and single chain behavior of weakly scattering bulk systems and dilute solutions of polymers in a solvent. Small angle scattering has also been combined with differential scanning calorimetry so that the thermal and morphological response of polymers undergoing phase transitions are evaluated in real time. Similarly, wide angle diffraction has been combined with small angle scattering such that detailed structural information is obtained over the ones to hundreds of angstrom size scale. Storage rings, with x-ray beams characterized by a low divergence and high brilliance, are being utilized for specular reflectivity and glancing angle diffraction experiments where information on the surface behavior of polymers is obtained. Thus, while the use of synchrotron radiation is relatively new to polymers, important information covering a broad spectrum of areas is being obtained. The development of brighter sources in the hard x-ray regime, as with the Advanced Photon Source will only expand these horizons.

In this presentation two unique aspects of storage ring sources, namely the small beam size and high beam flux, will be discussed in reference to two studies on block copolymers. It is emphasized, however, that the use of absolute intensities is necessary so as to fully use the information provided by the scattering studies. Not only do absolute intensities yield information on the electron densities of the scattering entities, absolute calibration limits the number of parameters necessary for modelling the scattering profile.

The small angle x-ray scattering (SAXS) discussed herein have been performed on beamline I-4 at the Stanford Synchrotron Radiation Laboratory. X-rays emanating from the storage fringe are focused vertically by a 50 cm, platinum coated float glass mirror bent to approximate an ellipse in shape. Horizontally a bent, asymmetrically cut Si(111) monochromator serves as a focusing element and delivers x-rays of wavelength 1.429Å into the experimental area. Vertical

and horizontal slits are used to limit the beam size and to eliminate parasitic radiation. Monitors directly before and after the specimen continuously monitor the incident beam flux onto the specimen and the attenuation factor of the specimen. The detector is a self scanning photodiode array detector containing 1024 pixels each with a dimension of 2mm x 25μm. At the specimen the beam is approximately 1mm in diameter in size whereas at the detector the beam is approximately 300μm x 1mm in size.

The first study deals with the order/disorder transition of symmetric diblock copolymers. In particular results on a poly (styrene)-hydrogenated poly(butadiene) as a function of temperature will be discussed [2,3]. At temperatures above the mesophase transition temperature, i.e. the temperature at which the copolymer undergoes a transition from a random mixture of the two component blocks to an ordered, mesophase morphology, the absolute scattering is given by [4,5].

$$I(q,T) = \frac{(\rho_1 - \rho_2)^2}{S(q,T) - 2\chi(T)} \qquad (1)$$

where ρ_i the electron density of segment i, S(q,T) is scattering function of the copolymer and χ is the Flory-Huggins binary interaction parameter. S(q,T) is defined in terms of the spatial correlations of A-A, B-B and A-B segments in an A-B copolymer and can be written in terms of the single chain scattering function of two blocks. Since all the terms in this equation are known with the exception of χ(T), χ(T) is varied to produce the best fit to the data. It should be noted that the form of equation (1) predicts a nonzero value of q where I(q,T) will be a maximum despite the fact that the system is disordered. This results from the connectivity of the chain segments on the polymer which produces non-random spatial correlations. Variation of the temperature yields χ(T) as a function of temperature and it is found that χ(T) varies inversely with temperature in agreement with other studies. Also, the variation in $1/I(q_{max},T)$ with T yielded the spinodal and microphase separation temperatures.

The second study deals with the formation of block copolymers via ionic interactions [6]. In particular, mixture of carboxy - and sulfonate - terminated poly(styrene) with tertiary amino terminated poly(isoprene) were prepared in a bluene solutions. Two separate mixtures were considered where the concentration of poly(styrene) was 33% and 50% by volume. Films of the mixtures were cast and the solvent was removed. SAXS profiles from the 33% and 50% mixtures both exhibited distinct reflections characteristic of a periodicity of several hundred angstrom. This feature alone demonstrates that the phase separation expected for these two polymers has been limited to a size scale comparable to the dimensions of the individual chains. This result also demonstrates that the morphology of the ionically interacting polymers forms a morphology that is quite similar to that seen in covalently bonded block copolymers.

Both specimens were heated at a rate of 10°C/min in a Mettler Hot Stage through which the incident beam passed. Evaluation of the total scattering invariant Q given by

$$Q(T) = \int_0^\infty I(q,T)q^2 dq \tag{2}$$

$$= 2\pi^2 Q_1 Q_2 (\rho_1 - \rho_2)^2 \tag{3}$$

as a function of temperature showed that up to the glass transition temperature of the poly(styrene) phase, the system remained unchanged. At slightly higher temperatures, the phases purity was enhanced i.e. ρ_1 - ρ_2 increased, as would be expected. The behavior of the 33% and 50% copolymers at more elevated temperatures differed markedly. Increasing the temperature resulted in a reduction of Q (T) and finally, a disappearance of the SAXS reflection. The 50% copolymer on the other hand exhibited an initial reduction in Q with temperature. However, prior to the point where the SAXS vanished a second reflection appeared. With increasing temperature this reflection increased in intensity and the position shifted to smaller q or larger spacing. This continued until the reflection vanished behind the beamstop.

The behavior of these two copolymers can be understood if one considers a phase diagram that takes into account the unusual characteristics of these ionically formed copolymers. First as with their covalently bonded counterparts, the glass transition temperatures, T_g, of the two microphases and the microphase separation temperature MST must be considered. The former dictates mobility of the constituents whereas the latter dictates the nature of the microphase separation. Two additional features enter however. First, is the temperature at which the ionic associations are disrupted, T_i at temperature in excess of this dissociation temperature, the ionically terminated homopolymers behave as an ordinary binary polymer mixture. This mixture will therefore, be governed by an upper critical solution temperature, UCST. If T < UCST, then the polymers will coarsely phase separate, whereas at higher temperatures the polymers will be miscibility. It is the location of T_g, Ti, MST and UCST, that will govern the morphology of the copolymers formed via ionic associations and therefore yields an understanding of the SAXS from these materials.

References

1. T. P. Russell and A. N. Goland, eds., "Polymer Research at Synchrotron Radiation Sources", BNL Report, 51847 UC-25 (1985).
2. J. N. Owens, I. C. Gancarz, J. T. Koberstein, T. P. Russell, Macromolecules, submitted.

3. J. N. Owens, Ph.D. Thesis, Princeton University, Princeton, NJ (1987).
4. L. Leibler, Macromolecules, 13, 1602 (1980).
5. P. deGennes, "Scaling Concepts in Polymer Physics", Cornell University Press, Ithaca, NY (1979).
6. T. P. Russell, R. Jerome, P. Charlier and M. Foucart, Macromolecules, 21, 1709 (1988).

MACROMOLECULAR STRUCTURE CHANGES IN SOLUTION OBSERVED BY TIME-RESOLVED SYNCHROTRON X-RAY SCATTERING

James C. Phillips

Chemistry Department, SUNY Buffalo and
SUNY X3 Beamline, NSLS, 725A,
Brookhaven National Laboratory, Upton, NY 11973, USA.

Abstract - SAXS experimental needs and synchrotron radiation properties have always been well matched. At APS this matching of needs and properties will become ideal. X-ray scattering using powerful sources appears to be the best way to obtain time-dependant structural information in solution. Studies of biological macromolecules and polymers are illustrative of the uses of the technique. Time-resolved data can give kinetic information and can identify intermediate structure especially if models, for example from electron microscopy, are available. Theoretical calculations indicate that greater details of structure may be obtained using information in the higher angle region. Count rates are much lower in such experiments, however. Anomalous dispersion information may resolve ambiguities remaining from fixed wavelength experiments. In these studies specialised SAXS optics, position sensitive detectors and time-resolving readout electronics are employed. Difficulties with beam noise and movement can be encountered. Experiments on the 'protein folding' problem are described as a case study of these techniques.

SAXS and Synchrotron Radiation - Small angle x-ray scattering (SAXS) is a weak effect compared to, for example, Bragg diffraction from crystals. Moreover, a highly collimated beam is required to achieve resolution in the measured pattern. Synchrotron radiation from bending magnets or wigglers has excellent collimation perpendicular to the machine plane and high intensity, particularly when horizontally focused. This matching of experimental needs and source properties ensured that SAXS experiments were one of the earliest to be performed with x-ray range synchrotron radiation. A pioneering study of note is the low angle diffraction of insect flight muscle performed with synchrotron radiation from the DESY synchrotron and published in 1971 (1)! Looking to the future, the APS machine planned for Argonne National Laboratory will be of sufficient e- beam energy and emittance to permit undulators in the 1 A range. The high intensity and narrow bandwidth (2) may permit SAXS experiments without the need for monochromators. Moreover, the beam is highly collimated in both planes. One could envision a beamline free from parasitic scatter from slits or optical elements permitting use of area detectors without compromising low angle resolution from scatter or beam size. Thus, **at APS undulators, the matching of SAXS experimental needs and source properties will become ideal**, with all source photons able to be incident on the sample and all scattered photons potentially detectable.

Time-Resolved Solution Scattering Studies - The most illustrative uses so far are in the study of proteins in solution and in polymer science. The initial results were of microtubule assembly induced by T-jump (3-5) and of aspartate transcarbamylase dissociation by mercurials by stopped-flow techniques (6,7). More recent results include the allosteric transition of aspartate transcarbamylase (8) and the unfolding of myoglobin (9). Examples of polymer work include epoxy hardening (figure 1) analysed with a fractal model (10) and polymer blend crystallisation (11). A static study of ionomers emphasised that synchrotron radiation can bring improved spatial resolution as well as time resolution (12).

Other Techniques - Other techniques used on solutions include NMR, circular dichroism, and differential scanning calorimetry. Only NMR gives good structural information, but the technique appears to be antithetical to time-resolved measurements on large molecules. Circular dichroism gives secondary structure information but not gross conformation. Only x-ray scattering using powerful sources appears to give generalised time-dependant structural information.

Information From These Studies - The small-angle region from any given sample can typically yield crude structural information, such as radius of gyration and deviation from spherical shape. Time-resolved data can give this information differentially, which can aid in identifying the appearance of intermediates and their structure. When combined with structural information from other techniques, for example electron microscopy, theoretical

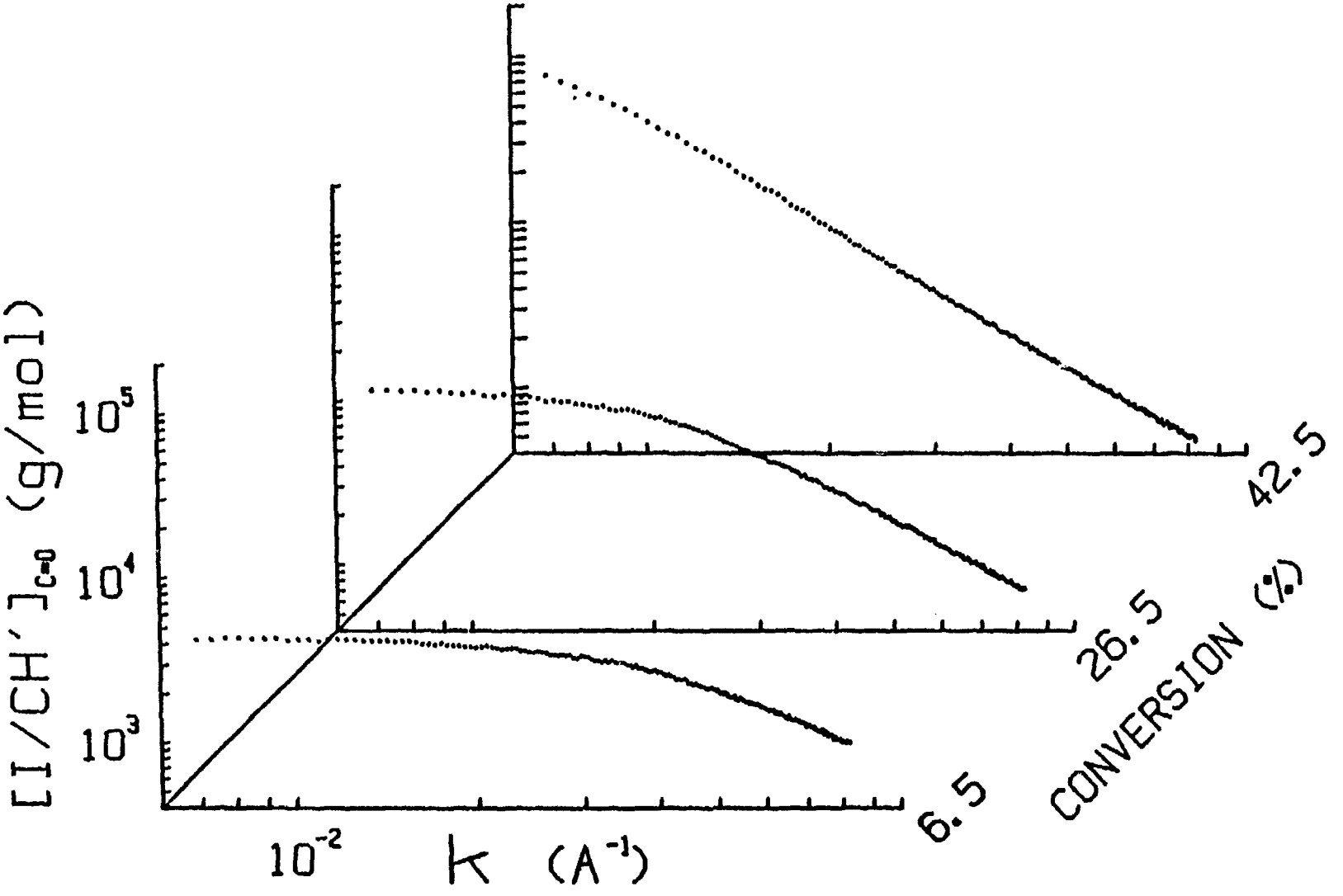

Figure 1. log-log plots of scaled absolute excess scattered x-ray intensity versus K at three stages of epoxy polymerisation before the gel point. (Figure 1 of reference 10)

curves from model structures can be compared with the experimental curves and model parameters refined by least squares procedures (4,13). If the possibilities are few, unambiguous results are possible. Of course kinetic data can be derived on reaction rates of intermediate and final product formation (8,11). Other possible techniques are combined contrast variation/time-resolved measurements which may help unravel the behavior of two component systems such as a protein/nucleic acid virus during assembly, the study of reaction inhibitors and promotors and their effects on structure and the effects of leaving out one or more components of multi-component systems. As with static SAXS data, the combination of measurements under varying conditions and the availability of other types of data aid the interpretation of time-resolved data to give a better picture of evolving structures.

Higher Angle Scattering - Greater details of structure may possibly be obtained using information in the higher angle region. Theoretical calculations of higher angle scattering have been made (9). Scattering from alpha-helices and beta-sheet configurations are shown in figure 2. There are clear differences in these curves, indicating that substantial information on secondary protein structure is available if data of sufficient resolution and statistical accuracy can be obtained. However, the scattering probability at these angles for these relatively small particles is 10^{-4} that of a small protein such as myoglobin, which is itself 2×10^{-8} (14). To observe the high angle region in the same timescale as was possible in the low angle region a four order of magnitude improvement in the experiment is required. Figure 3 shows the same curves as figure 2 but on an absolute scale and with noise artificially added. The counts correspond to the four orders of magnitude improvement needed. The four curves are clearly distinguishable, although the two beta-sheet curves are similar except at high angle.

Anomalous Dispersion Measurements - Anomalous dispersion is the term given to the wavelength dependance of the x-ray scattering power of an element. Near absorption edges the scattering power varies rapidly with wavelength in both amplitude and phase. Such edges occur at wavelengths characteristic of a particular element. With a tunable x-ray source, it is thus possible to selectively alter the contribution of a particular element to the diffraction or scattering pattern of a sample. A narrow bandwidth beam is required for the best results. This can be used in SAXS to measure the cross term between heavy and light elements, in a metallo-protein for example, and the inter-heavy atom vectors. Results on measuring cross-terms have been have been successfully performed (15-17). So far none of the studies cited has measured the inter-heavy atom distances but it is likely that present and future high brightness sources have experimental advantages to successfully do so. Anomalous dispersion information may resolve ambiguities remaining from fixed wavelength experiments (such as which end of a chain folds first as a polymer folds).

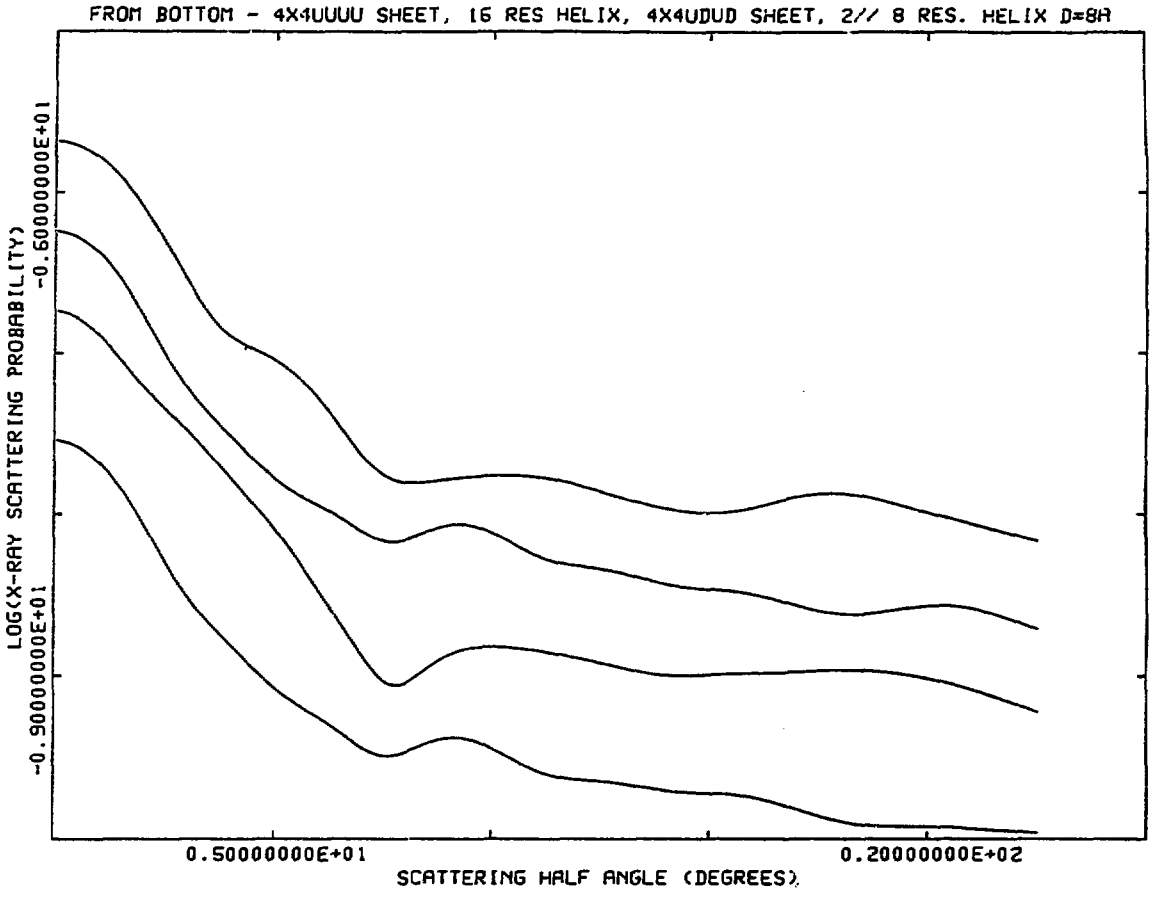

Figure 2. Theoretical scattering in 10 mMol aqueous solution of beta-sheet with 4 residues/chain and four chains and the chains of UUUU handedness (lowest curve) and UDUD (third from bottom) (U=up, D=down). Alpha-helix of 16 residues (second lowest curve) and of two parallel 8-residue helices separated by 8 Å (top curve) are shown for comparison. The curves have been separated vertically by constant increments of 0.65 for clarity. The second lowest curve is on the correct scale.

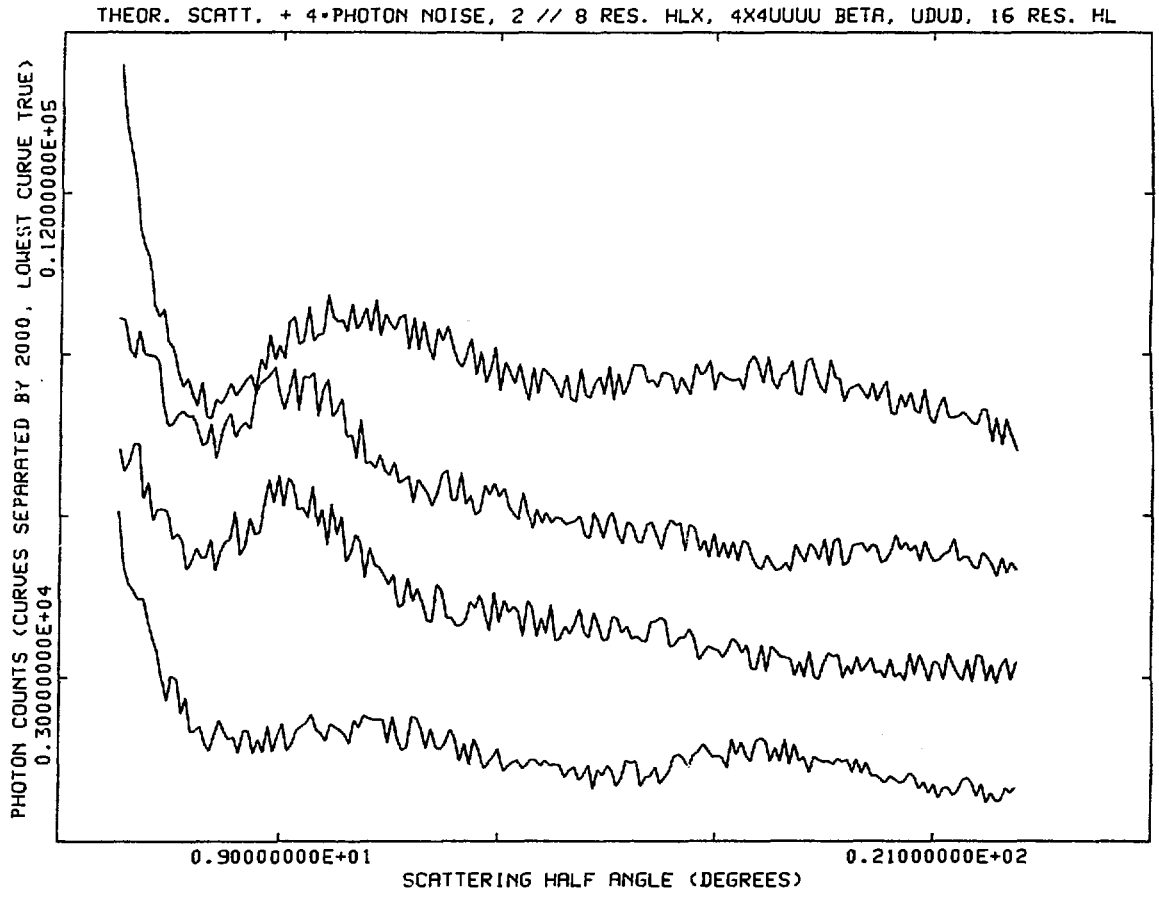

Figure 3. Theoretical scattering in 10 mMol aqueous solution of various configurations of 16 polypeptide residues. From the bottom - two parallel 8-residue alpha-helices separated by 8 A; beta-sheet with 4 residues/chain and four chains and the chains of UUUU handedness; as previous but UDUD; alpha-helix of 16 residues. The curves have been scaled to have 1000 counts in the smallest channel of the UDUD spectrum. Statistical noise has been added at 4 times the level of photon statistics.

Experimental Setups - In these studies high intensity synchrotron radiation SAXS cameras with position sensitive detectors and time-resolving readout electronics were used. Sideways deflecting bent triangular monochromators, usually with vertically focusing mirrors (18-20) are the most popular type of station. They are in use at DORIS, LURE, Daresbury, SSRL and the Photon Factory, sometimes combined with use for crystallography. At NSLS, the SUNY beamline has a unique combination of a a double crystal monochromator and doubly-focusing bent-toroidal mirror (21, 22; figure 4). This line gives, at 2.5 GeV, 140 mA a flux of 3.5×10^{11} photons/s in a focal spot 0.9x0.6 mm (fwhm) at 1.54 A. A toroidal mirror/ multilayer combination to enhance flux has been used by another NSLS group for experiments on alloys (23). Resolution in sideways diffracting lines is limited by slits defining scatter from the monochromator (19). For toroidal mirror lines slits (24) or a Kratky collimation system (25) must be used to eliminate parasitic scattering from the mirror. A typical small angle scattering apparatus includes optical bench, sample chamber, and adjustable vacuum paths between system components.

Detectors - Gas-filled proportional detectors, linearly position sensitive, are commonly used for time-resolved SAXS work (20, 26). There are some two-dimensional detection systems in use also (27, 28). A photodiode array as linear detector has been used successfully for time-resolved SAXS (23). The latest development is the use of luminescence readout storage phosphors for time-resolved experiment (8).

Data Acquisition System - In order to conduct time-resolved measurements the data acquisition system must be capable of monitoring experimental parameters while the detection system is measuring the scattering from the sample. Due to the nature of the synchrotron radiation x-ray source, the intensity fluctuates and and decays, the incident beam must be monitored. For most experiments a sample stimulus must be synchronized with the start of data collection. We have developed a versatile system for time-resolved x-ray scattering experiments at the SUNY X3 beamline, NSLS (24). It is based on a commercially available LPSD 64K MCA (Braun gas-filled proportional counter, available from Innovative Technology Inc., 205 Willow St. South Hamilton, MA 01982), a PDP-11/23 computer and a CAMAC-based data acquisition system. Figure 5 shows, schematically, how the system is configured for SAXS experiments. Many other systems work in a similar fashion (for example see reference 20). The Braun MCA may store up to 64 detector patterns of 1K channels by 64K counts. The position of the currently accumulating pattern in the MCA memory increments after a measurement period. The operator chooses the number of periods. The MCA and CAMAC timer are then programmed to collect data in synchrony. For each MCA pattern, the timer prompts the computer system to read the values of up to six external parameters, via the CAMAC scaler. At the end of the measurement the internal memory of the MCA is readout by the computer, through an RS232 link, and stored on disk, along

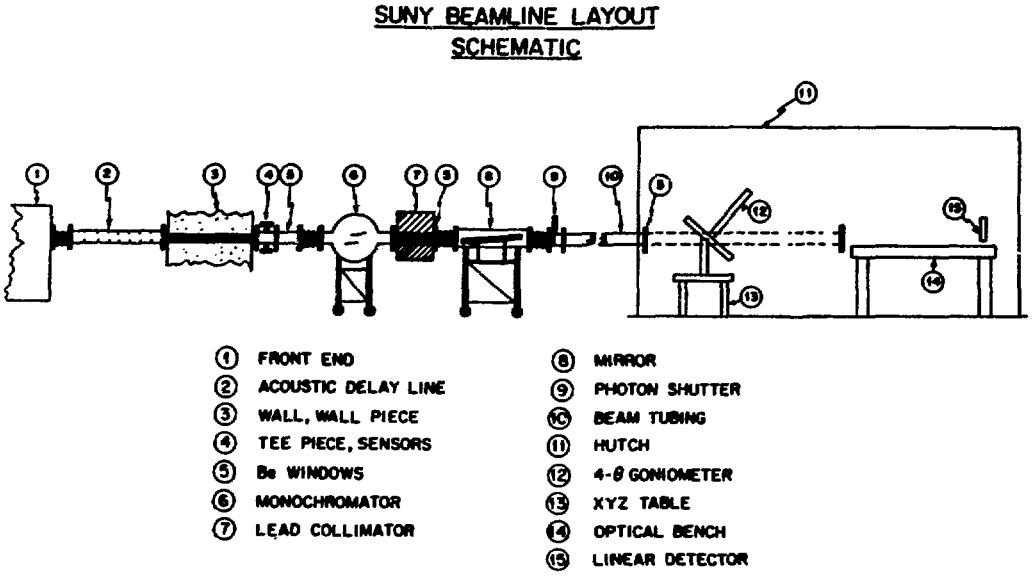

Figure 4(a)

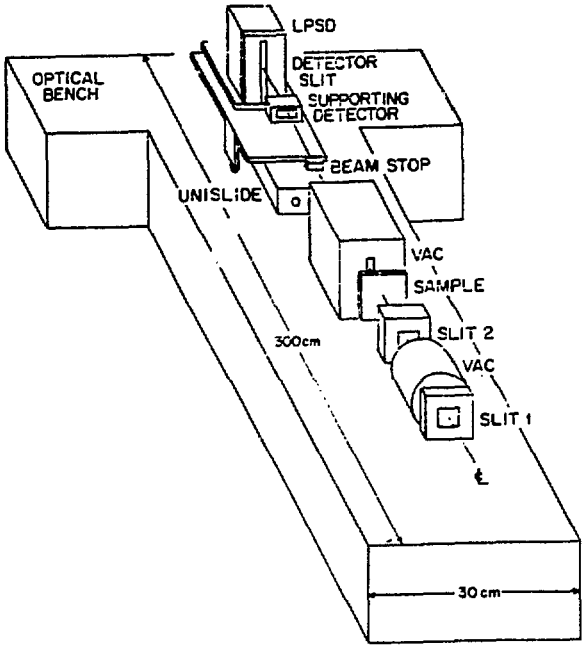

Figure 4(b)

Figure 4. The SUNY SAXS apparatus at NSLS (a) The beamline layout (adapted from Figure 1 of reference 22). (b) The optical bench.

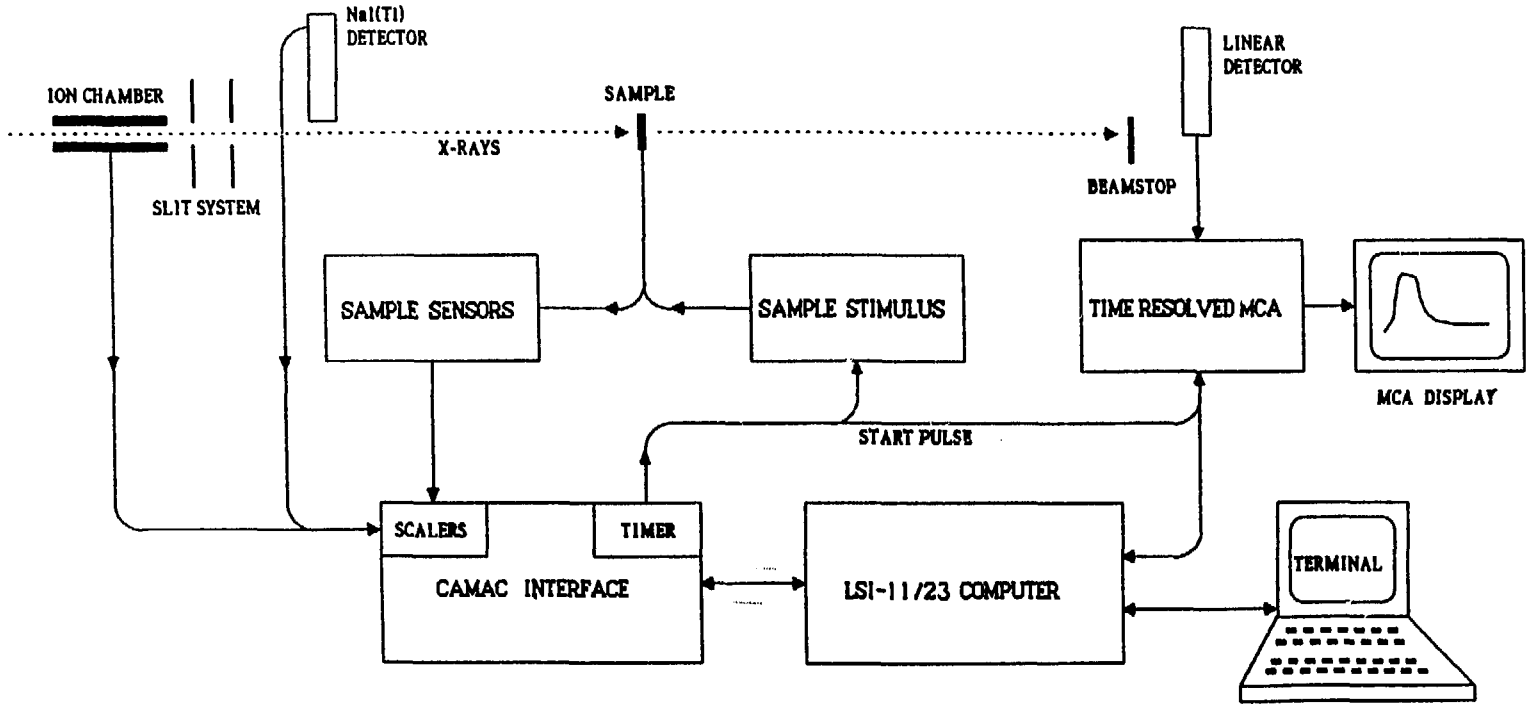

Figure 5. Schematic of the interconnection of the various components of the SUNY time-resolved data acquisition system (Figure 1 of reference 24).

with the parameter measurements. A remote MICROVAX II computer provides enhanced data analysis, plotting and theoretical calculation capability.

Problems Encountered with Beam Stability - The x-ray intensity decays and fluctuates while data is collected. Figure 6 shows the NSLS beam intensity decay over several hours and its insert shows a periodic fluctuation of 14 seconds, resulting from beam motion, occuring in a typical 100 second interval. Beam direction shifts have been observed also (24). These sort of phenomena are typical of all storage rings and have been observed before (29).

Protein Folding as a Case Study - There is much effort going on now to solve the 'protein folding problem', that is to predict three dimensional protein structure from amino acid sequence information. If this can be achieved then protein structures can be designed and correctly sequenced polypeptide chains can be made using the present knowledge of the genetic code and cloning techniques. Present theoretical calculations use energy minimisation to predict structure and crystal structure data (that is, end point of folding) as experimental data (see for example reference 30). The the best agreement is with chains of only a few amino acids (31). Experimental data on energy is available from calorimetric techniques (32). With time-resolved solution measurements, structural data along the folding pathway could be added, thus making available full experimental information to parallel the theoretical calculations. A temperature jump study of solutions of sperm whale myoglobin was chosen as a test case. With a powerful x-ray beam, radiation damage to the sample is a concern. Preliminary studies showed that it took approximately 50 min. before damage occured. Scattering of solutions of myoglobin in the angular range $2\emptyset$=1-50 mrad. was measured during temperature jumps between 26 and 76°C. The SUNY facilities described above (21,22,24) were used. Figure 7 show a T-raise. There are clear signs of time/temperature-dependant structural changes, in the small angle region, consistent with those from other, equilibrium, techniques. A tentative interpretation of this data (9) is that the 'high temperature maximum' is unfolded and aggregated protein as the temperature corresponds to that for full unfolding for the buffer and pH used (32), the scattering pattern is that of a higher molecular weight and/or radius of gyration and the effect is irreversible (ii) the transient 65°C peak represents a partially unfolded state, with radius of gyration slightly larger than the intact protein. The first five patterns, as the temperature rises through 30°, show some sign of of the 'cold denaturation' of myoglobin recently observed (32).

Lessons from this Feasibility Study - It was demonstrated that, with present high brightness synchrotron x-ray sources, changes in the small-angle x-ray scattering patterns of dilute protein solutions can be followed in a single pass experiment on the 10 s timescale. Theoretical considerations indicate that higher angle data, with detailed structural information is obtainable with a

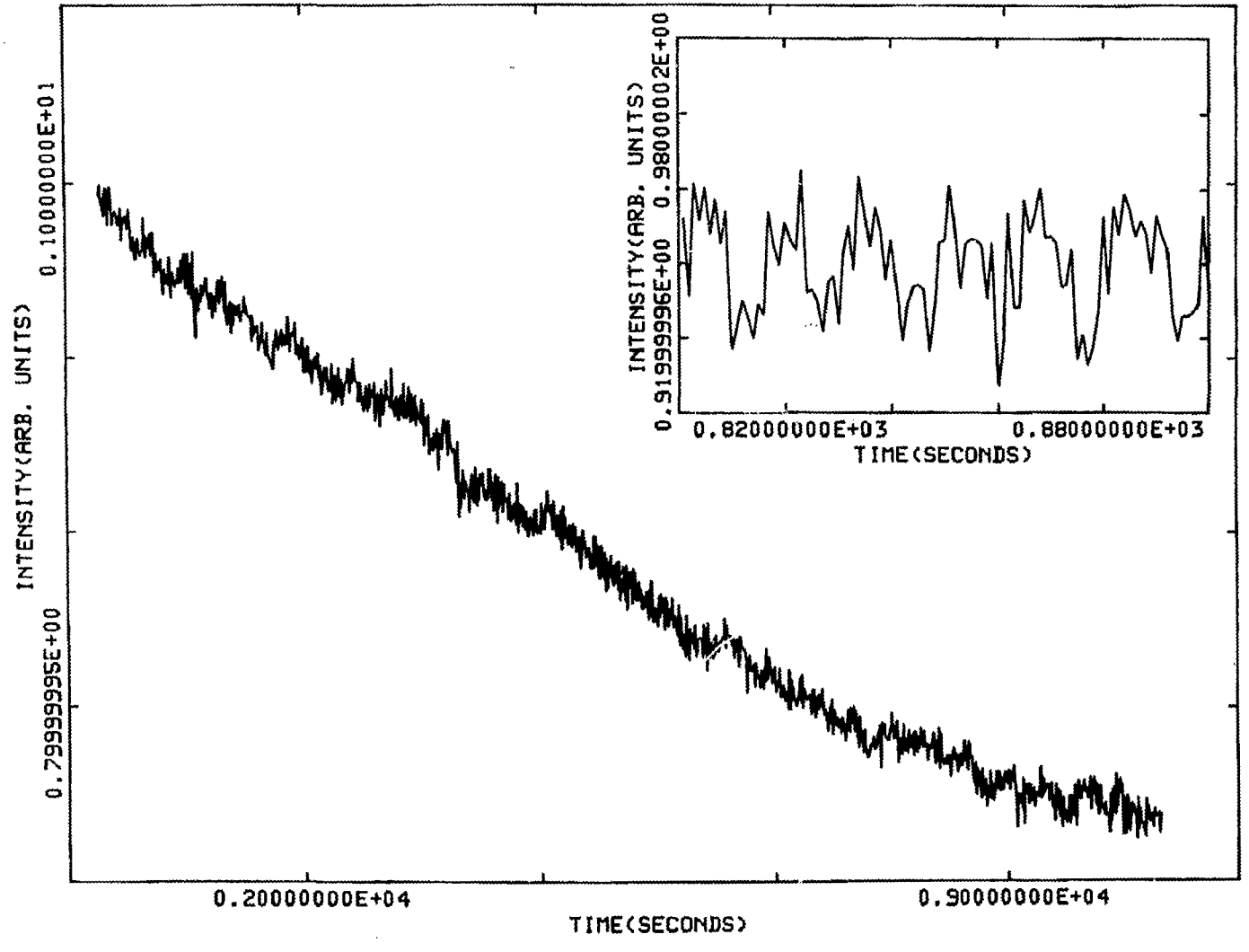

Figure 6. Incident x-rays, monitored by air scattering, showing the flucuations and decay in the beam. The insert shows periodic variations resulting from beam motion (figure 4 of reference 24).

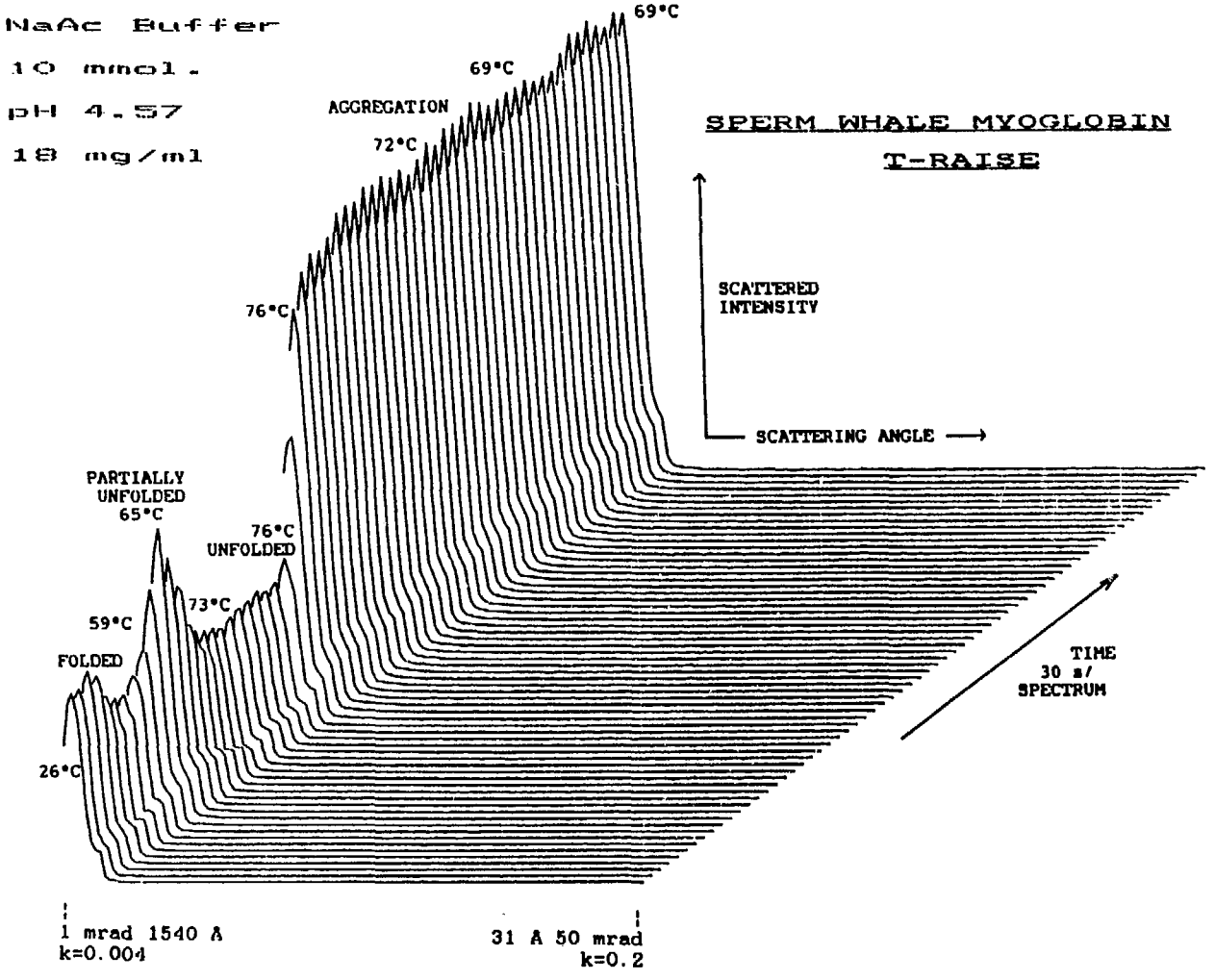

Figure 7. Time-resolved measurement of x-ray scattering of a solution of sperm whale myoglobin in the angular range 2Ø=1-50 mrad. as the temperature is raised (Figure 1 of reference 9).

ten thousand-fold greater difficulty. Such data could give detailed structural information. An area, rather than a linear, detector and averaging of multiple passes should make possible such measurements at 10 s resolution. Radiation damage would limit the use of any given sample to one or two passes, therefore a sample holder with pumps and a reservoir to change sample exposed to x-rays is neccessary. The availability of undulator x-ray sources, in combination with these experimental advances should allow work in the 1-100 ms range at high scattering angle. Most importantly, if all this is done the data would yield details of the self-assembly of proteins.

Acknowledgements

Ben Chu initiated and has contributed much to the SUNY SAXS apparatus at NSLS. His group performed the polymer work discussed above. Results on myoglobin were obtained in collaboration with Alan LeGrand, William Lehnert, Baozhong Dong and Alexander Darovsky.

This work was supported by the U.S. Department of Energy, Office of Basic Energy Research, Division of Materials Science under grant number DEFG0286ER45231 and the State of New York. Research carried out in part at the National Synchrotron Light Source, Brookhaven National Laboratory under contract DE-AC02-76CH00016 with the U.S. Department of Energy, Division of Materials Science and Division of Chemical Sciences.

References

(1) Rosenbaum, G., et al. *Nature* **230** 434 (1971).
(2) Shenoy, G.K., et al. in *An Overview of the Characteristics of the 6-GeV Synchrotron Radiation: A Preliminary Guide for Users* (Report number ANL-85-69, Argonne National Laboratory, Argonne Illinois, 1985).
(3) Mandelkow, E-M., et al. *Nature* **287** 595 (1980).
(4) Bordas, J., et al. *J. Mol. Biol.* **164** 89 (1983).
(5) Mandelkow, E., et al. in *Structural Biological Applications of X-ray Absorption Scattering and Diffraction.* H. Bartunik and B. Chance, editors. Academic Press, Orlando. p155 (1986).
(6) Moody, M.F., et al. *Proc. Natl. Acad. Sci. USA* **77** 4040 (1980).
(7) Moody, M.F., et al. in *Structural Biological Applications of X- ray Absorption Scattering and Diffraction.* H. Bartunik and B. Chance, editors. Academic Press, Orlando. p195 (1986).
(8) Kihara, H., et al. *J. Mol. Biol.* **198** 745 (1987).
(9) Phillips, J.C., et al. *Biophys. J.* **53** 461 (1988).
(10) Chu, C., et al. *Macromolecules* **20** 2642 (1987).
(11) Song, H.H., et al. *Macromolecules* **21** 1180 (1988).
(12) Chu, C., et al. *Macromolecules* **21** 523 (1988).

(13) Bordas, J., et al. in *Structural Biological Applications of X-ray Absorption Scattering and Diffraction.* H. Bartunik and B. Chance, editors. Academic Press, Orlando. p253 (1986).
(14) Stuhrmann, H.B. in *Synchrotron Radiation Research.* H. Winick and S. Doniach, editors. Plenum, New York. p513 (1980).
(15) Stuhrmann, H.B. *Acta Cryst.* **A36** 996 (1980).
(16) Stuhrmann, H.B., et al. *Proc. Natl. Acad. Sci. USA* **78** 6216 (1981).
(17) Miake-Lye, R., et al. *Biophys. J.* **41** 287 (1983).
(18) Lemmonier, M., et al. *Nucl. Instrum. and Meth.* **152** 173 (1978).
(19) Hendrix., J., et al. *J. Appl. Cryst.* **12** 467 (1979).
(20) Bordas, J., et al. *J. Phys. E Sci. Instrum.* **13** 938 (1980).
(21) Chu, B., et al. in *Polymer Research at Synchrotron Radiation Sources.* T.P. Russell and A.N. Goland, editors. Brookhaven National Laboratory Report BNL51847, Upton, NY. p126 (1985).
(22) Phillips, J.C., et al. *Nucl. Instrum. and Meth. in Phys. Res.* **246** 182 (1986).
(23) Stephenson, G.B., *Nucl. Instrum. and Meth. in Phys. Res.* **A266** 447 (1988).
(24) LeGrand, A.D., et al. *Nucl. Instrum. and Meth. in Phys. Res.* **A266** 659 (1988).
(25) Chu, B., et al. *Rev. Sci Instrum.* **58** 1158 (1987).
(26) Bordas, J., et al. *Nucl. Instrum. and Meth. in Phys. Res.* **A246** 545 (1986).
(27) Stuhrmann, H.B., et al. *J. Appl. Cryst.* **16** 563 (1983).
(28) Towns-Andrews, E., et al. *Rev. Sci. Instrum.* Submitted.
(29) Chance, B., et al. *Rev. Sci. Instrum.* **56** 581 (1985).
(30) Scheraga, H., *Israel J. of Chem.* **27** 144 (1986).
(31) Scheraga, H., *Proc. Natl. Acad. Sci. USA* **27** 144 (1986).
(32) Privalov, P.L., et al. *J. Mol. Biol.* **190** 487 (1986).

APPLICATIONS OF ANOMALOUS SMALL ANGLE X-RAY SCATTERING

J.J. Hoyt
Department of Mechanical and Materials Engineering
Washington State University

ABSTRACT

Applications of the technique of anomalous small angle x-ray scattering (ASAXS) are discussed. Representative examples of the use of this technique from the fields of biochemistry, polymer chemistry and material science are presented. In addition, special instrumentation considerations and methods of anomalous scattering factor determination are reviewed.

INTRODUCTION

Anomalous scattering refers to x-ray experiments in which the incident beam is of an energy close to the absorption edge of an element in the sample. The x-ray atomic scattering factor, denoted by f, varies very slowly with incident energy except for energies within approximately $\pm$ 100 eV of an absorption edge. In this energy regime, resonance effects for the bound electrons become important and as a result, f decreases quite rapidly. For an excellent review of the anomalous dispersion of x-rays, the reader is referred to James [1]. The ability to select a given incident energy of sufficient intensity is made possible with the advent of present day synchroton facilities.

Conventional small angle x-ray scattering (SAXS) which has countless applications in chemistry, physics and metallurgy, refers to the measurement of scattered intensity for wave vectors less than about $.5A^{-1}$. The combination of the anomalous dispersion phenomenon of x-rays and the techniques of small angle scattering is known as anomalous small angle x-ray scattering or ASAXS. The present review will describe representative applications of ASAXS from the fields of biophysics, polymer chemistry and materials science.

THE ANOMALOUS SCATTERING FACTORS

In general, the atomic scattering factor can be written:

$$f(k, E) = f_o(k) + f'(k, E) + if''(k, E) \tag{1}$$

where k is the magnitude of the scattering vector, E is the energy and f_o is the energy independent contribution to f. The quantities f' and f'' represent respectively, the real and imaginary dispersion corrections. In most ASAXS experiments it is necessary to obtain the energy dependence of the anomalous scattering factors f' and f''.

The determination of $f''(E)$ from measured or tabulated values of the absorption coefficient $\mu(E)$, is made possible through the use of the Darwin relationship (see [1]):

$$f''(E) = \frac{E}{2r_e ch} \frac{A}{\rho N} \mu(E) \tag{2}$$

In this equation r_e is the classical radius of an electron, c is the velocity of light, h is Planck's constant, ρ and A are the density and atomic weight of the anomalous scatterer and N is Avagadros number.

Although the determination of $f''(E)$ is relatively easy, obtaining the energy dependence of $f'(E)$ is much more difficult. Experiments to measure $f'(E)$ directly have included: measurements of the total intensity of Bragg reflections from a single crystal [2], measurements of the ratio of scattered x-ray intensity from Freidel-pair reflections [3,4], the use of an x-ray interferometer [5,6] and measurements of total reflection curves [7,8].

Perhaps the most straightforward technique to determine $f'(E)$ is by first computing $f''(E)$ from eq. 1 and subsequently calculating $f'(E)$ from the Kramers-Kronig integral [7-10]:

$$f'(E) = \frac{2}{\pi} \oint_0^\infty \frac{E' f''(E)}{E^2 - E'^2} \, dE' \tag{3}$$

The symbol $\oint$ denotes the Cauchy principal value of the integral. A technique for overcoming the problem of the singularity at $E = E'$ (eq. 3) and the infinite upper limit of integration is discussed by Hoyt et al. [11]. A computation from reference 11 of $f'(E)$ for Cu near its K absorption edge is shown in fig. 1. The accuracy of the Kramers-Kronig technique is demonstrated by the excellent agreement with the interferometry work of Bonse et al. [12] and with the f' deduced from integrated intensity measurements of Freund [2]. At the present time, most ASAXS studies employ the Darwin equation and the Kramer-Kronig integral for the computation of $f'(E)$ and $f''(E)$.

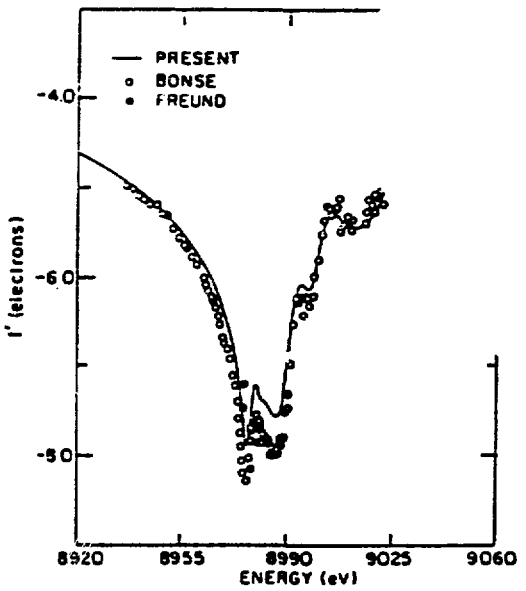

Figure 1. f' of Cu for energies near the K absorption edge. Data is compared with that of Bonse [12] and Freund [2]. Figure is reproduced from ref. [11].

INSTRUMENTATION

Beam lines dedicated to ASAXS experiments have been constructed at the synchrotron facilities LURE [13] and DESY [14]. Typical ASAXS systems consist of x-ray detectors (ionization chambers, photomultiplier tubes, etc.) positioned in front and behind the sample in order to monitor the incident beam intensity and to measure the sample transmission. A pair of, typically tantalum, slits provide a point collimated beam

and the beam travels through evacuated flight tubes. The scattered intensity is collected via an area or linear postion sensitive detector in conjunction with rapid data processing electronics. In short, ASAXS instrumentation is primarily the same as that found in conventional small angle scattering experiments. However, in ASAXS there are a few additional points which need to be considered.

Since the atomic scattering factor varies quite rapidly (fig. 1) for energies near the absorption edge, a nonochromator designed for ASAXS must provide a high energy resolution capability and the ability to eliminate harmonics in the incident beam. A narrow and stable energy bandpass of about $\Delta E/E \simeq 10^{-4}$ at an incident energy of 10 KeV is sufficient. In addition, the monochromator should cover a large energy range such that energies near the absorption edges of a large number of elements can be selected. Finally, since ASAXS experiments most often employ a series of incident energies, it is important to know or measure the response of all x-ray detection devices used as a function of photon energy [15].

APPLICATIONS

In many experimental situations, it is not clear what particle or heterogeneity is responsible for the observed small angle scattering intensity. Also, the scattered intensity is often times a sum of different scattering effects and a conventional SAXS experiment can offer no clues as to the magnitude of the contribution of each individual effect. The use of ASAXS however, can often provide solutions to the two aforementioned difficulties.

Pioneering work in the field of ASAXS was performed by H.B. Stuhrmann and coworkers. Many examples of applications of ASAXS to important problems in biophysics can be found [16-18], but for the present work we will review the work of Stuhrmann and Notbohm [19]. In this study the authors examined aqeous solutions of human hemoglobin in order to determine the configuration of the four iron atoms in this protein. Thus, the experiments were performed using energies in the vicinity of the Fe K edge.

Stuhrmann and Notbohm write the excess electron density of dissolved protein as:

$$\rho(\mathbf{r}) = \rho(\mathbf{r})_{solute} - \rho_{solvent} \tag{4}$$

This equation merely redefines, without loss of generality, the electron density ρ of the particle as being the difference between that and the solvent electron density. Within the volume defined by the electron density $\rho(\mathbf{r})$ there exist regions in which the anomalous scatterers, in this case Fe, add to the electron density. If one denotes these regions by $\rho_a(\mathbf{r})$, eq. 4 can be rewritten as:

$$\rho(\mathbf{r}) = \rho_s(\mathbf{r}) + (\bar{\rho}' + i\bar{\rho}'')\rho_a(\mathbf{r}) \tag{5}$$

where $\bar{\rho}'$ and $\bar{\rho}''$ are the anomalous scattering electron densities within the volume defined by $\rho_a(\mathbf{r})$ and $\rho_s(\mathbf{r})$ is the electron density of the normal or off resonant volume.

Given the above definitions, the intensity as a function of the magnitude of the scattering vector k can be written as:

$$I(k) = I_s(k) + \bar{\rho}' I_{as}(k) + \left[(\bar{\rho}')^2 + (\bar{\rho}'')^2\right] I_a(k) \tag{6}$$

where the additional contributions to the intensity are:

$$I_{as}(k) = 2 \int \int \rho_a(\mathbf{r}) \rho_s(\mathbf{r}') \frac{\sin\ k/\mathbf{r} - \mathbf{r}'/}{k/\mathbf{r} - \mathbf{r}'/} d^3\mathbf{r} d^3\mathbf{r}' \tag{7}$$

and

$$I_a(k) = \int \int \rho_a(\mathbf{r}) \rho_a(\mathbf{r}') \frac{\sin\ k/\mathbf{r} - \mathbf{r}'/}{k/\mathbf{r} - \mathbf{r}'/} d^3\mathbf{r} d^3\mathbf{r}' \tag{8}$$

The quantity $I_s(k)$ is the scattering which would be measured from a conventional SAXS experiment. The term $I_{as}(k)$ represents the convolution of that volume of particle which contains anomalous scatterers with the particle itself. Similarly, the term $Ia(k)$ represents the autocorrelation of the anomalous scattering volume. Whereas the $I_s(k)$ term yields information concerning the overall electron density of the sample, the terms $I_{as}(k)$ and $I_a(k)$ give clues as to the specific locations of the Fe atoms.

By performing a series of experiments employing 32 different energies near the Fe K edge, Stuhrmann and Notbohm were able to vary f' and f'' and hence $\bar{\rho}'$ and $\bar{\rho}''$. Thus, rather than a situation of one equation and three unknowns as in eq. 6, a system of equations is established which can, in principal, be solved to yield $I_s(k)$, $I_{as}(k)$ and $I_a(k)$. The results for the hemoglobin experiment are shown in fig. 2. (The accuracy of the experiment was too low to permit a measurement of $I_a(k)$; the curve shown is calculated from the derived model.) The $I_{as}(k)$ curve shows a rather prominent peak at $k \simeq .29A^{-1}$ and a smaller maximum at $k \simeq .48A^{-1}$.

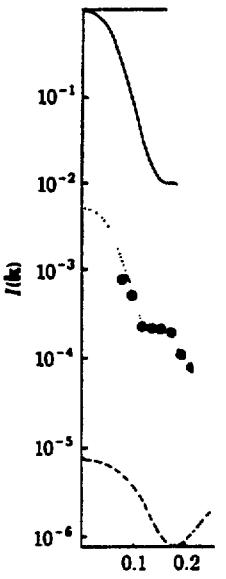

Figure 2. $I_s(k)$ top curve, $I_{as}(k)$ middle curve and $I_a(k)$ dashed curve for aqeous solution of human hemoglobin. Figure reproduced from ref [19].

From this additional scattering information, the authors were able to model the positions of the iron atoms in the hemoglobin molecule via a so called multipole analysis [20]. The multipole technique is beyond the scope of this review, but the important point to note is that any model describing the positions of the Fe atoms must reproduce the main features of both the $I_{as}(k)$ and the $I_s(k)$ curves. Stuhrmann and Notbohm were able to deduce a tetrahedral arrangement of Fe atoms with a mean spacing of 26A. The results of this ASAXS study is in good agreement with crystallographic data.

ASAXS has recently been useful in determining the morphology of ionomers. Conventional SAXS spectra of ionomers typically show a peak on the order of $k \simeq .2A^{-1}$ and a strong increase in intensity as the wave vector approaches $k = 0$. The peak is due to the ionomer aggregates immersed in a polymer matrix, but, until the ASAXS work of Ding et al. [21], the upturn at $k = 0$ was unexplained. Since no accepted model could explain both the peak and upturn in intensity, it had been suggested that the large near zero angle scattering was a result of impurities or voids in the sample. The technique of ASAXS was able to define the origin of this upturn and provide a much clearer understanding of the morphology of ionomers.

Ding et al. [21] examined ASAXS from a sample of nickel-neutralized sulfonated polystyrene ionomer at two different incident beam energies. The energies employed were 100 eV and 5 eV below the Ni edge. The results are shown in fig. 3 where the solid curve represents scattering at an incident beam energy 100 eV below the K edge of Ni and the open circles represent the difference between the solid curve and the intensity scattered at -5 eV.

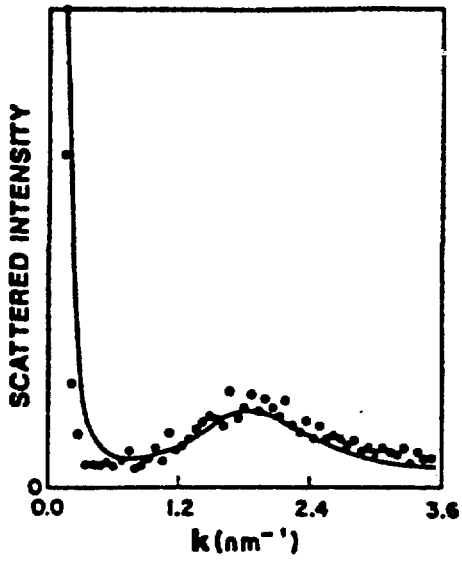

Figure 3. $I(k)$ from nickel-neutralized sulfonated polystyrene. Solid line is $I(k)$ for an incident energy 100 eV below the Ni K edge. Open circles are the difference between the solid curve and scattering at -5 eV. Figure reproduced from ref. [21].

From just the two spectra of fig. 3, one can conclude that the entity responsible for the large intensity upturn at near zero angles must contain Ni. Had voids or impurities been causing the upturn, the difference pattern (open circles) would have been zero near the origin in k space. The large difference pattern observed at the peak ($.2A^{-1}$) is consistent with the accepted model of aggregates of Ni^{2+} cations and some sulfonate groups dispersed in a polystyrene matrix.

Supplied with the above information, the authors were able to combine two previously proposed models of the ionomer structure to obtain an accurate fit to the data and thus provide a good description of the morphology. The large contribution of scattering near k=0 was explained by an inhomogeneous distribution of cations dissolved in the polystyrene.

Conventional SAXS has long been used to study precipitation phenomena in alloy systems. Not surprisingly then, ASAXS has found a number of applications in materials science.

Recently, Goudeau et al. [22] studied amorphous Cu_{67} -Ti_{33} alloys using ASAXS. In hydrogenated melt spun or splat cooled Cu-Ti alloys, a strong SAXS signal had been observed in previous studies but the origin of this scattered intensity was unknown. Possible explanations included the presence of hydrogen or argon bubbles, fluctuations in composition or the presence of small particles of a crystalline phase.

The authors employed four incident energies near both the Cu and Ti K-edges to identify the heterogeneity giving rise to a large ASAXS intensity. The results are shown in fig. 4. The fact that the intensity decreases as f_{Cu} is decreased but increases for a decreasing f_{Ti}, eliminates the possibility of a presence of bubbles. Recall that the intensity is proportional to the square of the difference between the electron density of the particle and that of the matrix. If scattering had been due to bubbles, the intensity would have decreased at both edges.

Furthermore, the authors eliminated the possibility of composition fluctuations by comparing intensity changes at small angles with that at the first diffraction halo ($\sim 3A^{-1}$). In fact, the qualitative changes observed in fig. 4 suggest that the scattering is due to particles rich in Ti with the electron density of the particle being less than that of the matrix. Gordeau et al. used the magnitude of the changes in ASAXS spectra to conclude that the particles were small crystallites of composition TiH_2.

A novel application of ASAXS has been the determination of the three partial structure functions (PSF) in ternary alloys. In a binary alloy, there exists just one independent pair correlation function which provides important information concerning local atomic order. The Fourier transform of this function is known as the structure function $S(k)$ and is directly proportional to the scattered intensity. A binary alloy when heated to high temperatures, quenched into a miscibility gap and subsequently aged for various times will exhibit a structure function peaked at small k. As aging progresses the maximum peak intensity increases while the position of the peak in k space decreases. The time dependent behavior of $S(k)$ is a measure of the kinetics of the first order transition known as phase separation. Because of the ease in which the structure function can be measured in a SAXS experiment, the various theories of phase separation are couched in terms of the time dependence of $S(k)$ thus allowing a direct comparison between theory and

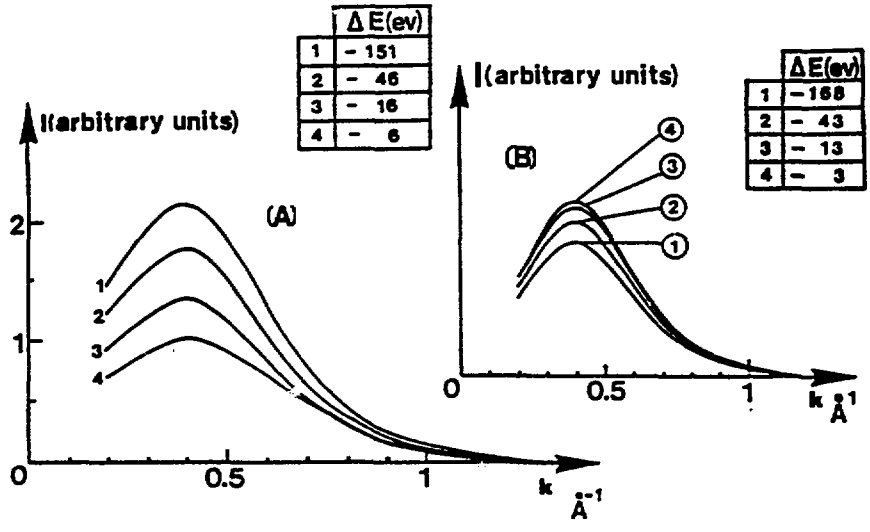

Figure 4. ASAXS spectra with incident energies near the Cu edge (A) and the Ti edge (B) from a splat cooled, hydrogenenated amorphous Cu-Ti alloy. Figure reproduced from ref [22].

Experimentally studying phase separation kinetics in the ternary case is, however, much more difficult and in fact, impossible without the aid of ASAXS. In a ternary system there exist three linearly independent PSF [23] and the scattered intensity is the linear combination of these PSF. The intensity is written as [24]:

$$I(k) = \sum_{i,j=1}^{2} (f_i - f_3)(f_j - f_3)^* \, S_{ij}(k) \tag{9}$$

where $S_{ij}(k)$ are the PSF describing the correlation between species i and j and the superscript * denotes the complex conjugate. The quantity f_3 represents the scattering factor of the "host" element; that is the component eliminated by the linear dependence of $S_{ij}(k)$.

Extracting the three PSF from eq. 9 with conventional SAXS would, of course, be impossible. However, by performing a series of experiments at different incident energies such that one or more of the f's is changing, one obtains a system of equations which in compact form is written as:

$$\bar{I}(E,k) = \bar{\bar{A}}(E)\bar{S}(k) \tag{10}$$

Here $\bar{\bar{A}}(E)$ is a 3x3 matrix whose elements involve products of atomic scattering factors as indicated in eq. 9. The above equations are solved for the $S_{ij}(k)$ by inverting $\bar{\bar{A}}(E)$.

The pioneering work on ternary alloys [25,26] examined ASAXS near the Zn K edge in Al-Zn-Ag alloys. An example of the decrease in ASAXS intensity with incident energies approaching the Zn edge is shown in fig. 5. The sample of fig. 5 is of composition Al - 14 at%Zn - 4 at%Ag and was aged for 4 minutes at 125°C. In these early studies, the three PSF could not be determined uniquely due to the fact that the matrix $\overline{\overline{A}}(E)$ is ill-conditioned. An ill-conditioned matrix implies that the relative change in f_{Zn} is small and as a result small errors in the measurement of the intensity lead to huge uncertainties in the PSF. Although $S_{ZnZn}(k)$, $S_{ZnAg}(k)$ and $S_{AgAg}(k)$ could not be determined, weighted sums of the PSF could be obtained quite easily. This information provides the direction of decomposition in concentration space; that is the slope of the tie-line in the Gibbs triangle. The time dependent behavior of the weighted PSF led to the observation of a rotation of the tie-line at early aging times [27,28]. The phenomenon of tie-line rotation is unique to ternary (and multicomponent) alloys and cannot be observed using conventional SAXS.

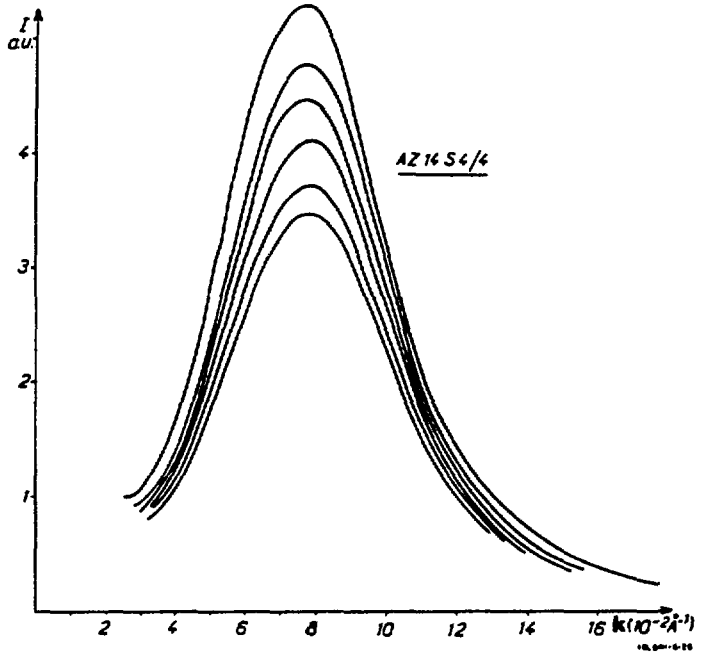

Figure 5. ASAXS spectra for Al-14% Zn-4% Ag aged for 4 minutes at 125°. Upper to lower curves were recorded at 8500, 9400, 9460, 9625, 9650 and 9657 eV. Figure reproduced from ref [15].

Subsequent ASAXS studies on ternary alloys involved the Cu-Ni-Fe system [29,30]. These studies found that reliable data for $S_{CuCu}(k)$, $S_{NiNi}(k)$ and $S_{FeFe}(k)$ could be extracted if an overdimensioned system of equations (eq. 10) is established by employing incident energies in the vicinity of two absorption edges (in this case Fe and Ni). In addition, it is known that the condition number of $\overline{\overline{A}}$ in eq. 10 is reduced if the three elements in solution have similar atomic numbers as is the case for Cu, Ni and Fe. The

results of this study are shown in fig. 6 where seven energies at the Ni and Fe edges were utilized to compute the PSF. The data of fig. 6 refer to a Cu-42.2at%Ni-15.2at%Fe sample heat treated for 9 hours at 500°C. The authors also show the $S_{CuCu}(k)$ curve computed from the relation $\sum_j S_{jj}(k) = 1$.

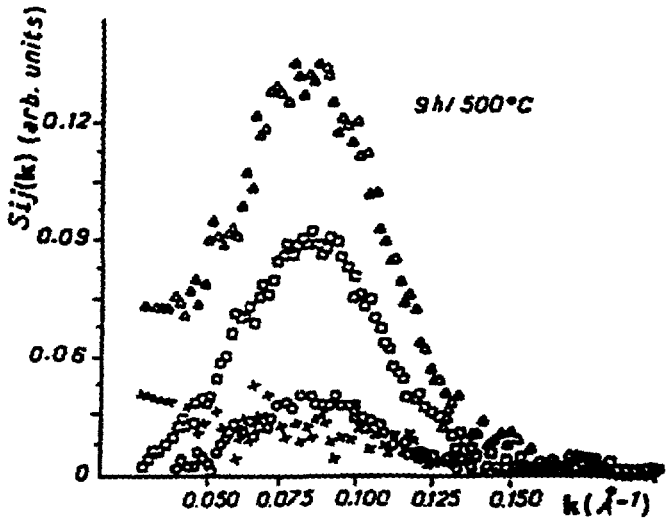

Figure 6. Partial Structure functions for a Cu-42.2% Ni-15.2% Fe sample aged for 9 hrs. at 500°C; $S_{CuCu}(k)$ open triangles, $S_{NiNi}(k)$ open squares, $S_{FeFe}(k)$ open circles and S_{NiFe} plus signs. Figure reproduced from ref. [30].

CONCLUSION

The technique of anomalous small angle x-ray scattering is a useful tool for determining the source of certain scattering characteristics of a given SAXS spectrum. In addition, in instances when a SAXS spectrum is the result of a sum of intensity contributions, ASAXS provides a means of determining the magnitude of each contribution.

At this point in time, the technique of ASAXS is in its infancy. The continued success of experiments such as those described in this review, indicates that ASAXS will become a widely used analytical tool in chemistry, physics and materials science.

ACKNOWLEDGEMENT

The author would like to thank Professor R.V. Subramanian for an explanation of the structure of ionomers.

REFERENCES

1. R.W. James, "The Optical Principles of the Diffraction of X-rays." London: G. Bell and Sons, (1965) pp. 135-192.

2. A. Freund, "Anomalous Scattering." Edited by S. Ramaseshan and S.C. Abrahams. Copenhagen: Munksgaard (1974) pp. 69-84.

3. T. Fukamachi and S. Hosoya, *Acta Cryst.*, **A31**, 215 (1975).

4. T. Fukamachi, S. Hosoya, T. Kawamura and M. Okunuki, *Acta Cryst.*, **A33**, 54 (1977).

5. U. Bonse and M. Hart, *Appl. Phys. Lett.*, **6**, 155 (1976).

6. M. Hart and D.P. Siddons. *Proc. R. Soc. London Ser*, **A374**, 465 (1981).

7. P. Fouss, Ph.D. Thesis, Stanford University (1980).

8. T. Fukamachi, S. Hosoya, T. Kawamura, S. Hunter and Y. Nakana, *Jpn. J. Appl. Phys.*, **17**. Suppl 17-2, 326 (1978).

9. D.H. Templeton, L.K. Templeton, J.C. Phillips and K.O. Hodgson, *Acta Cryst.*, **A36**, 436 (1980).

10. T. Kawamura and T. Fukamachi, *Jpn. J. Appl. Phys*, **17**, Suppl 17-2, 433 (1978).

11. J.J. Hoyt, D. de'Fontaine and W.K. Warburton, *J. Appl. Cryst.*, **17**, 344 (1984).

12. U. Bonse, I. Hartmann-Lotsch and H. Lotsch "EXAFS and Near Edge Structures." Springer Series in Chemical Physics, No. 27. Edited by A Bianconi, L. Incoccia and S. Stippich, New York: Springer Verlag (1983) p. 376.

13. J.M. Dubuisson, J.M. Dauvergne, C. Depautey, P. Vachette and C.E. Williams, *Nucl. Instr. Meth in Phys. Res.*, A246, 636 (1986).

14. H.B. Stuhrmann and A. Gabriel, *J. Appl. Cryst.*, **16**, 563 (1983).

15. J.J. Hoyt, Ph.D. Thesis, University of California (1986).

16. H.B. Stuhrmann, *Adv. Polym. Sci.*, **67**, 123 (1985).

17. H.B. Stuhrmann, *Q. Rev. Biophys.*, **14**, 433 (1981).

18. H.B. Stuhrmann, *Acta Cryst.*, **A36**, 996 (1980).

19. H.B. Stuhrmann and H. Notbohm, *Proc. Natl. Acad. Sci. USA*, **78**, 6216 (1981).

20. H.B. Stuhrmann, *A. Phys. Chem.*, **72**, 177 (1970).

21. Y.S. Ding, S.R. Hubbard, K.O. Hodgson, R.A. Register and S.L. Cooper, *Macromol.*, **21**, 1698 (1988).

22. P. Gouduau, A. Navdon, B. Rodmacq, P. Margin and A. Chamberod, *J. Physique, Coll.*, **48**, C8-479 (1985).

23. D. de Fontaine, *J. Appl. Cryst.*, **4**, 15 (1971).

24. D. de Fontaine, "Configurations and Thermodynamics of Solid Solutions" Solid State Physics, Vol. 24. Edited by H. Ehrenreich, F. Seitz and D. Turnbull. New York: Academic Press (1979).

25. O. Lyon, J.J. Hoyt, R.Pro, B.E.C. Davis, B. Clark, D. de Fontaine and J.P. Simon, *J. Appl. Cryst.*, **18**, 480 (1985).

26. J.J. Hoyt, O. Lyon, J.P. Simon, B. Clark, B.E.C. Davis and D. de Fontaine, *Sol. State Comm.*, **57**, 155 (1986).

27. O. Lyon and J.P. Simon, *Acta Metall.*, **34**, 1197 (1986).

28. J. J. Hoyt, M. Sluiter, B. Clark, M. Kraitchman, and D. de Fontaine, *Acta Metall*, **35**, 2315 (1987).

29. J.P. Simon and O. Lyon, *Phil. Mag. Lett.*, **55**, 75 (1987).

30. O. Lyon and J.P. Simon, *Phys Rev.*, **B35**, 5164 (1987).

SESSION IV

DIFFRACTION

Single Crystal Diffraction by Synchrotron Radiation*

Åke Kvick
Chemistry Department, Brookhaven National Laboratory
Upton, New York 11973

The tunability and access to short wavelengths in combination with high intensity and the low divergence of the X-ray radiation produced by synchrotron storage rings opens up new and challenging fields for single crystal diffraction. These areas include microcrystal diffraction, studies of time-dependent phenomena, element selective diffraction, studies of materials under extreme conditions, solution of the crystallographic phase problem either by the use of the wavelength dependency of the anomalous scattering or by direct experimental determination of the phases. Single crystal diffraction from proteins and macromolecules using photographic film as a detection medium has already reached considerable maturity but high-precision data collections using diffractometers at storage rings are still not routine because of the severe requirements for beam stability over extended periods of time.Development work at institutions such as the National Synchrotron Light Source, The Photon Factory, SSRL, CHESS, Hasylab and Daresbury however suggest that synchrotron single-crystal diffraction will become an essential part of the research at the synchrotron storage rings in the near future.

I. Diffraction from Small Crystals.

Many important classes of materials are only available to experimenters in the form of powders or as microcrystals. The catalytically important zeolite framework structures fall in this category, but other examples from ion conductors, mineralogical samples, biological materials,high- pressure applications etc. will also benefit from the high intensity and resolution of the synchrotron radiation X-rays. Single-crystal determinations using conventional X-ray sources are limited to crystal sizes of 50-60 μm on edge or larger thus excluding many materials from precise structure characterisation.The alternative powder diffraction analysis, although markedly improved by the use of synchrotron radiation in recent years, is limited to small to medium size structural problems and also complicated by the difficulty in space group determination and in obtaining an initial structure model.

The potential for single crystal diffraction at synchrotrons may be understood by inspection of a formula relating the observed integrated Bragg intensity to the intensity of the primary beam:

$$I_{Bragg} = (\frac{e^2}{mc^2})^2 \cdot \frac{1}{sin2\theta} \cdot (\frac{F_{hkl}}{V_{cell}})^2 \cdot \lambda^3 \cdot V_{cryst} \cdot I_{primary} \cdot \frac{1}{\omega}$$

where $\frac{1}{sin2\theta}$ is the Lorentz factor,V_{cell} andV_{cryst} are the volumes of the unit cell and the crystal sample respectively, and ω represents the angular velocity of the scan through the reflection.

It is clear from this formula that the high $I_{primary}$ intensity and the wavelength tunability give the experimenter a freedom to choose a small sample , a short wavelength, a complex structure , short recording times or combinations thereof in a fashion that will optimize his particular experiment. At the now existing sources the intensity is already 3-4 orders higher than the conventional X-ray sources ,and the X-ray facilities under construction will further increase the available flux .

The width of the Bragg diffraction peaks may be viewed as a convolution of beam divergence, wavelength bandwidth and crystal properties such as mosaic spread. The small divergence and the possibility for a narrow bandwidth at the synchrotrons make it possible to record sharp Bragg peaks(*i.e.* peakwidths dominated by the mosaic spread) increasing the peak/background signal from small crystals or weak scatterers.The high resolution also makes it possible study the diffraction profiles in detail in order to understand phase transitions , subtle space group ambiguities or thermal diffuse scattering. An example of the resolution and Bragg peak intensity obtained from a small crystal of the synthetic zeolite ZSM-5 is given in Fig.1 (Kvick and Rohrbaugh,1987).

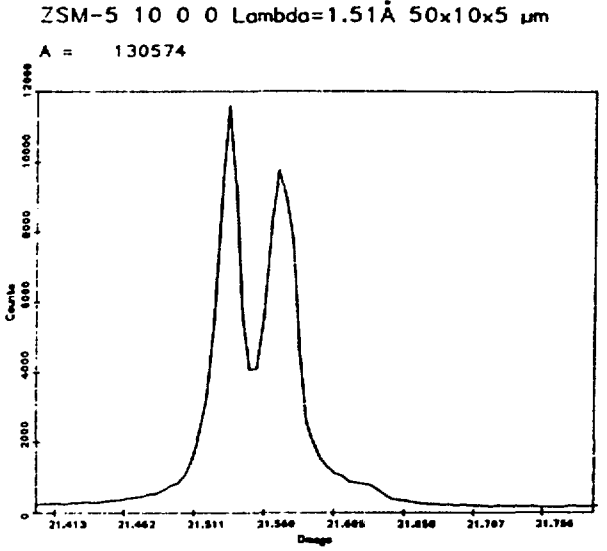

Fig.1. Diffraction profile of the $10,0,0$ reflection from a twinned $50 \cdot 10 \cdot 5 \mu m^3$ crystal of zeolite ZSM-5.

Early experiments at the now existing sources (Eisenberger *et.al.*,1984, Bachmann *et.al.* ,1985, Hoche *et.al.*,1986, Andrews *et.al.*,1987, Kvick, 1987, Newsam and King,1987) have shown that meaningful diffraction intensities may be obtained from microcrystals well below $10\mu m$ in diameter.

Structural studies under extreme conditions *i.e.* high pressures, high or low temperatures etc. frequently limit the size of the samples or attenuates the beam by the necessity for bulky sample chambers. The high intensity and collimation will also here markedly improve the experimental conditions.

II. Time-dependent Studies and Studies of Crystals In External Fields.

The resolution and high intensity can also be used in studying small changes in the

molecular structure and electron reorganization due to chemical reactions or external perturbations by for instance electric fields or high intensity electromagnetic radiation from lasers. The change in the electron density due to such perturbations can be estimated to be very small , and excellent counting statistics is therefor needed to obtain statistically significant results.Reactions in the solid state may also be monitored down to time-scales of to a few hundred μ secs with the present monochromatized synchrotron X-ray sources; even faster events may in the future be recorded by stroboscopic experiments using the time-structure of the synchrotron radiation. Fig.2. illustrates the converse piezoelectric effect in $LiNbO_3$ when the polarization along the polar *c* axes is reversed by an external electric field. The spatial resolution of the synchrotron radiation allows interplanar spacing shifts $\frac{\Delta d}{d}$ of well below 10^{-5} to be followed. The high intensity also makes it feasible to analyze the relative atomic shifts due to the variation in electric polarisation.

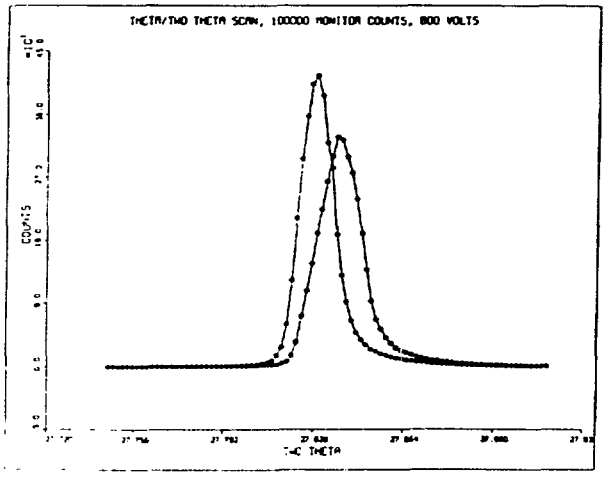

Fig.2. Changes in $\frac{\Delta d}{d}$ for the 006 reflection in $LiNbO_3$ as a function of an applied +/-V square wave electric field (50Hz) along the crystallographic *c* direction (Kvick ,Ståhl and Abrahams, 1987).

III. Systematic Errors.

Crystallographic work using conventional X-ray sources is frequently plagued by systematic errors such as absorption or extinction effects.The reduction in size of the crystals now possible will naturally reduce the absorption problem since absorption depends on the X-ray pathlength in the crystal. Extinction may similarily be reduced or completely eliminated by the use of small samples and/or the use of short wavelengths. These reductions of the systematic errors will particularily benefit the experimental charge density studies. These studies will also gain from the increased resolution in the data obtainable with short wavelengths giving a more precise definition of atomic positions and thermal motion parameters(Nielsen, Lee,Coppens,1986).

IV.Conclusions.

The pioneering applications of synchrotron radiation to chemical crystallography are very encouraging. The experimental set-up are now reaching a point of maturity where

extensive data collections under optimized conditions are feasible although not yet routine operations.The high intensity has been used to study extremely small samples, to improve counting statistics and to probe the structures during short time intervals. The excellent resolution has been used in new experiments of crystals perturbed by electric fields as well in preliminary studies of new methods for structure determinations.Further improvement in the synchrotron radiation sources and in the detection systems promises to further expand the applications into new areas particularily in the time-dependent region.

V. References

Kvick. Å and Rohrbaugh,W. (1986). Private Communication.

Eisenberger,P,Newsam,J.M., Leonowicz,M.E. and Vaughan, D.E. (1984), Nature,**309**,45.

Bachmann,R,Kohler,H,Schulz,H. and Weber,H.P. (1985),Acta Cryst, **A42**,106.

Hoche,H.R.,Schulz,H.,Weber,H.P.,Belzner,A.,Wolf,A. and Wulf,R.(1986), Acta Cryst,**A42**,106.

Andrews,J.S.,Hails,J.E.,Harding,M.M. and Cruickshank,D.W.J.(1987),Acta Cryst, **A43**,70.

Kvick,Å. (1987), Acta Cryst,**A43**,C-266.

Newsam,J.M. and King,H.E.Jr. (1987),Acta Cryst,**A43**,C-259.C

Kvick,Å., Ståhl,K. and Abrahams,S.C. (1987) Private Communication.

Nielsen,F.S,Lee,P. and Coppens,P. (1986),Acta Cryst,**B42**,359.

* Work performed under contract DE-AC002-76CH00016 with the U.S. Dept. of Energy and supported by its Div. of Chemical Sciences, Office of Basic Energy Sciences

CHEMICAL CRYSTALLOGRAPHY AND SYNCHROTRON RADIATION: RECENT EXPERIMENTS AND FUTURE STUDIES

Philip Coppens

Chemistry Department

State University of New York at Buffalo

Buffalo, NY 14214

Scope of the New Crystallography

It has become increasingly clear that Crystallography is being revolutionized by the availability of highly intense, tuneable, low divergence, pulsed synchrotron sources. New applications are developed at present "second generation" facilities which include the National Synchrotron Light Source, The Stanford Synchrotron Radiation Laboratory, the Cornell High Energy Synchrotron Source, the Hamburg Synchrotron Laboratory, the Photon Factory in Tsukuba, Japan, the Daresbury Synchrotron Laboratory in the U.K, and others. Third generation sources now in the planning or early construction stages, such as the Advanced Photon Source, will offer an additional increase in brightness of three to five orders of magnitude and practically unlimited new possibilities.

One of the great successes of X-ray crystallography has been the ability to perform almost routine structure determinations of small and moderately large structures. The new Crystallography goes beyond this now analytical technique, and concerns structure of and phase transitions at solid surfaces, microcrystallography of μ-sized samples, the response of crystals to external perturbations, modulations in crystals, the analysis of very large (up to 1000Å edge) unit cell structures of viruses and ribosomes, time-resolved phenomena, polarisation dependence of anomalous scattering, high pressure phases, and other applications.

Table 1 shows the effect of the increase in brightness. With typical scattering powers and conventionaly sized samples the counting rates achievable far outstrip the capability of today's counter technology. This

Table 1. Intensity Considerations

Typically with Present Sources $I_0 \sim 10^{11}$ Photons/mm^2/sec

and $10^{-6} < I/I_0 < 10^{-3}$

$10^5 < I < 10^8$ photons/sec

We have a counter problem!

We can study smaller crystals, surfaces, very weak reflections, very large unit cells.

Surfaces	*10Å diffracting layer*
	10Å/100μ = $10/10^6$ ----> $1 < I < 10^3$ p/s
Small Crystals	10μ x 10μ x 10μ ----> $10^2 < I < 10^5$ p/s
Very Weak Reflections	*example:* satellite reflections in TTF-TCNQ
	with intensity 10^{-4} times main reflections
	---> $10 < I < 10^4$ p/s
Very Large Unit Cells	*example:* viruses with 1000Å unit cell edge
	Roughly F increase with square of volume
	N decreases with cube of volume
N^2/F^2	reduced by factor 10^4 compared with 10Å unit cell
	$10 < I < 10^4$ p/s

means that we can study much smaller aggregates of atoms, such as surfaces, monolayers or microcrystals, or very large unit cell crystals of macromolecules, which have a much smaller scattering per unit volume. We can also study weak effects, such as the response of a crystal to an external electric field or a laser beam. Using very small crystals with very short wavelength radiation at low sample temperatures has the potential for an unparalleled increase in accuracy. The tunability of the beam is opening up a new field of contrast crystallography, in which scattering factors of atoms are varied near their absorption edges to obtain selective contrast of atomic species. This is of particular importance in complicated inorganic materials, such as the non-stoichiometric quinary high T_c ceramics.

We will give examples of several applications to chemical problems, taken from our work during the past three years at CHESS and the SUNY beamline at NSLS.

Measurement of Very Weak Reflections: Modulations in TTF-TCNQ[1]

It is well known that the one-dimensional conductor TTF-TCNQ (tetracyanoquinodimethanide-tetrathiofulvalene) undergoes a Peierls transition at 53K and further transformations at 49 and 38K. Though the modulation vectors have been determined with both X-ray and neutron scattering techniques and the average structure is known at 45K, no direct measurements of the molecular displacements have been reported.

The scarcity of experimental information is due to the weakness of the satellite intensities which are typically not more than 10^{-4} times the intensities of the main reflections. With the use of high-intensity synchrotron radiation it is possible, however, to measure at least the first-order satellites with adequate counting statistics.

Using the SUNY X21 (now X3) beamline at NSLS, we have measured a total of 1342 reflections, including 1154 satellite reflections with sin θ/λ in the range of 0.2-0.5$\AA^{-1}$, using a crystal with dimensions 2.40 x 0.96 x 0.52 mm, mounted in a DISPLEX cryostat. Satellite intensities on an absolute scale were obtained by scaling each of the measured intensities with the ratio of the main reflection F^2 value calculated with the parameters of the 45K structure determination and the measured intensity of the main reflection.

Analysis of the satellite structure factors shows that the main displacement is a translation of the TTF molecules with amplitude 0.0191(8) Å. The polarization vector for this translational displacement lies within experimental error along the long axis of the molecule, and thus does not affect the interplanar spacing of the molecules. The other translational displacements of TTF and all translations of TCNQ are smaller than 0.007 Å. All rotations are less than 0.2°, and about the long molecular axes.

The results show that the $2k_F$ charge density wave in the low temperature phase is mainly localized on the TTF chains; it has both transverse and longitudinal components as its main feature is a relative slip of the TTF molecules. The possibility that the $4k_F$ distortion is mainly localized on

the TCNQ chains requires measurement of the $4k_F$ satellites, which will be the subject of future studies.

Though the displacements associated with the Peierls transition are small, they have a dramatic effect on the properties as the organic metal becomes insulating at the transition point.

High-Resolution Studies of the Electron Distribution in Crystals[2,3]

During the past two decades methods have been developed which allow mapping of the charge density distribution in crystals with the help of carefully collected diffraction data. The methods have been used to calibrate theoretical calculations, and give charge densities which agree with advanced, but not with more approximate methods. In a number of cases it has been possible get information on the nature of the electronic ground state of complexes with closely spaced energy levels for which various theoretical methods gave contradictory results. It has also been possible to identify the effect of the molecular environment on the electron density in the case of strongly hydrogen bonded molecules. Presently an accuracy of about $0.03 e\text{Å}^{-3}$ can be achieved in such studies.

The limitations to further increases in accuracy of the experimental charge densities are summarized in table 2. They concern counting

Table 2. Limitations of Accuracy

- Absorption of beam in crystal
- Extinction
- Multiple reflection
- Counting statistics
- Data cut-off $d > \lambda/2$

Table 3. Formulae for Scattering from a Perturbed Crystal

$$I^+ = (A + \Delta A^+)^2 + (B + \Delta B^+)^2$$

$$I^- = (A - \Delta A^-)^2 + (B - \Delta B^-)^2$$

----->

$$I^+ - I^0 = 2(A\Delta A^+ + B\Delta B^+) + (\Delta A^+)^2 + (\Delta B^+)^2$$

$$I^0 - I^- = 2(A\Delta A^- + B\Delta B^-) - (\Delta A^-)^2 - (\Delta B^-)^2$$

for $\Delta A^+ = \Delta A^-$, $\Delta B^+ = \Delta B^-$

$$I^+ - I^- = 4(A\Delta A + B\Delta B)$$

statistics, rescattering of the photon beam within the sample, difficulty of accurate absorption corrections, thermal diffuse scattering, and lack of resolution due to wavelenth cut-off. With high intensity, low-divergence synchrotron radiation the sample size can be greatly reduced, counting statistics can be improved and a much shorter wavelenth can be selected for the experiment. Each of these reduces the the limitations listed in the table. The advantages are such that a much higher accuracy can be reached, provided, of course, the availability of a stable synchrotron source. Thus, the potential of the method as an analytical tool can be greatly increased.

We have done a first such study using the Cornell High Energy Synchrotron Source, using 0.3Å photons from the A2 wiggler beamline. In order to be able to judge the precision of the measurements a highly symmetric crystal with moderately sized unit cell was selected. Crystals of $Cr(NH_3)_6Cr(CN)_6$ are rhombohedral and belong to the space group $R\bar{3}c$. They are relatively hard and thus permit the collection of data to larger values of $\sin\theta/\lambda$.

The density deformation map is given in figure 1. It represents the difference between the experimental electron distribution and the distribution corresponding to a superposition of unperturbed, spherical atoms. The map shows lone pair peaks at the carbon and nitrogen atoms, bonding density in the CN bond and asymetric features around the chromium atoms, with the negative areas being more shallow in directions away from the ligands. The noise level in the regions away from the atoms attests to the quality of the results, which is as good or better than the best room-temperature results from conventional sources.

In order to take advantage of the high resolution possible with short wavelengths it is necessary to perform the studies at lower temperatures. A first such experiment was performed at the CHESS beam line using a focused beam and liquid helium temperature cryogenic equipment. The study on $Fe(NH_4)_2(SO_4)_2.6H_2O$ has achieved very high resolution, with data up to $\sin\theta/\lambda = 1.8\text{Å}^{-1}$ having been collected.[3] However, it is not yet of the accuracy required for a charge density study. Further improvements in the cryogenic equipment are now being implemented.

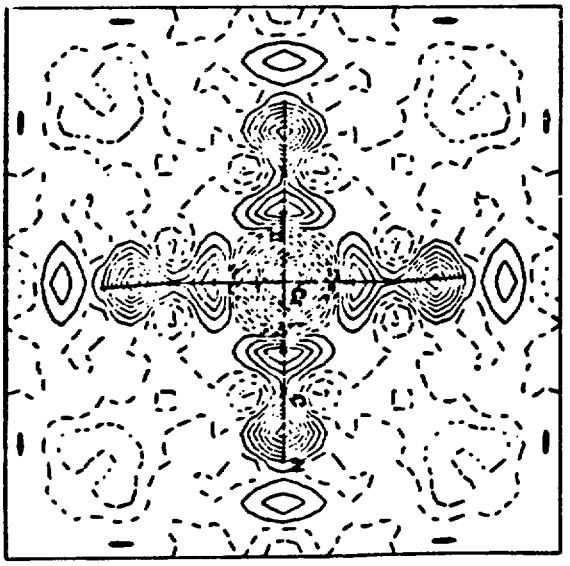

Figure 1. X-X deformation maps in the $Cr(CN)_4$ plane based on parameters from the high-order refinement ($\sin\theta/\lambda > 0.7\text{Å}^{-1}$. Contours at 0.05e Å^{-3}, negative contours broken. After averaging over chemically equivalent regions.

Non-linear Optical Crystals in an External Field[4]

The very high intensity of the synchrotron beam makes it possible to study small effects, such as the response of a crystal to an external magnetic field. Analysis of this response gives information on the polarizability at the atomic, rather than the macroscopic level.

We have examined the scattering of a crystal of 2-methyl 4-nitroaniline (MNA) in an external 50Hz electric field of 10^6 V/m, using the X13 (presently X7) beamline at NSLS. This organic solid is one of the best known non-linear optical materials. The X-ray scattering signal was gated to two different counting chains synchronized with the field frequency. The relative difference between the two measurements $\Delta I/I$ is reproducible and significant. An example is given in figure 2.

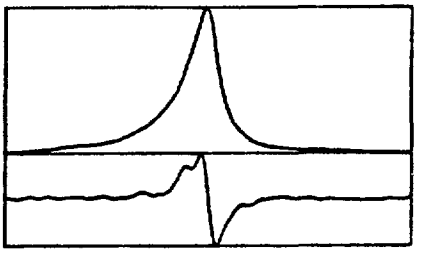

Figure 2. Plot of intensity versus angle for total scattering (top) and difference scattering (bottom) (x42.7) of the h,k,l=4,0,6 reflection of a crystal of 2-methyl-4-nitroaniline subjected to external fields of +106 and -106 V/m; voltage, 1000V; frequency, 35 Hz; scan width, 0.8000; maximum intensity (I_{max}), 169981; dI_{max}, 2497; I_{mean}, 4034343; dI/I, 0.2624%. The lower curve is the difference between the scattering with field up and field down.

The maximum value for the reflections measured is about 4%. Analysis of the data is in progress. There is evidence for both molecular reorientation and polarization of the molecule. The analysis requires novel algorithms for the scattering of a perturbed crystal. The equations derived are quite generally valid for crystals subject to external perturbations (table 3).

Selective Contrast Through Anomalous Scattering

In many inorganic and organomineral solids deviations from stoichiometry occur, which lead to substitutional disorder of the atomic sites. An early example of the ability of synchrotron radiation to identify the site occupants through the use of anomalous scattering near absorption edges is a study of Co-Fe spinel by Yakel.[5] The problem is especially pronounced for high T_c ceramics. Notwithstanding the very large number of published reports on the Bi and Tl copper-oxide superconductors, for example, the question of site occupancy has not been properly resolved.

Using crystals obtained from Dupont Research Laboratories, we have recently performed a series of measurements near the Cu absorption edge to indentify Cu occupancy of the Bi planes. A parallel series of mesurements near the Bi edge is to be made in the near future. The data are presently being analyzed.

Conclusion

Of the great many applications of synchrotron radiation in the field of Chemical Crystallography, few have been explored so far. In particular, APS and ESRF will give further orders of magnitude improvements, and open other novel possibilities, such as the study of very small microcrystals in external electric, magnetic and electromagnetic fields. Such experiments require very good sample stability and a stable beam, both in position and intensity. The changes ahead will be dramatic if such conditions can be met.

Acknowledgements

The work described has been supported by the National Science Foundation (CHE8711736). Installation of the single crystal diffractometer at the CHESS A2 beamline was funded by NSF-DMR-8213599. The SUNY X3 beamline at NSLS is constructed and operated through funding by the U.S. Department of Energy (DE-FG-0286ER45231). These sources are gratefully acknowledged.

References

1. Coppens, P.; Petricek, V.; Levendis, D.; Larsen, F.K.; Paturle, A.; Gao, Y., and LeGrand, A.D., "Synchrotron-Radiation Study of the Five-Dimensional, Modulated Phase of Tetrathiafulvalene-Tetracyanoquinodimethanide at 15K", Phys. Rev. Lett. 59, 1695-1697 (1987).

2. Nielsen, F.S.; Lee, P. and Coppens, P., "Crystallography at 0.3Å: Single Crystal Study of $Cr(NH_3)_6Cr(CN)_6$ at the Cornell High Energy Synchrotron Source", Acta Cryst. B42, 359-364 (1986).

3. Lee, P.; Levendis, D.; Gao, Y.; Paturle, A.; LeGrand, A.; White, J.P. and Coppens, P., "Short Wavelength Synchrotron Study at Low Temperature: Iron Ammonium Sulfate Hexahydrate at 20K as Measured at the CHESS Wiggler A2 Beamline", from Proceedings of the Annual Meeting of the American Crystallographic Association, Vol. 16, Philadelphia, PA, June 26 - July 1, 1988.

4. Paturle, A.; Wing, R.M.; Petricek, V.; Coppens, P., and Kvick, Å., "Synchrotron X-ray Scattering in an External Electric Field: Preliminary Application to the Non-linear, Optical Crystal MNA, from Proceedings of the Annual Meeting of the American Crystallographic Association, Vol. 16, Philadelphia, PA, June 26 - July 1, 1988.

5. Yakel, H.L., "Determination of the Cation Site-Occupation Parameter in a Cobalt Ferrite from Synchrotron-Radiation Diffraction Data", J. Phys. Chem. Solids 41, 1097 (1980).

PHYSICOCHEMICAL PROPERTIES OF BIOLOGICAL LIQUID CRYSTALS USING TIME-RESOLVED X-RAY DIFFRACTION.

Martin Caffrey, Department of Chemistry, The Ohio State University, Columbus, Ohio 43210

A method, referred to as time-resolved x-ray diffraction (TRXRD), has recently been developed which facilitates the direct and quantitative measurement of bulk biological liquid crystal (lipid) phase transitions (1-15, 20, 21). Mechanistic insights are provided by the ability to detect transition intermediates. The method combines the advantages of a focused, monochromatic synchrotron derived x-ray beam and a suitable live-time x-ray imaging device to continuously monitor diffracted x-rays from the transforming lipid. Kinetic and mechanistic studies are performed by using TRXRD in conjunction with relaxation measurements following the imposition of a rapid perturbation in one or more thermodynamic variables. The ultimate goal is to understand the mechanism of lipid phase transitions and the structural interrelationships of the different mesomorphs. This should greatly augment our appreciation of the physiological role of lipids and our understanding of the physicochemical properties of these liquid crystalline materials (16, 18, 19).

The method of TRXRD represents what amounts to a technological conjugation of diverse technologies in a way that is extending our knowledge and understanding of material properties. The relevant technologies encompass synchrotron radiation, x-ray optics, sample manipulation and applied variable measurement, x-ray imaging and data analysis.

Insofar as the dynamics and mechanism of phase transitions are concerned, TRXRD provides two important pieces of information: 1) transition kinetics obtained by following the relaxation of the system in response to an applied perturbation and 2) details of intermediates that from in the process. These data provide a basis for formulating, evaluating and refining transition mechanisms.

The TRXRD method is information-dense in the sense that an enormous amount of additional detail is provided in the course of the live-time measurements. Needless to say, the proposed mechanism must be consistent with such details. As an example, consider a TRXRD experiment conducted with a T-jump perturbation. The additional information gleaned from such an experiment includes: 1) the temperature dependence of the measured variable(s) in single and coexisting phase regions, 2) phase (and intermediate) lattice type and symmetry, lattice parameters, commensurability, 3) domain size, coherence length, disorder (in the form of diffuse scatter), 4) sample orientation, phase coplanarity, crystallinity, 5) reversibility, hysteresis in the transition temperature, phase type and lattice parameters, 6) continuous or discontinuous nature (order) of the transition, structural connectivity of adjacent phases, 7) temporality of changes in long- and short-range order, 8) cooperativity, thermal width of the transition, 9) lipid mixing, phase separations, and 10) temporal correlation of thermal events and structural rearrangements. Such a wealth of information supports the view that TRXRD is a powerful technique not only for establishing lipid phase transition kinetics but also for providing useful insights into transition mechanisms.

The experimental arrangement used by the author in making TRXRD measurements is shown schematically in Figure 1. The essential components of this system are the synchrotron source, monochromating and focusing optics, the sample, the detector and recording and image analyzing devices (2,3,6). The former includes an image intensifier tube, while the latter incorporates a charge coupled device (CCD) video camera, tape recorder and monitor and a digital image processor. Sample manipulation devices have been omitted from the figure for sake of clarity. It is emphasized that the system shown in Figure 1 represents but a single configuration and that there are many more possible arrangements. Furthermore, the experimental arrangement is constantly being modified, reconfigured and upgraded. Flexibility in terms of equipment and experimental design is one of the more critical aspects of successful TRXRD measurements.

A summary of the results to date pertaining to lipid phase transition kinetics established by TRXRD follows.

- Some lipid phase transitions are fast, occurring on a time-scale of milliseconds, while others are extremely sluggish requiring weeks to complete.

- Certain transitions are equally fast in the forward and reverse direction. Others have rates that differ by many orders of magnitude.

- Many of the transitions studied appear to be two-state in the sense that at any point during the transition only two phases co-exist (2,3,15). In contrast, other transitions are continuous, displaying a pronounced second order character (20) while others again reveal the presence of transition intermediates (3).

- While some transitions are readily reversible and non-hysteretic in phase type, lattice parameters and transition temperature, others are extremely hysteretic (2,3,15,20).

- For certain lipid systems, transition rates are independent of hydration, salt concentration, lipid identity, changes in the periodicity of the transforming phases and in long- and short-range order but are dependent on the magnitude and direction of the T-jump (2,3).

- Long-range order is preserved throughout many lipid phase transitions (2,3,15). This suggests that the transforming units remain coupled and undergo the transition cooperatively and that long-range order is established rapidly in the nascent phase. In contrast, other transitions involve an intermediate state devoid of long-range order. In such cases, the precipitous loss of the (ordered) phase undergoing change is accompanied or followed by the emergence of diffuse scatter and/or line broadening which sharpens up with time and eventually gives way to the ordered nascent phase (2,3,15,21).

- Depending on the system, temporal correlations of changes in long- and short-range order may (20) or may not (2,17) exist.

- In many of the transitions studied thus far, the interconverting phases appear to be incommensurate (2,3). This may reflect a bias toward the use of such systems which, by virtue of having distinct and well-resolved diffraction patterns, are more easily characterized.

- In certain systems, changes occur in short-range order without a corresponding adjustment in long-range order of the interconverting phases (20).

- In addition to rearrangements occurring during a phase transition, quite extensive and rapid changes take place within single phase regions. For example, the cubic phase unit cell volume in hydrated monoolein shrinks at a rate of 33% of its initial value per second during the course of a (66°C) T-jump (3). This implies facile lyotrope transport throughout the three-dimensional cubic network.

Despite the newness of the TRXRD technique, the data collected thus far show that a sizeable body of information has been gathered concerning the dynamics and mechanism of lipid phase transitions. Further, the data serve to illustrate the potential of this approach in revealing the molecular structure and compositional dependence of mesomorph stability and interconvertibility and, ultimately, the underlying transition mechanism.

References

1. Caffrey, M. 1984. Nucl. Instr. Meth. 222:329.

2. Caffrey, M. 1985. Biochemistry 24:4826.

3. Caffrey, M. 1987. Biochemistry 26:6349.

4. Caffrey, M. 1987. Biochim. Biophys. Acta 896:123.

5. Caffrey, M. 1987. Biophys. J. 51:444a (Abstract).

6. Caffrey, M. 1989. Annu. Rev. Biophys. Biophys. Chem. In Press.

7. Caffrey, M.., Bilderback, D. H. 1983. Nucl. Instr. Meth. 208:495.

8. Caffrey, M., Bilderback, D. H. 1984. Biophys. J. 45:627.

9. Caffrey, M., Bywater, M. T. 1988. J. Soc. Cosmet. Chem. 39:159.

10. Caffrey, M., Hing, F. S. 1987. Biophys. 51:37.

11. Caffrey, M., Mencke, A. 1988. CHESS Users Meeting, Cornell University, Ithaca, New York.

13. Grubb, D. T., Liu, J.-H., Caffrey, M., Bilderback, D. H. 1984. J. Polym. Sci., Polym. Phys. Ed. 22:367.

14. Gruner, S. M. 1987. Science 238:305.

15. Laggner, P. 1988. Topics in Current Chemistry. 145:173.

16. Luzzati, V. 1968. Biological Membranes, Physical Fact and Function. (Chapman, d., ed.) Vol. 1. pp 71-123, Academic Press, New York.

17. Ruocco, M. J., Shipley, G. G. 1982. Biochim. Biophys. Acta 691:309.

18. Shipley, G. G. 1973. Biological Membranes, (Chapman, D., Wallach, D. F. H., eds.) Vol. 2. pp 1-89, Academic Press, New York.

19. Small, D. M. 1987. Handbook of Lipid Research: The Physical Chemistry of Lipids from Alkanes to Phospholipids. Vol. 4. Plenum Press, NY, 672 pp.

20. Tenchov, B. G., Lis, L. J., Quinn, P. J. 1987. Biochim. Biophys. Acta, 897:143.

21. Tate, M. W. 1987. Equilibrium and Kinetic States of the Lα-HII Phase Transition. Ph.D. thesis, Princeton Univ., Princeton, 215 pp.

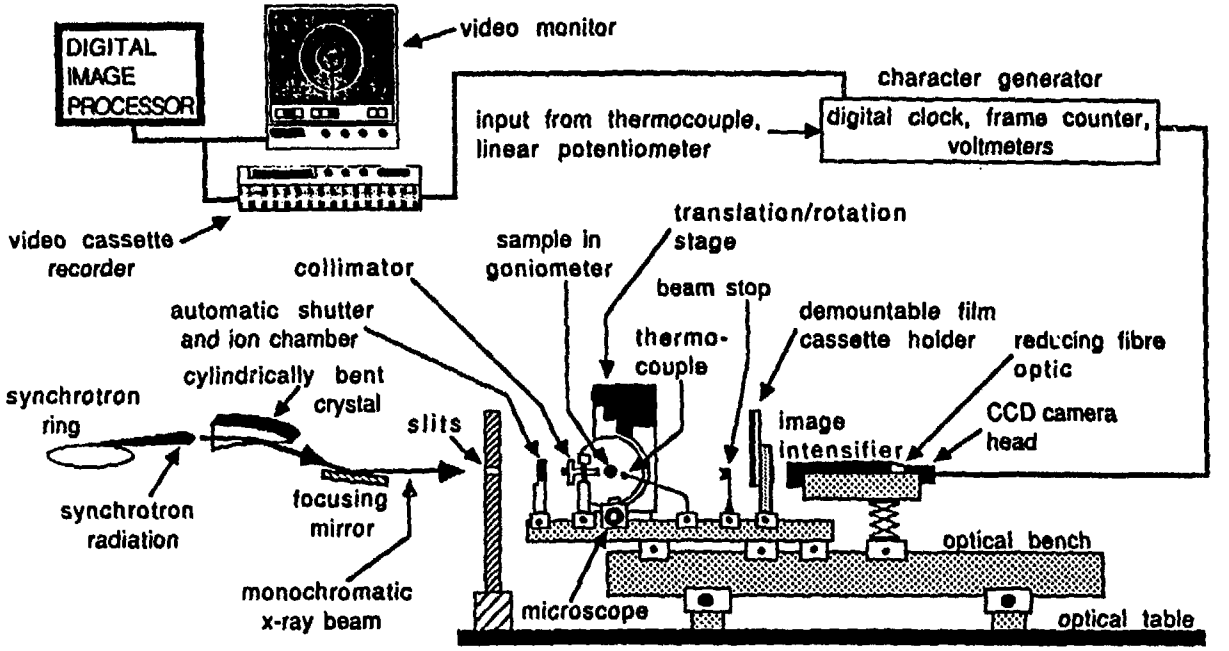

Figure 1. Schematic diagram of the experimental arrangement for monitoring x-ray diffraction in live-time using synchrotron radiation (not drawn to scale). White radiation from the synchrotron is simultaneously monochromatized (g = 1.57 Å , 7.9 keV) and horizontally focused by a 10 cm long, cylindrically bent germanium or silicon crystal. Higher order harmonic contaminants (g/3, etc) are eliminated and the 7.9 keV beam reflected and vertically focused by a 60 cm long nickel- or platinum-coated mirror. The monochromatic beam is focused to a point 1.5 mm wide x 0.2 mm high. X-rays diffracted from the sample are allowed to strike the fluorescent screen of a three-stage intensifier tube used for image intensification. The image is displayed dynamically on the intensifier tube and recorded using a CCD camera fibre optically coupled to the intensifier tube and a video cassette recorder. Lipid samples in glass or quartz capillaries are mounted in a goniometer on the low-angle diffraction camera. A thermocouple to monitor sample temperature is placed either in or next to the capillary as close to the x-ray beam as possible. Along with the two-dimensional diffraction image, the experiment number, elapsed time in seconds and frame number, sample temperature and incident intensity are recorded simultaneously on video tape. Typical operating conditions at the Cornell High Energy Synchrotron Source (CHESS) are as follows: electron beam energy, 5.3 GeV; three electron bunch mode with a total of 20-60 mA; repetition rate, 10^6 Hz; radiation pulse duration, 130 ps/electron bunch; total flux at the focal spot, 10^{12} photons s^{-1} (3 x 10^{10} photons delivered through a 0.3 mm diameter collimator).

SESSION V

TOPOGRAPHY AND IMAGING

The Application of Synchrotron Topography to Solid State Reactions.

MICHAEL DUDLEY, Department of Materials Science and Engineering, SUNY at Stony Brook, Stony Brook NY 11794.

Abstract.

The question as to the role of defects and generalized strain fields in solid state reactions occurring in single crystals has been the subject of an enormous amount of research over a period of many years. During this time, the techniques which have been most often employed in the endeavour to provide an answer to this question are optical microscopy and transmission electron microscopy. Unfortunately these techniques have inherent drawbacks which have restricted most conclusions which have been drawn in this area to being speculative or inferential. Nevertheless, these techniques have contributed greatly to this field. However, the prospects for vast enhancement of the extent of progress in this field have been greatly improved through the application of X-ray topographic techniques, particularly synchrotron topographic techniques. This paper discusses in detail the application of synchrotron topographic techniques to the study of solid state reactions. The advantages of these techniques over previously used techniques will also be discussed, as well as challenges for the future.

Introduction.

Over the years a considerable amount of interest has been generated in studying various topics relating to or derived from reactions which occur in the solid state. The growing importance of such reactions, which include, for example, organic solid state polymerization reactions and inorganic decomposition reactions (we will include solid state phase transformations in molecular crystals in the present discussion, albeit separately)[1] can be variously attributed to both technologically based driving forces on the one hand and purely esoteric research based driving forces on the other. In general, this growth has led to an increased demand for techniques capable of identifying the particular reactants, intermediates, and products, as well as providing information where possible on their respective internal structures and microstructures.

With respect to identification of species, the techniques of Electron Spin Resonance (ESR),[2] Electron Paramagnetic Resonance (EPR)[3] and Fourier Transform Infrared (FTIR) Spectroscopy have found widespread application.[3] With respect to internal structure, the demand has led to a resurgence in X-ray and electron structure determination techniques, with the necessity for particular emphasis to be laid on the need to avoid radiation damage or radiation induced reaction. Many of the reactions of interest occur only in the crystalline state, some only in single crystals, so that with respect to microstructure the demand requires imaging techniques capable of revealing crystallographic defect microstructures and general strain distributions in crystalline materials. In this context the impetus for microstructure determination is provided by the desire to determine the influence of crystalline defects and general strain fields on reaction mechanisms and subsequent reaction kinetics. Transmission electron microscopy (t.e.m.) has been widely used for such studies (for recent review see Ref.(4)), although the high potential of electron beam induced heating and damage in many molecular crystals (which, in some cases, can be overcome, to a certain extent, by the use of low voltages and cold stages[5]), can lead to only limited applicability. Damage potential, in addition to the potential for contamination in the microscope, usually rules out in situ studies of crystals undergoing reaction; a major failing of the technique which is still to be overcome. Nevertheless, useful information can be obtained before and after reaction has occurred (for example see Ref.(6)), although usually not on the same region of the same crystal. Further problems arise in t.e.m. due to the requirement for very thin specimens, which may be both difficult to prepare and perhaps may not be representative of bulk samples, although again this can be overcome in certain circumstances.[4] However, one unavoidable problem with the technique is its very small lateral field of view, which can make defect visualization in the relatively high quality crystals, which are desirable to be able

to discern the effects of defects on reactivity, a statistically difficult proposition. Generally, this small field of view makes it very difficult to obtain an appreciation of the changes that have taken place in the crystal as a whole, i.e. both on the surface and in the bulk. As a result of these various drawbacks some solid state chemists have turned to the technique of X-ray diffraction topography[7], hereafter referred to simply as topography.

The use of topography eliminates the need for sophisticated sample preparation procedures (crystals can, in some cases, be used virtually as grown, in other cases simple cleavage or cutting followed by washing usually suffices). Similarly the field of view can be made as large as required (anywhere from a few square centimetres up to hundreds of square centimetres, depending on the source). This, coupled with the vastly superior strain sensitivity of the technique compared to that of t.e.m. (which stems from the much weaker interaction of X-rays with materials, compared to electrons), makes the technique capable of discerning the potentially very weak long range effects of the localized strain fields which might be associated with the early stages of reaction, if reaction occurs heterogeneously, for example at defects. The weaker interaction of X-rays with materials compared to electrons also means that beam induced damage is generally less of a problem. As will be shown, the advent of bright synchrotron radiation sources, also opens up the possibility of conducting, real time, in situ studies of the influence of defects on single crystal reactivity.

Two main realms of topography have evolved over the years, those which utilize radiation from conventional X-ray generators (such as sealed tube or rotating anode generators) and those which utilize radiation from synchrotron X-ray sources. By way of introduction "conventional topography" will be described first, then "synchrotron topography" will be introduced along with its advantages.

Conventional Topography.

Generally speaking, topography is a diffraction imaging technique which is capable of revealing the defect microstructure in large (cm^3), near perfect, single crystal specimens. Several distinct techniques utilizing radiation from conventional generators have been developed. These include: the Berg-Barrett, Barth-Hosemann, and Lang Techniques, respectively (for a review see (8)). The most commonly used of these techniques is the transmission Lang technique. In this technique the crystal to be studied is set on a goniometer with the g vector of the intended diffracting planes lying parallel to the plane in which diffraction is to occur (usually the horizontal plane), and then oriented for diffraction of a $K\alpha_1$ characteristic line from these planes. The resulting diffracted beam is usually recorded on a

photographic detector. The angular resolution required to exclusively resolve this characteristic line is usually achieved by collimation of the incident beam via appropriately placed slits. This usually results in an incident beam which has been restricted to a thin vertical "sheet" of X-rays. Images recorded in this stationary configuration are known as section topographs since under the correct conditions one can discern a cross-sectional view of the defect content of the crystal. In order to get large volume coverage it becomes necessary to traverse the ensemble of crystal and detector in front of the incident beam. (It should be noted that the combination of drastic collimation and the necessity for translation usually leads to long exposure times). The image of the diffracted beam so produced, which is essentially a two dimensional projection of the diffracted intensity from the irradiated volume of crystal, constitutes a Lang or Projection X-ray topograph.

The real information available in an X-ray topograph is manifested in the form of contrast, so called topographic contrast, within the projected diffraction spot. This topographic contrast arises from differences in the intensity diffracted as a function of spatial coordinate inside the crystal. Diffracted intensity is a sensitive function of local crystal perfection. For example, highly mosaic regions of crystal will diffract kinematically, whereas more nearly perfect regions of crystal will diffract dynamically. Kinematical diffraction is characterized by an absence of the primary extinction effects which are the essence of dynamical diffraction. This leads to an increase in diffracted intensity with an increase in mosaicity, eventually reaching the limit of the "ideally imperfect crystal", as was nicely demonstrated by the work of White[9]. The difference between the intensities diffracted from one region of crystal which diffracts kinematically, and another which diffracts dynamically is one of the ways that dislocations can be rendered visible in topography (see later). However, the situation is not as simple as this. Even for a crystal which diffracts dynamically, the diffracted intensity is a sensitive function of the local distortion in the crystal. In addition, the type of contrast which arises from a particular type of distortion is also a function of the absorption conditions in the crystal. It will be a useful excercise to briefly review the contrast mechanisms which arise in topography. Particular attention will be paid to those mechanisms which give rise to dislocation images.

It is important to point out that the contrast from individual defects will only be discernible if the spatial resolution is adequate. There is no magnification involved in topography, due to the fact that no lenses (in the normal sense of the word) exist for X-rays, and spatial resolution is controlled solely by geometry. The geometrical factors arise as follows. With any kind of X-ray generator the source always has a finite size. For

example there is always a finite height to the source focal spot. Thus the possibility arises that at a given point in the crystal the diffracting planes will receive radiation at the correct Bragg angle, from several different points located at different heights on the focal spot. This imparts a finite vertical divergence to the diffracted beam, and hence gives rise to a blurring effect in the resultant image. The amount of blurring is proportional to the inverse of the distance between the crystal and detector. In the horizontal plane, diffraction occurs over a finite range of angles determined by the convolution of the crystal rocking curve width with the width of the K line. Effectively this finite acceptance angle means that a given point in the crystal receives radiation from a finite width on the source. This width can be determined by back projecting the fan of incident rays accepted at a point in the crystal, to the source itself. Again a finite divergence, this time in the horizontal plane, can be attributed to the diffracted beam, and again a blurring effect will be evident. However, as can be verified by simple calculation, the limiting factor in determining spatial resolution is the finite source height, rather than the finite effective source width.

Since the spatial resolution is inversely proportional to the distance between the crystal and detector, this distance should be minimized. However, the optimum spatial resolution of the photographic detectors typically utilized in topography is around 1 micron, so that the distance between detector and crystal is usually set to yield a calculated spatial resolution which approximately coincides with this. It should be noted that while this spatial resolution is greatly inferior to that of electron microscopy, it can be more than sufficient for the high quality crystals of many materials which can currently be grown, although admittedly, the growth of large near perfect crystals of some systems can prove to be an elusive task.

Before we enter into a discussion of topographic contrast mechanisms let us first introduce the technique of synchrotron topography.

Synchrotron Topography.

The advent of dedicated sources of synchrotron radiation has enabled the development of a new realm of topography, synchrotron topography. Synchrotron radiation has numerous advantages over conventional radiation when applied in topography. These advantages derive from the high brightness, tunability, and natural collimation of synchrotron radiation.

One of the most important synchrotron topographic techniques developed is White Radiation Topography.[10,11] This technique is basically analogous to the Laue Transmission technique, except with greatly enhanced capabilities which derive from the

aforementioned natural collimation and high intensity of the synchrotron beam. The natural collimation (typically $\sim 2 \times 10^{-4}$ radians in the vertical plane coupled with an acceptance angle of typically a few milliradians in the horizontal plane) allows the use of very long beamlines to maximize the area of the beam delivered at the sample without incurring significant losses in the total intensity originally available at the tangent point. This situation contrasts with that which would hold for the isotropic emission from a conventional source. The large beam area delivered at the sample location allows studies to be carried out on large scale single crystals, without the need for cumbersome translation mechanisms, such as those necessary in conventional topographic techniques. As will become apparent, this also opens up the possibility of carrying out in situ, dynamic experiments, a particularly important point when considering the application of the technique to the study of solid state reactions. Long beamlines also lead to small angles subtended by the source at points in the specimen, which in turn leads to excellent geometrical resolution capabilities. Thus, in summary, we have in a synchrotron source a large area X-ray beam, with inherent low divergence, and with excellent geometrical resolution capability.

Consequently, if a single crystal is oriented in this beam, and the diffracted beams recorded on a photographic detector, each diffraction spot on the resultant Laue pattern will constitute a map of the diffracting power from a particular set of planes as a function of position in the crystal with excellent point to point resolution (typically of the order of less than one micron). In other words each diffraction spot will be an X-ray topograph.

The excellent geometrical resolution capability has another important consequence since it relaxes to a certain extent the requirement of having very small specimen detector distances (<1 cm) in order to achieve good resolution. Thus, crystals can be surrounded with elaborate environmental chambers, necessitating considerable increases in specimen detector distances (which would lead to intolerable resolution losses in conventional systems), without significant loss of resolution. Again this is important if one is considering using the technique to study solid state reactions.

The high intensity over the wide spectral range of the radiation emitted has several important advantages. Not only are exposure times necessary to record a topograph drastically reduced from the order of days on conventional systems to seconds on a synchrotron, but since we have a white beam, a multiplicity of images is recorded simultaneously. This leads to an incredible enhancement in the rate of data acquisition. The multiplicity of images also enables extensive characterization of strain fields present in the crystal. For example, instantaneous dislocation Burgers vector analysis can become possible by comparison of

dislocation images obtained on several different Laue spots. Similarly, lattice rotation in the specimen can be characterized by analysis of the asterism observed on several different Laue spots. In addition the good signal to noise ratios obtained associated with the high intensity also open up the possibility of direct imaging of topographs. Thus it becomes possible to conduct truly dynamic, quasi real-time experiments making it particularly suitable for the study of solid state reactions.

Another important advantage of the white beam topographic technique over conventional topographic techniques, is its enhanced tolerance of lattice distortion. The wide spectral range available in the synchrotron beam, allows crystals which either exhibit a uniform range of lattice orientation (for example are uniformly bent by a small amount) or which contain several regions of distinctly different orientation (for example contain subgrains, grains or twinned regions) or regions of different lattice parameter (for example contain more than one phase) to be imaged in a single exposure. As already mentioned, analysis of Laue spot shape or Laue spot asterism (the deviation from the shape expected from an undistorted crystal) enables quantitative analysis of lattice rotation. Simultaneous measurement of the variation in diffracted wavelength as a function of position in the Laue spot, for example using a solid state detector, also enables determination of any variation in d spacing of the particular diffracting planes. It is also important to point out that useful microstructural information can often still be obtained from distorted Laue spots. Those crystals which exhibit a uniform range of lattice orientation give rise to either a magnified or reduced topographic image depending on whether the X-ray entrance surface is concave or convex. However, the local strain sensitivity of the technique is preserved, for example sensitivity to the strain fields around dislocations and precipitates and other defects. For those crystals which contain several regions of distinctly different orientation, each region of uniform orientation yields its own topographic image, which may, of course lead to image underlap or overlap, depending on the particular relative orientations. Again the strain sensitivity within each region giving rise to a topographic image is preserved. Similar effects to these latter are observed in the case of crystals containing regions of distinctly different lattice parameter. Thus the technique might be used to examine crystals which are being subjected to the internal distortion fields associated with the initiation and progress of solid state reaction.

By comparison, in the conventional topographic case the maximum tolerable range of misorientation is defined by the convolution of characteristic line width with the beam divergence. Since both of these quantities are small (typical line widths are of the order of 10^{-3} A, typically equivalent to an angular divergence of 0.5x10-3 radians, and typically, beam divergences

must be less than 10-4 radians in order to obtain the necessary angular resolution in the plane of diffraction), misorientations greater than a few arc seconds lead to the situation where only part of the crystal fulfils the diffracting condition at a given time. In other words Bragg Contours are produced, effectively giving blind spots in the crystal. Clearly this is a very undesirable situation if dynamic type studies of, for example, solid state reactions in large single crystals are to be conducted.

Contrast mechanisms operative in white beam topography are largely similar to those which are operative in Lang topography, with some notable subtle differences.[12] Some of these differences are due to the fact that in white beam topography one has the added complication of harmonic contamination which may lead to a situation where more than one contrast mechanism operates in a single topograph. Nevertheless, it is informative to review basic contrast mechanisms as being pertinent to both Lang and white beam topography, since differences encountered are usually the exception rather than the rule.

Contrast Mechanisms in Topography.

It is customary to classify topographic contrast mechanisms according to the absorption regime within which the experiment is being conducted. Absorption conditions are usually defined by determining the product of the linear absorption coefficient, μ, and the thickness of crystal, t, traversed by the X-ray beam, or simply μt. Generally three regimes of absorption are identified, low, intermediate and high, corresponding to μt values of < 1-2, 2-4, and >10, respectively. For convenience, each of these regimes will be dealt with separately, although, as will become evident, they are all interrelated.

(a) Low Absorption Conditions.

Topographic contrast mechanisms under low absorption conditions are by far the simplest to understand, and it is for this reason that topographers often strive to work within this regime, preferring to avoid the more complicated dynamical effects which can arise under higher absorption conditions. The main mechanism of contrast formation under these conditions is related to the presence or absence of primary extinction effects. As briefly mentioned earlier, in regions of crystal which diffract dynamically, primary extinction effects are operative, whereas in regions which diffract kinematically these effects are absent. The phase shifts associated with primary extinction effects lead to an overall reduction in diffracted intensity, so that the absence of primary extinction effectively leads to enhanced diffracted intensities. Consequently, if the mode of diffraction - dynamical or kinematical - varies as a function of location in the crystal, contrast should become evident according to these differences in diffracted intensity.

By way of illustration consider the distortion field around a dislocation in an otherwise perfect single crystal. It has been shown[13] that there is a region of crystal which surrounds the dislocation line where the distortion field is such that dynamical diffraction, along with its associated extinction effects, is no longer operative. Rather, the region behaves like a miniature mosaic crystal which is embedded in the parent crystal, and which diffracts kinematically. This effect can be quantified as follows. When a crystal diffracts dynamically it does so over a finite range of incidence angles, . This range is determined by the particular diffraction conditions, and is typically of the order of a few seconds of arc. Usually the divergence of the incident beam is somewhat greater than this, which means that typically only a small proportion of a given incident beam will actually undergo diffraction, with most of the incident beam passing straight through the crystal, and simply undergoing normal photoelectric absorption. However, if the undiffracted portion of the incident beam should encounter distorted regions present inside the crystal, it becomes possible that these regions be set at the correct orientation for diffraction of this portion of the beam, provided that their misorientation, or what the X-ray beam detects as a misorientation (see paragraph which immediately follows), is not greater than the incident beam divergence.

Basically, in diffraction of a monochromatic X-ray beam, there are two ways a distortion field can influence the local diffracting conditions; it can either change the spacing of the diffracting planes or change the orientation of the diffracting planes, or both. Both of these translate, as far as the incident beam is concerned, into a misorientation, as illustrated in the differential form of Braggs Law.

$$\Delta\theta = \Delta d/d \tan\theta \pm \omega$$

where ω is the contribution of lattice rotation to the misorientation.

It is usual to define this misorientation with respect to some reference orientation, such as the condition for exact fulfilment of the Bragg condition. This latter misorientation is referred to as the deviation from the exact Bragg condition, $\Delta\theta_B$. Generally an incident beam will not initially be set exactly in fulfilment of the Bragg condition i.e. it will start out in the perfect region of crystal with a finite deviation. Subsequently, a distortion field may give rise to a further deviation, and it is then customary to define an "effective misorientation", $\delta(\Delta\theta_B)$,[14] which is simply the change in the deviation from exact Bragg condition which is encountered by the incident beam as it traverses the crystal. If this effective misorientation is larger than the perfect crystal rocking curve width, yet smaller than the effective beam divergence, then the distorted region

will give rise to a new diffracted beam. Further, if the distorted region is small in size, as is the case for the volume of interest surrounding the dislocation, then the region itself should diffract kinematically. In addition, since the distorted region is misoriented with respect to the parent crystal the resulting diffracted beam will not be at the correct orientation with respect to the relevant perfect crystal planes to undergo the primary extinction effects which are otherwise operative. As a result the diffracted beam which emanates from the distorted volume of crystal will only undergo normal photoelectric absorption on passing through the crystal and will not suffer the effective enhanced absorption associated with extinction effects to which the diffracted beams from the perfect region of crystal are subjected. Hence there is an enhancement of diffracted intensity from this volume compared to the rest of the crystal, or topographic contrast. This is known as Direct or kinematical image formation. Note that in thicker crystals the diffracted beam from the distorted region will not survive the photoelectric absorption in the crystal, and thus the effect disappears.

(b) Intermediate Absorption Conditions.

As t increases, dynamical effects become more dominant, and the complexity of the operative contrast mechanisms increases. In order to be in a position to appreciate the phenomena involved it is useful here to review some of the basic principles of the dynamical theory of X-ray diffraction.

Brief Review of Basic Dynamical Theory.[15]

When a perfect single crystal is set for diffraction of a monochromatic X-ray beam of zero divergence, i.e. a plane wave, (which incidentally is not attainable in practice but it serves here to illustrate a point) from a particular set of planes, dynamical diffraction can occur. This differs fundamentally from kinematical diffraction in several ways. For example, in the case of kinematical diffraction of a slightly divergent beam from a mosaic crystal each incident ray is considered to undergo a single scattering event, so that for each such ray one can define a diffracted beam:- the incident beam is considered unchanged by each scattering event. Only single scattering events are considered since each individual crystal (i.e. each unit in the mosaic structure) is assumed to be so small that the diffracted ray escapes before having the opportunity to take part in a second scattering event, such as diffraction from the backside of the same crystal planes. However, in dynamical diffraction the single crystal units involved are larger, and multiple scattering events must be considered. In dynamical diffraction, it no longer becomes possible to distinguish between incident and diffracted beams inside the crystal. Instead, the incident (or forward diffracted) and diffracted components become coupled inside the crystal in a way that they lose their individual identities and can only be considered as a coupled unit or as a so called

wavefield, which propagates through the crystal. Each of these wavefields is made up of a superposition of plane waves corresponding to the aforementioned incident (or forward diffracted) and diffracted beams. These wavefields are a manifestation of the extinction effects discussed earlier. In simplistic terms these effects arise from the possibility that, in a perfect (or near perfect) crystal, the diffracted beam resulting from a single diffraction event may become an incident beam for a second diffraction event, and so on. This continues throughout the crystal, with the result that a complex cascade of multiple scattering events occurs from a single set of diffracting planes. In this way a complicated interference pattern is set up inside the crystal consisting of sets of coupled plane waves, or wavefields. Each of these wavefields represents a valid solution of Maxwell's equations inside the crystal. For an unpolarized incident beam there are four such solutions each one being a superposition of an incident and diffracted beam component.

These solutions are conveniently represented on a construction, known as the Dispersion Surface.[16] This construction involves a slight modification of the more familiar Ewald Sphere construction in that the excited reciprocal lattice points are located at the origins of the constructed spheres rather than at their surfaces. Initially, spheres of radius equal to magnitude of the free space wavevector of the incident beam are constructed. Then the effects of the average index of refraction inside the crystal are taken into account in constructing a set of concentric spheres (of shorter radius since the refractive index for X-rays is slightly less than unity). Away from the intersections of the spheres (the so called Lorentz point and Laue point) the directions and lengths of the wavevectors defining these spheres represent the situation when the incident beam is far from fulfilling the Bragg condition. As soon as the Bragg condition, i.e. the Lorentz point on the diagram, is approached, the wavevectors inside the crystal can no longer be represented on the spheres of radius k, rather wavevectors corresponding to the solutions of Maxwell's equations, i.e. the wavefields, are represented by so called Tie Points on the Dispersion Surface. This Dispersion surface consists of a hyperboloid of revolution of two branches each of which necessarily deviates slightly from the spheres. Note that there are two dispersion surfaces one for each polarization. For an incident unpolarized plane wave a tie point is excited on each of the two branches, of each of the two dispersion surfaces. Each tie point represents a single wavefield consisting of a superposition of an incident plane wave and a diffracted plane wave. The wavefields represented by these tie points only retain their identity whilst under the influence of the periodic potentials inside the crystal. As soon as this influence is removed (eg as the wavefield leaves the crystal), or is subject to an abrupt discontinuity (eg some kind of planar defect inside

the crystal, such as a twin lamella or stacking fault), the wavefields decouple into their incident and diffracted beam components.

Some important interference effects become evident inside the crystal as a direct result of the presence of these wavefields. It can be shown that the propagation direction for a wavefield is given by the direction of the normal to the dispersion surface at its Tie Point. Therefore if Tie points are excited in the center of each branch of the dispersion surface, the respective wavefields will have identical propagation directions inside the crystal. Since their wavevectors only differ by the vector joining the two tie points, interference phenomena ensue. These phenomena result in a spatial modulation of the wavefield and are collectively known as Pendellosung, after the analogy with the transfer of energy back and forth between coupled pendula, since they result in a periodic tranfer of energy back and forth between incident and diffracted beam components as the wavefield traverses the crystal. The planes of constant phase for this periodic exchange of energy are parallel to the crystal surface in the plane wave case, and the spatial period is known as the Extinction Length or alternatively, Pendellosung Length. Further beating effects can occur between the interference fields set up for each polarization. In addition to this modulation due to the wavevector components in the direction of propagation, there are further interference effects due to the components perpendicular to the direction of propagation, or normal to the diffracting planes. Standing waves result, one set for each branch of the dispersion surface. For a given polarization, the antinodes of these standing waves lie at the atomic planes for Tie Points on one branch of the dispersion surface, and inbetween the atomic planes for the other branch.

In reality all incident beams have a finite divergence, and as mentioned earlier, dynamical diffraction occurs over a very small range of incident angles. Therefore, if we consider an incident beam of finite divergence, only a small proportion of that beam will participate in diffraction, with the remaining components of the incident beam simply being transmitted through the crystal and undergoing only normal photoelectric absorption. This latter portion of the incident beam is often referred to as the direct or "transmitted" beam). However, the results briefly described for an incident plane wave generally hold true for an incident spherical wave,[17] since a spherical wave can be treated as a superposition of plane waves, so that a series of wavefields are excited simultaneously in the crystal. The Dispersion Surface is said to be completely illuminated. Analogous phenomena to Pendellosung exist due to interference between wavefields at conjugate positions on the two branches of the dispersion surface, although such phenomena exist over a wider range of angles than in the plane wave case. Since the wavevector difference between wavefields represented by the two branches of

the dispersion surface is now a function of tie point position, being a minimum at the symmetric position, the planes of constant phase for the periodic transfer of energy back and forth between incident and diffracted beam directions consist of a series of hyperbolic cylinders. If a section topograph is recorded from a parallel sided crystal, a set of parallel fringes corresponding to the intersections of this set of parabolae with the exit surface of the crystal will be observed. If the crystal is wedge shaped, hook shaped fringes will be observed, which are evidence for the intersection of the crystal surface with the parabolic planes of constant phase.

As mentioned earlier, in general when a wavefield reaches the crystal boundary, or exit surface, it decouples into its incident and diffracted beam components. For a given thickness of crystal, and at a given position on the exit surface, the proportion of wavefield which is made up of diffracted component determines the strength of the diffracted beam at that position. This proportion is determined by the position of the relevant Tie Points on the dispersion surface (see p.74, Ref. 15(c)). For a perfect crystal the Tie Point position is solely determined by the incident boundary conditions. However, for a imperfect crystal the local lattice distortion can modify the position of the Tie Point of a wavefield as it passes through the crystal. There are two mechanisms by which this can occur, depending on the nature of the distortion field encountered by the wavefield. These mechanisms are known as Tie Point Migration[18] and Interbranch Scattering.[19,20] Tie Point Migration occurs when the wavefield encounters a very shallow misorientation gradient upon passing through the crystal. It has been shown that in order for this to occur, the variation of the effective misorientation must be inferior to the rocking curve width, over a Pendellosung length, i.e. $G \ll \delta / \Lambda$, or $G = \beta \delta / \Lambda$, where β is of the order of a few tenths, or in terms of lattice curvature,[21]

$$\rho \gg \Lambda .$$

Interbranch Scattering occurs when the wavefield encounters a more abrupt distortion field, characterized by a steeper misorientation gradient. Wavefields undergoing Tie Point Migration follow a curved trajectory through the crystal, whereas wavefields undergoing Interbranch Scattering can be subjected to a more abrupt change in direction depending on the relative positions of the Tie Points on the original and subsequent branch of the dispersion surface.

In general then, the strength of diffracted beam recorded as a function of position on the exit surface of the crystal is determined by the detailed history of distortion fields encountered by all of the wavefields which converge on that position.

As an example consider the contrast which arises from dislocations under intermediate absorption conditions. The effect of tie point migration occurs in the long range distortion field of the dislocation, and can lead to either an enhancement or a reduction in diffracted intensity. This type of contrast can be used to determine the sign of dislocations. It should be noted that for a given distortion field of the type required to give rise to Tie Point migration, Tie Points on the two branches of the dispersion surface migrate in opposite senses, effectively cancelling out the effect. However wavefields associated with branch 1 of the dispersion surface suffer enhanced absorption and for situations of intermediate absorption asymmetry arises, and as a consequence, contrast. The effect of interbranch scattering can occur in the regions of greater misorientation gradient closer to the dislocation core. The new wavefields so created can potentially meet old wavefields before they exit the crystal, and in this way interference effects become apparent, which can give rise to fringe type contrast.This effect is only possible when tie points from both branches of the dispersion surface survive absorption in the crystal. Therefore at higher values of t, the effect disappears (see next section).

(c) High Absorption Conditions.

Contrast under high absorption conditions arises due to a local breakdown of the phenomenon of anomalous transmission, otherwise known as the Borrmann effect. As mentioned earlier, for each pair of wavefields associated with a the two branches of the dispersion surface there are two sets of standing waves parallel to the diffracting planes which arise. One of these standing waves has its antinodes at the atomic planes, and the other has its antinodes inbetween the atomic planes. It can be shown that for the case where the antinodes are located at the atomic planes the wavefield suffers absorption which is greater than the normal photoelectric absorption, and for the case where the antinodes lie inbetween the atomic planes, the wavefield suffers less than the normal photoelectric absorption. Thus it becomes possible to obtain diffracted beams in transmission geometry from crystals where calculated ordinary t values would predict effectively zero intensity. The possibility of this effect occurring only arises in perfect crystals so that any lattice distortion will lead to a breakdown of the effect. The sensitivity of this effect to local lattice distortion affords another mechanism of topographic contrast formation. For example, the breakdown of this effect in the distortion field of a dislocation gives rise to a relative decrease in local diffracted intensity, or a Borrmann dislocation image.[22]

Dislocation Analysis.

Topography, both synchrotron and conventional, is well suited for analysis of low densities (< 10-6 cm2) of dislocations in crystals. The restriction to low densities arises from the fact that topographic dislocation images are around 10-20 microns wide, so that greater densities would lead to image overlap and therefore loss of information. We have briefly reviewed the four possible types of dislocation image;- the direct or kinematical, the dynamical, the intermediary, and the Borrmann types of image. Much of the analysis of dislocations that has been conducted in molecular crystals has been done in the low absorption regime, using Direct images. For example Burgers vector analysis can be performed, using the familiar g.b =0 criterion for invisibility of screw dislocations, and the combination of g.b=0 and g.b x l=0 criterion for invisibility of edge dislocations. Using this basic approach, several groups have performed detailed analysis of the dislocations produced in crystal growth phenomena (see for example Refs.(23),(24)). In addition the projected directions of Direct dislocation images have been used very successfully to compare with line energy calculations designed to determine why particular line directions are preferred by growth dislocations in crystals (for review see (25)).

Applications of X-ray Topography to the Study of Solid State Reactions.

(a)Conventional Topography.

Conventional topography has been used by several workers to study solid state reactions [26,27,28] (as mentioned earlier solid state phase transformations in molecular crystals will be included in this discussion, but will be treated separately). The technique can be used, for example in solid state reactions, to characterize the initial defect structure in the reactive crystals. Following this the influence of subsequent treatment (thermal, radiolytic, photolytic) on the solid can be examined in detail. This can be achieved via the monitoring of the development of substructure at various stages in the reaction and the correlation of this substructure with the well-defined initial structure.

In solid state phase transformations conventional topography has also found application in, for example, the observation of domain formation, and also in the study of transformation kinetics via the monitoring of the advance of phase boundaries.[29]

However, limitations arise in the application of conventional techniques in conducting experimental studies of solid state reactions since such studies can generally only be conducted in a sequential manner; characterization, treatment, recharacterization, further treatment, etc. This is fine if the

reaction can be effectively frozen for the duration of the exposure, something which is not always possible in solid state reactions. In phase transformations, if temperature control is adequate, phase boundaries can be effectively frozen into position, so that time lapse topographs can be recorded. However even here, the long exposure times necessary, even with rotating anode generators, can lead to problems. For example as pointed out by Klapper et al[29], phase boundary movements due to temperature fluctuations may blur contrast and obscure important information.

Another major disadvantage of the technique (as outlined in earlier) is its very low tolerance of lattice distortion. This can become particularly problematic in solid state reactions, where reaction induced strains, or sometimes strains present in the crystals prior to reaction, can lead to the formation of Bragg contours, i.e. prevent imaging of large volumes of crystal, and thus lead to the presence of "blind spots" in the crystal. This was found to be the case by Begg et al in their studies of the decomposition of sodium chlorate monocrystals, where as soon as reaction progressed beyond around 1 per cent conversion, the lattice was seen to twist beyond the acceptable mosaic spread. However useful information was obtained at lower conversions. Detailed discussion of this work will be postponed until later, following discussion of preferential reactivity at dislocations. Formation of Bragg contours also posed similar problems for Schultz[26], and also Rosemeier et al[27] in their studies of diacetylene polymerization.

In summary then, while useful studies have been conducted using the conventional technique with the sequential methodology, the technique of synchrotron topography is much more ideally suited to the task for several important reasons;-
(a) White beam topography has an enhanced tolerance of lattice distortion over conventional topographic techniques.
(b) The improved resolution capabilities enable the crystal to be surrounded by elaborate environmental chambers, which might be needed to induce reaction, with tolerable loss in resolution.
(c) The high source brightness and subsequently short exposure times (typically of the order of seconds) enable in situ dynamic studies to be conducted.
(d) The spot positions in the Laue pattern itself can yield important structural information, about the phases involved i.e. reactant and product phases.
(e) Distortions in spot shape (asterism) can yield useful information on lattice rotations, without necessarily obscuring microstructural information within the Laue spot.

Thus, not only is it possible to characterize crystals prior to reaction, using a series of topographs recorded simultaneously as a Laue pattern, but it is also possible to monitor the contrast present in these topographs, in either a continuous or time

lapsed manner, during induced reaction. At the same time the spot positions and any spot distortions, afford information on the phases present, and induced lattice rotations, respectively.

(b)Synchrotron Topography.

Synchrotron topographic studies of solid state reactions can be conveniently divided into two main categories,
(1) studies of the effects of grown in and mechanically induced defects and general strain fields on single crystal reactivity, and (2) studies of phase transformations in single crystals, exploiting the phase identification capability of the Laue patterns. Often these two categories are combined in a single study, although for the purposes of this description they will be treated separately.

(1) The effects of grown in and mechanically induced defects on reactivity.

Over the years, numerous observations have indicated that solid state reactions very often nucleate and grow from specific sites in a crystal. In some cases optical microscopic examinations have been used to identify these sites as dislocations. However, due to the nature of the technique, such examinations have been confined for the most part to surface examinations. For example etching techniques have been used to reveal the emergent ends of dislocations. Subsequently reaction has been shown to initiate at equivalent sites and to progress at a rate proportional to their concentration.[30,31,32,33,34]

Similarly electron microscopic techniques (for example, t.e.m. and replica electron microscopy) have been used in such studies, although since in situ studies of crystals undergoing reaction remain elusive,[6] conclusions remain largely inferential. For example the absence of contrast arising from separation of phases or the presence of interfaces was used by Jones as the criterion to decide whether or not the polymerization reaction in DSP had occurred heterogeneously at defect sites. Meanwhile in the same system, Meyer et al using the technique of replica electron microscopy, found that by subliming unreacted monomer away from irradiated crystals, islands of polymer remained, indicating heterogeneous reaction, presumed to occur at dislocations. The indirect and inferential nature of both of these observations is evident and is symptomatic of the fact that in neither case was it possible to conduct in situ studies. The contradictory nature of these results and the question of homogeneous or heterogeneous reaction have yet to be resolved.[35]

The use of synchrotron topographic techniques on the other hand enables in situ studies to be undertaken of the role of the bulk defect structure and general distribution of localized strain fields in crystals undergoing solid state reactions. White beam

synchrotron topography is the technique best equipped to achieve this, although the elegant work of McBride,[3] using EPR and FTIR deserves mention at this point. McBride has used the FTIR frequency shifts experienced by intermediates generated during reaction to calculate the stresses to which these specific molecules are being subjected. EPR was used to determine the relative dispositions of species generated during reaction. However, these techniques are not capable of imaging the defect content of crystals, and so no assessment was made as to the role played by defects in reactivity. The strain sensitivity of synchrotron topography is unsurpassed in this field, since not only does it render visible the defect content of the crystal, but it can monitor the generation of defects and/or localized strain fields during progress of reaction. In this way in situ studies of preferential reactivity at dislocations can be undertaken. The development of the strain fields due to any inhomogeneous reaction which might occur can be observed directly during reaction, in contrast to the indirect electron microscopic evidence based on post-reaction observations of the manifestations of inhomogeneous reaction.

When considering the role played by dislocations in reactivity, it has been recognized by several workers that in the distortion field of a dislocation, a different stereochemical arrangement of ions or molecular groupings might be formed which may be more favorable to reaction. Such stereochemical arrangements may also act as traps for excitation energy, as well as providing favorable reaction configurations. As postulated by Thomas and coworkers, both undissociated and extended (dissociated) dislocations can be important from both these points of view. For example, in the case 9-cyanoanthracene, in order to explain the observation of the trans as opposed to the cis dimer, it was postulated that a particular stacking fault bounded by partial dislocations could bring the lattice into the required registry.[36] Exciton trapping at such defects would then ensure preferred reaction. However no such faults were observable by transmission electron microscopy,[37] and the observation of the trans dimer remains unexplained. In the meantime, electron microscopic observation of the undissociated dislocations present in crystals of p-terphenyl, which is closely related to anthracene but more beam stable, affords insight into possible ways in which similar defects in anthracene itself can lead to the formation of the topochemically forbidden dimer. Again, it is thought that excitons migrate through the crystal and are trapped at the dislocations which thus favor the production of the dimer.[38]

However other factors can become significant in determining whether or not preferential reaction occurs at dislocations, depending on the reaction of interest. For example, one might envisage a situation where growth dislocations could be decorated with impurity atoms or molecules. The modified chemistry resulting from this may be conducive (or prohibitive) to

reaction.

Beyond this it has been customary to simply regard the dislocation as a high energy site in the lattice and therefore to assign to it the potential for enhanced reactivity. There has been much discussion concerning the detailed mechanism by which this occurs. Among the most important questions discussed relates to whether the core energy or the strain energy of the dislocation plays the most important role in modifying local reaction kinetics. Faced with this situation, the solid state chemist can benefit very much from the detailed studies conducted by materials scientists and elasticians regarding the role of dislocations in solid state phase transformations in metals.[39,40,41,42] Using this as a basis, let us briefly review the possible reasons why dislocations, in particular the energy (strain and/or core) associated with dislocations, might play a role in reactivity. Meanwhile, it is recognized that the aforementioned factors of stereochemistry, the energy trapping capability resulting from this stereochemistry, and impurity decoration can also be of greater or lesser significance, depending on the particular reaction of interest.

The possible role played by the energy associated with dislocations in the reactivity of a single crystal depends on the nature of the reactants, intermediates (where relevant), and products involved, and also on the detailed reaction mechanisms which are operative. We will consider two kinds of reaction here; solid state polymerization in diacetylenes, and inorganic decomposition reactions of the kind,

$$A(solid) \longrightarrow B(solid) + C(gas).$$

The solid state polymerization reaction which we will consider in detail is that of the diacetylene PTS, which is a single crystal to single crystal reaction. With regard to mechanism this reaction is thought to be governed by the topochemical principle. The decomposition reactions which we will consider are the decomposition of sodium chlorate and the dehydration of nickel sulphate hexahydrate, which can be considered to be single crystal to polycrystal plus gas, or single crystal to amorphous (crystallite size too small to yield diffraction peaks) plus gas. These reactions can be modelled using a classical nucleation and growth mechanism.

However it will be shown that there can be significant areas of overlap between treatments valid for these two general mechanisms, in that some of the fundamental concepts which come into play during nucleation and growth reactions in the solid state, can also be applied to topochemical reactions.
These areas of overlap derive from the obvious fact that all reactions in solids are subject to significant degrees of spatial restriction. As a result, whenever reactions (or phase

transformations) occur in the solid state, the volume changes (for example, per molecule) that inevitably take place lead to the generation of stresses and strains in either reactant or product (or both), especially if the reaction occurs heterogeneously, although some strain effects will also be present even if reaction occurs completely homogeneously. These effects can be taken into account as follows.

Let us first consider the case of the single crystal to single crystal polymerization of PTS, occurring in a dislocation free crystal. When reaction occurs the product crystal structure must form in the presence of the reactant crystal. In other words a "nucleus" of polymer must form against the constraints of the "matrix". It is well noted that, the solid state polymerization of diacetylenes, nucleation as such does not occur. Rather, groups of product molecules, or oligomers, form a solid solution in the monomer crystal. Nevertheless the same arguments with respect to formation of product against the constraints of the matrix will hold (Baughman used this as a basis for describing the kinetics of diacetylene polymerization[43]). When this occurs, the matrix and/or nucleus, depending on the magnitudes of the relevant elastic moduli, must undergo elastic (or sometimes plastic) deformation. In this way elastic energy, or strain energy, is stored in the system, and the system must do work. This additional work generally makes it more difficult for reaction to occur, for example, it can increase the effective initiation barrier by an amount equal to the strain energy term. It is worth noting here that this concept of the distortions associated with reaction occurring against the constraints of the matrix was considered in a very qualitative manner by Cohen with regard to photolytically induced reactions.[44] Cohen introduced the concept of a reaction cavity within which the molecular movements and distortions required for reaction must take place. The strain energy approach traditionally adopted by materials scientists in studying solid state phase transformations in metals, which is described above constitutes a very useful quantification of this reaction cavity concept.

In the case of preferential polymerization occurring in the vicinity of a dislocation, some of the reaction induced strain, can be relaxed by the presence of the strain field of the dislocation. For example if a lattice dilatation is normally required of the matrix (i.e. in the absence of the dislocation) for reaction to occur, reaction might occur more readily in the region of the dislocation strain field where the lattice is already dilated. In this way the strain energy term can be effectively reduced, thereby making reaction more probable. This effect can be quantified by computing a so called elastic interaction term, which simply computes the elastic energy change which occurs when a nucleus forms in the presence of a dislocation. Since we are considering a single crystal to single crystal reaction, the dislocation exists in both reactant and

product crystal. Therefore, since there is usually a change in elastic properties associated with a reaction, there will also consequently be a change in the line energy of the dislocation. This constitutes a second contribution to the elastic interaction term.[41] This contribution can be positive or negative depending on the reaction. One further term which should be included is the change in core energy experienced by the dislocation.[42] This is much more difficult to calculate, and at best only its sign and approximate magnitude can be estimated. Generally if the total interaction energy term is negative the possibility arises that it may influence the effective initiation barrier and as a consequence promote preferential reactivity. The probability of such preferential reactivity should increase as the magnitude of this negative term and its influence on the initiation barrier increase. It should be noted that in the radiation induced polymerization of PTS (photolytic, radiolytic etc.) there is effectively no initiation barrier since the photon energy promotes the ground state reactant molecules to an excited state which usually far surpasses any such barrier. Consequently, it is unlikely in such cases that the interaction energy term would have any influence on initiation processes. Similarly, unlike the case of anthracene and its derivatives, in PTS the trapping of energy at dislocations is not expected to be significant.[45] Therefore dislocations are expected to play no role in radiation induced solid state polymerization of PTS. However, on the other hand it is expected that dislocations can play an important role in thermally induced reactions, where there is an effective initiation barrier which may be influenced by the elastic interaction energy term. Early evidence supporting this claim can be found in the work of Schermann et al.[45]

The elastic interaction term can be computed as follows. As is customary in phase transformations, one can define a "stress free reaction strain" which would correspond to the structural changes undergone by the reactant crystal if it were allowed to tranform to product crystal without any constraints from it surroundings (i.e. the matrix). Using this concept, Eshelby[46] has defined the first contribution to the elastic interaction term as;

$$W1 = -\int_V e^T_{ij} \; \sigma^d_{ij}$$

Where e^T_{ij} is the stress free transformation strain, σ^d_{ij} is the stress field of the dislocation, and V is the volume of the "inclusion". Clearly the magnitude and the sign of W1 will depend on the precise nature of the stress free reaction strain, and the dislocation of interest. The form of the second contribution to the elastic interaction term, involving the change in line energy of the dislocation during reaction can be be found in Ref. 41. The magnitude and the sign of W2 depends on the nature of the change in elastic properties experienced by the crystal during

reaction.

For the case of reactions which are single crystal to amorphous, such as some solid state polymerization and dimerization reactions, the situation is slightly different in that the dislocation can only be defined in the starting crystal, since in this case there is no simple structural relationship between reactant and product. Following the work of Cahn,[40] if preferential reactivity occurs around dislocations, it is customary to then assume the strain energy of the dislocation is released into the lattice as free energy, and in this way can aid the initiation process. In all cases, energy is released and so the contribution to the total free energy of the system is negative. However, as pointed out by Gomez-Ramirez and Pound,[42] there is also an interaction energy term to compute, since the displacement field due the formation of the precipitate of product interacts with that of the remaining dislocation segments in the reactant crystal. The loss of core energy should also be included, although this has been ignored in previous treatments since it is expected to have a negligible influence on the state of disorder in the product. Again, these strain energy terms are expected to have no influence on initiation barriers in radiation induced reactions for the reasons outlined above, although such influence is again expected in thermally induced reactions if the strain energy term is comparable to the relevant effective initiation or nucleation barrier. As an example, t.e.m. observations of the single crystal to amorphous photoinduced dimerization reaction in 9-cyanoanthracene showed no evidence for preferential reactivity at dislocations, although basal dislocations present do seem to exert some influence on the shape of the islands of amorphous photoproduct.[37] The author is aware of no topographic experiments reported to date to test the above hypothesis, although studies of the solid state polymerization of hexadyiene diol and other diacetylenes are currently being undertaken.

As mentioned earlier, for the case of single crystal to polycrystal (or amorphous state) plus gas, which applies to many solid state decomposition reactions, classical nucleation and growth theory can often be directly applied to describe the reaction kinetics, although one must be careful to account for the fact that one of the components is rapidly removed from the locus of reaction. As pointed out by Young[47] the molecular volume of the solid product phase is usually smaller than that of the reactant (with some exceptions), giving rise to a strain energy term. Clearly, in this case, as well as considering volume changes occurring in the solid reaction components involved, one must also consider the evolution of gas during reaction which may become trapped in the lattice. Generally, as pointed out by Young,[47] energy trapping probabilities of excited species, and the possibility for escape of the gaseous product are major influences on the locus of nucleation in solid decompositions.

Generally, the diffusion of gas molecules may be influenced by the stress field of a dislocation, or of other defects, causing segregation. This kind of interaction could occur after the initiation process, and could potentially constitute a secondary source of interaction between reaction products, this time gaseous, and dislocations. In such cases, even if dislocations played no role in the initial nucleation process, they may become involved at a slightly later stage via this type of process. In cases where this occurs, it is expected that it should occur irrespective of how the reaction was initiated, i.e. thermally or using radiation.

To illustrate the effects described above for a single crystal to single crystal reaction, we will consider the work of Dudley et al, applying white beam synchrotron topography to the study of the solid state polymerization of the diacetylene PTS.[48,49,50,51,52,53,54] This polymerization process can be effected using UV radiation, X-radiation, Gamma radiation, heat, and mechanical stress. According to the arguments outlined above, and also as borne out by the earlier work of Schermann et al,[45] dislocations are not expected to influence reactivity in radiation induced reaction, although they are expected to play a role in thermally induced reaction. How this claim is supported by the synchrotron topographic observations will be described shortly, however the detailed experimental set up deserves brief mention first.

The basic premise to the use of synchrotron topography in investigating the role of dislocations and other defects in the polymerization of PTS is the ability to be able to detect, in a non-destructive way, the generation of inhomogeneous strain fields which would be associated with differential reaction rates at the defect sites. Since polymerization can be effected by X-radiation, it would appear at first sight that X-ray topography could not be used as a non-destructive technique to monitor strain fields generated during reaction. However the potential problem of unwanted X-ray induced polymerization can be effectively eliminated by filtering the incident synchrotron white beam to remove the more highly absorbed, and therefore more damaging (i.e. more effective in inducing reaction) longer wavelength components. The resultant incident beam spectrum is still sufficiently broad to be able to record a partial Laue pattern, although the removal of the longer wavelength components inhibits X-ray induced reaction sufficiently that the crystal can be exposed to the filtered X-ray beam for several hours without introducing any unwanted radiation induced effects (see figures 1-5 for the effects of filters on the incident beam profile and the energy absorbed as a function of depth into the crystal). In this way the filtered synchrotron beam can be used as an effectively non-destructive investigative probe to monitor, in situ, the potential generation of defects and/or localized strain fields during reaction induced by UV radiation, Heat, and

even the X-ray beam itself (by selective removal of filter material; aluminum filters are used). In the latter case of X-ray induced reaction, filtering also enables the distibution of X-ray energy as a function of depth to be rendered almost completely uniform, minimizing stresses generated by inhomogeneous reaction occurring as a function of depth in the crystal. In all experiments topographs were recorded on relatively fast X-ray film, in a time lapsed manner to minimize X-ray exposure.

As mentioned earlier, should preferential reaction occur around dislocations, a localized strain field is expected to be set up due to the volume change which occurs upon polymerization. As pointed out earlier, no nucleation is expected, merely a volume in which reaction is more advanced than neighbouring regions i.e. a more dense solid solution, since polymer forms a solid solution in monomer. The long range effects of this strain field would be expected to affect the propagation of X-ray wavefields through the crystal, and therefore should give rise to topographic contrast within the Laue spots. Analysis of the variation of this contrast on different reflections should enable some characterization of the strain field. Eventually the strain field is expected to anneal out as reaction in the bulk "catches up" with that in the vicinity of dislocations, or perhaps via other mechanisms such as crack propagation. On the other hand if no preferential reaction occurs then no such localized strain fields should be induced, and therefore no such contrast within Laue spots should be discernible. The Laue pattern of the monomer structure is expected to distort gradually into that corresponding to the polymer structure.

Results obtained comply with the above models. For example in the X-ray induced reaction, no contrast changes are discernible within the Laue spots during reaction. This can be seen by comparison of figures 6(a) and (b). The detailed defect structure of the polymer crystal is shown in figures 7-10. The Laue pattern of the monomer distorts in a continuous manner into that of the polymer (see figure 11), with the exact defect structure present in the monomer being frozen into the polymer crystal. The extra asterism visible in the figure arises from the slight residual non-uniformity of the absorption profile of the X-rays as a function of depth, despite the filtering, leading to a slightly faster reaction rate on the entrance surface than the exit surface. As a result, a strain field ensues which, in the case of filtered radiation) tends to slightly bend the crystal (this bending is much more severe in the case of unfiltered radiation). This strain manifests itself as lattice curvature which shows up as asterism on the laue pattern. Note that microstructural information is preserved on topographs recorded throughout most of the reaction.

On the other hand in the thermally induced reaction, well defined contrast becomes discernible within the Laue spots during

reaction, as shown in figures 12 and 13. This contrast, due to preferential reaction in the vicinity of a group of growth dislocations, anneals out as reaction progresses and is eventually fully relaxed via the formation of microcracks. That this contrast is indeed due to preferential reaction was verified by examining the strain field due to a small island of polymer which was deliberately introduced into a similar dislocated region in a similar crystal by irradiation with a filtered synchrotron beam through a pinhole collimator. This contrast was found to be of identical form to that which becomes evident during thermally induced reaction (see figures 14 (a) and (b)).

Semi-quantitative (due to insufficient elastic constant data) strain energy calculations similar to those outlined above have been performed for this case,[54] and these confirm that the dislocations of the kind observed in PTS (mixed dislocations with Burgers vector [010]) should play a role in relaxing reaction induced stress, and therefore should promote reaction.

With regard to applications of synchrotron topography to single crystal to amorphous or polycrystalline reactions the only work of which the authors are aware concerns the solid state polymerization of hexadyene-diol, (M.Dudley, and J.N. Sherwood, unpublished work) although poor crystal quality has prevented conclusive experiments.

With regard to single crystal reactions where gases are evolved the potential of the topographic technique is clearly demonstrated by the detailed work of Begg et al[28] on the thermal decomposition of sodium chlorate single crystals using conventional topography. Although the strain induced during this reaction prevents monitoring of reaction beyond about 1% conversion, the information obtained in the early stages of reaction serves as a excellent example of the applicability of the general topographic technique in problems of this nature, while at the same time defining the limitations of conventional topography, thereby providing impetus for the subsequent application of synchrotron topography in this area.

In this work Begg et al found no evidence for preferential reaction occurring at dislocations, rather evidence for preferential reaction occurring at "strained volumes" in the crystal was obtained. This evidence initially consisted of the modification of the strain field associated with the original strained volumes, discernible as a change in contrast. The nature of the original contrast from these strained volumes indicates that the "inclusion" or "precipitate" responsible for the strain, occupies a smaller volume than the space provided for it by the crystal. In other words the surrounding lattice is under tension. It was speculated that the original strain centers could be impurity centers or vacancy clusters, both of which may have the correct kind of strain field associated with them. Another

possibility which was not considered, was that these strain centers could be germ nuclei which were present in the crystal initially, following localised decomposition which may have occurred at low temperature before the decomposition proper, or following decomposition during heating to the proposed decomposition temperature (as pointed out by Young[47] these germ nuclei may have originally formed at vacancy, interstitial or impurity clusters). This possibility would perhaps be just as feasible, since these too would have the correct kind of strain field associated with them (the volume per molecule in the solid component of the product phase is likely to be smaller than that of the reactant phase). Following the initial contrast change, observations indicated that as reaction progresses dislocation loops are punched into the lattice surrounding the strained volumes, as the strain energy associated with the nucleation processes occurring in the vicinity of the interfaces of the germ nuclei is relaxed via plastic deformation, which becomes possible at the elevated reaction temperature (sodium chlorate is brittle at room temperature).

In this case it appears that the volumes surrounding the precipitates are preferred to those surrounding dislocations, as far as promoting preferential reaction is concerned. If, as suggested earlier, these precipitates are in fact germ nuclei, then interfacial energy considerations would predict that reaction should occur preferentially at the interface between reacted and unreacted volumes, and this would explain the observed effects. On the other hand strain energy considerations would predict that reaction would be more difficult in the dilated regions surrounding the germ nucleus, since compressive rather than tensile stresses would be required to relax reaction induced stresses. Therefore, even though interfacial energy considerations would favor reaction at the interface of the precipitates, such reaction will lead to even greater stresses than would occur in the perfect crystal. This constitutes an argument in favor of the germ nuclei hypothesis, since the gain with respect to interfacial energy obtained in the case of the germ nucleus would not be obtained from vacancy, interstitial, or impurity clusters. However, the topographic evidence clearly shows that these reaction induced stresses are relaxed via plastic deformation which becomes possible at the elevated reaction temperature. On the other hand, there is another important consideration, that of generation of gas during reaction. The stresses generated by the presence of gas would be readily relaxed in the dilated regions surrounding the "germ" nuclei. Overall, the combination of favorable interfacial energy considerations, the possibility of plastic deformation to relax the stresses generated during the solid to solid part of the reaction, and the ready accomodation of gas in the regions surrounding the germ nuclei, lead to conditions conducive to nucleation in the vicinity at these sites in the crystal. This analysis, coupled with the observation that the growth

dislocations do not appear to become involved in reaction, may provide evidence that in this particular reaction, strain energy developed due to the volume changes incurred in the solid components is not the all important factor in determining sites for nucleation of reaction, but that a combination of several factors comes into play. If in fact solid state strain energy alone were the controlling factor, one would first of all not expect to see preferential reaction at the precipitate sites, and secondly one might expect to see some nucleation at dislocation sites as well as precipitate sites. However, one should also note that the potential for relaxation of volume stresses may not be as great at dislocation sites, as it is at precipitate sites, both from an elastic and plastic point of view. For example, the dilatation around the precipitates may be greater in both magnitude and extent than that around dislocations. Similarly, the relative ease for relaxation of the reaction induced stresses via plastic deformation may be easier at the precipitate sites than at growth dislocation sites.

Among the synchrotron topographic studies of decomposition reactions the work of Sheen et al[55] and Herley et al[56] deserve mention. In the work of Sheen et al synchrotron topographs recorded during X-ray induced dehydration of, for example nickel sulphate hexahydrate single crystals showed evidence for strain centers which appear throughout the crystal. These strain centers, which resemble those observed by Begg et al in sodium chlorate (adding further weight to the germ nuclei argument presented above), are likely to be nuclei. Sheen et al claim that some of these were located at specific points along dislocations and along growth horizons in the crystal, although many also seem to nucleate in perfect regions of crystal. In this case no evidence for relaxation of reaction induced stresses by plastic deformation was observed, which, as pointed out by Sheen et al[55], is what one might predict from the brittle nature of this material at room temperature.

Previous studies of thermally induced dehydration of nickel sulphate hexahydrate[57,58], showed that surface dehydration patches were readily formed at sites equivalent to those giving rise to etch pits corresponding to the surface intersections of dislocations of both screw and edge character (although the authors admit that etch pits may also have been formed at impurities or point defect clusters[57]), and also at cleavage steps. However, the same behaviour as that which occurs in the thermal reaction may not necessarily be expected in radiation induced reactions.

The observations of Sheen et al of strain centers which develop close to dislocations during the X-ray induced dehydration might presumably be caused by a lowering of the effective initiation barrier promoting preferential reaction, due to the solid state strain energy effects described above. Alternatively the

dislocations could act as energy trapping sites, thereby promoting reaction in their vicinity. Another possible explanation, in the light of the arguments presented earlier concerning radiation induced reactions, would be that the formation of these strain centers is associated with the secondary interaction of the gaseous reaction product with the dislocation strain field. Similar studies (using a filtered synchrotron beam to minimize X-ray induced effects) of vacuum dehydration, brought about by pumping, showed that no such strain centers could be associated with dislocations. In this case it is claimed that dislocations play no role in this reaction. Since the only one of the three possible explanations presented above for the X-ray induced reaction which can be discounted in the vacuum dehydration is the energy trapping capability of the dislocations, this latter observation may provide evidence in favor of the energy trapping argument for the X-ray induced reaction. However, it is possible that a small degree of X-ray induced reaction occurred during the topographic exposures recorded during vacuum dehydration which would detract somewhat from this argument.

In the white beam topographic work of Herley et al no evidence for any preferential reactivity around dislocations was observed in either the UV or X-ray induced decomposition reactions in single crystals of sodium nitrate. Also no multiplication of defects upon gamma irradiation was observed contrary to previous studies, where an increase in etch pit density was attributed to the plastic deformation resulting fron the strain induced by oxygen being trapped in the lattice. Generally, attempts to correlate etch pits with dislocation images on topographs were successful for some of the pits, but unsuccessful for the majority. As a result it was suggested (similarly to Thomas et al[57]) that some of the pits could be due to defects other than dislocations, such as, for example, point defect clusters or gas bubbles. The latter possibility would explain the previously observed increase in etch pit density with gamma irradiation. However, it is always possible that some of the pits may be due to dislocation loops near the surface of the specimen (perhaps introduced by handling) which are too small to be resolved by topography.

Similarly no evidence was found for preferential reaction at dislocations in the X-ray induced decomposition reaction of ammonium perchlorate, although experiments were hampered by the instability of the crystal to irradiation by the synchrotron beam, even when filtering was employed. In the case of the thermally induced decomposition of ammonium perchlorate no conclusions could be drawn as to the role of microstructure due to acceleration of the decomposition process by irradiation in the synchrotron beam. In this case time lapsed methodology similar to that employed by Dudley et al in PTS may improve the prospect of detailed analysis.

To illustrate the application of synchrotron topography in solid state phase transformations in molecular crystals, the work of El-Korashy et al[59] on the study of modulated phases in nearly perfect single crystals of tetramethylammonium tetrachlorozincate has been chosen. Using a pinhole collimated white beam well resolved satellite reflections consistent with the superspace groups postulated to describe the structures formed during phase transformations which occur in these crystals. This is an excellent illustration of the application of the structural identification capability of the technique. Topographs were also recorded by increasing the area of the incident beam, and revealed interesting anomalous transmission or Borrmann images of dislocations.

Future Prospects.

The advances made through the application of Synchrotron Topographic Techniques in the study of solid state reactions, as evidenced in the brief outlines of the pioneering studies presented above, can only be greatly improved upon by the application of the new generation synchrotron sources such as that earmarked for Argonne National Laboratory. Improved brightness will make real time topography (using TV imaging systems) that much easier. It is worth noting that the field would benefit greatly if the beamlines to be used for topography were extended to lengths such that the area of beam delivered at the crystal, was in excess of several tens of square centimetres. This would allow studies to be made of very large crystals. Improved monochromator designs would also benefit the field in that finer bandpass incident beams would allow for more accurate strain measurement, and also allow for plane wave imaging conditions to be achieved, which simplifies quantitative topographic contrast interpretation. Synchotron topography will, without doubt, play an important role as a non-destructive characterization technique capable of revealing fundamental information on reaction mechanisms and kinetics, in the future development of new solid state reactions, such as those which may yield products which have novel electro-optic, or electronic properties.

References.

1. The similarity between solid state phase transformations in molecular crystals and many solid state reactions is recognized here, in that both can involve changes on the structural level and on the bonding level, and as such will both be treated, albeit somewhat separately.

2. H. Sixl, Advances in Polym. Sci., 63, 49, (1984)

3. (a) J.M. McBride, B.E. Segmuller, M.D. Hollingsworth, D.E. Mills, and B.E. Weber, Science, 234, 830, (1986).
(b) M.D. Hollingsworth, and J.M. McBride, Mol. Cryst. Liq. Cryst.,(1988).
(c) J.M. McBride, S.B. Bertman, D.Z. Cioffi, B.E. Segmuller, and B.E. Weber, Mol. Cryst. Liq. Cryst., (1988).
(d)J.M. McBride, S.B. Bertman and T.C. Semple, Proc. Nat. Acad. Sci. USA, 84, 4743, (1987).

4. W. Jones and J.M. Thomas, Prog. Solid St. Chem., 12, 101, (1979).

5. R.T. Read and R.J. Young, J. Mater. Sci., 19, 327, (1984).

6. H. Nakanishi, W. Jones, J.M. Thomas, M. Hasegawa, and W.L. Rees, Proc. Roy. Soc. Lond. A 369, 307, (1980).

7. B.K. Tanner and D.K. Bowen (eds), "Characterization of Crystal Growth Defects by X-ray Methods, NATO ASI B63. New York, Plenum (1980).

8. D.K. Bowen and C.R. Hall, "Microscopy of Materials", Macmillan, (1975).

9. J.E. White, J. Appl. Phys., 21, 855, (1950).

10. T. Tuomi, K. Naukkarinen, P. Rabe, Phys. Stat. Sol., (a) 25, 93, (1974).

11. J. Miltat, p. 401 in Ref. 5.

12. M. Hart, J. Appl. Cryst., 8, 436, (1975).

13. (a) A. Authier, Adv. in X-ray Analysis, 10, 9, (1967).
(b) A. Authier, in "Modern Diffraction and Imaging Techniques", (Ed. Amelinckx et al.), p. 481, (1970).

14. A. Authier, Journal de Physique, 27, 57, (1966).

15. Among the many comprehensive reviews are;
(a) R.W. James, "The Optical Principles of the Diffraction of X-rays", Ox Bow Press, Woodbridge, Connecticut, (1982).

(b) B.W. Batterman and H. Cole, Rev. Mod. Phys., 36, 681, (1964).
(c) B.K. Tanner, "X-ray Diffraction Topography", Pergamon, (1976).

16. For a useful review of the concept of the Dispersion surface and its properties see p. 4, Ref. 13(c).

17. (a) L.V. Azaroff, K. Kaplow, N. Kato, R.J. Weiss, A.J.C. Wilson, and R.A. Young, "X-ray Diffraction, McGraw Hill, New York, (1974).
(b) N. Kato, "Crystallography and Crystal Perfection", p153, Academic Press, New York, (1963).
(c) N. Kato, Acta. Cryst., 13, 349, (1960).
(d) N. Kato, J. Appl. Phys., 39, 2231, (1968).

18. (a) N. Kato, J. Phys. Soc. Jap., 18, 1785, (1963).
(b) N. Kato, J. Phys. Soc. Jap., 19, 67, 971, (1964).

19. For review see Ref. 13(c).

20. A. Authier, Phys. Stat. Sol., 27, 77, (1968).

21. A. Authier and F. Balibar, Acta Cryst., A26, 647, (1970).

22. G. Borrmann, W. Hartwig, and H. Irmler, Z. Naturforschung, 13a, 423, (1958).

23. For example see;
(a) F. Lefaucheux, M.C. Robert, and H. Arend, J. Cryst. Growth, 47, 313, (1979).
(b) F. Lefaucheux, M.C. Robert, E. Manghi, and H. Arend, J. Cryst. Growth, 51, 551, (1981).
(c) M.C. Robert and F. Lefaucheux, J. Cryst. Growth, 65, 637, (1983).

24. For example see;
(a) P.J. Halfpenny, K.J. Roberts, and J.N. Sherwood, J. Cryst. Growth, 65, 524, (1983).
(b) H.L. Bhat, K.J. Roberts, and J.N. Sherwood, J. Appl. Cryst., 16, 390, (1983).

25. For review see, H. Klapper, p. 133 in Ref. 5.

26. J.M. Schultz, J. Mater. Sci. 12, 2258, (1976).

27. R.G. Rosemeier, R.E. Green, Jr., and R.H. Baughman, J Appl. Phys., 52, 7129, (1981).

28. I.D. Begg, P.J. Halfpenny, R.M. Hooper, R.S. Narang, K.J. Roberts, and J.N. Sherwood, Proc. Roy. Soc. Lond., A 386, 431, (1983).

29. H. Klapper, K.J. Roberts, D. Gotz, and N. Herres, J. Cryst. Growth, 65, 621, (1983).

30. J.M. Thomas, Advances in Catalysis, 10, 293, (1970).

31. J.M. Thomas and G.D. Renshaw, J. Chem. Soc. A 2058, (1967).

32. P.J. Herley, P.W.M. Jacobs, and P.W. Levy, Proc. Roy. Soc. Lond., A318, 197, (1970).

33. P.J. Herley, P.W.M. Jacobs, and P.W. Levy, J. Chem. Soc., A2338, (1971).

34. P.J. Herley and P.W. Levy, "Reactivity of Solids", Proc. 7th International Symposium, (Ed. J.S. Anderson, M.W. Roberts, and F.S. Stone), p. 387., London: Chapman and Hall, (1972).

35. H.-G. Braun and G. Wegner, Mol. Cryst. Liq. Cryst., 96, 121, (1983).

36. M.D. Cohen, Z. Ludmer, J.M. Thomas, and J.O. Williams, Proc. Roy. Soc. Lond., A324, 459, (1971).

37. W.L. Rees, M.J. Goringe, W. Jones, and J.M. Thomas, J. Chem. Soc., Farad. Trans. II.,75, 806, (1979).

38. W. Jones, J.M. Thomas, J.O. Williams, and L.W. Hobbs, J. Chem. Soc., Farad. Trans. I., 71, 138, (1975).

39. J.W. Christian, "The Theory of Transformations in Metals and Alloys, Part 1, Equilibrium and General Kinetic Theory", Second Edition, Pergamon, (1981).

40. J.W. Cahn, Acta Met., 5, 169, (1957).

41. D.M. Barnett, Scripta Met., 5, 261, (1971).

42. R. Gomez-Ramirez and G.M. Pound, Met. Trans., 4, 1563, (1973).

43. R.H. Baughman, J. Chem. Phys., 68, 3110, (1978).

44. M.D. Cohen, Angew. Chem. Internat. Ed., 14, 386, (1975).

45. W. Schermann, G. Wegner, J.O. Williams, and J.M. Thomas, J. Polymer Sci., Polymer Phys. Ed., 13, 753, (1975).

46. J.D. Eshelby, Proc. Roy. Soc., A241, 376, (1957).

47. D.A. Young, "Decomposition of Solids", Pergamon, (1966).

48. M.Dudley, J.N. Sherwood, D. Bloor, and D. Ando, J. Mater. Sci. Lett., 1, 479, (1982).

49. M. Dudley, J.N. Sherwood, D.Bloor, and D. Ando, "Application of Synchrotron Radiation to Problems in Materials Science", Proceedings of Daresbury Study Weekend, Daresbury Preprint DL/SCI/R19, (1982).

50. M. Dudley, J.N. Sherwood, D. Bloor, and D. Ando, Mol. Cryst. Liq. Cryst., 93, 223, (1983).

51. M. Dudley, J.N. Sherwood, D. Bloor, and D. Ando, in "Polydiacetylenes", D. Bloor and R.R. Chance (eds), NATO ASI Series E (Applies Sciences), no 102, p. 87. Martinus Nijhoff, Dordrecht, (1985).

52. M. Dudley, J.N. Sherwood, D. Bloor and D. Ando, in "Proceedings of 10th Int. Conf. on Reactivity of Solids", Dijon, France, (1984).

53. M.Dudley, J.N. Sherwood and D. Bloor, Proceedings of ACS Division of Polymeric Materials: Science and Engineering, 54, 426, (1986).

54. M.Dudley and J.N. Sherwood, To Be Submitted to Proc. Roy. Soc.

55. D.B. Sheen and J.N. Sherwood, Chemistry in Britain, June 1986, 535, (1986).

56. (a) P.J. Herley and J. Laia, Unpublished Work.
(b) J. Laia, Thesis, Stony Brook, (1986).

57. J.M. Thomas and G.D. Renshaw, J. Chem. Soc. (A)., 2749, 2753, 2756, (1969).

58. J.M. Thomas, E.L.Evans, and T.A. Clarke, J. Chem. Soc. (A)., 2338, (1971).

59. A. El-Korashy, K.J. Roberts, and T. Scheffen-Lauenroth, J. Appl. Cryst., 20, 512, (1987).

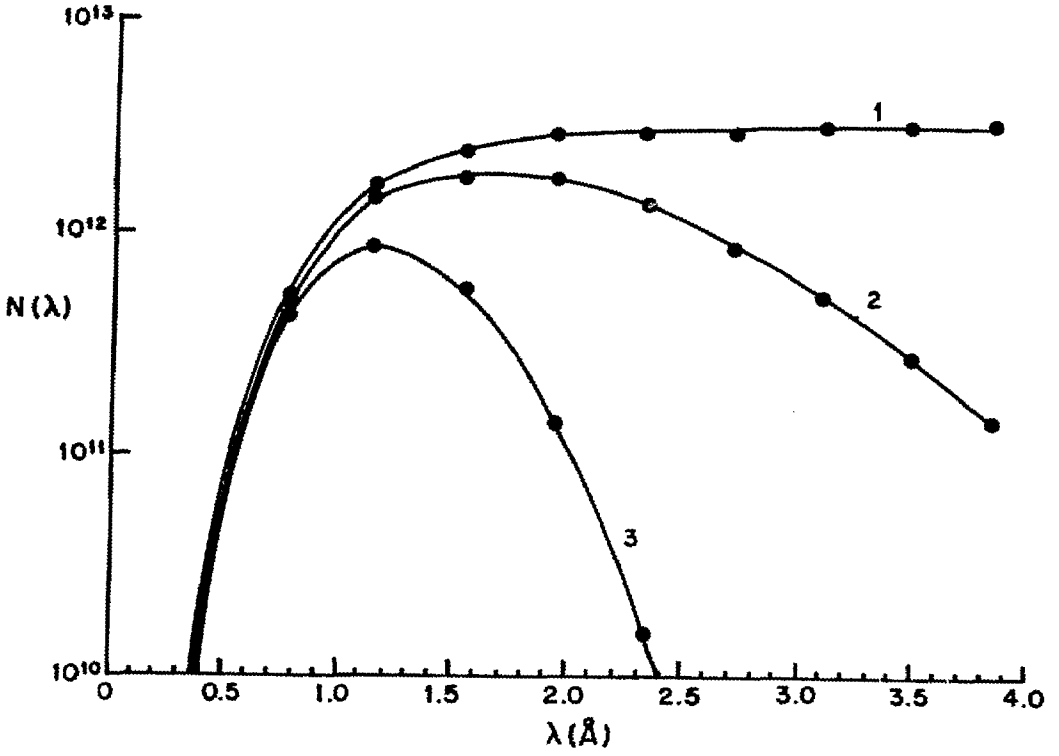

Figure 1. Spectrum emitted from the Daresbury Synchrotron Radiation Source. N (λ) in units of photons sec^{-1} $mA^{-1}mrad^{-1}$ for 0.389A bandwidth, (Energy=2 GeV). Curve (1) spectrum at tangent point; curve (2) spectrum after 889 μm thick Berrylium window; curve (3), curve (2) after additional 1m of air.

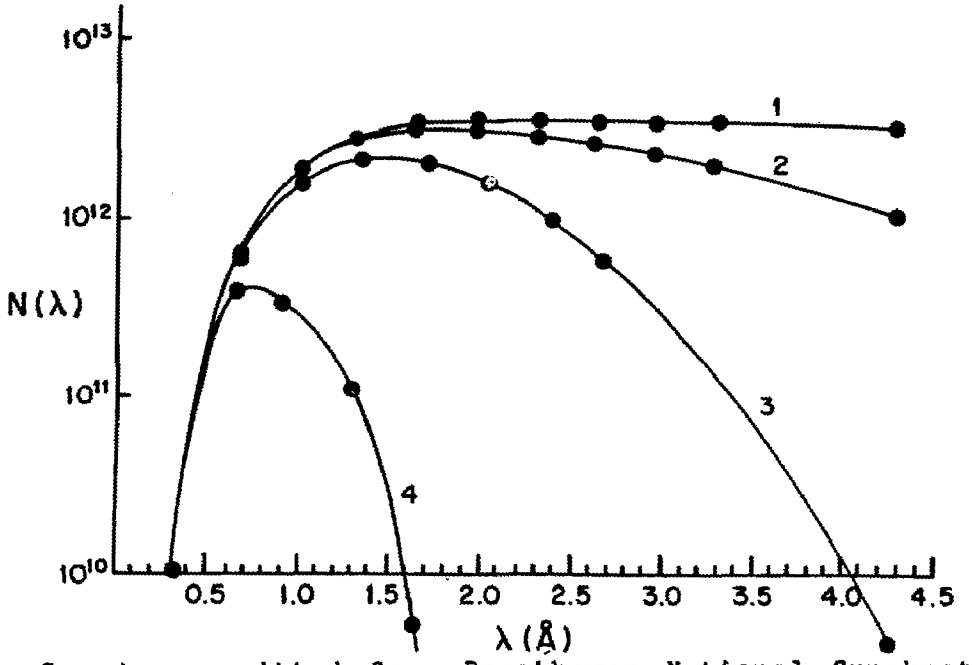

Figure 2. Spectrum emitted from Brookhaven National Synchrotron Light Source. N (λ) in units of photons sec^{-1} $mA^{-1}mrad^{-1}$ for 0.3304A bandwidth, (Energy=2.4 GeV). Curve (1) spectrum before Berrylium window; curve (2) after Berrylium window; curve (3), curve (2) after additional 25.4 μm of aluminum; curve (4), curve (3) after additional 4m of air.

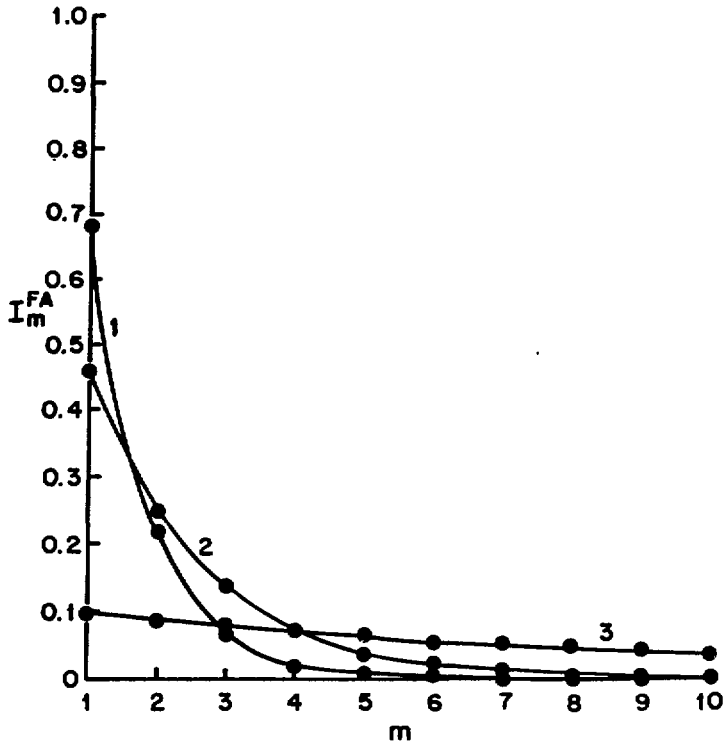

Figure 3. Fractional absorbed intensity plotted as a function of layer number m. Curve (1), λ =2.5A, curve (2), λ =1A.

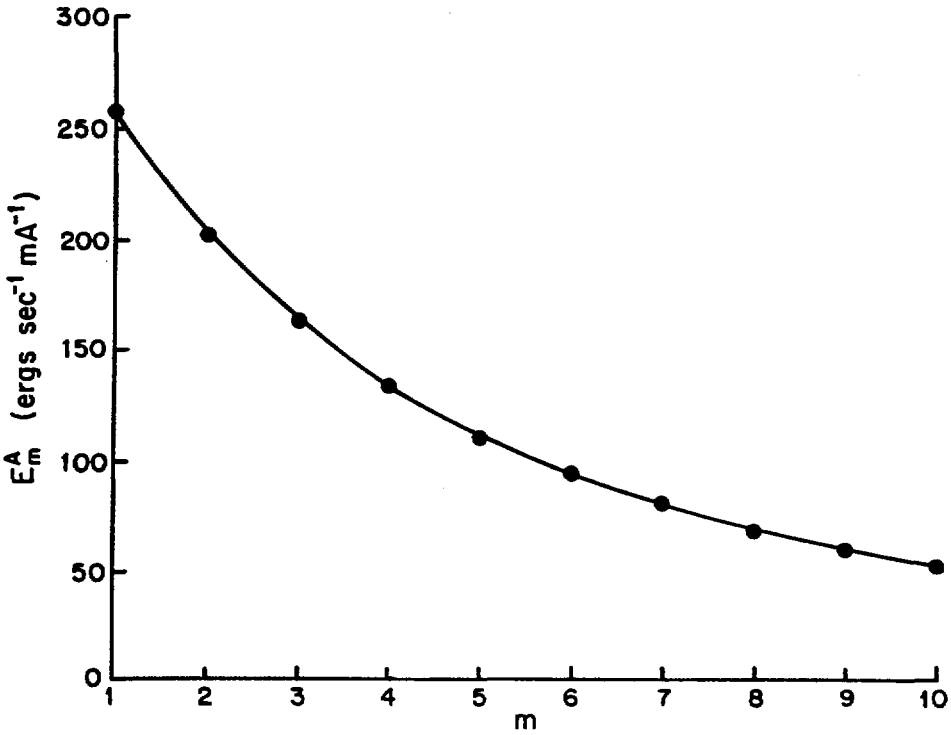

Figure 4. Total energy absorbed (over whole spectrum) in the sample, versus m.

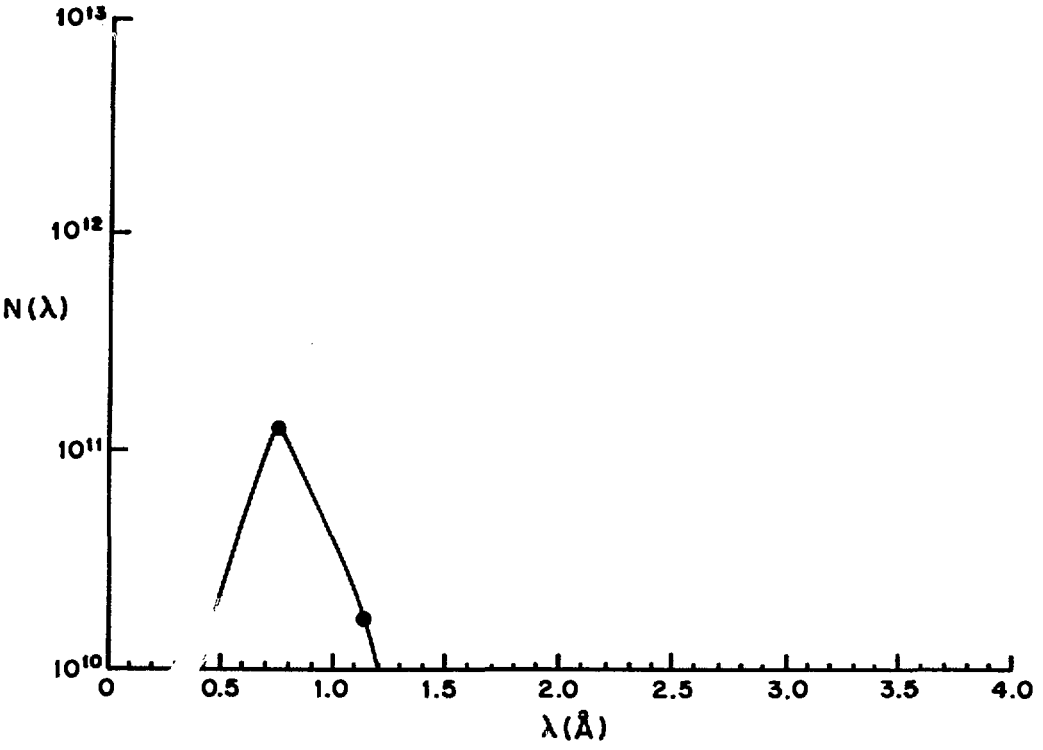

Figure 5. (a) SRS incident beam spectrum after use of aluminum filter.

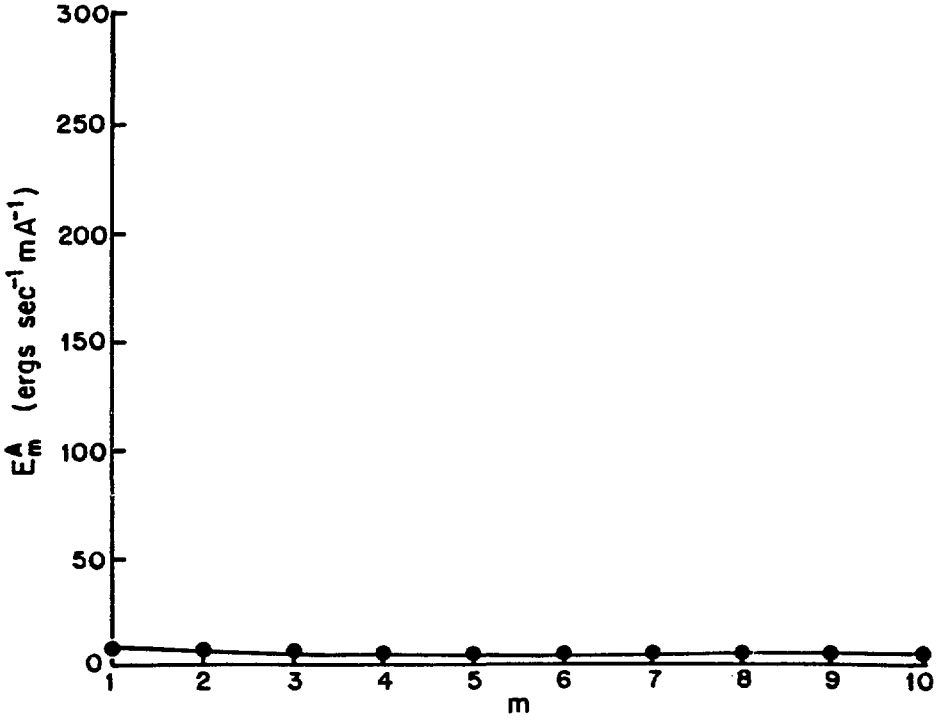

(b) Resultant total energy absorbed in the sample versus m.

g

1mm

Figure 6(a)

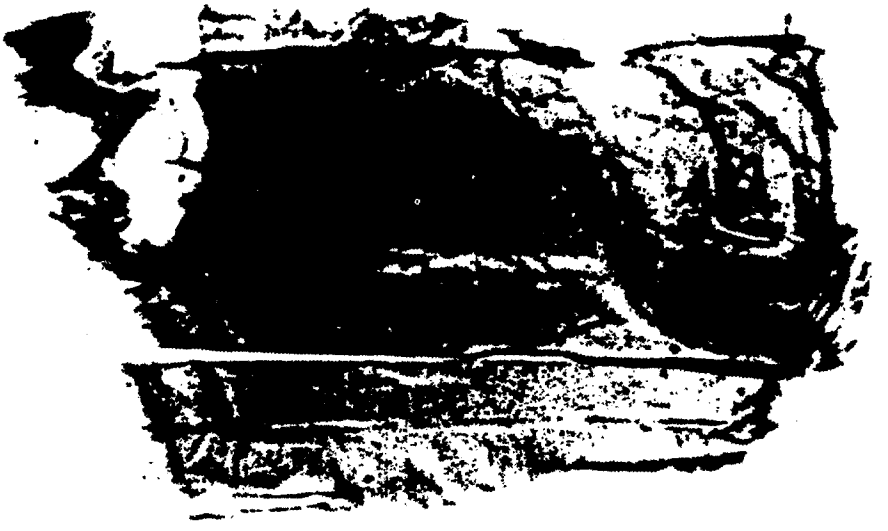

Figure 6(b)

Figure 6. White Beam Synchrotron Topographs (g = [0$\bar{1}$1], λ = 1.25Å), taken from (a) a monomer crystal, and (b) the same crystal after x-ray induced poylmerization.

Figure 7. White Beam Synchrotron Topograph ($g = [\bar{1}\bar{1}2]$, $\lambda = 1\text{Å}$), showing the detailed defect structure in the polymer crystal.

Figure 8. Detail from figure (7) showing central dislocation images.

Figure 9

Figure 9. Detail from figure (7) showing images from twin lamellae.

Figure 10. Detail from a $21\bar{4}$ reflection (λ =1A) from the same crystal showing growth sector boundary images.

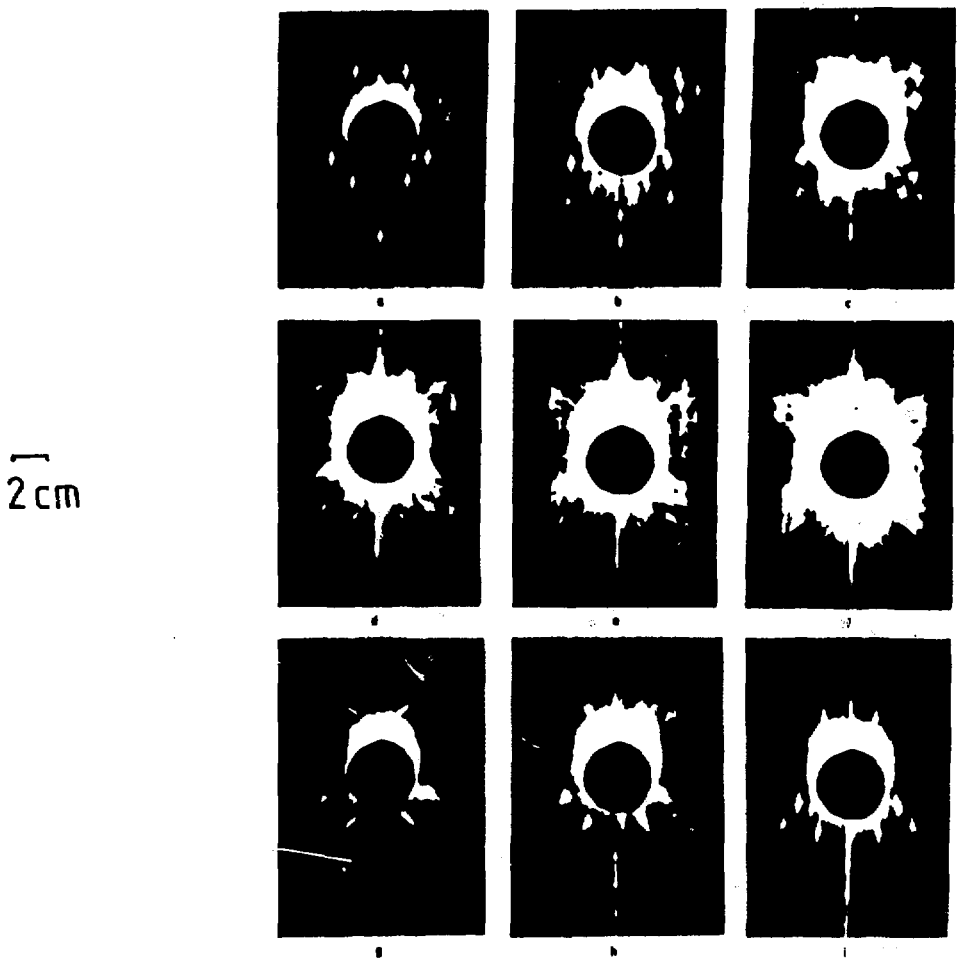

Figure 11. Series of Laue patterns recorded during room temperature X-ray induced polymerization using a filtered beam.

Figure 12.White Beam Topograph (g = $\bar{1}04$, λ =0.8A) recorded from a PTS monomer crystal on fast X-ray film.

g

1mm

Figure 13.Similar topograph recorded from the same crystal after initiation of thermal reaction.

Figure 14(a)

g

1mm

Figure 14(b)

Figure 14.(a) White Beam Topograph (g = [$\bar{1}$04], λ =0.8A), of PTS crystal similar to that topographed for figure (12). (b) Similar topograph recorded after deliberate introduction of an island of polymer into the central dislocated region showing resultant strain contrast.

X-ray Microprobe Elemental Analysis using Synchrotron Radiation

Stephen R. Sutton Mark L. Rivers
Joseph V. Smith
Department of the Geophysical Sciences
University of Chicago, Chicago, IL 60637

Keith W. Jones
Department of Applied Science
Brookhaven National Laboratory
Upton, NY 11973

1 Introduction

The development of trace element microprobes has revolutionized chemical analytical capabilities for of a wide variety of materials and has opened new areas of research in geochemistry, biochemistry and materials development. Charged particle and photon excitation sources have been successfully employed in these instruments. Synchrotron radiation sources (SRS) have been exploited to develop a trace element microprobe based on the x-ray fluorescence technique. This approach is advantageous for several reasons. First, the x-ray flux from SRS is several orders of magnitude greater than attainable with conventional x-ray tubes. Second, synchrotron radiation is highly collimated so that small, intense spots can be readily produced. Third, the natural polarization of synchrotron radiation can be exploited to minimize scattered, background radiation. The consequence of these improvements is the ability to achieve high elemental sensitivity with high spatial resolution. The purpose of this paper is to report the status and planned upgrades of the x-ray microprobe (XRM) at the National Synchrotron Light Source (NSLS), Brookhaven National Laboratory (BNL), summarize chemical applications of the XRM and outline anticipated enhancements using the Advanced Photon Source (APS).

2 Synchrotron X-ray Microprobe

2.1 Collimated X-ray Microprobe at NSLS

A first generation synchrotron XRM has been developed on the x-ray ring (2.5 GeV electrons, 200 mA) at NSLS (beamline X26C) [1,2]. White, bending magnet synchrotron radiation is used as the excitation source. X-ray beams down to 20 μm are produced with a four-jaw, motor-driven slit assembly and fluorescence spectra are obtained in air with an energy dispersive Si(Li) detector (figure 1). Specimens are mounted vertically on a Klinger translation and rotation stage which allows 1 μm motion for line scans or two-dimensional imaging [3]. A petrographic microscope equipped with transmitted and reflected light and TV camera is used to view the sample during analyses.

Detection limits (defined as 3 times the square root of the background for a 30 μm spot after a 10 minute acquisition) with this simple yet powerful instrument are typically 1 ppm for K transitions of elements with atomic number between 15 and 55 and about 10 ppm for L transitions for elements with atomic number between 55 and 92. Thus, virtually all elements above silicon can be measured with high sensitivity. The accuracy of the technique has been demonstrated for a variety of matrices including biological specimens, metals, carbonates and silicates [4].

Quantitative analyses with this "white light/energy dispersive" system are complicated in several ways. First, fluorescence from elements in major proportions in the sample readily saturate the detector unless filtering is employed to suppress its intensity. Second, Laue spots produced when the continuum incident radiation is diffracted by well-ordered specimens can fall within the acceptance solid angle of the detector resulting in diffraction peaks in the x-ray spectra [5]. Specimen rotation is usually sufficient to alleviate this interference. Third, trace element standards which are homogeneous on the micro-scale are extremely rare. Standard-less analyses (i.e., concentration determinations on individual spectra based on theoretical relative elemental sensitivities and the known content of a major element) are often feasible, however, since the physics of photon interactions with matter is reasonably well understood [4].

Several upgrades are in progress to improve the performance of this instrument. First, an ellipsoidal, grazing incidence focusing mirror will be installed to increase

the flux at the specimen [6]. Second, a wavelength dispersive detector will be used to increase energy resolution and eliminate diffraction interferences. Third, a monochromator will be added to allow tuning of the incident energy to selectively excite particular absorption edges. These improvements are expected to lower detection limits to below 100 ppb.

2.2 Advanced Photon Source

The availability of the Advanced Photon Source (APS) will greatly enhance the capabilities of the synchrotron x-ray microprobe [7]. The undulators will produce very high flux in the 5-40 keV range and their low emittance will allow the production of much smaller, perhaps sub-micron, beams thereby improving spatial resolution. The hard x-ray wigglers will produce orders of magnitude more flux at high energy than currently available from the NSLS bending magnets [8].

The APS undulator "A", the energetically softer of the two proposed undulators, is ideally suited for an x-ray microprobe in the 5-40 keV range. Its fundamental can be tuned from 5 to 14 keV with the 3rd harmonic varying from 15 to 42 keV. With the fundamental tuned to 10 keV, a flux of about 10^9 photons/sec/μm^2/1% bw will be produced. Moreover, the beam will be so well collimated that a 1 μm pinhole could be placed several centimeters from the sample without appreciable "blowup" of the beam diameter. (This blowup effect hampers attempts to produce μm spots on a focused, bending magnet beam line.) Alternatively, the pinhole could be replaced with a Kirkpatrick-Baez mirror [9] which will increase the flux into a $1\mu m^2$ spot by another factor of about 1000. These high fluxes into small spots will allow the use of high resolution monochromators and wavelength dispersive detection systems.

Fluorescent transitions above 40 keV will be accessible with the hard x-ray wiggler (wiggler "A"). The brightness of this wiggler at 60 keV is about 10^{15} photons/sec/mrad^2/0.1% bw, i.e., 10 and 10^6 times greater than the brightness of an NSLS bending magnet at 10 and 60 keV, respectively. High fluxes at high energy will permit sensitive fluorescence measurement of high atomic number elements, e.g., rare earth elements and noble metals, using K transitions. This approach will avoid peak overlap problems encountered when using the lower energy, L transitions for these measurements.

Such intense x-ray sources are not without their complications. The high radiation levels are likely to produce severe shielding restrictions on experimental apparatus.

Perhaps the most important concern, however, is specimen radiation damage. Quantitative work remains to be done on the effects of such intense photon fluxes on a variety of materials. It is conceivable, for example, that the excitation process itself will severely modify the structure and composition of many specimens. Under the synchrotron beam, trace elements may be redistributed, chemical speciation may be modified, and lattice parameters may be altered.

It is clear from the above considerations that an XRM at the APS will require time on each of the insertion devices - the optimum source depends on the specific experiment. In order to provide the required flexibility, a modular system of beam line components is desirable. This approach will allow apparatus to be moved essentially intact from one beam line to another. Experimental setup in a staging area will also increase the the efficient use of the synchrotron photons.

An XRM will be one of many synchrotron-based analytical devices employed by the chemistry community. XRM, EXAFS and diffraction studies will routinely be required on individual samples. It is therefore essential that an organization be established to coordinate chemical research at the APS. In the earth science community, for example, the GeoSync committee was established to serve this function. At BNL, an analogous task is performed by the Regional Center for Trace Element Geochemistry (RECETEG). The experience of RECETEG has demonstrated the value of an in-house core of scientists which develops instrumentation and techniques, conducts its own research and facilitates access to the instruments by outside users. In this way, the unique capabilities of synchrotron radiation are exploited to the maximum.

3 Chemical Applications of the XRM

The availability of high elemental sensitivity (< 1 ppm) for small masses (< 1 ng) offers two main advantages in chemical research. First, compositional microdistributions of natural and synthetic materials can be determined for a large number of elements. Second, trace element analyses are possible on extremely small samples. These enhanced capabilities have opened new areas of geochemical, biochemical and materials research. Advanced synchrotron sources will continue this explosion of activity.

Geochemistry: The ability to determine the trace element contents of minerals in fine-grained assemblages has many important geochemical applications. *Elemental partitioning* among co-existing phases are extremely valuable in inferring the physical and chemical evolution of igneous systems, such as geothermal centers. Research on igneous meteorites has been done at the NSLS (figure 2) [10,11]. Microdistribution determinations are normally required on both natural rocks and the minute, crystalline run-products from laboratory, simulation experiments. The XRM allows these experiments to be performed at temperatures, pressures, and compositions which approximate geological environments more closely than ever before. Trace element analyses can presently be done on small, isolated samples down to about 5 μm(figure 3). Many economically-important ore minerals, such as noble metal-bearing sulfides, are fine-grained, multi-phased assemblages and the XRM permits analyses on the individual phases in their petrographic contexts [12]. Microdistribution analyses of Carlin-type ore demonstrated the concentration of Au in the matrix and subsequent optical and electron microscopy revealed an association with the clay mineral illite [13]. The APS will allow elemental partitioning studies to be extended to other elements in lower concentrations. *Diffusion mechanisms* are important in crystal growth and magma contamination. The XRM permits diffusion couple research at low concentrations and wide ranges of pressure and temperature. An experiment on silica-rich glasses yielded trace element diffusion rates similar to those of the major elements and no correlation between rates and ionic radii was observed [14]. Major element diffusional gradient control of the trace element redistribution is one interpretation that will be fully testable with the APS. *Fluid evolution in coal-forming environments* is feasible to study with the XRM by analysing sulfides of different temporal association. Analyses have been made at NSLS on pyrite (FeS_2), marcasite (FeS_2), and chalcopyrite ($CuFeS_2$) originating from a series of localities within the Yorkshire and East Midland Coalfields in Great Britain [15]. The small grain size of some of this

mineralization will be well suited for the small beams that will be achievable with the APS undulator sources.

Biochemistry: Studies of the detailed function of specific organisms and toxicity effects of particular elements are complicated by the extreme heterogeneity of biological specimens. Trace elements are important in many biological areas including cell physiology, disease processes, catalytic reactions, and the regulation of cell function. Trace element interactions in biological systems are extremely complex and the multi-element, high spatial resolution capabilities of the XRM are advantageous in this research [17]. For example, the microdistribution of Ga in bone is being studied to investigate the effects of gallium nitrate in the treatment of tumor related bone loss [18]. At BNL, a Biomedical Resource Center coordinates the use of the XRM at NSLS for biological applications. Greater elemental sensitivity and spatial resolution obtainable with the APS will allow time-resolved experiments on trace element microdistributions with better than micrometer spatial resolution. Microtomography of organisms will also be improved with extremely intense and small x-ray beams.

Materials research: Trace element distributions are valuable in materials science research. The distributions and contents of trace impurities in high T_c superconductors may lead to important insights on the manufacture of these materials. Siting information for impurities in semiconductors is required to improve purity and advance the development of electronic devices. Development and testing of waste management materials, such as nuclear waste encapsulators, is aided by laboratory simulations under physical and chemical conditions which closely approximate natural environments. Development of new catalysts depend on detailed chemical analyses of experimental run products. These specimens also tend to be minute and trace chemical constituents often play important roles in determining physical properties.

It should be emphasized that trace element microprobe analysis is one aspect of an interdisciplinary, chemical research program which includes other analytical techniques such as EXAFS and x-ray diffraction. A significant advantage of the advanced synchrotron sources will be the ability to obtain chemical, structural and physical information with extremely high spatial resolution and sensitivity on individual samples.

4 Conclusion

Synchrotron radiation is an extremely useful and powerful source for a trace element microprobe based on the x-ray fluorescence technique. A simple, collimated instrument has been constructed at NSLS beam line X26 and analyses have been made of geological and biological specimens. These initial results demonstrate the unique role that this instrument plays in chemical research. Work is in progress to add a focussing mirror, monochromator and wavelength dispersive spectrometer to the X26 XRM which will enhance elemental sensitivity. The insertion devices on the Advanced Photon Source will advance this instrument even further in sensitivity and spatial resolution. Undulators and wigglers will both be useful and a modular beam line system is desirable for this flexibility. The enormous cost of such beam lines will almost certainly require a cost-sharing approach among related disciplines and funding agencies.

References

[1] B. M. Gordon and K. W. Jones (1985) Design criteria and sensitivity calculations for multielemental trace analysis at the NSLS x-ray microprobe. Nucl. Instrum. Methods B10/11, 293-8.

[2] A. L. Hanson, K. W. Jones, B. M. Gordon, J. G. Pounds, W. M. Kwiatek, M. L. Rivers, G. Schidlovsky and S. R. Sutton (1987) Trace element measurements using synchrotron radiation. Nucl. Instrum. Methods, in press.

[3] M. L. Rivers (1987) X-ray fluorescence imaging with synchrotron radiation. In "X-Ray Microscopy II", 56, 233-9.

[4] Fang-Qiong Lu, Joseph V. Smith, Stephen R. Sutton, Mark L. Rivers, and Andrew M. Davis (1988) Synchrotron x-ray fluorescence analysis of rock-forming minerals: I. Comparison with other techniques; II. White-beam energy-dispersive procedure for feldspars. Chem. Geol., in press.

[5] S. R. Sutton, M. L. Rivers, and J. V. Smith (1986) Synchrotron x-ray fluorescence: diffraction interference. Anal. Chem. 58, 2167-71.

[6] K. W. Jones, P. Z. Takacs, J. B. Hastings, J. M. Casstevens and C. D. Pionke (1987) Fabrication of an 8:1 ellipsoidal mirror for a synchrotron x-ray microprobe. Proc. SPIE 749 "Metrology: Figure and Finish", 37-44.

[7] S. R. Sutton, M. L. Rivers, K. W. Jones and J. V. Smith (1988) X-ray Fluorescence Microprobe Analysis, In "Synchrotron X-ray Sources and New Opportunities in the Earth Sciences", Argonne National Laboratory Technical Report ANL/APS-TM-3, 93-112.

[8] M. L. Rivers (1988) Characteristics of the Advanced Photon Source and comparison with existing synchrotron facilities. In "Synchrotron X-ray Sources and New Opportunities in the Earth Sciences", Argonne National Laboratory Technical Report ANL/APS-TM-3, 5-22.

[9] R. D. Giauque, A. C. Thompson, J. H. Underwood, Y. Wu, K. W. Jones, and M. L. Rivers (1987) Measurement of femtogram quantities of trace elements using an x-ray microprobe. Anal. Chem. 60, 855-8.

[10] S. R. Sutton, J. Delaney, J. V. Smith, and M. Prinz (1987) Copper and nickel partitioning in iron meteorites. Geochim. Cosmochim. Acta 51, 2653-62.

[11] D. S. Woolum, M. L. Johnson, D. S. Burnett and S. R. Sutton (1988) Refractory lithophile partitioning in type B CAI materials (abstract). Lunar Planet. Sci. XIX, 1294-1295.

[12] L. Cabri, M. L. Rivers, J. V. Smith, and K. W. Jones (1985) Trace elements in sulfide minerals by milliprobe x-ray fluorescence using white synchrotron radiation. Eos, Trans. Am. Geophys. Union 66, No. 46, 1150.

[13] J. R. Chen, E. C. T. Chao, J. A. Minkin, J. M. Back, W. C. Bagby, M. L. Rivers, S. R. Sutton, B. M. Gordon, A. L. Hanson, and K. W. Jones (1987) Determination of the occurrence of gold in an unoxidized Carlin-type ore sample using synchrotron radiation. Nucl. Instrum. Methods B22, 394-400.

[14] D. R. Baker and E. B. Watson (1987) Diffusion of major and trace elements in compositionally complex Cl- and F-bearing silicate melts. Proceedings of the 9th University Conference on Glass, Rensselaer Polytechnic Institute, NY.

[15] R. N. White, D. A. Spears, and J. V. Smith (1987) Synchrotron x-ray fluorescence trace element analysis of sulfides in United Kingdom coals (abstract). GSA meeting, San Antonio, TX.

[16] S. R. Sutton and G. J. Flynn (1988) Stratospheric Particles: Synchrotron X-ray Fluorescence Determination of Trace Element Contents. Proceedings of the 18th Lunar and Planetary Science Conference, 607-614.

[17] J. G. Pounds, G. J. Long, W. M. Kwiatek, K. W. Jones, B. M. Gordon, and A. L. Hanson (1987) The role of high-energy synchrotron radiation in biomedical trace element research. In "X-Ray Microscopy II", 56, 425-8.

[18] R. Bockman, M. Repo, R. Warrell, J. G. Pounds, W. M. Kwiatek, G. J. Long, G. Schidlovsky and K. W. Jones (1987) X-ray microscopy studies on the pharmacodynamics of therapeutic gallium in rat bones. In "X-Ray Microscopy II", 56, 391-4.

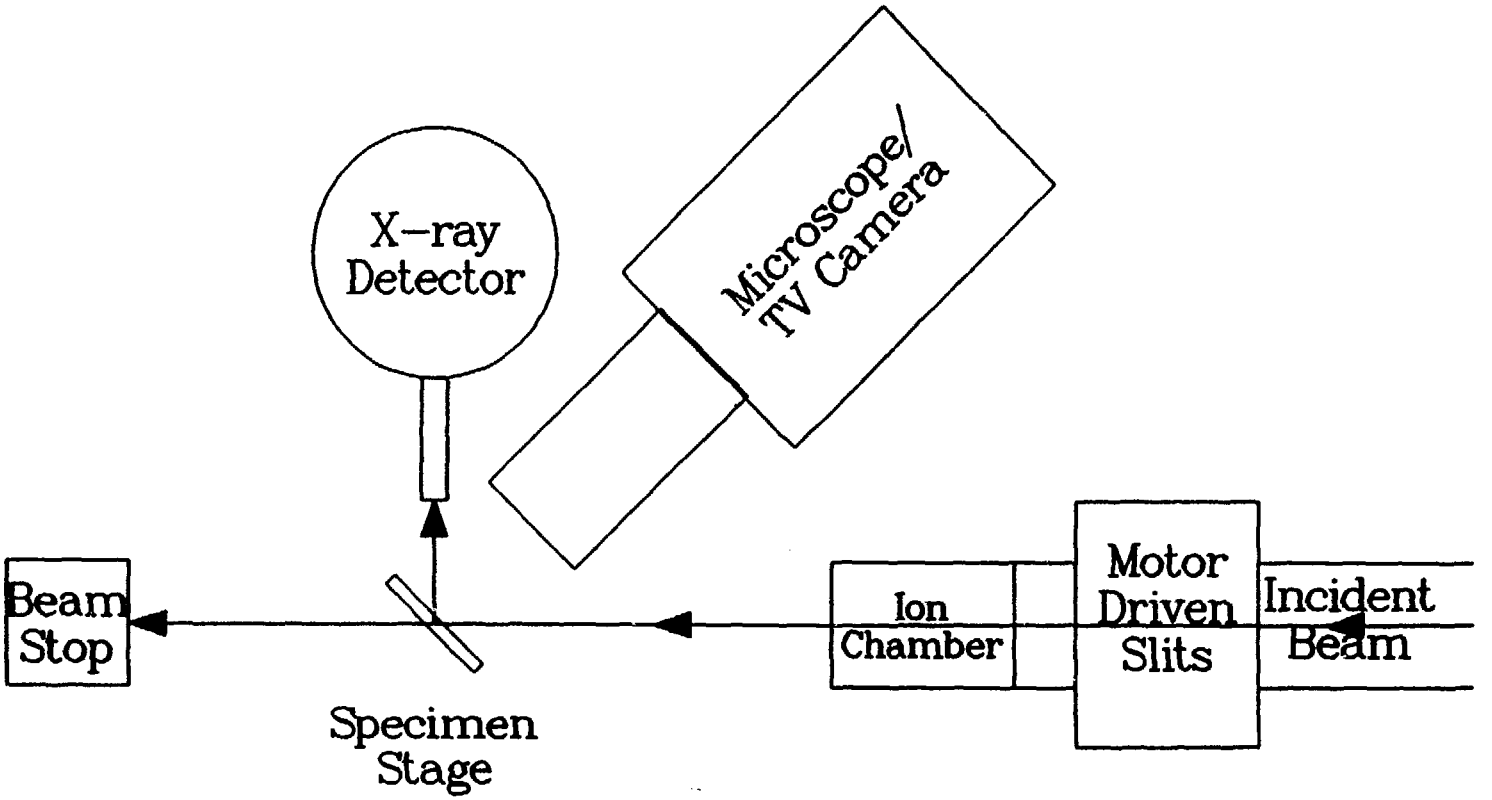

Figure 1: Schematic of the collimated x-ray microprobe (XRM) at NSLS beamline X26 (top view).

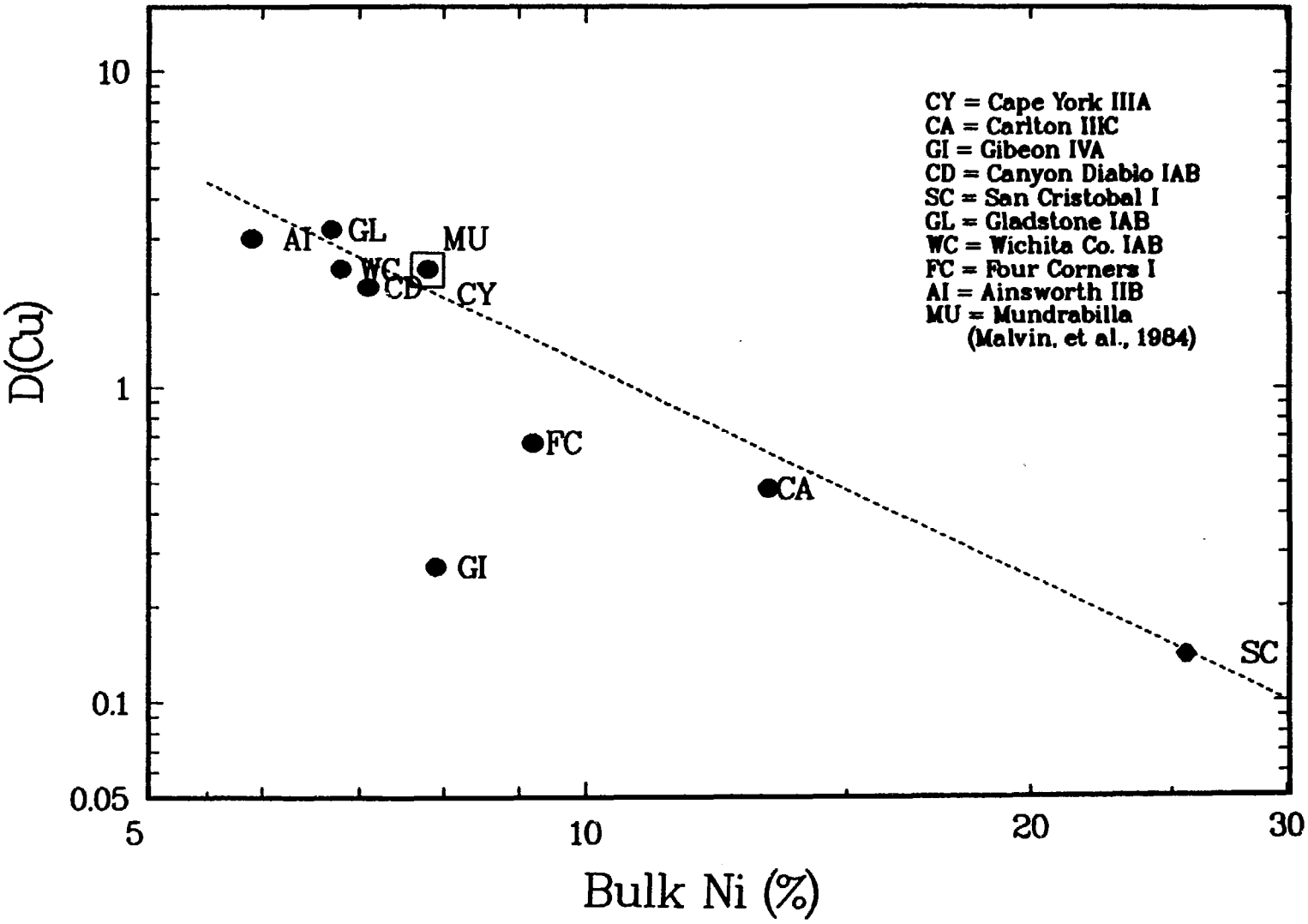

Figure 2: Copper partitioning between metal (Fe-Ni) and troilite (FeS) in iron meteorites determined using the XRM in figure 1. Copper distribution coefficient D(Cu) (troilite/metal) is negatively correlated with bulk Ni content. The relative depletion of Cu in troilite for high Ni meteorites is interpreted as a subsolidus redis-

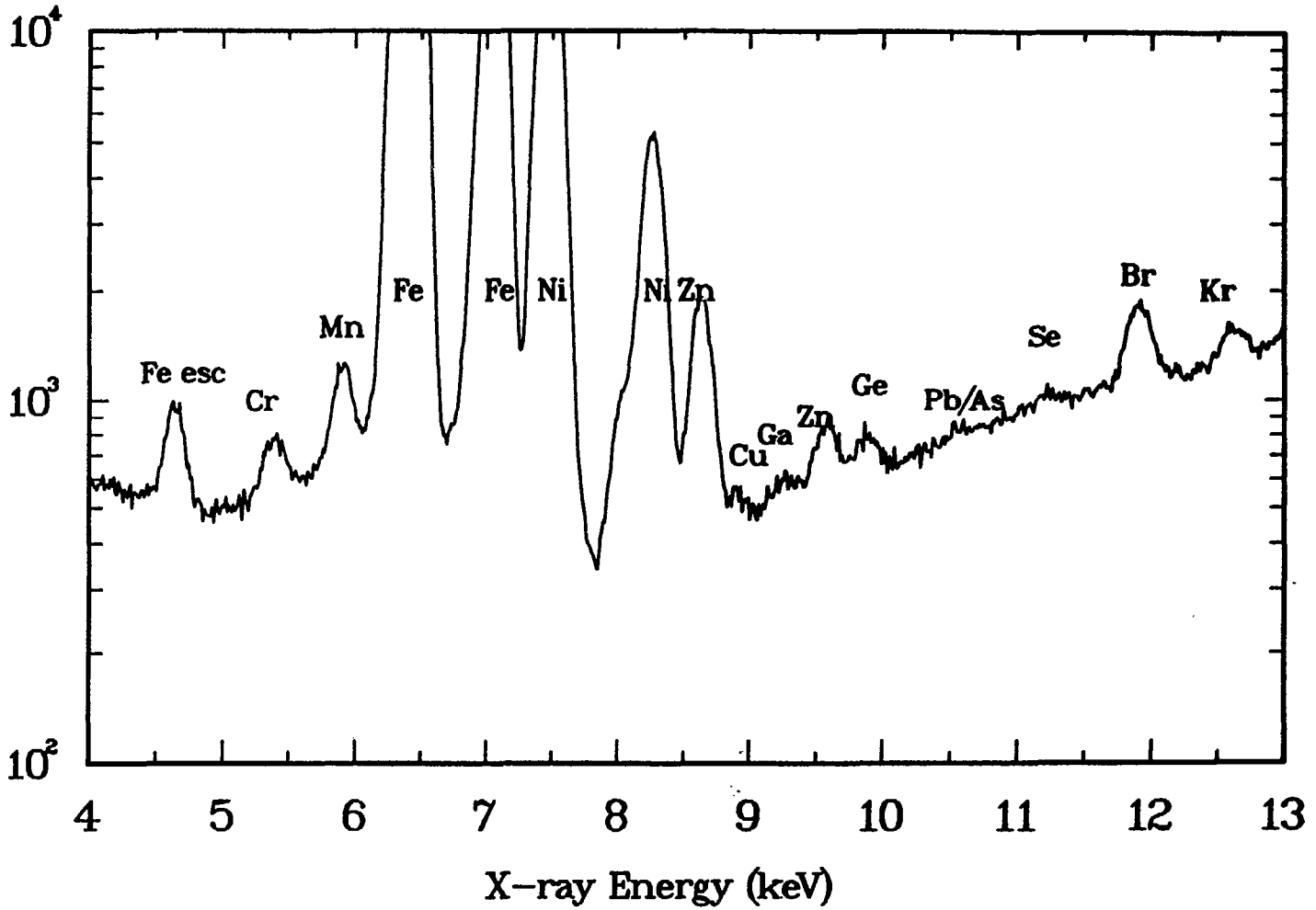

Figure 3: Synchrotron x-ray fluorescence spectrum using the apparatus in figure 1 for a 20 μm micrometeorite collected from the stratosphere (mounted on polyimide film, measurement in air with an 85 μm Al detector filter, 180 min. acquisition time). Kr derives from the air along the incident beam path. The composition is similar to that of carbonaceous meteorites with the exception of the particle's much higher Br content (130 ppm). (From [16].)

Bonding and Structure of Molecular Adsorbates on Surfaces Using X-Ray Absorption Spectroscopy

Joachim Stöhr
IBM Almaden Research Center
San Jose, CA 95120

The use of the near edge x-ray absorption fine structure (NEXAFS) technique is discussed for the study of low-Z molecules bonded to surfaces. The origin of the observed NEXAFS structures, their energy position and their polarization dependence reveal the hybridization of the intramolecular bond, the intramolecular bond length and the molecular orientation on the surface. Using these concepts we discuss examples of the determination of the bonding and structure of simple chemisorbed molecules (e.g. CO, O_2 or C_2H_4) and their transformations in response to sample conditions. With increasing size and complexity of the molecules, even for molecular chains and polymers, NEXAFS spectra are found to be characteristic of the individual functional groups of the molecules. As examples we discuss complex alcohols and acids, Langmuir-Blodgett chains and polymers such as polybutadiene, polystyrene or PMMA. As for simple molecules the polarization dependence of the resonances can be used for the determination of the orientation of the different functional groups on the surface.

For recent reviews see:
J. Stöhr, Z. Physik, 61, 439 (1985).
J. Stöhr and D. A. Outka, J. Vac. Sci. Technol. 5, 919 (1987).

PROGRAM

CHEMICAL APPLICATIONS OF SYNCHROTRON RADIATION

October 3-4, 1988
Argonne National Laboratory
Bldg. 200, Auditorium

Monday, October 3

8:30 - 9:15	Registration
9:15 - 9:30	*Opening Remarks* - Leon Stock, Chemistry Division Director, Argonne National Laboratory
9:30 -10:00	*Welcome and An Overview of the Advanced Photon Source* - David E. Moncton, Associate Laboratory Director for the Advanced Photon Source, Argonne National Laboratory

Session I — Surfaces and Kinetics

Chairperson: S. Rice, University of Chicago

10:00 -10:30	"*The Use of X-ray Reflectivity as a Surface Probe*" - Dr. Eric Sirota, Exxon Research and Engineering
10:30 -11:00	"*Structures and Phase Transitions of Organic Monolayers on the Surface of Water (Langmuir Films)*" - Pulak Dutta, Northwestern University
11:00 -11:30	Break
11:30 -12:00	"*X-Rays as Probes of Electrochemical Interfaces*" - Hector Abruna , Cornell University
12:00 -12:30	"*X-ray Scattering Studies of Transitions on Metal Surfaces*" - Dr. Glenn Held, IBM Watson Research Center, Yorktown Heights
12:30 - 1:30	LUNCH/Cafeteria

Session II **Spectroscopy**

Chairperson: L. Soderholm, ANL

1:30 - 2:00 "*Recent Applications and Future Developments of X-ray Absorption Spectroscopy*"- Dale Sayers, N. C. State University, Raleigh

2:00 - 2:30 "*EXAFS: Basic Principles, Data Analysis, and Applications*" - Boon Teo, University of Illinois at Chicago

2:30 - 3:00 "*The Role of Polarization Measurements in X-ray Absorption Spectroscopy*" - James Penner-Hahn, University of Michigan

3:00 - 3:30 "*Using X-ray Absorption Spectroscopy for the Study of Electronic Structure*" - Ercan Alp, Argonne National Laboratory

3:30 - 4:00 Break

Session III **Small Angle Scattering**

Chairperson: P. Thiyagarajan, ANL

4:00 - 4:30 "*Potential Applications of SAXS in Chemistry using Synchrotron Sources*" - John W. White, The Australian National University, Canberra and Argonne National Laboratory

4:30 - 5:00 "*Synchrotron Radiation Studies on Polymers*" - Thomas P. Russell, IBM Almaden Research Center, San Jose

5:00 - 5:30 "*Macromolecular Structural Changes by Time Resolved Synchrotron X-ray Scattering*" - James C. Phillips, SUNY at Buffalo and NSLS, Brookhaven National Laboratory

5:30 - 6:00 "*Applications of Anomalous Small Angle X-ray Scattering*" - Jeffrey J. Hoyt, Washington State University

Tuesday, October 4

Session IV — **Diffraction**
Chairperson: M. Beno, ANL

8:00 - 8:30 "*Single Crystal Diffraction Using Synchrotron Radiation*" - Ake Kvick, Brookhaven National Laboratory

8:30 - 9:00 "*Chemical Crystallography and Synchrotron Radiation: Recent Experiments and Future Studies*" - Philip Coppens, SUNY at Buffalo

9:00 - 9:30 "*The Use of Powder Diffraction Techniques to Solve Structures of Molecular Sieves*" - John M. Bennett, Union Carbide

9:30 -10:00 "*Physico-Chemical Properties of Biological Liquid Crystals Using Time Resolved X-ray Diffraction*" - Martin Caffrey, Ohio State University

10:00 -10:30 Break

Session V — **Topography and Imaging**
Chairperson: R. Winans, ANL

10:30-11:00 "*Synchrotron X-ray Microtomography, Applications to Chemical Systems*" - Kevin D'Amico, Exxon Research and Engineering

11:00 -11:30 "*Applications of X-ray Synchrotron Topography to Solid State Reactions*" - Michal Dudley, SUNY at Stony Brook

11:30 -12:00 "*X-ray Microprobe Elemental Analysis Using Synchrotron Radiation*" - Stephen R. Sutton, University of Chicago and Brookhaven Laboratory

12:00 -12:30 "*Bonding and Structure of Atomic and Molecular Adsorbates on Surfaces using X-ray Absorption Spectroscopy*" - Joachim Stohr, IBM Almaden Research Center, San Jose

12:30 - LUNCH/Cafeteria - Discussion of the possible formation of a Chemistry Users Group.

PARTICIPANTS

ke Abney
ological, Environmental and
Medical Research
gonne National Laboratory
ilding 202
00 South Cass Avenue
gonne, IL 60439

Ercan E. Alp
Materials Science Division/
Advanced Photon Source
Argonne National Laboratory
Building 223
9700 South Cass Avenue
Argonne, IL 60439

ofilo Aniag Abrajano
emical Technology Division
gonne National Laboratory
ilding 205
00 South Cass Avenue
gonne, IL 60439

Donald Paul Ames
McDonnell Douglas Research
Laboratories
P.O. Box 516
St. Louis, MO 63166

ctor D. Abruna
partment of Chemistry
rnell University
ker Laboratory
haca, NY 14853-1301

Ronald H. Arendt
Corporate Research & Development
General Electric Company
Room 169M8
Building K-1
P.O. Box 8
Schenectady, NY 12301

chael J. Albarelli
partment of Chemistry
rnell University
x 21
ker Laboratory
haca, NY 14853

James V. Beitz
Chemistry Division
Argonne National Laboratory
Building 200
9700 South Cass Avenue
Argonne, IL 60439

J. Allen
terials Science and
Engineering Department
rthwestern University
chnological Institute
45 Sheridan Road
anston, IL 60208

John Michael Bennett
Center Scientific Laboratory
Union Carbide Corporation
Old Saw Mill River Road
Tarrytown, NY 10591

Mark Beno
Chemistry Division
Argonne National Laboratory
Building 200
9700 South Cass Avenue
Argonne, IL 60439

Robert E. Botto
Chemistry Division
Argonne National Laboratory
Building 200
9700 South Cass Avenue
Argonne, IL 60439

Christy Bergman
Chemical Technology Division
Argonne National Laboratory
Building 205
9700 South Cass Avenue
Argonne, IL 60439

Merwyn Brodsky
Materials Science Division
Argonne National Laboratory
Building 223
9700 South Cass Avenue
Argonne, IL 60439

Bruce M. Biwer
Chemical Technology Division
Argonne National Laboratory
Building 205
9700 South Cass Avenue
Argonne, IL 60439

Fred A. Cafasso
Chemistry Division
Argonne National Laboratory
Building 200
9700 South Cass Avenue
Argonne, IL 60439

Allen E. Blaurock
Research & Development
Kraft, Inc.
801 Waukegan Road
Glenview, IL 60025

Martin D. Caffrey
Chemistry Department
Ohio State University
120 West 18th Avenue
Columbus, OH 43210-1173

John Karl Bohlke
Chemical Technology Division
Argonne National Laboratory
Building 205
9700 South Cass Avenue
Argonne, IL 60439

Keith G. Calkins
Chemical Technology Division
Argonne National Laboratory
Building 205
9700 South Cass Avenue
Argonne, IL 60439

G. Slade Cargill
IBM T. J. Watson Research Center
30-060
P.O. Box 218
Yorktown Heights, NY 10598

Stephen P. Cramer
Electromagnetics Department
Schlumberger-Doll Research
Old Quarry Road
Ridgefield, CT 06877

Kathleen A. Carrado
Chemistry Division
Argonne National Laboratory
Building 200
9700 South Cass Avenue
Argonne, IL 60439

Larry A. Curtiss
Chemical Technology Division
Argonne National Laboratory
Building 200
9700 South Cass Avenue
Argonne, IL 60439

Chong-Hwan Chang
Biological, Environmental and
Medical Research
Argonne National Laboratory
Building 202
9700 South Cass Avenue
Argonne, IL 60439

Kevin L. D'Amico
Exxon Research & Engineering
Route 22
East Clinton Township
Annandale, NJ 08801

Yanglai Cho
Advanced Photon Source
Argonne National Laboratory
Building 360
9700 South Cass Avenue
Argonne, IL 60439

Mukund Shrikrishna Deshpande
Division of Chemistry and
Chemical Engineering
IIT Research Institute
10 West 35th Street
Chicago, IL 60616

Philip Coppens
Chemistry Department
State University of New York
157 Acheson Hall
Buffalo, NY 14214

Michael Dudley
Materials Science and
Engineering Department
State University of New York
at Stony Brook
Stony Brook, NY 11794

Daniel J. Duke
X-Ray Optics Department
Ovonic Synthetic Materials Company, Inc.
1788 Northwood Drive
Troy, MI 48084

Thomas J. Emge
Corporate Research Department
The Procter & Gamble Company
Miami Valley Laboratories
P.O. Box 398707
Cincinnati, OH 45239

Bob Dunlap
Materials Science Division
Argonne National Laboratory
Building 223
9700 South Cass Avenue
Argonne, IL 60439

Laura L. Feezel
Chemistry Division
Argonne National Laboratory
Building 200
9700 South Cass Avenue
Argonne, IL 60439

Pulak Dutta
Department of Physics and Astronomy
Northwestern University
2145 Sheridan Road
Evanston, IL 60208

Gian Felcher
Materials Science Division
Argonne National Laboratory
Building 223
9700 South Cass Avenue
Argonne, IL 60439

Jeff Eastman
Materials Science Division
Argonne National Laboratory
Building 212
9700 South Cass Avenue
Argonne, IL 60439

John R. Ferraro
Chemistry Division
Argonne National Laboratory
Building 200
9700 South Cass Avenue
Argonne, IL 60439

Bruce Edwards
Materials and Components
Technology Division
Argonne National Laboratory
Building 212
9700 South Cass Avenue
Argonne, IL 60439

Frank Y. Fradin
OTD-PR
Argonne National Laboratory
Building 221
9700 South Cass Avenue
Argonne, IL 60439

Mary F. Garbauskas
Corporation Research & Development
General Electric Company
K-1/2C35
P.O. Box 8
Schenectady, Ny 12301

David W. Green
Analytical Chemistry Laboratory
Argonne National Laboratory
Building 205
9700 South Cass Avenue
Argonne, IL 60439

Didier Gavillet
Materials Science and
Engineering Department
Northwestern University
2145 Sheridan Road
Evanston, IL 60208

Dieter M. Gruen
Materials Science Division/
Chemistry Division
Argonne National Laboratory
Building 200
9700 South Cass Avenue
Argonne, IL 60439

Urs W. Geiser
Chemistry Division
Argonne National Laboratory
Building 200
9700 South Cass Avenue
Argonne, IL 60439

Jun Guo
Physics Department
Northwestern University
2145 Sheridan Road
Evanston, IL 60208

David T. Goldman
Assistant Manager for
Laboratory Management
U.S. Department of Energy
9800 South Cass Avenue
Argonne, IL 60439

Richard L. Harlow
Central Research and
Development Department
E. I. Du Pont De Nemours & Co., Inc.
E228/316
P.O. Box 80228
Wilmington, DE 19880-0228

Gordon L. Goodman
Chemistry Division
Argonne National Laboratory
Building 200
9700 South Cass Avenue
Argonne, IL 60439

Robert G. Hayes
Department of Chemistry
University of Notre Dame
Notre Dame, IN 46556

Edvard Heiberg
Physics Department
The University of Chicago
GHJ-116
5747 South Ellis Avenue
Chicago, IL 60637

Jeffrey J. Hoyt
Mechanical and Materials
Engineering Department
Washington State University
Pullman, WA 99164

Glenn Held
Physical Sciences Department
IBM Watson Research Center
20-158
P.O. Box 218
Yorktown Heights, NY 10598

Russell H. Huebner
Advanced Photon Source/PA
Argonne National Laboratory
Building 360
9700 South Cass Avenue
Argonne, IL 60439

Brent D. Hermsmeier
Chemistry Department
University of Hawaii
2545 The Mall
Honolulu, HI 96822

Lennox E. Iton
Materials Science Division
Argonne National Laboratory
Building 200
9700 South Cass Avenue
Argonne, IL 60439

Jan Paul Hessler
Chemistry Division
Argonne National Laboratory
Building 200
9700 South Cass Avenue
Argonne, IL 60439

Pete R. Jemian
Materials Science and
Engineering Department
Northwestern University
2145 Sheridan Road
Evanston, IL 60208

Celia Hooper
United Press International
360 North Michigan Avenue
Room 1500
Chicago, IL 60601

Guy Jennings
Materials Science Division
Argonne National Laboratory
Building 223
9700 South Cass Avenue
Argonne, IL 60439

Robert C. Johnson
Central Research &
Development Department
E. I. Du Pont De Nemours & Co., Inc.
228/210
P.O. Box 80228
Wilmington, DE 19880-0228

Thomas E. Klippert
Advanced Photon Source
Argonne National Laboratory
Building 360
9700 South Cass Avenue
Argonne, IL 60439

James Jorgensen
Materials Science Division
Argonne National Laboratory
Building 223
9700 South Cass Avenue
Argonne, IL 60439

Theodore R. Krause
Chemical Technology Division
Argonne National Laboratory
Building 205
9700 South Cass Avenue
Argonne, IL 60439

Rajiv Kalia
Materials Science Division
Argonne National Laboratory
Building 223
9700 South Cass Avenue
Argonne, IL 60439

Ake H. Kvick
Department of Chemistry
Brookhaven National Laboratory
Building 555
Upton, NY 11973

Mineo Kimrua
Biological, Environmental, and
Medical Research Division
Argonne National Laboratory
Building 202
9700 South Cass Avenue
Argonne, IL 60439

Elizabeth M. Larson
Condensed Matter and Materials Science
Lawrence Livermore National Laboratory
L-356
P.O. Box 808
Livermore, CA 94550

Robert J. Klingler
Chemical Technology Division
Argonne National Laboratory
Building 205
9700 South Cass Avenue
Argonne, IL 60439

Hsin-Yi Lee
Department of Materials Science
and Engineering
University of Illinois
1304 West Green Street
Urbana, IL 61801

Ron Lutha
U.S. Department of Energy-AAO
Building 201
9800 South Cass Avenue
Argonne, IL 60439

Carlos A. Melendres
Materials Science Division/
Chemical Technology Division
Argonne National Laboratory
Building 205
9700 South Cass Avenue
Argonne, IL 60439

Victor A. Maroni
Materials Science Division/
Chemical Technology
Argonne National Laboratory
Building 205
9700 South Cass Avenue
Argonne, IL 60439

Paul E. Melnicoff
Chemistry Division
Argonne National Laboratory
Building 200
9700 South Cass Avenue
Argonne, IL 60439

Dan Meisel
Materials Science Division/
Chemistry Division
Argonne National Laboratory
Building 200
9700 South Cass Avenue
Argonne, IL 60439

Tomasz J. Michalski
Chemistry Division
Argonne National Laboratory
Building 200
9700 South Cass Avenue
Argonne, IL 60439

John Meiser
Chemistry Department
Ball State University
Muncie, IN 47304

Dennis Mills
Advanced Photon Source
Argonne National Laboratory
Building 360
9700 South Cass Avenue
Argonne, IL 60439

George Meitzner
Corporate Research Department
Exxon Research & Engineering Co.
Route 22 East
Annandale, NJ 08801

Susan M. Mini
Materials Science Division/
Advanced Photon Source
Argonne National Laboratory
Building 223
9700 South Cass Avenue
Argonne, IL 60439

A. Narayanasamy
Materials Science Division
Argonne National Laboratory
Building 212
9700 South Cass Avenue
Argonne, IL 60439

David E. Moncton
Office of the Director/APS
Argonne National Laboratory
Building 360
9700 South Cass Avenue
Argonne, IL 60439

Darius Nassiry
Biological, Environmental and
Medical Research
Argonne National Laboratory
Building 202
9700 South Cass Avenue
Argonne, IL 60439

Lester R. Morss
Chemistry Division
Argonne National Laboratory
Building 200
9700 South Cass Avenue
Argonne, IL 60439

James R. Norris
Chemistry Division
Argonne National Laboratory
Building 200
9700 South Cass Avenue
Argonne, IL 60439

Harold Myron
Department of Educational Programs
Argonne National Laboratory
Building 223
9700 South Cass Avenue
Argonne, IL 60439

Jens Wolfgang Otto
Materials Science Department
Cornell University
Bard Hall
Ithaca, NY 14853

Zoltan Nagy
Chemical Technology Division
Argonne National Laboratory
Building 200
9700 South Cass Avenue
Argonne, IL 60439

John B. Parise
CR&D Department
DuPont
Experimental Station
Wilmington, DE 19880-0356

Jong-Hee Park
Materials and Components Technology
Argonne National Laboratory
Building 212
9700 South Cass Avenue
Argonne, IL 60439

Leigh Christopher Porter
Chemistry Division/
Materials Science Division
Argonne National Laboratory
Building 200
9700 South Cass Avenue
Argonne, IL 60439

James E. Penner-Hahn
Department of Chemistry
The University of Michigan
930 North University
Ann Arbor, MI 48109-1055

Mohan Ramanathan
Materials Science Division
Brookhaven National Laboratory
Building 510E
Upton, NY 11973

James Christopher Phillips
Chemistry Department
State University of New York at Buffalo
National Synchrotron Light Source
Brookhaven National Laboratory
Upton, NY 11973

Jerome W. Rathke
Chemical Technology Division
Argonne National Laboratory
Building 205
9700 South Cass Avenue
Argonne, IL 60439

Joseph J. Pluth
Department of Geophysical Sciences
The University of Chicago
5734 South Ellis Avenue
Chicago, IL 60637

Stuart A. Rice
Chemistry Department and
James Franck Institute
The University of Chicago
5640 South Ellis Avenue
Chicago, IL 60637

Carl W. Ponader
Corporate Analytical Services
Corning Glass Works
SP-FR-01-8
Corning, NY 14831

Jim Richardson
Intense Pulsed Neutron Source
Argonne National Laboratory
Building 360
9700 South Cass Avenue
Argonne, IL 60439

Nicolas Y. Rivier
Materials Science Division
Argonne National Laboratory
Building 223
9700 South Cass Avenue
Argonne, IL 60439

Tsun K. Sham
Chemistry Department
The University of Western Ontario
London N6A 5B7
CANADA

Thomas P. Russell
IBM Almaden Research Center
650 Harry Road
San Jose, CA 95120

Gopal Shenoy
Advanced Photon Source
Argonne National Laboratory
Building 360
9700 South Cass Avenue
Argonne, IL 60439

Dale E. Sayers
Physics Department
North Carolina State University
Box 8202 - Cox 417
Raleigh, NC 27695-8202

Richard W. Siegel
Materials Science Division
Argonne National Laboratory
Building 212
9700 South Cass Avenue
Argonne, IL 60439

Arthur J. Schultz
Chemistry Division
Argonne National Laboratory
Building 200
9700 South Cass Avenue
Argonne, IL 60439

Eric B. Sirota
C.R.S.L.
Exxon Research and Engineering Company
Route 22 East
Annandale, NJ 08801

John Delmoth Scott
CAMD Project Office
Louisiana State University
60 University Lakeshore Drive
Baton Rouge, LA 70803

Donald W. Slocum
Department of Educational Programs
Argonne National Laboratory
Building 223
9700 South Cass Avenue
Argonne, IL 60439

Robert Smither
Advanced Photon Source
Argonne National Laboratory
Building 360
9700 South Cass Avenue
Argonne, IL 60439

Joachim Stohr
Department K31
IBM, Almaden Research Center
650 Harry Road
San Jose, CA 95120

Joel A. Snow
OST
The University of Chicago
Building 201
9700 South Cass Avenue
Argonne, IL 60439

W. Elane Streets
Chemical Technology Division
Argonne National Laboratory
Building 205
9700 South Cass Avenue
Argonne, IL 60439

Lynda Soderholm
Chemistry Division
Argonne National Laboratory
Building 200
9700 South Cass Avenue
Argonne, IL 60439

Stephen R. Sutton
Department of the Geophysical Sciences
Brookhaven National Laboratory
Building 318
Upton, NY 11973

Shaila Srinivasan
Biological, Environmental and
Medical Research
Argonne National Laboratory
Building 202
9700 South Cass Avenue
Argonne, IL 60439

Jan Tang
Chemistry Division
Argonne National Laboratory
Building 200
9700 South Cass Avenue
Argonne, IL 60439

Leon M. Stock
Chemistry Division
Argonne National Laboratory
Building 200
9700 South Cass Avenue
Argonne, IL 60439

Ben S. Tani
Chemical Technology Division
Argonne National Laboratory
Building 205
9700 South Cass Avenue
Argonne, IL 60439

Boon Teo
Chemistry Department
University of Illinois
Chicago, IL 60680

David Tiede
Chemistry Division
Argonne National Laboratory
Building 200
9700 South Cass Avenue
Argonne, IL 60439

P. Thiyagarajan
IPNS/Chemistry Division
Argonne National Laboratory
Building 200
9700 South Cass Avenue
Argonne, IL 60439

Frans Trouw
Intense Pulsed Neutron Source
Argonne National Laboratory
Building 360
9700 South Cass Avenue
Argonne, IL 60439

Al C. Thompson
Center for X-Ray Optics
Lawrence Berkeley Laboratory
80-101
1 Cyclotron Road
Berkeley, CA 94720

Trevor A. Tyson
Chemistry Department
Stanford University
Box #30
Stanford, CA 94305

Carol Thompson
IBM Research Division
T. J. Watson Research Center
29-201
P.O. Box 218
Yorktown Heights, NY 10598

John P. Unik
Support Services Division
Argonne National Laboratory
Building 201
9700 South Cass Avenue
Argonne, IL 60439

Marion C. Thurnauer
Chemistry Division
Argonne National Laboratory
Building 200
9700 South Cass Avenue
Argonne, IL 60439

Priya Vashishta
Materials Science Division
Argonne National Laboratory
Building 223
9700 South Cass Avenue
Argonne, IL 60439

Boyd Veal
Materials Science Division
Argonne National Laboratory
Building 212
9700 South Cass Avenue
Argonne, IL 60439

John W. White
Argonne National Laboratory/
Australian National University
Building 360
9700 South Cass Avenue
Argonne, IL 60439

P. James Viccaro
Advanced Photon Source
Argonne National Laboratory
Building 360
9700 South Cass Avenue
Argonne, IL 60439

Hartmut Wiedersich
Materials Science Division
Argonne National Laboratory
Building 212
9700 South Cass Avenue
Argonne, IL 60439

Karl S. Vorres
Chemistry Division
Argonne National Laboratory
Building 211
9700 South Cass Avenue
Argonne, IL 60439

Jack M. Williams
Chemistry Division/
Materials Science Division
Argonne National Laboratory
Building 200
9700 South Cass Avenue
Argonne, IL 60439

Soichi Wakatsuki
Chemistry Department
Stanford University
Stanford, CA 94305

Randall E. Winans
Chemistry Division
Argonne National Laboratory
Building 200/F163
9700 South Cass Avenue
Argonne, IL 60439

Hau Wang
Chemistry Division/
Materials Science Division
Argonne National Laboratory
Building 200
9700 South Cass Avenue
Argonne, IL 60439

Michael J. Winokur
Department of Physics
University of Wisconsin
1150 University Avenue
Madison, WI 53706

Joe Wong
Department of Chemistry and
Materials Science
Lawrence Livermore National Laboratory
P.O. Box 808 - L-356
Livermore, CA 94550

Bernard T. Wood
Department of Geological Sciences
Northwestern University
1847 Sheridan Road
Evanston, IL 60208

Jorg Zegenhagen
Department of Materials, 11542
AT&T Bell Laboratories
Room 1E-442
600 Mountain Avenue
Murray Hill, NJ 079747

Hong Zhang
Chemistry Department
University of Illinois
Chicago, IL 60680